The FAA's Center of Excellence for UAS Research
ASSURE
Alliance for System Safety of UAS through Research Excellence

Final Report

A35 – Identify Wake Turbulence and Flutter Testing Requirements for UAS

17 April 2023

NOTICE

LEGAL DISCLAIMER

The information provided herein may include content supplied by third parties. Although the data and information contained herein has been produced or processed from sources believed to be reliable, the Federal Aviation Administration makes no warranty, expressed or implied, regarding the accuracy, adequacy, completeness, legality, reliability or usefulness of any information, conclusions or recommendations provided herein. Distribution of the information contained herein does not constitute an endorsement or warranty of the data or information provided herein by the Federal Aviation Administration or the U.S. Department of Transportation. Neither the Federal Aviation Administration nor the U.S. Department of Transportation shall be held liable for any improper or incorrect use of the information contained herein and assumes no responsibility for anyone's use of the information. The Federal Aviation Administration and U.S. Department of Transportation shall not be liable for any claim for any loss, harm, or other damages arising from access to or use of data or information, including without limitation any direct, indirect, incidental, exemplary, special or consequential damages, even if advised of the possibility of such damages. The Federal Aviation Administration shall not be liable to anyone for any decision made or action taken, or not taken, in reliance on the information contained herein.

TECHNICAL REPORT DOCUMENTATION PAGE

1. Report No. A11L-UAS-1875.UAS075	**2. Government Accession No.**	**3. Recipient's Catalog No.**

4. Title and Subtitle Final Report: A35 - Identify Wake Turbulence and Flutter Testing Requirements for UAS	**5. Report Date** 17 March 2023 **6. Performing Organization Code**
7. Author(s) Mark S Ewing, PhD, University of Kansas, https://orcid.org/0000-0001-5982-6219 Zhi J Wang, PhD, University of Kansas, https://orcid.org/0000-0002-6203-6303 Shawn Keshmiri, PhD, University of Kansas, https://orcid.org/0000-0002-7371-1255 Haiyang Chao, PhD, University of Kansas, https://orcid.org/0000-0001-5883-8138 ZhongQuan Charlie Zheng, PhD, Utah State University Matthew McCrink, PhD, Ohio State University, https://orcid.org/0000-0003-2212-2132 Dhuree Seth, PhD, Ohio State University, https://orcid.org/0000-0001-7759-6453 Rohith Giridhar, PhD, University of Kansas, https://orcid.org/0000-0002-0156-0611 Salman K. Rahmani, University of Kansas, salmanr@ku.edu Mozammal Chowdhury, University of Kansas, mmhc@ku.edu Aaron McKinnis, University of Kansas, amckinnis@ku.edu Jeffrey Xu, University of Kansas, jeffreyxu@ku.edu Hady Benyamen, University of Kansas, hady@ku.edu Justin Matt, University of Kansas, jmatt1998@ku.edu Zhenghao Lin, University of Kansas, lin.zhenghao@ku.edu Mosarruf Hossain Shawon, University of Kansas, mosarruf@ku.edu Ross Heidersbach, Ohio State University, heidersbach.2@buckeyemail.osu.edu	**8. Performing Organization Report No.**
9. Performing Organization Name and Address University of Kansas: 1450 Jayhawk Blvd. Lawrence, KS 66045-7535 Ohio State University: 281 W Lane Ave, Columbus OH 43210	**10. Work Unit No.** **11. Contract or Grant No.** 15-C-UAS-KU-05
12. Sponsoring Agency Name and Address Federal Aviation Administration Washington, DC 20591	**13. Type of Report and Period Covered** Final Report (11 Aug 2020-17 Apr 2023) **14. Sponsoring Agency Code** **5401**

15. Supplementary Notes
16. Abstract There are two studies reported here. The first is to identify the severity of a wake vortex encounter for an Unmanned Aircraft System (UAS). The purpose is to assist the FAA in formulating a risk analysis. Both mathematical simulations and flight tests are used to replicate wake encounters. Metrics to establish conditions leading to loss of control are proposed. Flight tests of UAS through real wake vortices are recommended. A process for mitigation of threat of loss of control via separation is proposed. The other study is focused on establishing appropriate testing requirements for fixed wing UAS to avoid wing flutter. The purpose is to assist the FAA setting testing requirements. A flutter flight test vehicle has been designed, built, and flight tested.

17. Key Words Unmanned Aircraft System (UAS), wake vortex, wake vortex encounter, simulation, loss of control, correlation of aircraft states	**18. Distribution Statement** No restrictions. This document is available through the National Technical Information Service, Springfield, VA 22161.

19. Security Classification (of this report) Unclassified	**20. Security Classification (of this page)** Unclassified	**21. No. of Pages** 195	**22. Price**

Form DOT F 1700.7 (8-72) Reproduction of completed page authorized

TABLE OF CONTENTS

LIST OF FIGURES

LIST OF TABLES

LIST OF ACRONYMS

AAA	Advanced Aircraft Analysis
AC	Aerodynamic Center
AGL	Above Ground Level
ANN	Artificial Neural Network
AOA	Angle of Attack
AOS	Angle of Sideslip
APA	AVOSS Prediction Algorithm
AVOSS	Aircraft Vortex Spacing System
BM	Base Model
CFD	Computational-Fluid-Dynamics
CG	Center of Gravity
CPR	Correction Procedure via Reconstruction
D2P	Deterministic 2-Phase Model
DOF	Degree of Freedom
DRB	Disturbance Rejection Bandwidth
DRP	Disturbance Rejection Peak
EDR	Eddy Dissipation Rates
FAA	Federal Aviation Administration
FR	Flux Reconstruction
FRF	Frequency Response Function
GM	Gain Margin
GPS	Global Positioning Satellite
GVT	Ground Vibration Testing
ILES	Implicit Large Eddy Simulation
IMU	Inertial Measurement Unit
KU	University of Kansas
LAANC	Low Altitude and Notification Capability
LE	Leading Edge
LES	Large Eddy Simulation
LoC	Loss of Control
LoRC	Limit of Reliable Simulation
LTI	Linear Time-Invariant
LWFAM	Linear Wind Field Approximation Method
LQR	Linear Quadratic Regulator
MC	Monte Carlo
MPC	Model Predictive Controller
MUSCL	Monotonic Upstream-centered Scheme for Conservation Laws
NAS	National Airspace System
NASA	National Aeronautics and Space Administration
N.S	Navier-Stokes
OSU	Ohio State University
PCR	Pitch Control Ratio

PD	Proportional Derivative Controller
PID	Proportional-Integral-Derivative Controller
PFM	Parametric Flutter Margin
PM	Phase Margin
RANS	Reynolds-Averaged Navier Stokes
RMC	Roll Moment Coefficient
RCR	Roll Control Ratio
RMSE	Root Mean Square Error
RPM	Revolutions Per Minute
S&C	Stability and Control
SCD	Stability and Control Derivative
sUAS	Small Unmanned Aircraft System
SWC	Sliding Window Correlation
TAS	True Airspeed
TASS	Terminal Area Simulation System
TDP	TASS Driven Algorithms for Wake Prediction
TE	Trailing Edge
TRC	Transportation Research Center
UAM	Urban Air Mobility
UAS	Unmanned Aircraft System
VLM	Vortex Lattice Method
WVE	Wake Vortex Encounter

LIST OF SYMBOLS

b	Wingspan
c	Chord Length
l	Rolling Moment
m	Pitching Moment
n	Yawing Moment
p	Roll Rate
q	Pitch Rate
r	Yaw Rate, Pearson’s Correlation Coefficient
u	Body X-axis Velocity
v	Body Y-axis Velocity
w	Body Z-axis Velocity
ρ	Air Density
ϕ	Roll Angle
θ	Pitch Angle
ζ	Damping Coefficient
ψ	Yaw Angle
Γ	Wake Vortex Circulation
a_x	Acceleration in Aircraft Body X-axis
a_y	Acceleration in Aircraft Body Y-axis
a_z	Acceleration in Aircraft Body Z-axis
b_0	Initial Wake Vortex Separation
C_D	Drag Coefficient
C_l	Rolling Moment Coefficient
C_L	Lift Coefficient
C_m	Pitching Moment Coefficient
C_n	Yawing Moment Coefficient
C_X	Force Coefficient in the X Direction
C_Y	Force Coefficient in the Y Direction
C_Z	Force Coefficient in the Z Direction

f_x	X Component of the Resultant Pressure Force Acting on the Vehicle
f_y	Y Component of the Resultant Pressure Force Acting on the Vehicle
f_z	Z Component of the Resultant Pressure Force Acting on the Vehicle
K_d	Derivative Controller Gain
K_i	Integral Controller Gain
K_p	Proportional Controller Gain
p_d	Aircraft Down Position
p_e	Aircraft East Position
p_g	Wake Rotational Velocity X-Component
p_n	Aircraft North Position
p_r	Relative Roll Rate
q_g	Wake Rotational Velocity Y-Component
q_r	Relative Pitch Rate
r_c	Wake Vortex Core Radius
r_g	Wake Rotational Velocity Z-Component
r_r	Relative Yaw Rate
u_g	Body X-axis Wake Velocity
u_r	Body X-axis Relative Velocity
v_g	Body Y-axis Wake Velocity
v_r	Body Y-axis Relative Velocity
w_g	Body Z-axis Wake Velocity
w_r	Body Z-axis Relative Velocity
W_{leader}	Weight of the Leader Aircraft
V_{LAS}	Leader Aircraft Speed
δ_a	Aileron Deflection
δ_e	Elevator Deflection
δ_r	Rudder Deflection
δ_t	Throttle Percentage
ω_n	Natural Frequency
Γ_0	Vortex Circulation

EXECUTIVE SUMMARY

The Federal Aviation Administration (FAA) has determined that there is a need to identify the analysis and testing requirements to assess: the severity of inadvertent Unmanned Aircraft System (UAS) wake vortex encounters (WVE) and the severity of wing flutter for a fixed wing UAS. These studies, along with associated safety analyses, are needed to support policy, guidance, and procedures to mitigate the risk of UAS upset due to wake encounter and flutter.

The approach taken to address WVEs is to use simulation of wake encounters for a range of UAS, and to validate simulation via flight test. The simulation and flight test procedures thus developed are general in nature and can be used to extrapolate to a wider range of UAS.

The overall benefit of this research is to support safe integration of UAS into the National Airspace System (NAS) by assisting the FAA assess risks of UAS upsets due to wake vortex encounters and flutter events. As such the results of simulation and testing are aimed at providing methods to support rule-making by the FAA.

The sponsor has provided a number of research questions which have been considered and which form the overall guidance for the studies reported here. These are:

- What are the important parameters when assessing UAS response to wake vortex encounters?
- What is the severity of UAS upset due to wake vortex encounters?
- What mitigations might be considered to decrease the severity of UAS upset?
- What degree of flight testing is required to validate wake encounter assessments?
- What are the important parameters when assessing the potential for flutter for fixed-wing UAS?
- What degree of flight testing is required to validate flutter potential assessments?

The key findings are:

- Wake vortices from large aircraft pose a significant risk of upset to small UAS over long distances, up to multiple miles, below the path of the wake-generating aircraft, including directly below and laterally in the presence of a cross-wind.
- The severity of an adverse UAS wake vortex encounter includes the possibility of either loss of control or structural failure—possibly leading to impact with the ground.
- When the ratio of wake-induced velocities to UAS cruise velocity is high, linear aerodynamic models used for response simulation fail to faithfully predict UAS response.
- The severity of adverse UAS wake vortex encounters can be reduced to the severity of encounters with ambient meteorological conditions by physical segregation from volumes of airspace below and along-side known, large aircraft flight paths.
- The severity of adverse UAS wake encounter might be able to be reduced by employing an autopilot with the ability to recover from an entry into loss of control, especially if the UAS has the ability to sense the entry into loss of control, and especially if significant excess thrust is available to "power through" entry into loss of control.
- The potential of the ability to predict the approach to the loss of control (e.g., using the aircraft's state and control input correlations) and to adopt mitigating guidance commands (e.g., increasing cruise velocity) may prove to be useful for autonomously avoiding unrecoverable loss of control.

- Reducing ~~for~~ the expected uncertainties in engineering level dynamic models through system identification flight testing is essential to reliably predict the response of UASs during wake vortex encounters.
- Flights through air velocity fields representative of wake vortices provide one method of determining the susceptibility of a UAS to upset; to be most useful:
    - the velocity of the air through which the UAS fly must be known in some way.
    - the degree of upset seen in flight test must be predicted in simulation.
- Flights through actual large aircraft vortices are the best type of flight test to assess UAS response to a WVE.
- The stiffness and mass distribution of a UAS wing must be known and verified by ground vibration testing to assess flutter risk.
- Flight testing of a wing is essential if it has a predicted, air-density-adjusted flutter speed approaching the maximum expected dive speed.

Key Conclusions:

The comparisons between physics-based simulations and actual flight test validations highlight the shortcomings of UAS Linear Time-Invariant (LTI) dynamic models in predicting small Unmanned Aircraft System (sUAS) response to a wake vortex encounter. Although nonlinear 6 Degree of Freedom (6DOF) simulations retain some degree of nonlinear effects (i.e. the coupling of longitudinal and lateral states), they cannot capture the accurate response of hazardous wake encounters because of the use of linear aerodynamic models. These issues are rooted in the unsteady and nonlinear nature of aerodynamic forces and moments during UAS wake encounters. Complex time and angular rate-dependent couplings between dynamic states cannot be captured by simplified, engineering-level linear dynamic models. This is why the aerodynamic forces predicted in the simulations deviate significantly from actual validation flight tests.

The research team recommends the following for potential follow-on work:

- Flight testing of a range of small UAS through actual wake vortices with:
    - Some method of identifying where the wakes are, for instance, using ADS-B transmissions from the generating aircraft to provide guidance as well as adequate separation.
    - Some method of measuring the air velocity through which it flies.
    - Simulations which predict the response.
- Further development of a process to mitigate the risk of UAS loss of control in a wake vortex encounter by physical separation distances.
- To enhance the simulation capabilities to capture the extreme response:
    - Continue development of the non-linear force, moment and propulsion algorithms pioneered in the current research.
    - Continue flights through air velocity fields generated by wind machines, including larger wind fields.

1 INTRODUCTION & BACKGROUND

The FAA has determined that there is a need to identify the analysis and testing requirements to assess: the severity of inadvertent UAS wake vortex encounters; and, the severity of wing flutter for a fixed wing UAS. These studies, along with associated safety analyses, are needed to support policy, guidance, and procedures to mitigate the risk of UAS upset due to wake encounter and flutter.

The approach taken to assess the severity of a WVE is to use simulation of wake encounters for a range of UAS, and to validate simulation via flight test. The simulation and flight test procedures thus developed are general in nature and can be used to extrapolate to a wider range of UAS.

The overall benefit of this research is to support safe integration of UAS into NAS by assisting the FAA assess risks of UAS upsets due to wake vortex encounters and flutter events. As such the results of simulation and testing are aimed at providing methods to support rule-making by the FAA.

1.1 Background

Wake vortex encounters for crewed aircraft are known to be a safety hazard; so, much has been done to mitigate risk of loss of aircraft control during a wake vortex encounter. In particular, aircrew training and spatial/temporal spacing of aircraft on takeoff and landing have proved successful.

For small UAS, little is known about the process to predict the level of vortex "strength" which would be expected to cause loss of control. There are several models of wake vortices which predict vortex strength as a function of time since vortex generation and the Eddy Dissipation Rate (EDR) in the ambient atmospheric state. Therefore, vortex strength can be predicted as a function of the properties of the wake-generating aircraft, that is, weight, flight velocity and wingspan. But, especially when the vertical component of a vortex is large with respect to the airspeed of the UAS, UAS dynamic models fail to faithfully predict response, including the likelihood of loss of control.

Further, much is known about the avoidance of wing and empennage flutter of crewed aircraft. Extensive analysis and flight test—and, often wind tunnel tests as well—are used to certify a wing against flutter. However, especially because UAS and crewed aircraft wings use vastly different structural concepts, little is known about the steps needed to avoid wing and empennage flutter in a UAS.

1.2 Research questions

- What are the important parameters when assessing UAS response to wake vortex encounters?
- What is the severity of UAS upset due to wake vortex encounters?
- What mitigations might be considered to decrease the severity of UAS upset?
- What degree of flight testing is required to validate wake encounter assessments?
- What are the important parameters when assessing the potential for flutter for fixed wing UAS?
- What degree of flight testing is required to validate flutter potential assessments?

A gaps analysis was conducted and reported in the Research Task Plan. The key findings with regard to wake vortex encounter were:

- Many wake vortex models have been developed and are available to provide the air velocity environment through which a UAS may fly.
- Very little research has been conducted on the response of UAS to wake vortex encounter.
- Very little research has been conducted on the prediction of flutter of UAS lifting surfaces.

1.3 Top –level answers to research questions

The key findings, listed in terms of the research questions from the sponsor follow.

- The most important parameters to assess UAS response to wake vortex encounters:
  - Vortex strength
  - Ratio of UAS velocity to wake vortex velocity
  - Robustness of controller, especially the ability to identify onset of loss of control
  - Availability of reserve thrust to power through a wake encounter
- Severity of UAS upset due to wake vortex
  - Possible structural failure due to high accelerations
  - Loss of control, potentially hitting crewed aircraft, but more likely people or property on the ground
- Mitigate the severity of UAS upset in a wake vortex encounter
  - Spatial and/or temporal separation from vortices, both vertically and horizontally, based on commercial aircraft flight paths as their wakes descend and drift in cross-winds
  - High robustness controllers for UAS
  - Reserve thrust for UAS with controllers capable of identifying potential loss of control
- Degree of flight testing required to validate wake encounter assessments
  - Flight testing is required to validate aircraft dynamic models for use in simulation: otherwise, uncertainty limits the usefulness of modelling.
  - Flight testing to loss of control necessary to establish bounds of operation: intentional flight up to and beyond stall has been shown to be one way of establishing bounds

- The most important parameters when assessing the potential for flutter for fixed wing UAS
  - The stiffness and mass distribution of a UAS wing—and the natural frequencies of vibration–must be known and verified by ground vibration testing to assess flutter risk.
- The degree of flight testing is required to validate flutter potential assessments
  - Flight testing of a wing to at least the maximum expected dive speed is essential

1.4 Navigating this document

Section 2 covers the use cases studied, the basics of the wake vortex models used, and the description of large fans/wind machines used to simulate segments of wake vortices for the flight tests conducted.

Section 3 focuses on simulation of fixed wing UAS models encountering a wake vortex. Two physics-based mathematical models are presented, the Vortex Lattice Method (VLM) and the Linear Wind Field Method (LWFM). Using the LWFM, attitude hold controllers are used for the simulations. Then another model using the VLM for aerodynamic forces and moments is used, but with non-linear lift curve coefficients as an attempt to include one of many known non-linearities. Finally a path-following controller is used for simulated wake vortex encounters. The simulation methods used are representative of available engineering-level modelling techniques in simulation. A range of candidate methods of predicting entry into loss of control are presented, including heuristics, such as likely un-recoverable pitch rates, limits of control authority and exceedance of stall angle of attack, among others. A novel method for loss of control prediction, the Sliding Window Correlation (SWC) method is also presented and shown to be useful for flight data. The section then moves to a discussion of the validation flight testing conducted, simulation of the flight tests conducted and using the SWC to identify entry into loss of control. Embedded in the section is a lengthy discussion of the importance of proper tuning of mathematical models through flight testing.

Section 4 focuses on multirotor response to wake vortices.

Section 5 describes the design, construction, and flight test of a UAS flutter flight test vehicle

2 UAS WAKE ENCOUNTER DESCRIPTION

2.1 UAS use cases studied

Wake vortex encounters can occur when a UAS flies behind or below a wake vortex-generating aircraft. Since most UAS currently fly below 400 feet Above Ground Level (AGL), the most likely location for an encounter is near an arrival or departure path at an airport, specifically below and beside commercial aircraft takeoff and landing glide slopes. As such, most of the simulations reported here are for UAS flight through aircraft wake vortices at a variety of trajectory "cut" angles, ranging from a path perpendicular to the direction of the wake-generating aircraft, to a path parallel to the path of the generating aircraft. Figure 2.1 depicts two UAS encounter scenarios below the wake vortex pair of a "wake-generating aircraft" landing.

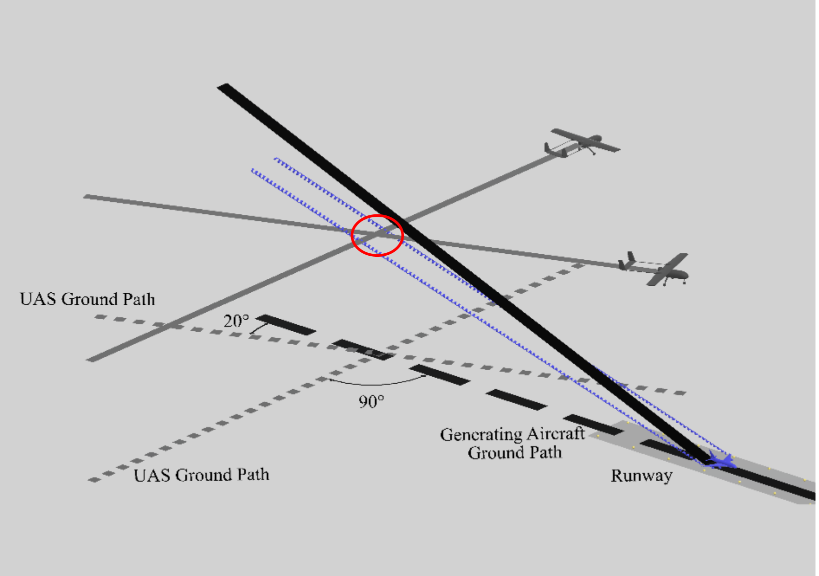

Figure 2-1. Two UAS encounters with a descending wake vortex pair from an arriving aircraft.

For a given flight altitude, the severity of the encounter in a 90 degree or some smaller degree "cut" behind the wake is a function of the time (or distance) since the wake was generated as well as the Eddy Decay Rate (EDR). Therefore, if it is known at what vortex strength a loss of control is likely, a “safe” distance from the end of the runway can be determined. Simulation of such wake encounters are presented in this report.

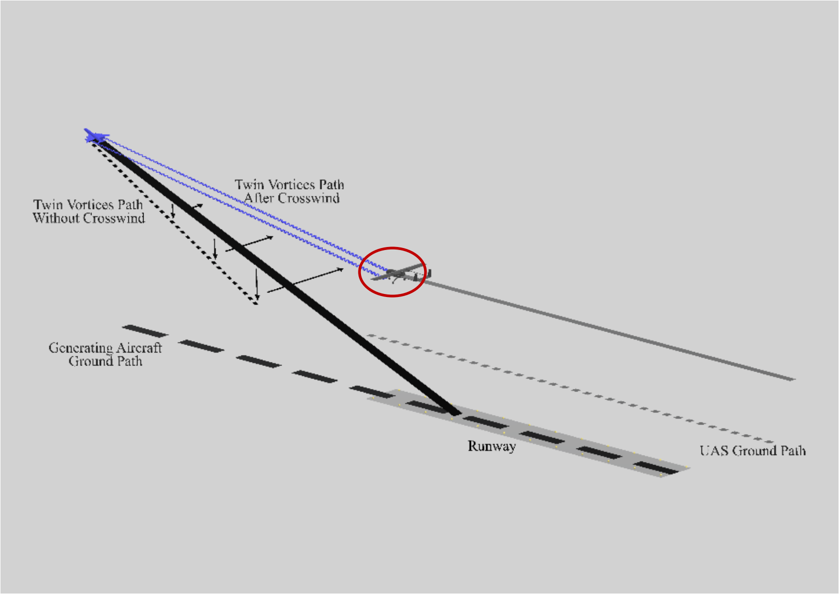

Figure 2-2. UAS encounter with a wake vortex pair—from a departing aircraft—which is descending and being blown laterally by a cross-wind.

Figure 2-2 depicts a UAS encounter with the wake vortex pair of a generating aircraft on departure which has been “blown” laterally by a cross-wind. For a given vortex strength, EDR and cross-wind, there is a lateral distance from the runway at which a UAS may be put into loss of control. Simulations of this type of wake encounter are also presented in this report.

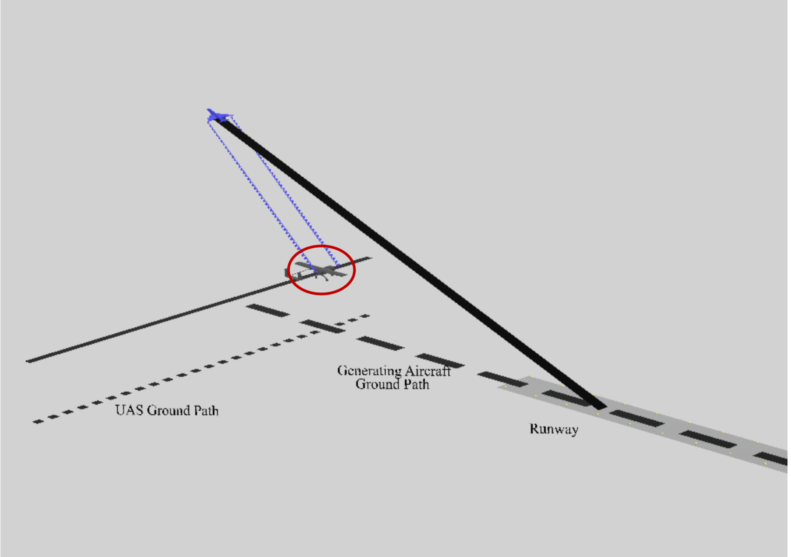

Figure 2-3. UAS encounter with a wake vortex pair descending below a departing aircraft.

Figure 2-3 depicts a UAS encounter with the wake vortex pair of a generating aircraft after takeoff which is sinking in the absence of a cross-wind. This type of encounter is also presented herein.

2.2 Wake vortex models used to provide air velocity environments for study

Aircraft wake vortices are vortical structures in the atmosphere generated by the passing of an aircraft in flight. They are caused by air drawn from the lower surface of the wing to the upper surface following the pressure distribution field to form a vortex to trail from each wingtip. The strength of wake vortices is mainly determined by the aircraft wingspan, weight, and airspeed [1].

Many wake vortex models have been developed and used for simulation of wake flow fields generated by manned aircraft [2]. Two types of widely used wake models are flow field models (e.g., Lamb-Oseen, Burham-Hallock, Proctor [3]) and wake transport and decay prediction models (e.g., Aircraft Vortex Spacing System (AVOSS) including AVOSS Prediction Algorithm (APA), Terminal Area Simulation System (TASS) Driven Algorithms for Wake Prediction (TDP) [4], and the deterministic 2-Phase Model (D2P) [5]). The Burnham-Hallock flow field model and Sarpkaya decay model were selected in this project due to their wide uses in air traffic management.

2.2.1 Burnham-Hallock Model

The Burnham-Hallock model is a flow field model that describes the wake velocity field for a single wake vortex in a 2D plane perpendicular to the vortex rotational axis. It can be written as [1, 6]:

$$v_\theta(r) = \frac{\Gamma_0}{2\pi r}\frac{r^2}{r^2+{r_c}^2} \tag{1}$$

$$r = \sqrt{(y-y_0)^2+(z-z_0)^2} \tag{2}$$

where (y_0, z_0) is the vortex center, Γ_0 is the vortex circulation, r is the distance from vortex center and r_c is the vortex core radius defined at the maximum tangential velocity. The tangential velocity field around the wake cores of a B747-400 is calculated using the Burnham-Hallock model and is shown in Figure 2-4, which has an initial circulation of $565\ m^2/s$.

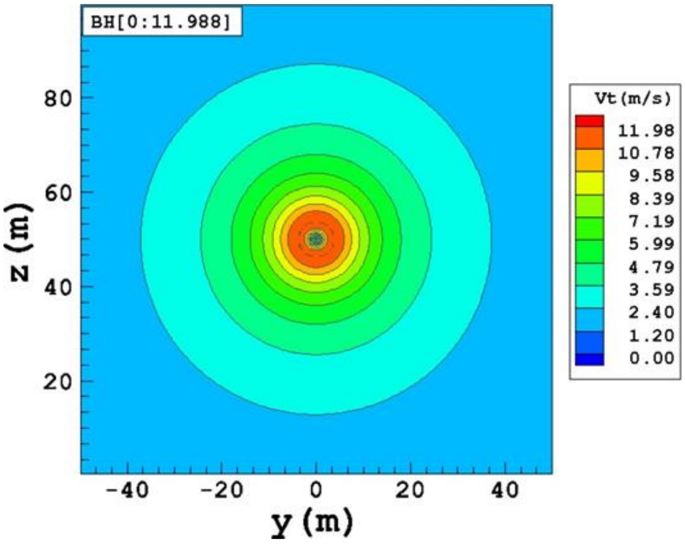

Figure 2-4. Burnham-Hallock model for B747-400 at initial circulation $\Gamma = 565\frac{m^2}{s}$.

2.2.2 Sarpkaya Decay Model

In addition to the wake flow field model, wake vortex decay models, or Eddy-dissipation models, are also needed for wake encounter simulation and predictions. Sarpkaya wake decay model was implemented in this project due to its wide use and easy implementation [6]. It can be described as:

$$\frac{\Gamma_i}{\Gamma_0} = \exp(-0.45\frac{d(\varepsilon\Gamma_0)^{0.25}}{\rho V b_0}) \tag{3}$$

$$\Gamma_0 = \frac{W_{leader}}{\rho b_0 V_{LAS}} \tag{4}$$

where ε is the turbulence constant, EDR, b_0 is the vortex span (π/4 of the wingspan of the leading aircraft), W_{leader} is the weight of the leader aircraft, ρ is the air density, d is the distance from the vortex generation, and V_{LAS} is the speed of leader aircraft.

An example for Sarpkaya wake decay prediction is shown in Figure 2-5 including high, medium, and low EDR for a Boeing 737-800 aircraft. It can be observed that the wake decays faster in the high EDR case (0.047 $m^{2/3}s^{-1}$) than medium and low EDR cases (0.0121 and 0.001 $m^{2/3}s^{-1}$, respectively). It is worth emphasizing that the overall trend and decay magnitude predicted by the Sarpkaya model are comparable with a similar study using the APA model of the National Aeronautics and Space Administration (NASA) AVOSS software [4, 8].

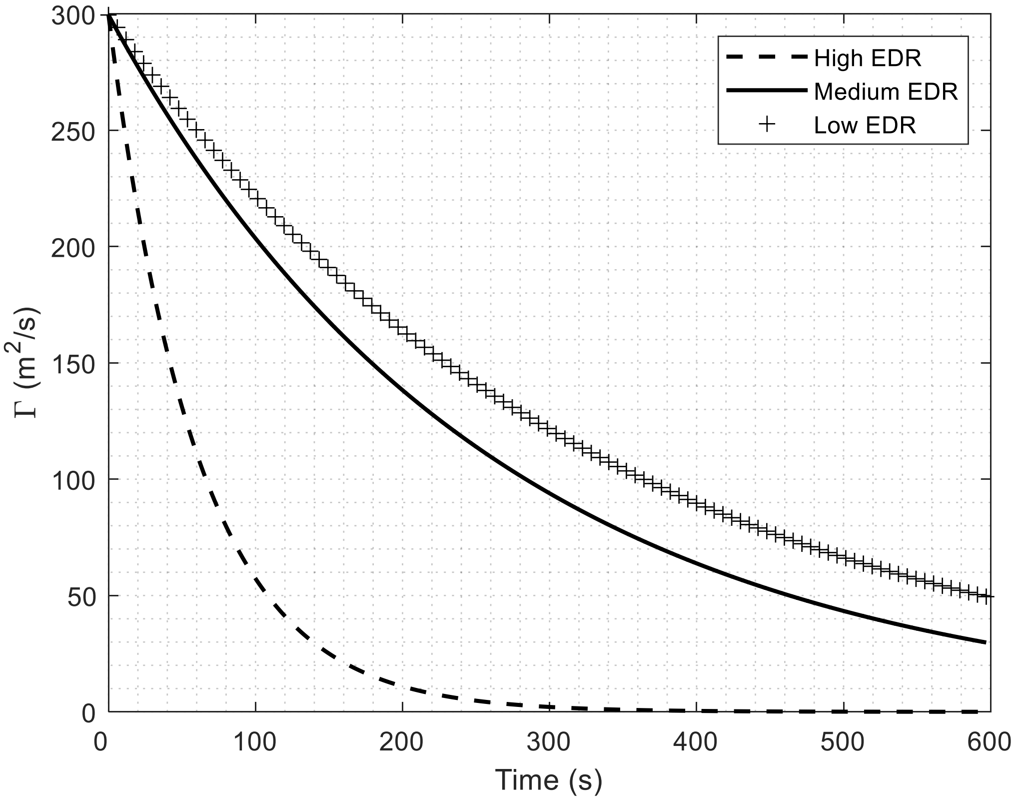

Figure 2-5. Sarpkaya decaying model prediction for a B737-800.

2.3 Potential wake hazard zones for UAS operations

This section shows potential wake vortex regions predicted by the above models at or close to an airport, which may be dangerous for UAS operations. The targeted airspace is less than 200 m altitude and within 5 nautical miles of the airport runway. Example case studies are provided on the predicted wake vortex regions generated by a landing aircraft in different cross wind and experimental conditions.

The wake vortex regions at or close to an airport can be predicted by the NASA AVOSS[4], DLR D2P [5], or other methods based on the flight path of the wake generating aircraft and the ambient weather conditions (e.g., cross wind, head wind, EDR, temperature). Once formed, wake vortices will normally sink slowly to the ground while moving with the ambient wind. The wake descent rate can be approximated by (5) [1]:

$$w_w = \Gamma_0/(2\pi b_0) \tag{5}$$

Since the initial departing and final approaching path for most commercial airliners are straight (ascending or descending along the runway), the generated wake vortices may stay in the airspace along the runway or above at an airport during calm days. For a more general case with either cross wind or head wind, the wake vortices may be carried to regions far away from the flight path of the wake generating aircraft. NASA and DLR have developed AVOSS and D2P software to predict the wake transport and decay during the final approach of a landing aircraft [4, 5]. Additionally, the wake trajectory can also be predicted using a simplified wake transport model after combining the flight path information of wake-generating aircraft with ambient wind conditions and empirical wake descent estimates. The simplified wake transport model can be further coupled with the Sarpkaya decay model for predictions of wake vortex location and magnitude at an airport, which can generate similar results with the APA prediction results [7].

A simple example illustrates the particulars of the simplified wake transport and decay model for the landing of a hypothetical transport aircraft. The aircraft flight path angle was set to be 4.3

degrees, shown in Figure 2-6**Error! Reference source not found.**b. The runway is aligned to the north-south direction. The head wind is set to be zero and the cross-wind profile is shown in Figure 2-7**Error! Reference source not found.**a, including moderate wind and strong wind scenarios from the west to the east (10 and 20 knots at 10 m above ground.).

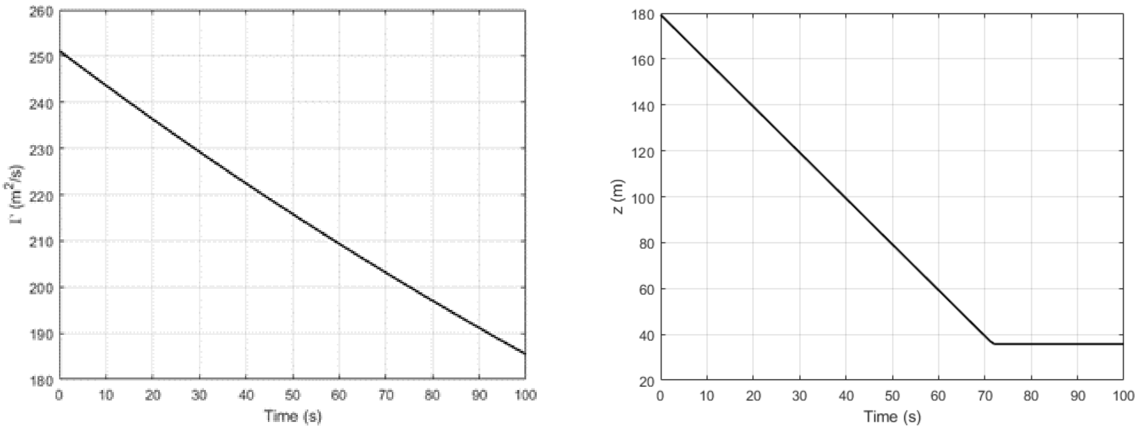

(a) Wake circulation decay (0-100 s) (b) Wake descent (0-100 s)

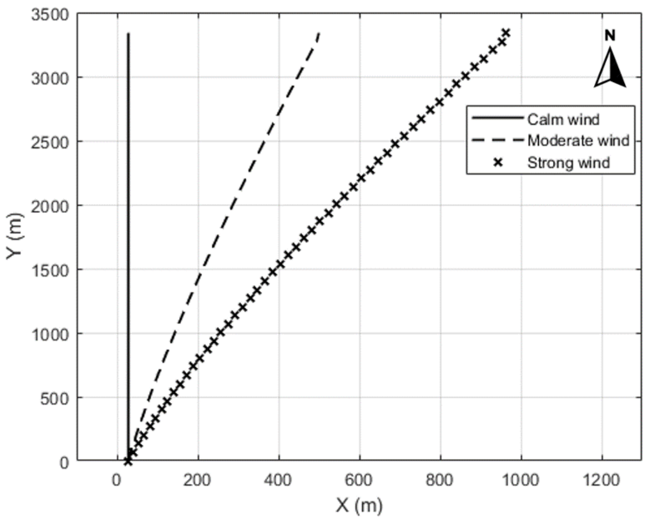

(c) Predicted wake vortex location after vortex generation (up to t = 100 s)

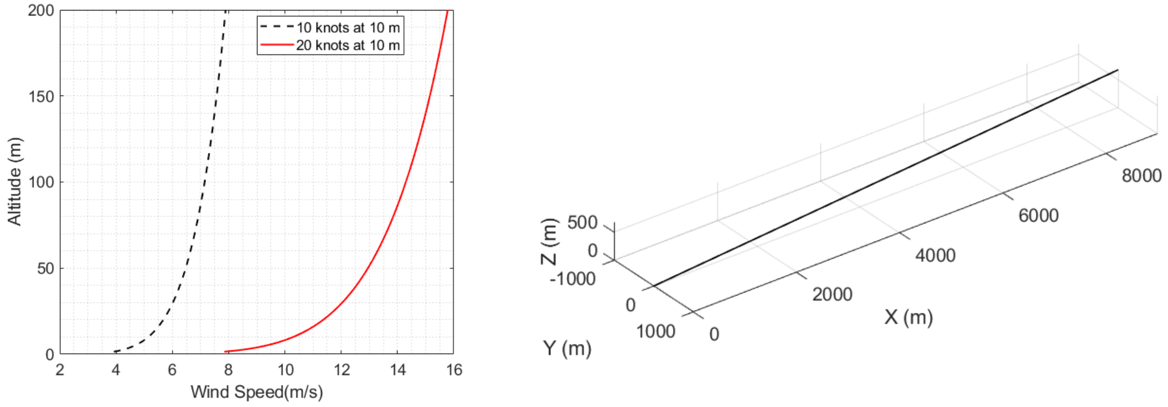

(a) Cross-wind profile using 1/7 power law (moderate and strong)

(b) Hypothetical aircraft approach trajectory

Figure 2-6. Crosswind profile and hypothetical transport aircraft approach trajectory.

The $1/7th$ power law is used to describe the cross-wind profile at low altitudes, shown in (6):

$$V_{W_h} = V_{W_{h_r}} (z/z_{ref})^{1/7} \tag{6}$$

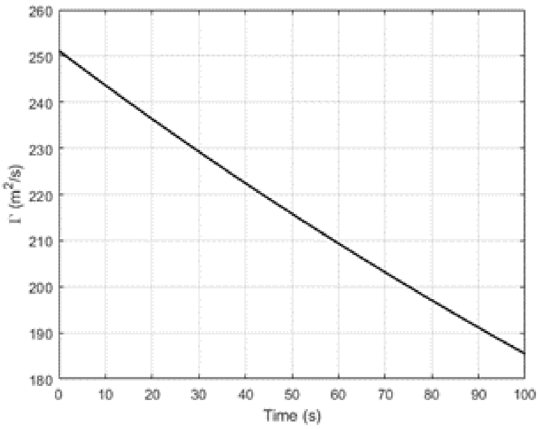

(b) Wake circulation decay (0-100 s)

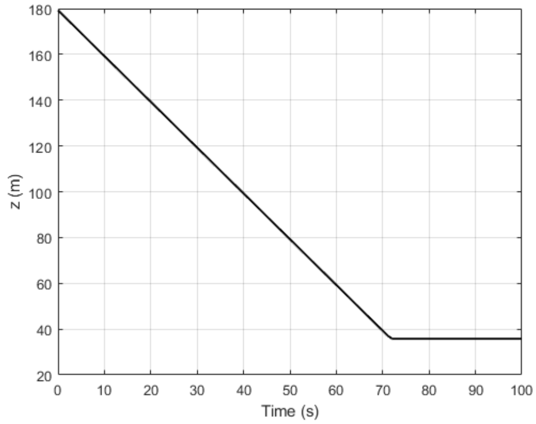

(b) Wake descent (0-100 s)

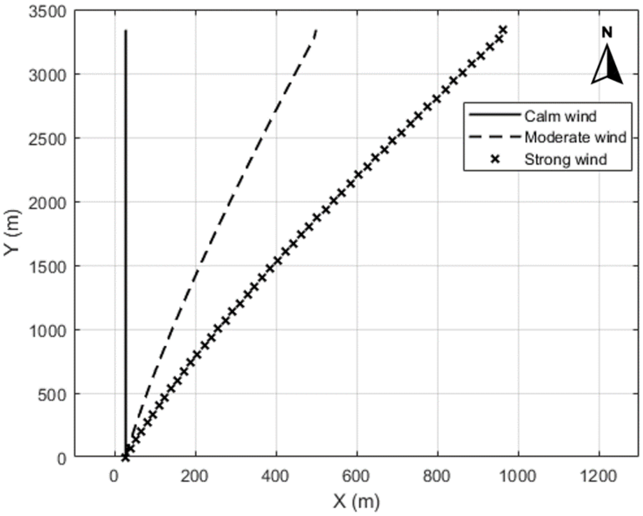

(c) Predicted wake vortex location after vortex generation (up to t = 100 s)

Figure 2-7. Wake vortex intensity and location predictions for a hypothetical wake generating aircraft.

The predicted wake vortex circulation and locations with respect to the wake-generating aircraft are calculated and shown in

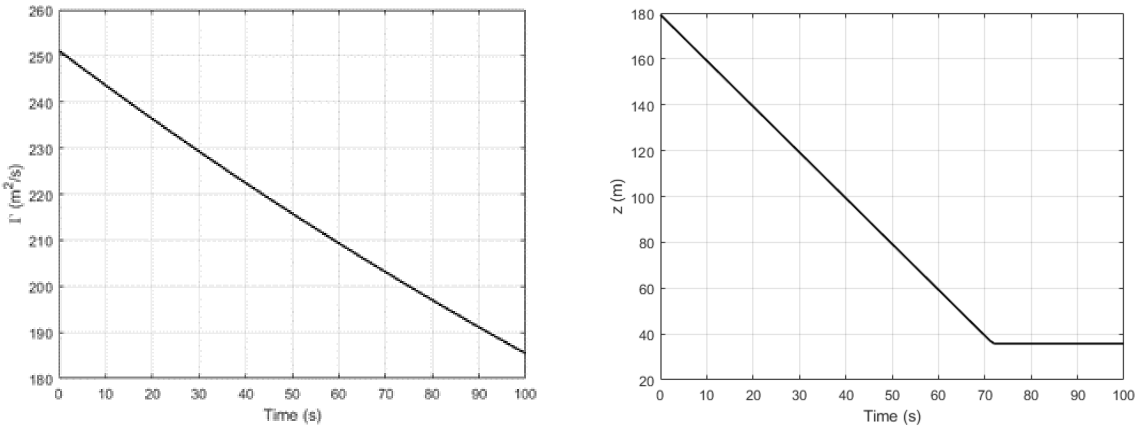

(c) Wake circulation decay (0-100 s) (b) Wake descent (0-100 s)

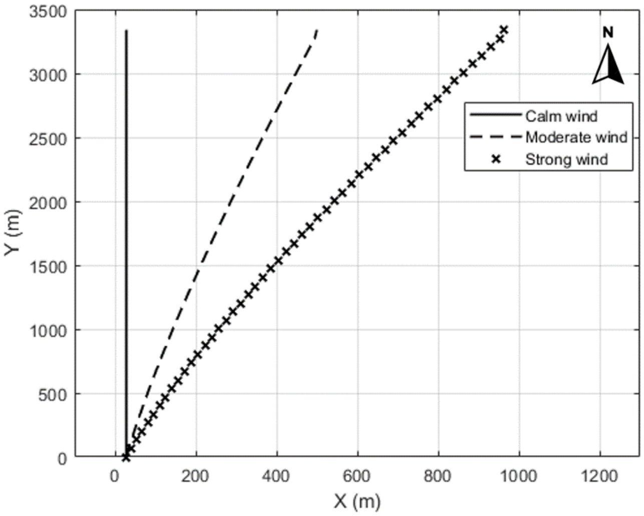

(c) Predicted wake vortex location after vortex generation (up to t = 100 s)

Figure 2-7. The initial wake vortex altitude was set to be 180 m. Both wake transport and strength need to be taken into consideration for sUAS wake hazard evaluations near airports. It can be observed in Figure 2-7a and

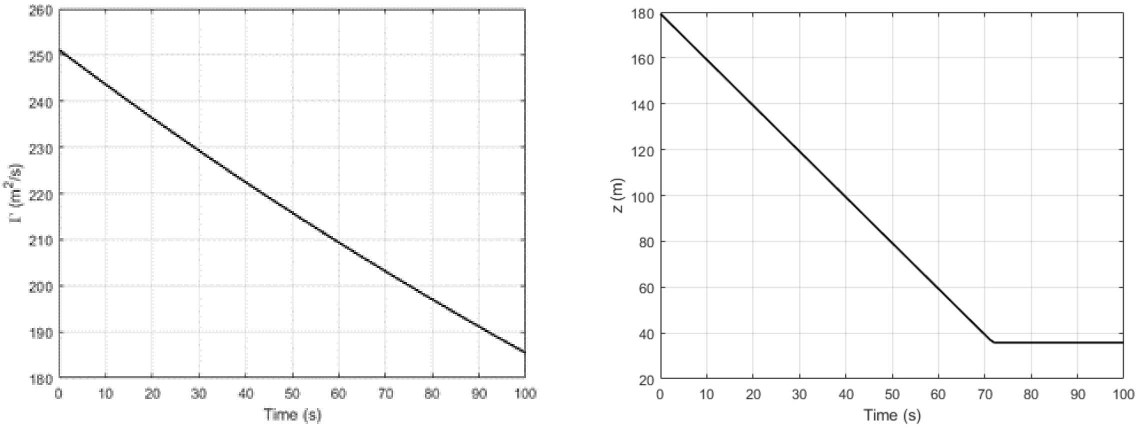

(d) Wake circulation decay (0-100 s)

(b) Wake descent (0-100 s)

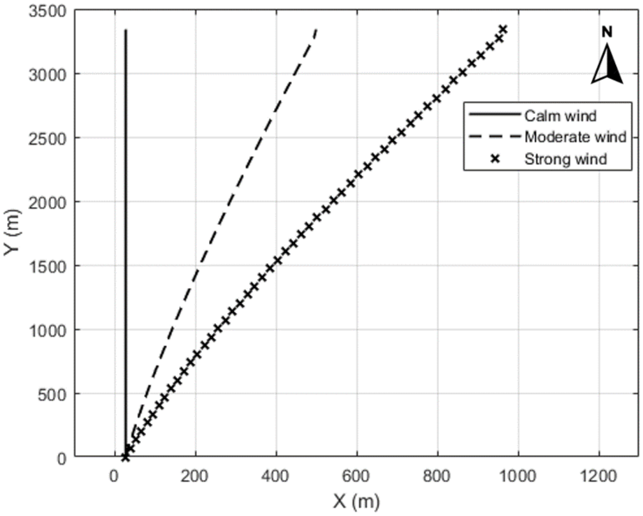

(c) Predicted wake vortex location after vortex generation (up to t = 100 s)

Figure 2-7b that the wake vortices descend to the ground at a rate of about 2 m/s and the wake circulation decays from 250 m^2/s to 186 m^2/s in 100 s for an EDR of 0.0121 $m^{2/3}s^{-1}$. For the analyses presented here, the descending of wake vortices stop descending at around one wingspan of the generating aircraft above the ground since the ground effect is not considered in this study.

Based on existing literature, it is difficult to predict the aircraft wake vortex location after they decay close to the ground. This is because there are secondary vortices or even tertiary vortices generated near the ground due to the induced ground flow separation. As the rotation of the secondary vortices are in the opposite sign of the primary wake vortices, the effective circulation is reduced, leading to decreased hazard levels. Although sometimes the rebound of the primary wake vortices induced by the secondary vortices can cause a concern, the somewhat unstable or much contorted primary vortices at this stage, such as “linking to the ground” as termed in the literature, still pose reduced hazard levels.

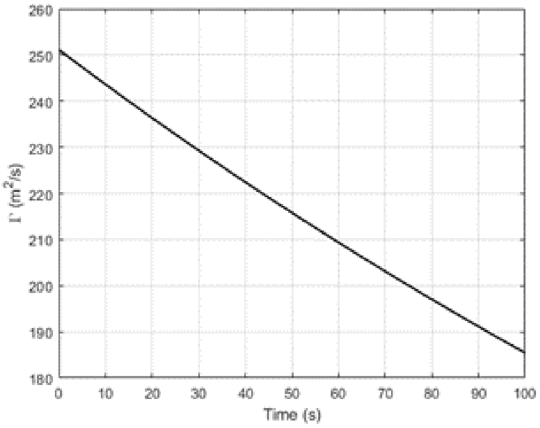

(e) Wake circulation decay (0-100 s)

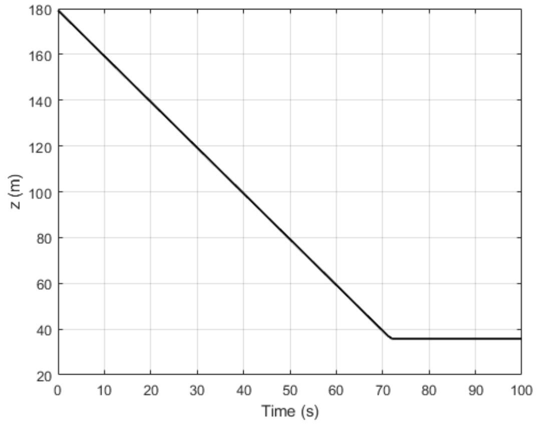

(b) Wake descent (0-100 s)

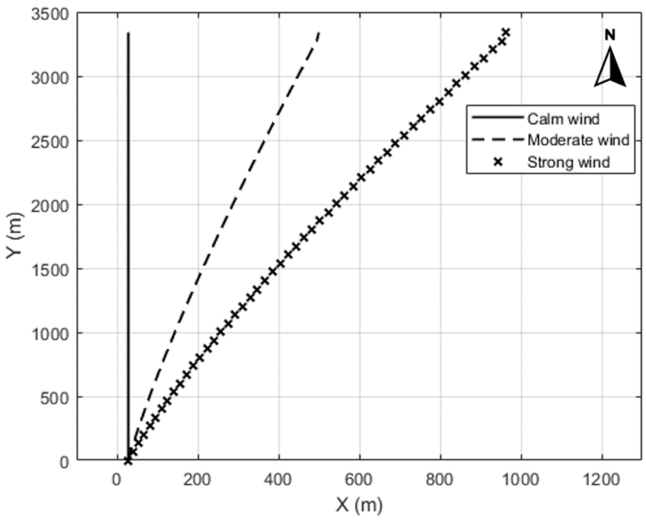

(c) Predicted wake vortex location after vortex generation (up to t = 100 s)

Figure 2-7c shows the wake vortex location after aircraft touchdown on the runway in three wind conditions: calm, moderate cross wind (10 knots) and strong cross wind 20 knots) using the wind profile data in Figure 2-6a**Error! Reference source not found.**. It can be seen that the cross winds can transport the wake vortex laterally as far as 950 m from the runway after 100 s.

Clearly then, for UAS flying below a landing aircraft, the descending vortices pose a potential for loss of control. However, if the vortex strength diminishes to that of the ambient vorticity, somewhere in the vicinity of 75 m^2/s, it is likely a UAS will not be affected at all by the vortices. It makes sense, therefore to consider the distance from a generating aircraft runway touch-down at which the vortex circulation has diminished to ambient levels. This would establish the extent of a very conservative "no-fly zone" at 500 ft AGL beneath a landing aircraft. Table 2-1 shows the distance from a Boeing 737-800 touch-down at which the vorticity has decayed to ambient levels at 500 ft AGL for a range of wake descent rates and EDR. The wake descent rate for a Boeing 737-800 has been estimated to be 1.69 m/s.

Table 2-1. Distance from a Boeing 737-800 touchdown to its wake diminishing to 75 m^2/s at 500 ft AGL.

Wake Descent Rate	High EDR (84s to 75$\boldsymbol{m^2/s}$)	Medium EDR (358s to 75$\boldsymbol{m^2/s}$)	Low EDR (460s to 75$\boldsymbol{m^2/s}$)
$w_0 = 1.5\ m/s$	2.00 NM	4.95 NM	6.05 NM
$w_0 = 1.69\ m/s$	2.11 NM	5.44 NM	6.67 NM
$w_0 = 2.5\ m/s$	2.60 NM	7.52 NM	9.35 NM

Figure 2-8 is a schematic of the region below a Boeing 737-800 where its wake vortex circulation in landing configuration (Γ_{LG} = 300 m^2/s) exceeds the ambient circulation (or "vorticity"), $\Gamma_{AMB,}$ in a medium EDR environment, assuming the wake descent rate (V_{sink} in the figure, or w_w in equation 5, above) is 1.69 m/s. Assuming a uniform sink rate, the vortex strength would decay to ambient vorticity (75 m^2/s) in 358 seconds, thereby sinking 1984 ft. The distance from touchdown to where the sinking vortex decreases to ambient vorticity would be 5.44 NM. Beyond this distance, using a conservative definition of a no-fly zone to mitigate UAS upset, the Airport Facility Map in the LANCC system would indicate 500 ft AGL as the acceptable flight altitude. For the assumed 4.3^o landing glide slope, the circulation at the surface would be 75 m^2/s at approximately 1.1 miles closer to the touchdown point, as shown in the figure. Therefore, for a distance of 4.34 NM from the touchdown point, the Airport Facility Map would indicate 0 ft AGL as the acceptable flight altitude.

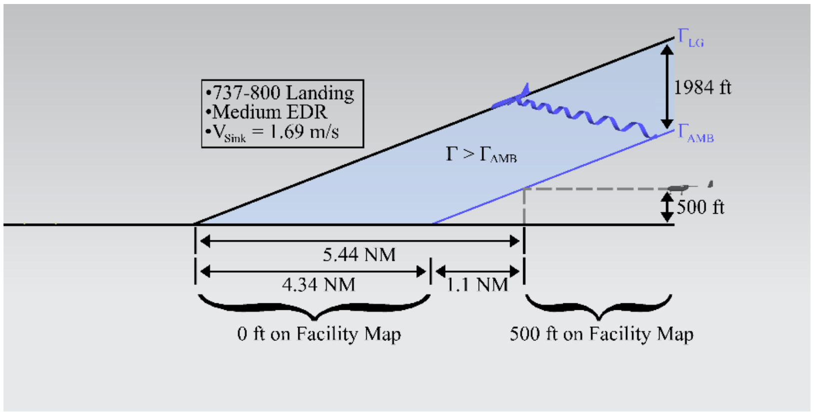

Figure 2-8. Very conservative no-fly zone for UAS flight below a landing Boeing 737-800.

Similar no-fly zones could also be constructed based on the allowable vortex strength for a given UAS, or perhaps a class of UAS.

2.4 Simulation of wake vortex air velocity environments

Flying UAS through wake vortices is difficult for two reasons: the vortices are hard to identify and it is expensive to acquire knowledge of the actual velocity field through which the UAS has flown. Light Detection and Ranging systems have been used before, however the cost of an appropriate system has a cost exceeding $1,000,000. Therefore, two assemblies of high-power fans, or wind machines, have been used to provide wind fields which simulate the wind field within a vortex. The University of Kansas (KU) has two wind machines which produce airflows inclined at approximately 45 degrees from the horizon. A bank of 5 wind machines has been used by the Ohio State University (OSU) to provide horizontal and slightly inclined wind fields.

2.4.1 Wind machines at KU

A set of 2 wind machines have been outfitted at KU with adjustable ramps which have been used to divert the (horizontal) fan output to approximately 45 degrees from the horizon. [The original plan was to have 4 wind machines, but the wind machine manufacturer went out of business shortly after the purchase order for the additional fans was sent.]

Figure 2-9 shows the two wind machines aligned in-line. Sketches in the figure represent the streamlines of velocity in both side and top views. A sketch also shows the notional wind velocity field when both fans are in-line but with the Revolutions Per Minute (RPM) of the “leading” wind machine set lower than the “trailing” machine. This creates a gradient of wind velocity which crudely simulates a portion of a single vortex where the circulation decreases with distance from the vortex core and is oriented 45 degrees to the horizon. If a UAS trajectory is perpendicular to this alignment of the fans, this has been shown to cause the UAS to respond primarily in roll. If the trajectory is along the axis of the wind machines, this imposes increasing air velocity seen as the UAS flies closer to the vortex core, causing the UAS to respond primarily in pitch.

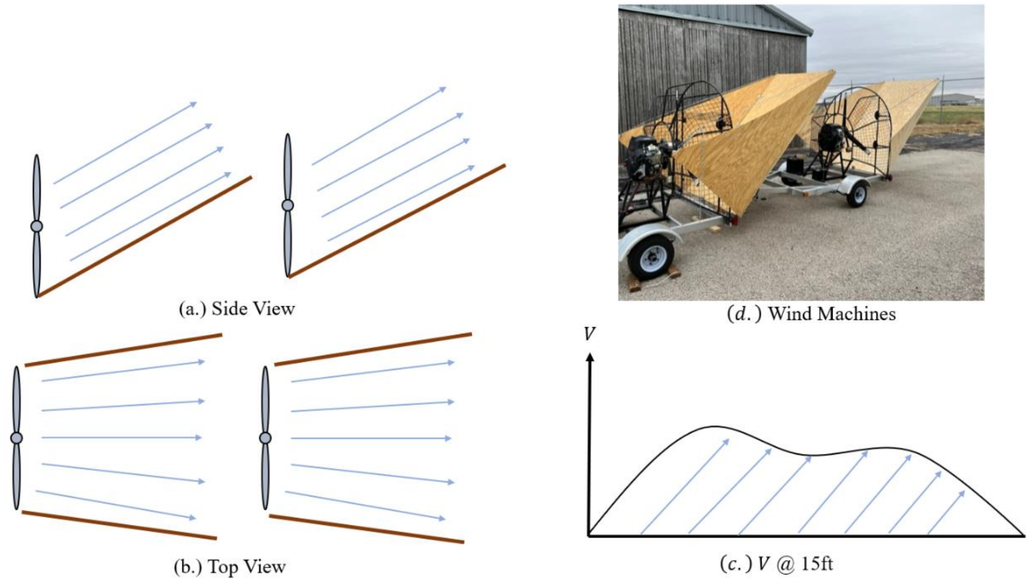
(a.) Side View

(d.) Wind Machines

(b.) Top View

(c.) V @ 15ft

Figure 2-9. KU Wind Machines aligned inline: At left – side view and top view of velocity streamlines, At bottom right – velocity field at 15 ft above the ground.

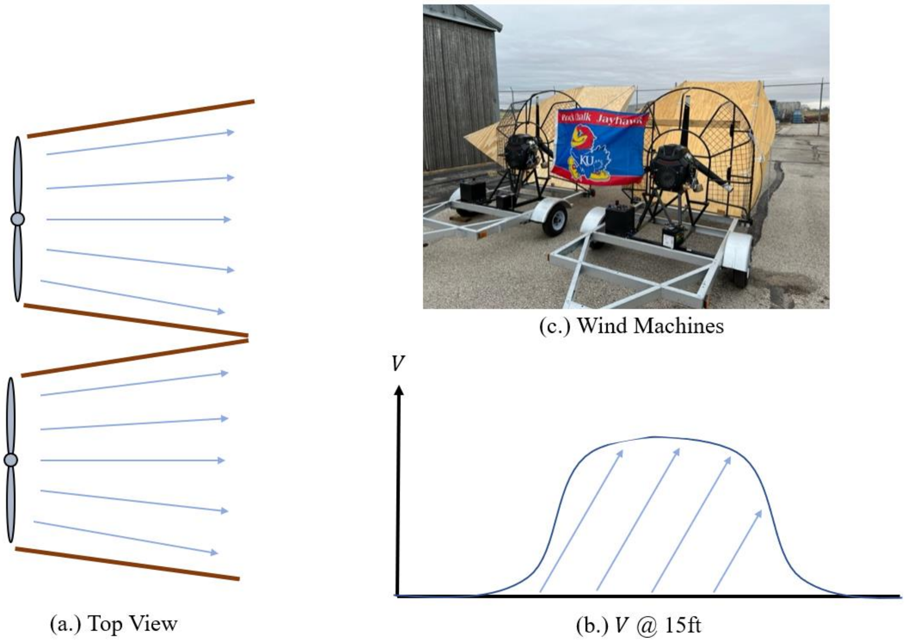
(a.) Top View

(c.) Wind Machines

(b.) V @ 15ft

Figure 2-10. KU Wind Machines aligned side by side: At left – top view sketches of velocity streamlines, At below right – velocity field at 15 ft above the ground.

Figure 2-10 shows the two wind machines aligned side by side. Sketches in the figure represent the streamlines of velocity in a top view. A sketch also shows the notional wind velocity field created by the wind machines. When the fans are aligned side-by side, this crudely represents the very abrupt circulation corresponding to encounters close to the vortex core.

In both cases, the air velocity field provided by the wind machines only simulates one section of the vortex: to get down-wash, fans would need to be positioned *above* the UAS flight path with air being diverted down, which is beyond the scope of this project. That said, simulation has shown that down-wash causes a generally less severe response for a fixed-wing UAS but a more severe response for a multirotor (or helicopter) UAS.

2.4.1.1 Measurement of air velocity field provided

2.4.1.1.1 3-D Anemometer

Early in the project, a fully 3-axis Gill R3-50 anemometer was affixed to a telescopic mast on a wheeled base to measure wind machine output. The anemometer was used to measure the 3-dimensional velocity field in a 9 ft by 6-ft grid with 1-foot spacing, 12 feet above the wind machine with the 45 degree ramp. The wind velocities at the 54 locations are plotted as vectors in Figure 2-11, where the vector length is proportional to the velocity and the direction is the total velocity. The plot is a side-view of the air velocity vectors. Note that the bulk flow direction is at approximately 45 degrees from the horizon. But also, there are significant departures from that direction, especially at the "edges" of the 9-foot by 6-foot region interrogated. This measurement study informed the decision to create a 32-anemomemeter array to better understand the wind machine velocity output. With this task accomplished, the 3-D anemometer is available to measure ambient wind conditions during flight tests over the wind machines.

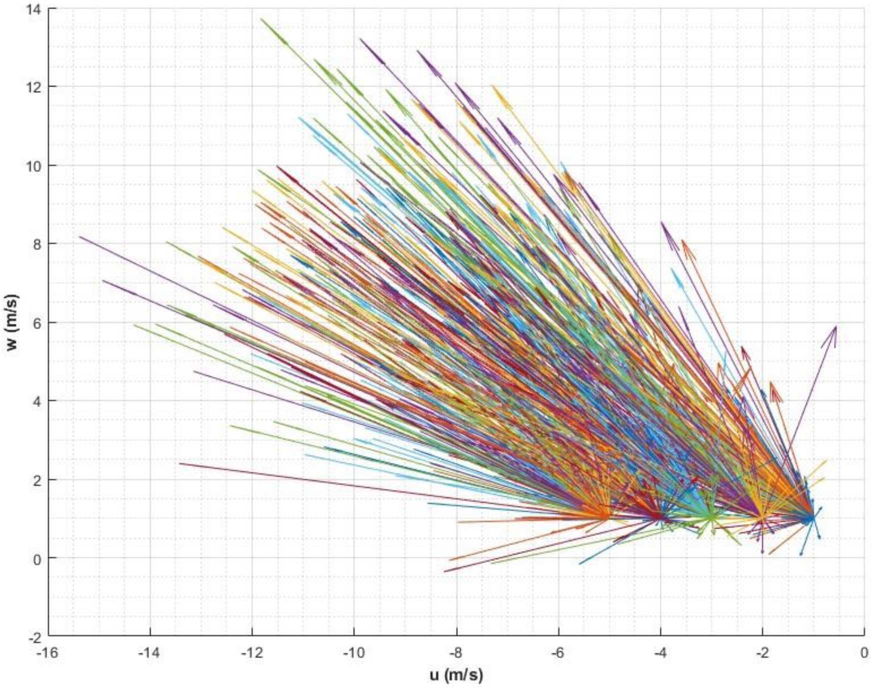

Figure 2-11. Side view of velocity vector field obtained from 3-D anemometer measurements on a plane at 12 feet above the floor (the base of the wind machine).

2.4.1.1.2 2-D+ anemometer array

A moveable array of anemometers has been used to characterize the output of the wind machines. These Anemoment TriSonica mini anemometers are described in detail in Section 2.4.2.1.1. They are "2-D+" anemometers, meaning they can resolve air velocities over a 360-degree range in a plane—their “base plane’—and within 20-30 degrees out of the plane both above and below the base plane. Therefore, they are not actually 3-D anemometers.

In wind machine output measurements, the anemometers are oriented such that the main airflow aligns with the anemometer’s base plane. Figure 2-12 shows the wooden frame on which the anemometers are installed, with the wind machine positioned below it. The frame has moveable cross-members which can be spaced as desired. The anemometers can also be positioned along the cross-members as desired. The wooden frame was initially suspended from its four corners by a pulley system which is used to hoist the system to the desired height.

Figure 2-12. Anemometer array positioned horizontally to measure wind machine output.

There are 8 data loggers used in a 32-anemometer experimental set-up, with 4 anemometers connected to each data-logger. Pairs of data-loggers are connected to a small Jetson Nano computer which therefore logs 8 channels of data. For 32-channel tests, four Jetson Nano units provide the data for analysis.

2.4.1.1.2.1 *Initial wind machine output measurements*

Experiments were conducted with a 4 by 4 grid of anemometers spaced at 2 feet to map the velocity field generated by the wind machine with a ramp which directs the flow at an angle of approximately 45° to the floor. The velocity field from such experiments provides the flow field—plus any ambient airflow—through which UASs are flown in flight test.

Figure 2-13 shows a snapshot of the velocities which were recorded with a 20 Hz sampling rate at a height of 11 ft above the floor, with the wind machine RPM set to its maximum. This figure shows a side view of the 16-channel “quiver plot” at height of 11 ft above the floor. The direction of the vectors in the quiver plot display the direction in which a wind sock would respond to the air velocity. The magnitudes of the vectors indicate the magnitude of the velocity. Velocity vectors at each instant of time have been scaled to unit size. Each “bunch” of velocity vectors includes velocities recorded at the 4 anemometers in each of the 4 rows of anemometers in the array.

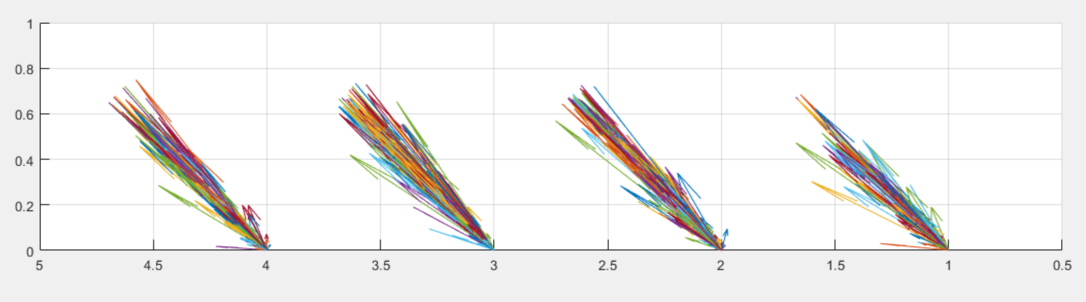

Figure 2-13. Side view of 16 channel velocity vectors from anemometer array at 11 ft above the floor.

From the 16-channel quiver plot, it is found that the flow produced by the fan is non-uniform, though the predominant direction of airflow is at 45 degrees. It is observed that velocity vectors have components of significant magnitude perpendicular to the direction of the flow, which may be indicative of flow circulation caused by the wind machine propellers.

2.4.1.1.2.2 *<u>Wind machine output measurement with the anemometer array oriented vertically</u>*

The anemometer array was oriented vertically for the most extensive velocity measurements, as shown in Figure 2.13.

Figure 2-14. 30-channel TriSonica anemometer array in a vertical orientation.

By positioning the wind machines at several horizontal positions away from the array, the wind field has been characterized in the volume of space through which UAS have flown.

Figure 2-15. Two fans side-by-side being characterized, positioned in front of an anemometer array.

The data generated by the anemometer array has been analyzed to determine the uniformity of the flow generated by the wind machines and flow-diverting ramps. Figure 2-16 is a quiver plot of the average flow at the 30 anemometer locations in front of a single fan. Although the flow is seen to be mostly forward and up, at approximately 45 degrees from the horizon, there are large deviations. It is likely that some form of flow-straightening can reduce the variability in flow. Unfortunately, the velocity field is clearly not uniformly “up and inclined 45^o to the horizontal” as desired. Therefore, the velocity field produced by the wind machines matches neither the air velocity assumed in the simulations nor the air velocity field encountered by the UAS in flight testing. This discrepancy might be able to be improved by a number of highly-engineered wind machines, likely with specially-designed diverter vanes, which are often found in wind tunnels to improve the uniformity of air flow.

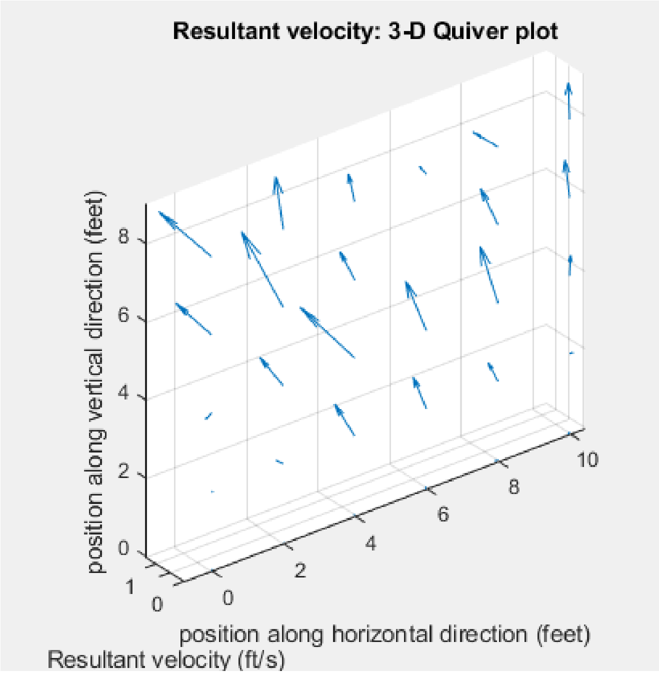

Figure 2-16. Quiver plot of the velocity field 6 feet in front of the diverting ramp for one fan

Figure 2-17 shows the projection of the total velocity onto the vertical plan, giving some indication that there at least does not seem to be significant vorticity about the horizontal axis. Rather, the flow seems to be generally up and to the sides—in this case, more-so on the left side.

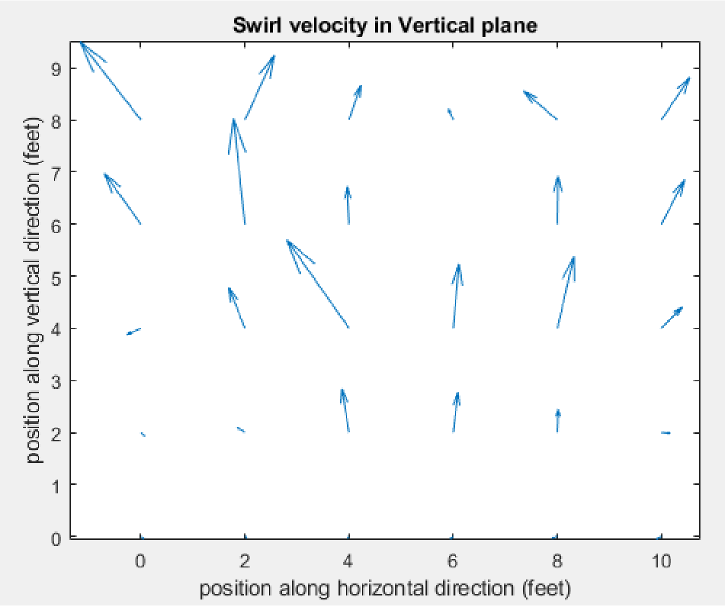

Figure 2-17. Projection of total velocity measurements onto the vertical plane.

2.4.2 Ohio Transportation Research Center (TRC) wind machines

A unique test facility at the TRC was used to generate the simulated gust encounters. The Skid-Pad Facility at the TRC outside of East Liberty, Ohio, has a unique array of six large fans that are mounted on the ground level of the track to simulate crosswind conditions for road vehicle testing, as shown in Figure 2-18. Each fan has four horizontal vanes and six vertical vanes that can be adjusted to direct the flow of air. The fan opening on the output side is 1.73 m (68 in) tall by 2.77 m (109 in) wide. Each fan has six blades and each of them is 1.02 m (40 in) long, not including the central hub. Further, each of these fans is driven by a gasoline engine and have variable speed, which can be adjusted in an open-loop fashion. These fans can be individually throttled to produce gradients in the wind field and have turning vanes to allow the individual jets to be angled both horizontally and vertically. The fans can generate wind speeds up to 15 ms^{-1} (49.2 fts^{-1}). Of note, the fans are of a blow-down configuration with an intake in the rear of the fan housing. This means that ambient winds will create additional fluctuations or mean-flow offsets in the output of the fan. To some degree this can be controlled by adjusting individual fan speeds as previously mentioned. Ultrasonic anemometers were used to characterize the outputs of individual fans, and the combined array as described in the next section.


(a.) Front View

(a.) Rear View

Figure 2-18. Front and rear view of the crosswind fan array at the Skid-Pad Facility located at the Transportation Research Center (TRC).

2.4.2.1 Measurement of wind machine output

2.4.2.1.1 Ultrasonic anemometer

The gust and wake encounter are measured using a Trisonica 3-D mini Ultrasonic anemometer, which has a bandwidth up to 10 Hz, allowing for rough atmospheric turbulence information to be gathered in addition to mean-flow data. The anemometer can measure wind speeds up to 50 ms^{-1} (164.04 fts^{-1}) with a resolution of 0.01 ms^{-1} (0.03 fts^{-1}) and is able to operate in temperatures ranging from $-45°$ to $85°$. The Trisonica 3-D mini ultrasonic anemometer with pipe-mount base was chosen for characterization purposes because of its lightweight structure, simple mounting interface, and ability to be mounted on the sUAS in future testing. The Trisonica anemometer outputs data in an ASCII character string over a standard serial port connection at a chosen sampling rate of 5 Hz. Calibration of the anemometer was conducted in the Batelle Subsonic Wind Tunnel with a 0.91 m (3 ft) × 1.52 m (5 ft) test section. This wind tunnel facility is able to produce speeds up to 45 ms^{-1} (147.64 fts^{-1}). However, wind speeds for this calibration testing were limited to the wind speeds predicted by the encounter scenarios outlined in the previous section, which is approximately 20 ms^{-1} (65.66 fts^{-1}). The wind tunnel has a nominal turbulence intensity of 0.25% across its operational speed range. The anemometer was approximately 0.76 m (30 in) from the inlet of the test section and was mounted along the centerline of the test section. The anemometer calibration was performed for speeds ranging from 7 ms^{-1} (22.97 fts^{-1}) to 20 ms^{-1} (65.62 fts^{-1}) for a full $0°$ to $360°$ rotation in both the counterclockwise and clockwise directions to determine the azimuthal accuracy of the anemometer.

2.4.2.1.2 Calibration of anemometer

Figure 2-19 shows the results from this calibration testing characterized by full counterclockwise and clockwise azimuth rotations at varying wind speeds. The measured wind speed from the ultrasonic anemometer accurately tracks the known wind speed for all azimuth angles except for azimuth angles in the range of $300°$ to $330°$ for all wind speeds. This deviation was only measurable in the wind tunnel and did not persist in outdoor testing. The wind tunnel walls are likely source of reflection for the ultrasonic anemometers as one wall of the tunnel is acrylic for flow visualization purposes, and the other walls are painted plywood, which better attenuates the ultrasonic pulses generated by the anemometer. Additionally, the mean and standard deviation of the measured wind speed for each of the wind tunnel speeds tested were computed to determine the accuracy of the ultrasonic anemometer. These values can be seen in Table 2-2, as well as in Figure 2-19 where the measured mean wind speed is represented by the solid black line and one standard deviation is represented by the dashed black line. Generally, the ultrasonic anemometer over-predicts the actual wind tunnel speed, although this trend diminishes with increasing wind tunnel speed. Nonetheless, it can be seen that the anemometer measurements are within one standard deviation for the higher speeds ranging from 10 ms^{-1} (32.80 fts^{-1}) to 20 ms^{-1} (65.61 fts^{-1}) and within two standard deviations for the lower 7 ms^{-1} (22.97 fts^{-1}). This larger discrepancy between the actual and measured wind tunnel speeds at 7 ms^{-1} (22.97 fts^{-1}) could be due difficulties maintaining the wind tunnel at lower speeds.

Table 2-2. Mean and standard deviation for ultrasonic anemometer wind tunnel testing.

U_∞ (ms^{-1})	Mean (ms^{-1})	Standard Deviation (ms^{-1})
7	7.57	0.42
10	10.53	0.68
15	15.11	1.13
20	20.10	1.46

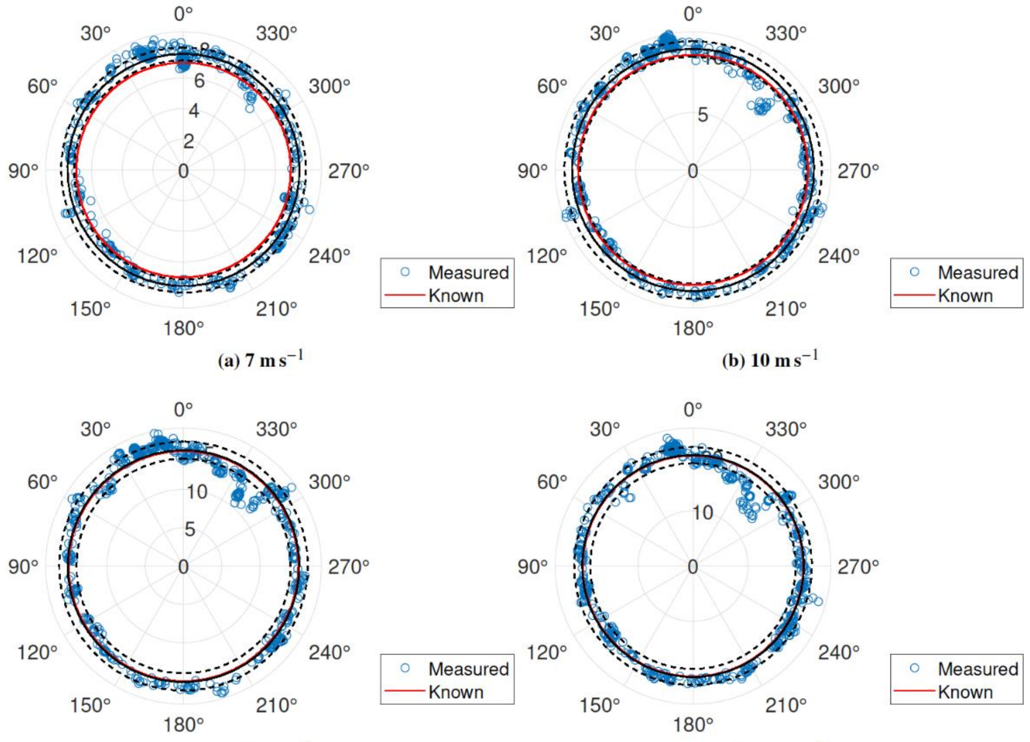

(a) 7 m s^{-1} (b) 10 m s^{-1}

(c) 15 m s^{-1} (d) 20 m s^{-1}

Figure 2-19. Ultrasonic anemometer wind tunnel calibration results.

2.4.2.2 Ultrasonic anemometer array

In addition to calibrating the ultrasonic anemometer, an ultrasonic anemometer array with 10 stations was developed to enhance our capabilities of making spatial and temporal multiple point wind measurements at various locations, as shown in Figure 2-21. The Ultrasonic anemometer array was developed and designed at OSU. Each station consists of components shown in Figure 2-20: Trisonica 3D mini anemometer, Arduino, Global Positioning Satellite (GPS) module and wireless transceivers. The Arduino serves as an onboard computer to establish communications between the GPS, anemometer, and control station. The GPS module will be used to gather an accurate measurement location.

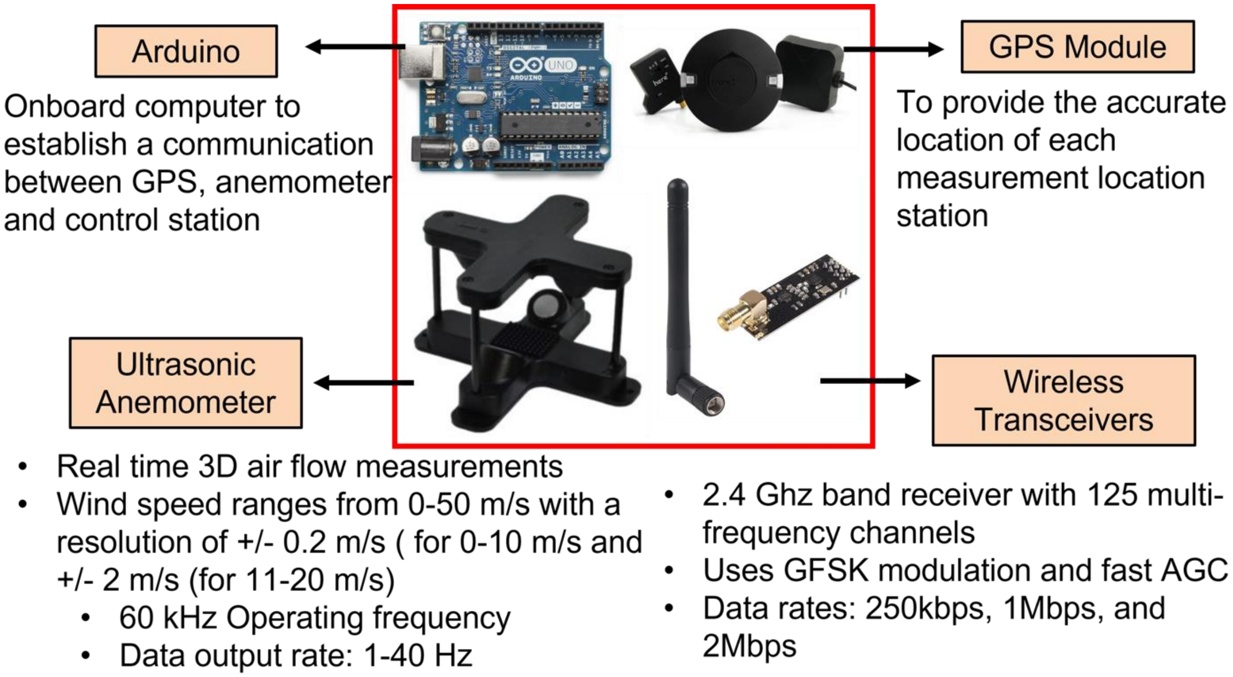

Onboard computer to establish a communication between GPS, anemometer and control station

To provide the accurate location of each measurement location station

- Real time 3D air flow measurements
- Wind speed ranges from 0-50 m/s with a resolution of +/- 0.2 m/s (for 0-10 m/s and +/- 2 m/s (for 11-20 m/s)
    - 60 kHz Operating frequency
    - Data output rate: 1-40 Hz

- 2.4 Ghz band receiver with 125 multi-frequency channels
- Uses GFSK modulation and fast AGC
- Data rates: 250kbps, 1Mbps, and 2Mbps

Figure 2-20. Components of ultrasonic anemometer station.

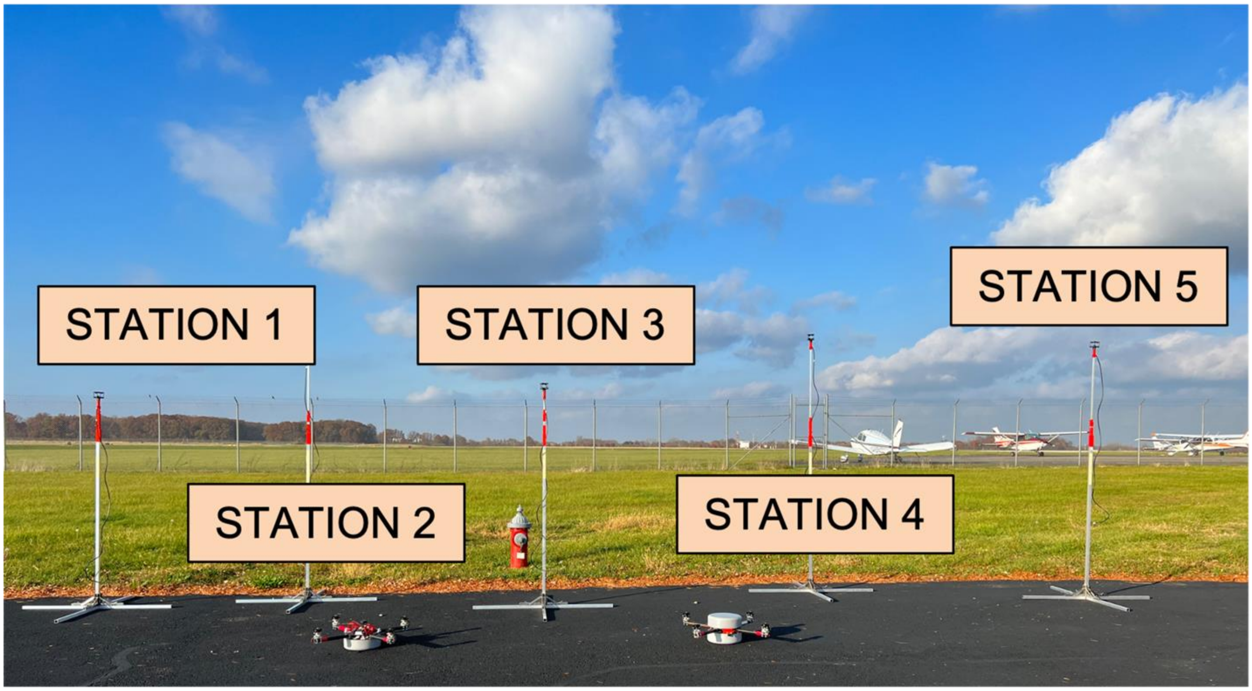

Figure 2-21. Ultrasonic anemometer array developed and designed at OSU.

2.4.2.3 Single wind machine characterization

Temporal single fan measurements were collected at the fan's center 1.52 m (5 ft) along the fan, which is with respect to the starting point, 6.09 m (20 ft) offset from the fan, and at a height of

2.43 m (8 ft). Wind data was collected for 3-5 minutes at two fan speed at 10 ms^{-1} (32.80 fts^{-1}) and 5 ms^{-1}. Figure 2-22a depicts the collected wind measurements for the 5 ms^{-1} fan speed. This figure also shows the 60 sec moving average wind speed every minute and the average wind speed over the entire test. There was significant deviation in the wind speed measurements over time due to the open-loop control of the crosswind fans. Despite this, the average wind speed measured remains consistent (excluding the last minute of the test, which is most likely due to ambient air speed interference. Frequency peaks shown in the power spectral density Figure 2-22b may represent long-period oscillations in the fan, or in the ambient winds. However, further testing would be required to definitively determine the sources of these frequency peaks. It should be noted that only flow features up to 2.5 Hz were resolved, as the sampling frequency was chosen to be 5 Hz.

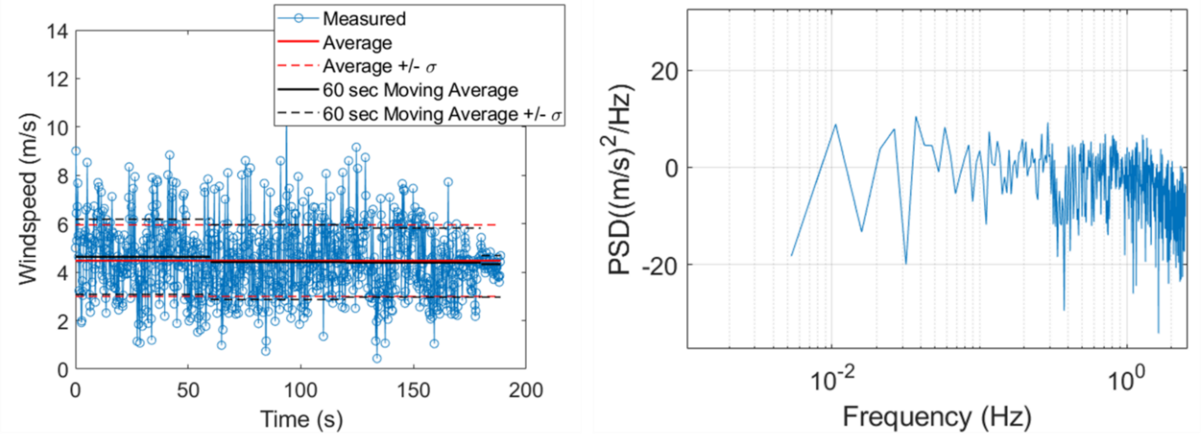

(a.) Wind measurements

(b.) Power spectral density

Figure 2-22. Temporal measurements for a single fan at locations (x, y, z) = (1.52 m, 6.09 m , 2.43 m) for 10 m/s (32.80 ft/s).

2.4.2.4 Crosswind wind machine array characterization

Flow field measurements were collected at fifteen lateral distances across the fan array in increments of 1.52 m (5 ft). Flow measurements were collected from the crosswind fans for a ramping up and ramping down gust profile at two distinct heights above the ground: 1.22 m (4 ft) and 2.44 m (8 ft). Figure 2-23a shows the ramp up and ramp down gust profile tested at TRC. Additionally, Figure 2-23b shows the average wind speed magnitude at each lateral distance across the fan array. The measured wind speed at 1.22 m (4 ft) has a significantly larger magnitude compared to the 2.44 m case (8 ft). This reinforces the indication that the measurements at 2.44 m (8 ft) above the ground are outside the core region. Measurements taken at a height of 1.22 m (4 ft) show behavior consistent with close proximity to the core region; however, further testing around this altitude would be required to be able to definitively pinpoint the exact core location.

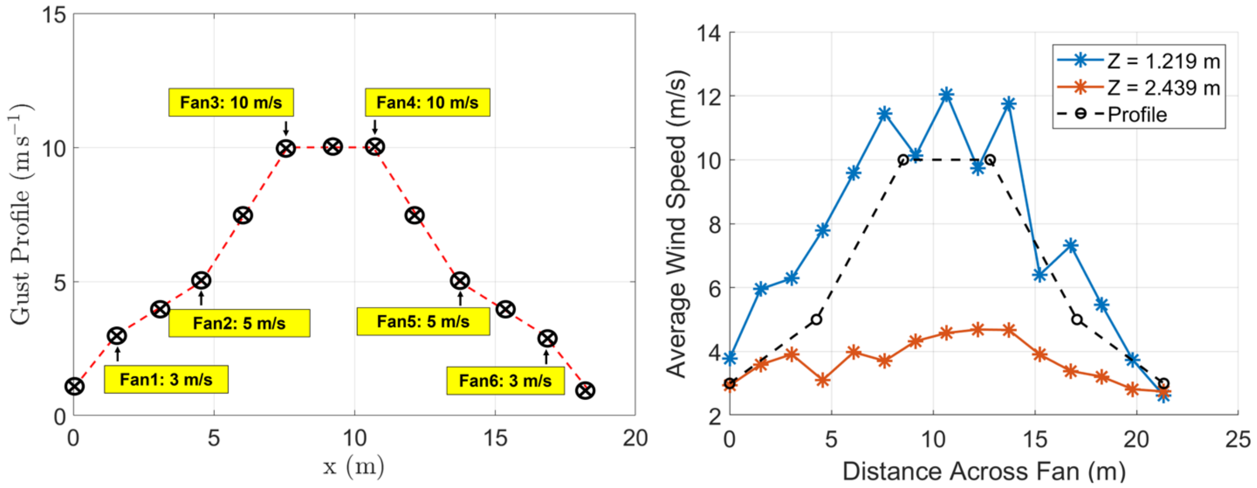

(a.) Ramping up and ramping down gust profile

(b.) Average wind speed

Figure 2-23. Ramp up and ramp down gust profile tested at TRC and wind measurements obtained from the test.

2.5 References

[1] T. Gerz, F. Holzäpfel, and D. Darracq, "Commercial aircraft wake vortices," *Progress in Aerospace Sciences*, vol. 38, no. 3, pp. 181–208-181–208, 2002.

[2] J. N. Hallock and F. Holzäpfel, "A review of recent wake vortex research for increasing airport capacity," *Progress in Aerospace Sciences*, vol. 98, pp. 27–36-27–36, 2018.

[3] A. He, H. Chao, Z. C. Zheng, and P. Tian, "Development of a Coupled CFD Simulation with Flight Control Algorithm," in *International Mechanical Engineering Congress and Exposition*, 2016.

[4] T. J. Dasey, R. E. Cole, R. M. Heinrichs, M. P. Matthews, and G. H. Perras, "Aircraft vortex spacing system (AVOSS) initial 1997 system deployment at Dallas/Ft. Worth (DFW) Airport," 1998.

[5] D. Fischenberg, "A method to validate wake vortex encounter models from flight test data," in *27th International Congress of the Aeronautical Sciences*, 2010, pp. 2010–6-2010–6.

[6] T. Sarpkaya, "New model for vortex decay in the atmosphere," *Journal of Aircraft*, vol. 37, no. 1, pp. 53–61-53–61, 2000.

[7] N. N. Ahmad and F. Proctor, "Review of idealized aircraft wake vortex models," in 52nd *Aerospace Sciences Meeting*, 2014, pp. 0927-0927.

[8] F. Proctor and D. Hamilton, "Evaluation of fast-time wake vortex prediction models," in 47th *AIAA Aerospace Sciences Meeting including The New Horizons Forum and Aerospace Exposition*, 2009, pp. 344-344.

3 FIXED-WING UAS WAKE ENCOUNTER STUDIES

Modeling and simulation of fixed wing UAS response to wake vortex encounters has been conducted using 6 DOF models of aircraft flight dynamics. Simulation includes open-loop response to wake vortices as well as the response with two types of controller. Further, flight testing has been used to validate the simulations and to identify metrics which indicate loss of control. Finally, the potential of using physics-based response analyses coupling computational fluid dynamics with UAS motion has been explored.

3.1 Simulation of fixed-wing UAS wake encounters

3.1.1 Coupled aerodynamics and flight dynamic simulations with wake hazard predictions

This section focuses on simulating sUAS responses during wake encounters and concludes with suggestions for predicting wake hazard metrics. Two UAS wake vortex encounter modeling methods are developed and implemented as HawkWakeSim v2.1 including the VLM and the Linear Wind Field Approximation Method (LWFAM). Both methods are validated with flight data for flight in uniform flow fields, then cross-validated in simulated wake vortex fields. Then, a range of UAS wake encounter scenarios are simulated with an attitude-hold controller for flight paths with two different “cutting angles” with respect to the path of the wake-generating aircraft. Finally, alternative metrics for defining wake hazard are presented

3.1.1.1 Aerodynamic modelling for UAS wake vortex encounters

Aircraft wake encounter modeling has been studied in the past using a variety of methods, including lifting-line theory, strip method, vortex lattice method, panel method, and other computational fluid dynamics-based methods [2, 3]. For example, a pre-computed data set was generated by large-eddy simulation for predicting wake vortex interaction in a real-time flight simulation[4]. Vicroy combined a series of wake encounter flight test data in the cruise condition for improved understanding of wake vortex physics and atmospheric interaction [5]. Strip theory for Wake Vortex Encounter (WVE) hazard prediction was studied through simulation in [6]. In [7], a VLM from [8] and the strip theory method from [6] were compared with wind tunnel data, with both methods showing similar results. Although there are many WVE modeling and simulation efforts, few focus on validation with flight data and identified models. A strip theory-based method was developed and validated against manned aircraft WVE flight data [9]. In this section, VLM and LWFAM are used for the wake encounter simulation and initial flight validation. VLM was chosen because it uses perturbed states for calculating Stability and Control (S&C) derivatives on each panel, which can generate accurate estimates of aerodynamic coefficients [9]. LWFAM was selected because it uses less time for calculation while still maintaining good accuracy in predicting aircraft responses [4, 10].

3.1.1.1.1 Vortex Lattice Method

The 3-D Vortex Lattice Method can be used to calculate aircraft forces/moments in wake fields. The VLM takes aircraft geometry, incoming flow information and aircraft angular rates as inputs and provides S&C derivatives as outputs. The calculated S&C derivatives can then be used in a 6-DOF, nonlinear flight dynamics simulator. One implementation example of the VLM is Tornado, an open-source MATLAB program based on standard vortex lattice theory and stemmed from potential flow theory [9].

The VLM divides an aircraft into small panels. On each panel, the Kutta-Jukovski theorem is applied to calculate forces acting on these panels. VLM computes the total aerodynamic forces and moments acting on the aircraft, and allows for rapid calculation compared to traditional computational fluid dynamic methods, which are often based on Naiver-Stokes equations [11]. Additionally, Tornado is used for calculation of rate-dependent stability and control derivatives such as C_{l_p}, the derivative of rolling moment coefficient with respect to roll rate. The aerodynamic forces can be calculated as:

$$F = \sum_{i=1}^{N} \rho(V_{ind} \times \Gamma_i) l_i \tag{1}$$

where F is the forces vector, ρ is the air density, V_{ind} is the induced velocity, Γ_i is the vortex strength and l_i is the length at each cross segment of panel.

VLM provides solutions for calculating forces acting on each panel and it accounts for the rigid body angular rates by adding them into induced flow velocity:

$$V_{wind} = V_{wind} + (C_{xyz} \times [p, q, r]) \tag{2}$$

where V_{wind} is the velocity of upcoming flow, C_{xyz} is the collocation point on each panel and $[p, q, r]$ are the rotation rates.

The VLM is a quick and straightforward method for calculating aerodynamic coefficients. It has a good balance between calculation time and accuracy, and can process complicated aircraft geometries as input. The VLM method can simulate the wake vortex field on each panel of the aircraft while LWFAM assumes the wake field is linearly distributed across the aircraft. However, this method does not include viscosity effects, resulting in potentially nontrivial errors when estimating drag forces and drag related parameters. Also, further validations of VLM are needed, especially with UAS flight data or identified models.

3.1.1.1.2 Linear Wind Field Approximation Method (LWFAM)

VLM and other Computational-Fluid-Dynamics (CFD) based aircraft wake response models generally offer increased accuracy when compared to standard flight dynamics simulators. However, these high-fidelity models typically require accurate aircraft geometry information and many computational resources. Researchers have also developed simplified methods to simulate the aircraft WVE using classical flight dynamic models. One example is the linear wind field approximation method, originally proposed by Etkin [10], which was utilized in this section to provide a comparison and validation with the VLM results as well as for controller evaluation. In this method, the nonuniform wind field experienced by the aircraft is approximated as three translational wind velocities and three wind velocity gradients, which are equivalent to body rotational velocities relative to the air. The wind components are then used to compute the aircraft velocities relative to the wind, as:

$$\begin{aligned} u_r &= u - u_g, & p_r &= p - p_g \\ v_r &= v - v_g, & q_r &= q - q_g \\ w_r &= w - w_g, & r_r &= r - r_g \end{aligned} \tag{3}$$

where (u, v, w) are translational velocities, (p, q, r) are angular velocities, subscript g indicates gusts or turbulence, and subscript r indicates the velocities relative to the wind. For typical aircraft flight, these components are generated from spectral functions such as those specified by the Dryden turbulence model.

For deterministic wind fields, such as a wake vortex model, the equivalent linear wind field can be generated directly based on the wake vortex model. One approximation method is to use an identified linear wind field to represent the wake vortex field, or a linear changing wind field across the wing to represent the wake vortex field, which is the closest approximation to the wake-generated wind field. In [4], this method was used to estimate the wake generated forces and moments during aerial refueling. The wind components were determined by taking weighted averages of the wind components over a finite number of grid points along the aircraft. The model was compared to wind tunnel data and was shown to accurately predict the trend in forces and moments at different lateral and vertical spacings. In subsequent sections, a similar approach will be used to provide a fast-time prediction of UAS wake response and to provide some empirical validation with the results from the VLM in this section. The inputs of LWFAM are basic aircraft wing and fuselage geometry and S&C derivatives or aircraft state-space model. The outputs of the LWFAM are wake induced changes of aircraft states as well as forces and moments. LWFAM has the advantage of a faster calculation time while the prediction accuracy is theoretically lower compared to VLM in certain wake vortex regions.

3.1.1.2 Fixed-wing UAS considered in this section

Two types of fixed-wing UAS platforms are used in our study including a conventional T-tail UAS and a tailless flying-wing UAS. Phastball UAS, as shown in Figure 3-1, is a T-tail wing developed by West Virginia University researchers [12-14]. The wingspan of the aircraft is 2.4 m and the chord length is 0.35 m. The geometry specifications can be found in [5]. Key specifications of Phastball are shown in Table 3-1.

(a) Phastball UAS Platform

(b) Khawk55 UAS Platform

Figure 3-1. UAS geometry and modeling.

The KHawk55 UAS, a small-flying wing UAS developed at KU, was shown in Figure 3-1b. KHawk55 UAS has a wingspan of 1.4 m and is powered by a brush-less throttle motor. The main control surfaces are two elevons which is a combination of elevators and ailerons.

The geometries of Phastball and KHawk55 were mapped into Tornado, and the 3-D model, shown in Figure 3-2, was used for calculation of aerodynamic coefficients. The current mesh element settings are based on mesh convergence studies based on previous investigation [6, 15].

Table 3-1. Phastball and KHawk55 specifications.

UAS Specifications	Phastball	KHawk 55
Mass	10.5 kg	2.7 kg
Wingspan	2.4 m	1.42 m
Wing area	0.78 m^2	0.51 m^2
Wing Chord length	0.32 m	0.43 m
Fuselage Chord Length	2.2 m	0.37 m
C.G. Location	1.18 m from nose	0.23 m from nose
Cruise Speed	30 m/s	20 m/s

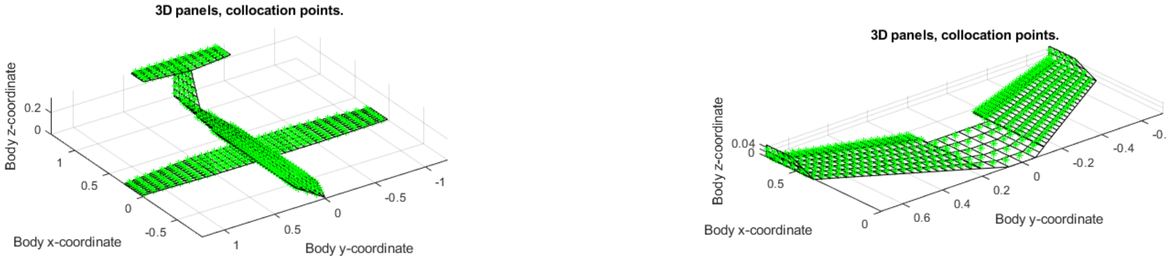

(a) Phastball UAS Platform (b) Khawk55 UAS Platform

Figure 3-2. UAS mesh elements and collocation points(green) in Tornado.

3.1.1.3 Open loop wake vortex encounter simulation with HawkWakeSim

In this section, the details of HawkWakeSim 2.1 are explained, which includes both VLM implementation and LWFAM implementation. HawkWakeSim 2.1 was developed using MATLAB Simulink [6, 15].

3.1.1.3.1 HawkWakeSim 2.1-VLM Simulation Platform

HawkWakeSim v2.1-VLM was developed based on previous studies on the T-tail Phastball UAS [6, 7]. The aerodynamic analysis is based on Tornado [9] and the flight dynamic simulation follows Newton's second law and corresponding coordinate transformations . Tornado is an open source VLM program which can calculate aircraft S&C derivatives based on the given flight condition. The obtained S&C derivatives will be passed to the flight dynamics simulator for the prediction of aircraft states at the next time step. After that, Tornado will use the result calculated by the flight dynamic simulator to update all the coefficients. Tornado was modified to implement the wake encounter models discussed previously. The outputs for the flight dynamic simulator are the twelve aircraft state variables, including the translational and rotational states, $[p_n, p_e, p_d]$,$[u, v, w]$, $[\phi, \theta, \psi]$, $[p, q, r]$ used in the equations of motion. HawkWakeSim v2.1-VLM has the ability to simulate UAS wake encounters at desired encounter angles and for different leader aircraft. It is also capable of simulating various wake vortex models. The overall diagram of the HawkWakeSim v2.1-VLM model is provided in Figure 3-3.

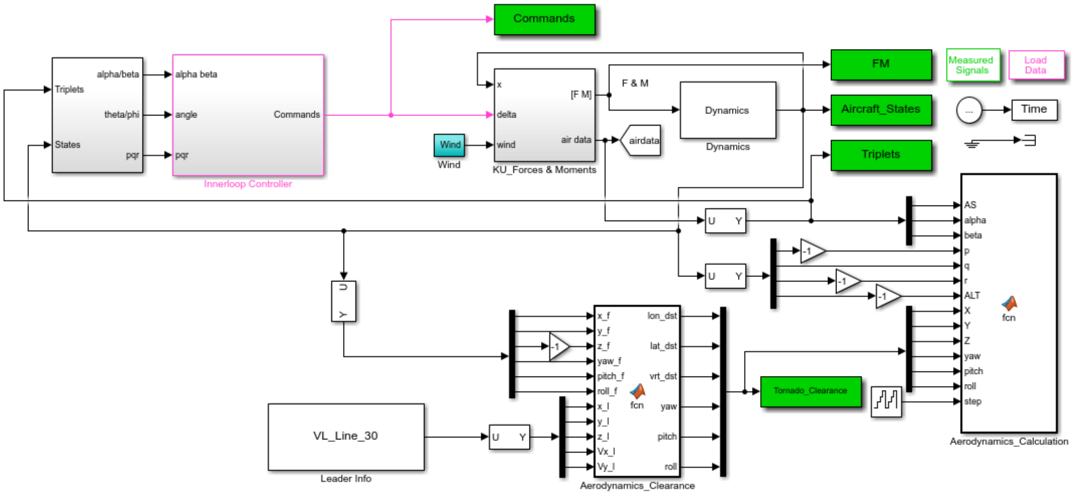

Figure 3-3. System diagram for HawkWakeSim v2.1-VLM.

3.1.1.3.2 HawkWakeSim 2.1- LWFAM Structure

The LWFAM can be implemented by generating a set of discrete points along the wing and fuselage of the UAS and computing the wake-induced velocity at each point using the Burnham-Hallock model. Then, the unknown terms of (4) can be estimated using least squares regression. Among the parameters from aircraft geometry, only rudimentary characteristics such as the wingspan or total length are needed. Additionally, the method is relatively robust to different realizations of the discrete points. This is because only the average wind over the body of the aircraft needs to be estimated. In contrast, strip theory method computes the forces and moments at each discrete point.

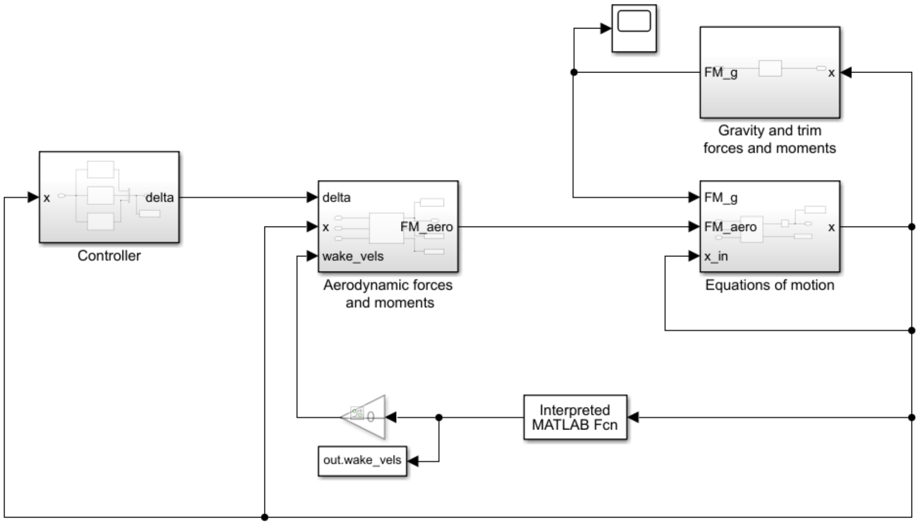

Figure 3-4. System diagram for HawkWakeSim V2.1-LWFAM.

3.1.1.4 Validation of HawkWakeSim and LWFAM

3.1.1.4.1 Validation in uniform flow fields

As an initial validation, S&C derivatives computed from HawkWakeSim v2.1-VLM are compared with those identified from flight data using frequency domain-based system identification methods.

The longitudinal stability coefficients are shown for comparison with the flight identified ones in Table 3-2. C_L and C_m are the terms of interest for longitudinal analysis during the UAS WVE. For flight dynamic simulation, the lift and pitching moment coefficients can be expanded using first-order Taylor series:

$$C_L = C_{L_0} + C_{L_\alpha}\alpha + C_{L_q}\frac{c}{2V_a}q + C_{L_{\delta_e}}\delta_e \tag{4}$$

$$C_m = C_{m_0} + C_{m_\alpha}\alpha + C_{m_q}\frac{c}{2V_a}q + C_{m_{\delta_e}}\delta_e \tag{5}$$

where C_L is the lift coefficient and C_m is the pitch moment coefficient. The wake induced C_L and C_m will consequently show up in the changes of force (f_x,f_z), moment (m), acceleration(a_x,a_z), and translation and rotation velocity(α or w,q).

The Tornado calculated aerodynamic parameters are compared with those identified from flight test in Table 3-2. In the lateral loop, C_Y, C_l, C_n are the terms of interest, the lateral aerodynamic force and moments coefficient can be expanded as:

$$C_Y = C_{Y_0} + C_{Y_\beta}\beta + C_{Y_p}\frac{c}{2V_a}p + C_{Y_r}\frac{c}{2V_a}r + C_{Y_{\delta_a}}\delta_a + C_{Y_{\delta_r}}\delta_r \tag{6}$$

$$C_l = C_{l_0} + C_{l_\beta}\beta + C_{l_p}\frac{c}{2V_a}p + C_{l_r}\frac{c}{2V_a}r + C_{l_{\delta_a}}\delta_a + C_{l_{\delta_r}}\delta_r \tag{7}$$

$$C_n = C_{n_0} + C_{n_\beta}\beta + C_{n_p}\frac{c}{2V_a}p + C_{n_r}\frac{c}{2V_a}r + C_{n_{\delta_a}}\delta_a + C_{n_{\delta_r}}\delta_r \tag{8}$$

Table 3-2. Comparison of Tornado and flight-identified Khawk55 stability derivates.

Method	C_{L_α}	C_{m_α}	C_{l_p}
Tornado	3.6132	-0.2151	-0.3633
Upper Bound 95% Confidence Range	5.5912	-0.2754	-0.1551
Flight Identified	4.5725	-0.3717	-0.2499
Lower Bound 95% Confidence Range	3.7774	-0.4882	-0.3580

It can be observed that the Tornado predicted longitudinal stability derivatives are fairly accurate compared to the flight identified parameters while the lateral S&C derivatives show some error such as C_{n_β}, C_{l_p} and C_{n_r}. Further investigations are needed for the lateral loop comparison.

The HawkWakeSim v2.1-VLM model is further validated through comparison with flight data. Figure 3-5 presents the elevator doublet comparison between VLM predictions and flight data. The flight data was generated by an elevator doublet from -3 degrees to 5 degrees. The overall trend for HawkWakeSim v2.1-VLM matches with flight data. The pitch rate prediction matches with flight data with about 2% error at the first peak. The vertical acceleration has about 30% error at the peak. The magnitude differences come from the difference between flight-identified and Tornado computed parameters. The VLM can provide accurate predictions of lift coefficients, but not the drag coefficients. This is the partial reason for the variance of HawkWakeSim v2.1-VLM prediction with flight data shown in Figure 3-5.

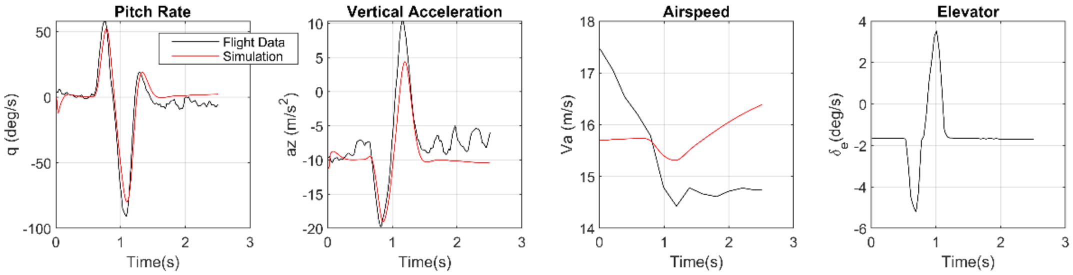

Figure 3-5. Comparison between HawkWakeSim v2.1-VLM and flight data for an elevator doublet.

3.1.1.4.2 Cross Validation in Wake Flow Fields

The LWFAM was also used to provide some empirical validation of the VLM results in this section. The wake induced forces and moments experienced by the UAS were estimated at different lateral spacings from the wake vortex under steady-state conditions. The vertical spacing was held constant, aligned with the vortex core. This computation was done for both parallel and perpendicular encounters (0 degree and 90 degree encounters) with the wake vortex.

The results for a perpendicular encounter for both Phastball and Khawk55 are shown in Figure 3-6. The lift prediction matches very well for the two methods. The LWFAM predicts a larger pitching moment for the Khawk55, but has a similar prediction as VLM for Phastball.

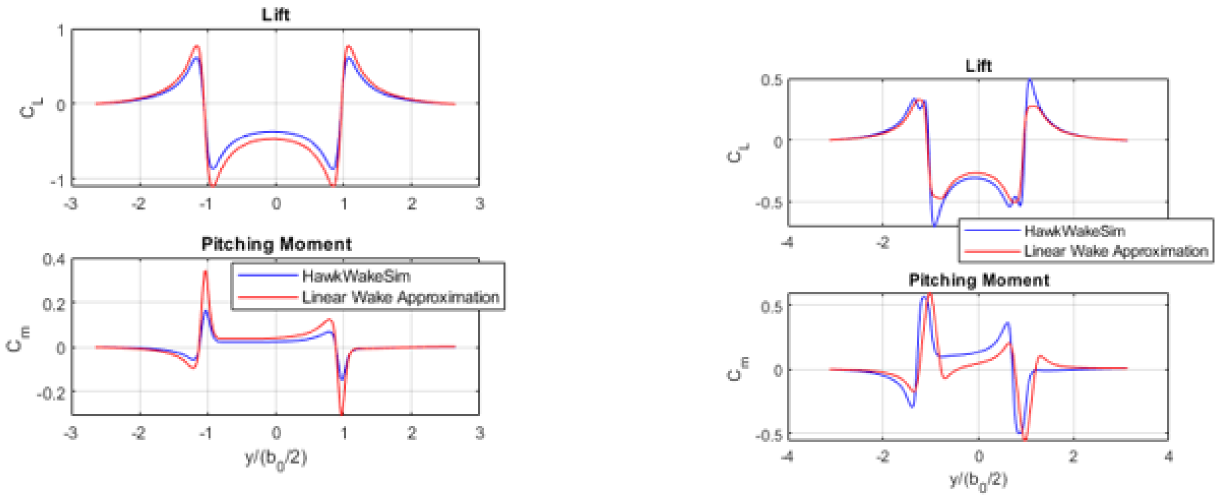

(a) Khawk55

(b) Phastball

Figure 3-6. Comparison between VLM and linear approximation for perpendicular wake encounters.

The results for a parallel encounter (0 deg.) are shown in Figure 3-7 and Figure 3-8. The rolling moment and lift prediction are shown to have a good match between the two methods. Yawing moment and pitching moment show a match in trend, however there are differences in magnitude. Side-force has the least similarity between the two methods.

In general, the trend between the two methods matches well, which provides some cross validation of the developed HawkWakeSim v2.1-LWFAM and VLM. Lift and rolling moment, which are arguably the most important measurements during the wake vortex encounter, show a good match in both magnitude and trend. Side-force has the least consistent match between the two methods; however, this force is typically less critical for wake vortex encounters. In this section, the researchers used HawkWakeSim v2.1-VLM for predicting the magnitude of the wake vortex encounter, and used HawkWakeSim v2.1-LWFAM for fast-time evaluation and controller analysis, since the LWFAM simulation takes less time than VLM-For a Xeon Windows machine, the LWFAM takes about 40 s computation time to finish one case of UAS wake encounter simulation while the VLM takes about 40 mins.

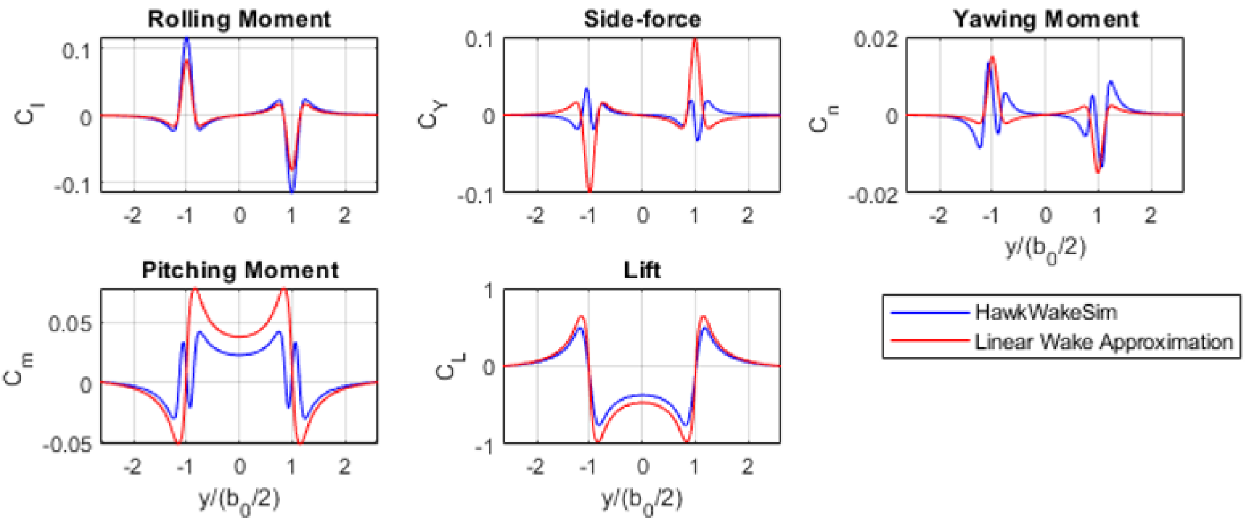

Figure 3-7. Comparison between VLM and linear approximation for Khawk55 parallel wake encounter.

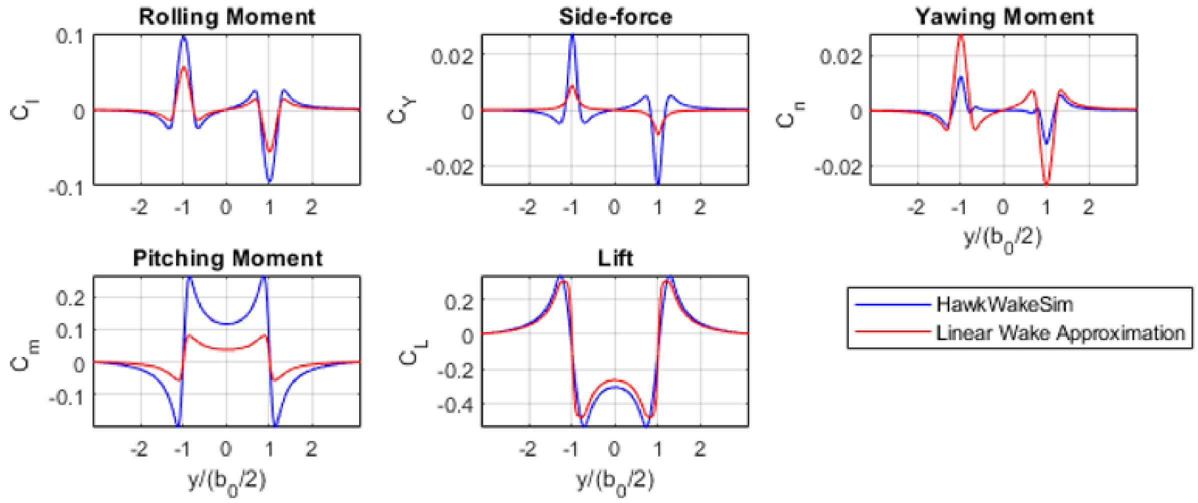

Figure 3-8. Comparison between VLM and linear approximation for Phastball parallel wake encounter.

3.1.1.4.3 Inner-loop attitude controller

Small UAS are typically equipped with various types of controller during flight test, including an inner loop attitude controller and an outer loop path tracking controller. In Sections 3.1.1.6 and 3.1.1.7, an inner loop attitude tracking controller is implemented and analyzed. An Linear Quadratic Regulator (LQR) controller is used for the roll hold and pitch hold of the Phastball UAS. The controller gains are selected based on identified Phastball state-space model and fine tuned in flight tests. A similar model-based inner loop attitude controller design approach is used for Khawk 55 UAS as well. Note that servo actuators are better modeled here including system delay, second order servo response model, and control surface saturation. The pitch controller was set up as a Proportional-Integral-Derivative (PID) controller while the roll controller was set up as a Proportional-Derivative (PD) controller. The controllers were tuned to hold the desired pitch and roll angles, respectively.

The rise time for the pitch hold controller is about 0.5s, with no overshooting and about 8% final tracking error. The current controller setting is used for simulating the autopilot reaction of Phastball and Khawk 55 during a WVE. The controller gains for Khawk55 sUAS are: $K_p = 0.4610, K_d = 0.0630$ for the roll hold controller, and $K_p = 0.2250,\ K_i = 0.1000, K_d = 0.0100$ for the pitch hold controller. The controller gains for Phastball UAS are $K_p = 0.63250, K_d = 0.1308$ for the roll hold controller, and $K_p = 0.5385,\ K_d = 0.0450$ for the pitch hold controller.

3.1.1.5 UAS wake encounter simulation with an attitude hold controller

The major goal in the development of HawkWakeSim is to predict small UAS WVE responses behind other aircraft and analyze the hazard levels especially at or close to the airport. Additionally, HawkWakeSim can be used as an initial prediction of UAS WVE encounter magnitude for potential UAS WVE flight tests. As an initial study, two types of wake encounter angles (90 deg. And 20 deg.) behind three representative leading aircraft (a Cessna 172, a Cessna Citation, and a Boeing 737-800) are simulated using both Phastball UAS and Khawk55 UAS. The leading aircraft were selected to provide a variety of wake circulation strengths ($20/94/250 m^2/s$) and vortex core separation distance. The leader aircraft and wake information are shown in Table 3-3. The 90-degree WVE represents UAS flying across the runway after takeoff of a leading aircraft while the 20-degree WVE represents a general aircraft wake encounter flight during cruise [16]. In all the 90 deg. and 20 deg. Wake encounter cases, the controller was set to hold desired roll and pitch attitude (zero roll and trim pitch) for the follower UAS.

Table 3-3. Specifications for wake vortex of leading aircraft.

Leader Aircraft	MTOW (N)	Circulation (m^2/s)	Core Radius (m)	Wingspan (m)
Cessna 172	7517	20	0.57	11
Cessna Citation	136916	94	1.14	22
Boeing 737	691243	250	1.87	36

3.1.1.5.1 90 degrees wake vortex encounter

The 90-degree wake encounter scenario is simplified due to the decoupled longitudinal and lateral-directional dynamics. The longitudinal UAS response will be dominant for 90 degree WVE, especially for this type of follower aircraft since the wake decay across the wingspan of a small UAS is negligible. The 90-degree wake encounter can be dangerous to sUAS due to wake generated stall possibilities. The following UAS WVE metrics will be focused on hazard analysis for 90-degree UAS WVEs: body frame accelerations a_z/a_x, body frame pitch rate q, local Angle of Attack (AOA), pitch angle, stall status, and maximum elevator deflection. The local AOA is defined as the local angle of attack at the location where the flow angle sensor is installed. During UAS WVE, the local AOA at the nose could be different than the AOA at the center of gravity or at the wingtip. In simulation, it can be calculated with respect to the nose panel of the geometry to simulate a vane or a 5-hole probe installed on the nose of an UAS.

Both Khawk 55 UAS and Phastball UAS are used for this WVE simulation study. The cruise speed is 20 m/s for the Khawk55 UAS and 31 m/s for the Phastball UAS. Due to the time constraints, Khawk55 UAS is only used for one case (WVE behind Cessna 172). The trajectory of Phastball UAS cutting through different wake vortices is shown in Figure 3-9. It can be observed that with the increasing size of leader aircraft and the increasing strength of wake vortex, the follower aircraft was pushed away and deviated from the wake vortex core.

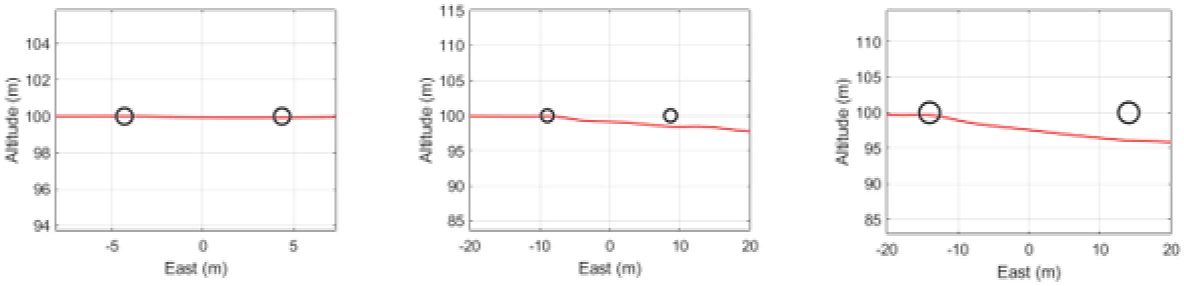

(a) Cessna 172 (b) Cessna Citation (c) Boeing 737-800

Figure 3-9. 90-degree wake encounter: reconstructed wake positions (o) and flight path in the wake axis y/z plane.

The Khawk55 UAS 90-deg. WVE responses behind a Cessna 172 aircraft is shown in Figure 3-10, with the dotted line showing the wake vortex core location. Pitch hold controller is enabled to track the trim angle. It can be observed that the local AOA reached above 10 deg., the vertical body acceleration reached -2.9 g, and the pitch rate showed minor oscillations between -25 and 25 deg/s during about 0.8 second of the wake encounter. The elevator moved between -2.5 and 2.5 degrees during the WVE.

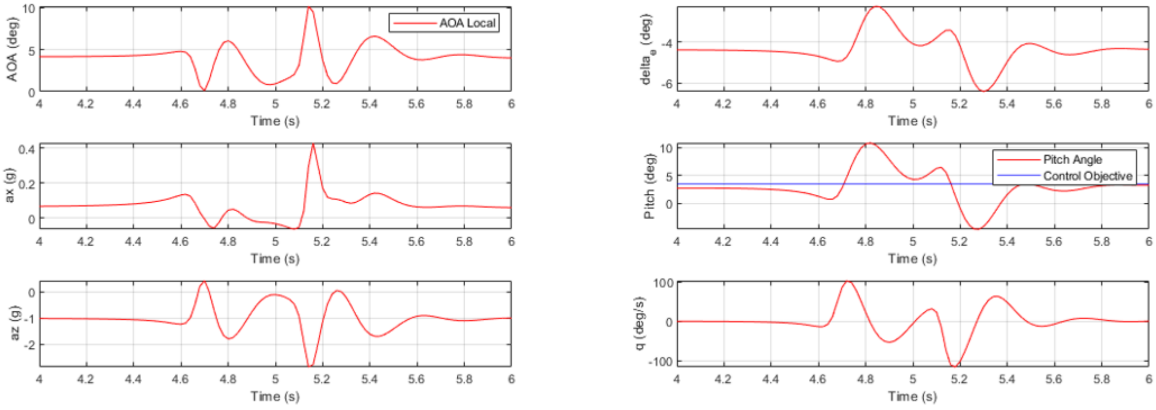

(a) α, a_z, a_x plot

(b) δ_e, θ, q plot

Figure 3-10. Khawk55 behind Cessna 172 90-degree WVE.

The Phastball UAS 90-degree WVE responses behind a Cessna 172 are shown in Figure 3-11. It can be observed that the local AOA went between -5 and 4 deg. During about 0.5 second of the wake encounter with the pitch hold controller in the loop. The smaller change in local AOA is mainly caused by the faster cruise speed of the Phastball UAS compared with the Khawk55 UAS. The other UAS responses are similar.

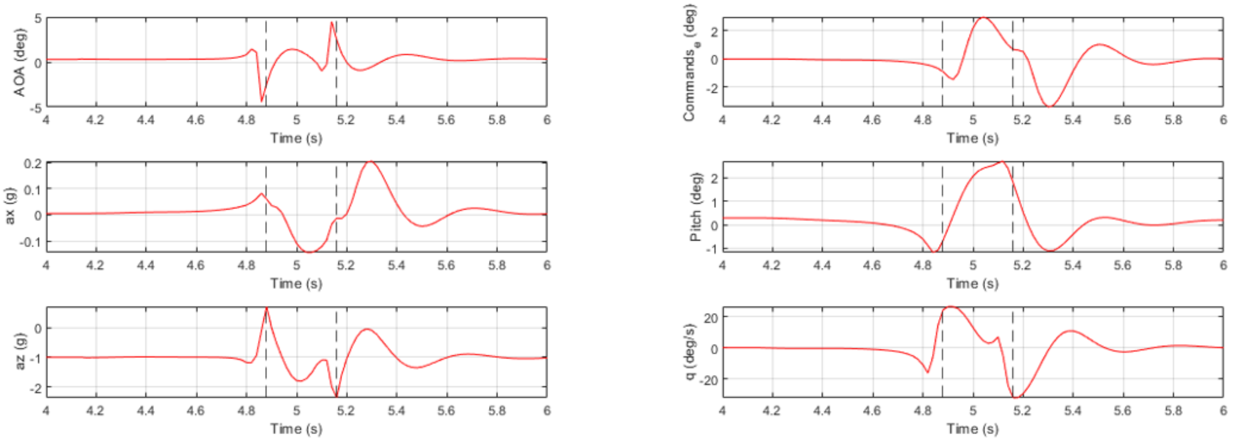

(a) α, a_x, a_z plot

(b) δ_e, q, θ plot

Figure 3-11.Phastball behind Cessna 172 90-degree WVE.

The Phastball UAS 90-deg. WVE responses behind a Cessna Citation and a Boeing 737-800 are further shown in Figure 3-12 and Figure 3-13 . It can be observed that the WVE time period increased for Cessna Citation and Boeing 737 due to the same reason explained in the previous paragraph. As the size of leader aircraft increases, elevator deflection reaches the limitation for 15 deg. both in Cessna Citation and Boeing 737 cases. From Figure 3-13, the elevator reaches its limitation for 0.05 s and AOA drops to -20 deg. The Phastball UAS is predicted to experience an approximately 7 g z-axis acceleration since the wake vortex generated by a Cessna Citation is three times bigger than a Cessna 172.

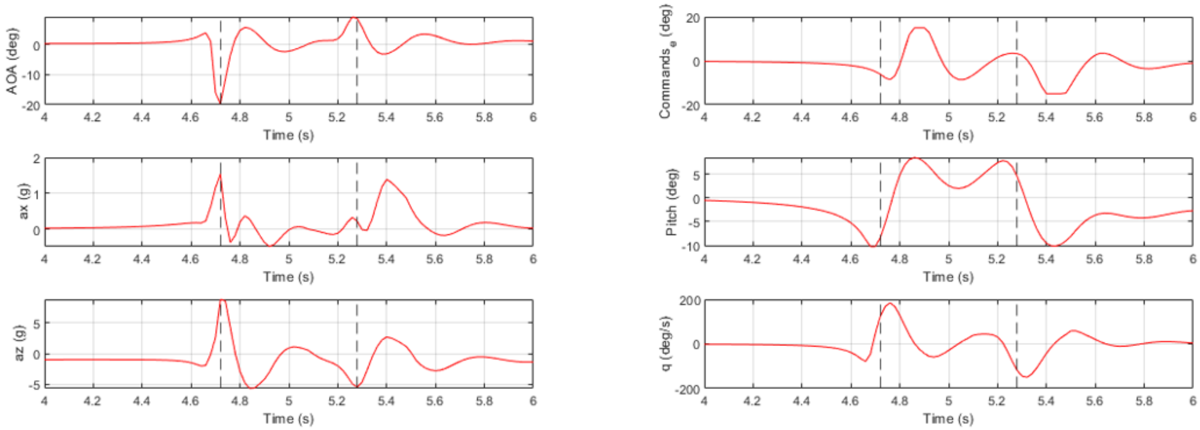

(a) α, a_x, a_z plot

(b) δ_e, q, θ plot

Figure 3-12. Phastball behind Citation 90-degree WVE.

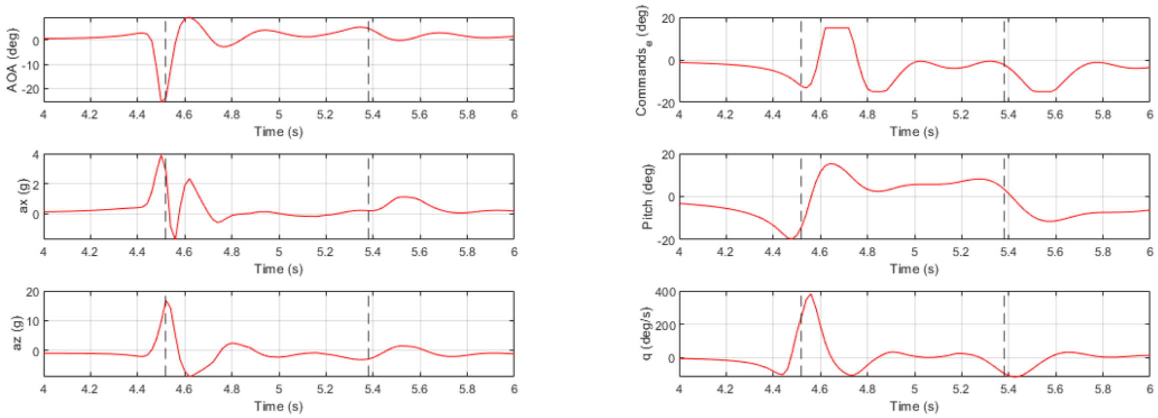

(a) α, a_z, a_z plot

(b) δ_e, q, θ plot

Figure 3-13. Phastball behind Boeing 737-800.

The 90-degree UAS WVE metrics are summarized in Table 3-4. There is a focus on five parameters: max AOA local, max q, max a_x, max a_x, and max δ_e. The local AOA is crucial for determining the stall condition of UAS and max pitch rate and max a_z can act as indicators for potential structural failures. The table illustrates that with increasing wake vortex strength, the magnitude of all the parameter values also increase. Future work is needed to determine the maximum tolerance point for a small UAS during a WVE. The maximum AOA reaches 25 deg during the Phastball encounter behind a Boeing 737-800, which could likely cause stall. Also, during this wake encounter, Phastball experienced a maximum vertical acceleration of 16.5g which may also lead to structural failure. The Khawk55 experienced a more significant response when compared to Phastball. This can be explained by its lower mass and inertia and by the tailless flying-wing configuration, which will have reduced longitudinal stability compared to conventional configurations. As seen in the table, Khawk55 will have a larger longitudinal response than Phastball for the same wake strength.

Table 3-4. Metrics for 90 deg. Wake encounter.

90 deg WVE	Max AOA local (deg)	Max q (deg/s)	Max a_x (g)	Max a_z (g)	Max δ_e (deg)
Khawk55 / Cessna 172	12	110	0.35	1.8	2
Phastball / Cessna 172	4.8	25	0.2	1.5	3
Phastball / Cessna Citation	18	190	1.5	9	15
Phastball / Boeing 737	25	380	4	16.5	15

3.1.1.5.2 20 degrees wake vortex encounter

A 20 degree UAS WVE response is analyzed next. This scenario was selected to be similar to previous WVE flight tests of manned aircraft [16] and UAS [6]. During a 20-degree WVE, both the lateral and longitudinal UAS responses will be excited, with the lateral impact being more noticeable due to the large wake induced rolling moment. Wake vortices with more strength pushed the UAS away from the vortex core, which is shown in Figure 3-14 and Figure 3-15, the y-z and x-y plot of Phastball WVE. The following UAS metrics are focused on 20 degree WVE: body frame accelerations $a_z/a_y/a_x$, body frame rotation rate $q/p/r$, local AOA and Angle of Sideslip (AOS), and maximum aileron and elevator deflection angles generated by the controller.

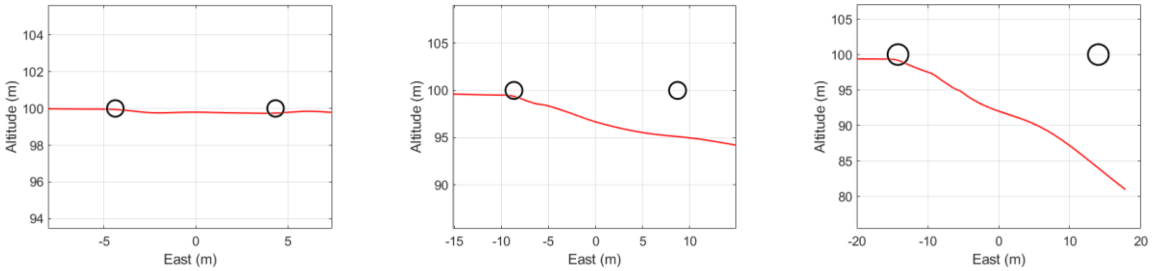

(a) Cessna 172 (b) Cessna Citation (c) Boeing 737

Figure 3-14. 20-degree Phastball wake encounter: reconstructed wake positions (o) and flight path in the plane perpendicular to the wake axis.

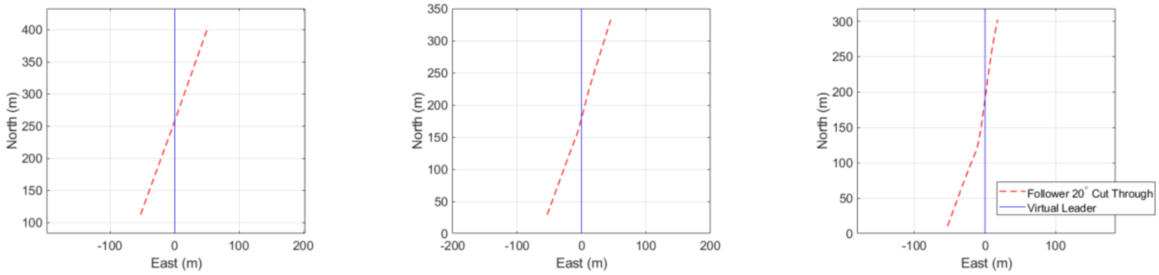

(a) Cessna 172 (b) Cessna Citation (c) Boeing 737

Figure 3-15. 20-degree Phastball wake encounter: flight path in the horizontal plane.

The response of the 20 deg. WVE cases are shown in Figure 3-16 and Figure 3-17. As observed in Figure 3-16, with a Phastball UAS behind a Cessna 172, the aileron command reaches up to 8 degrees and the elevator command reaches -5 degrees during the wake encounter to react to the wake disturbance. The wake vortex generated around 100 deg./s roll rate changes and around 40 deg./s pitch rate changes. The wake generated disturbances increased for the larger Cessna Citation and Boeing 737. As is shown in Figure 3-17 and Figure 3-18, the increasing vortex strength will push the follower UAS away from the wake vortex. Phastball UAS experienced a maximum 5 g acceleration in the z-direction and 3 g in the y-direction and a maximum of 150 deg/s pitch rate, behind a Cessna Citation. In the last case, the Boeing 737 vortex is strong enough to push the Phastball off from the original trajectory and, as a result, Phastball does not fly close to the second vortex core.

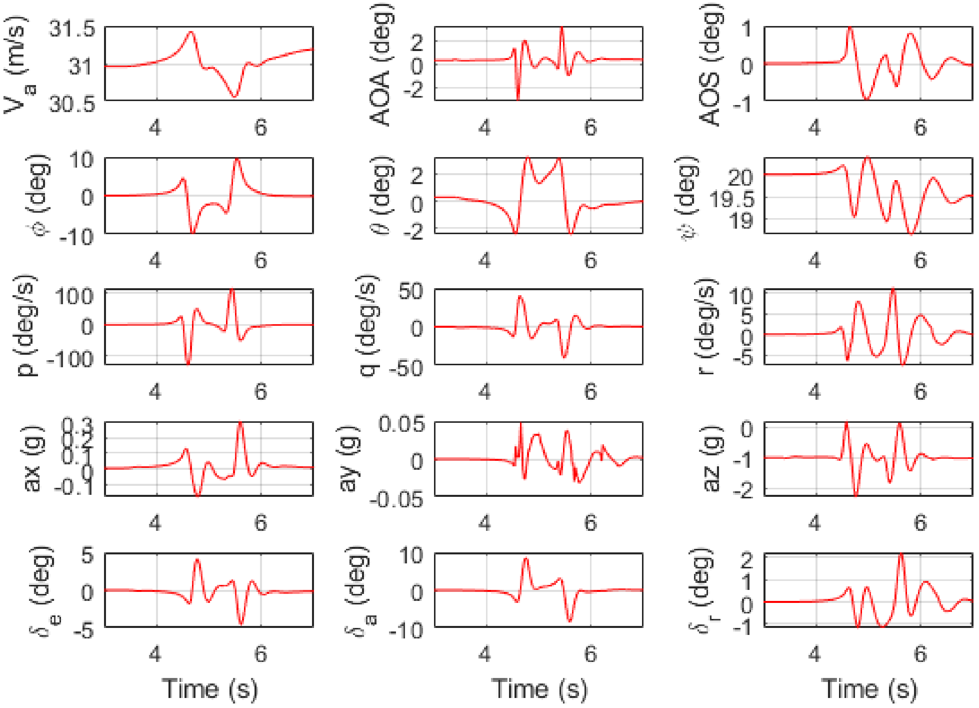

Figure 3-16. Phastball behind Cessna 172 20-degree WVE.

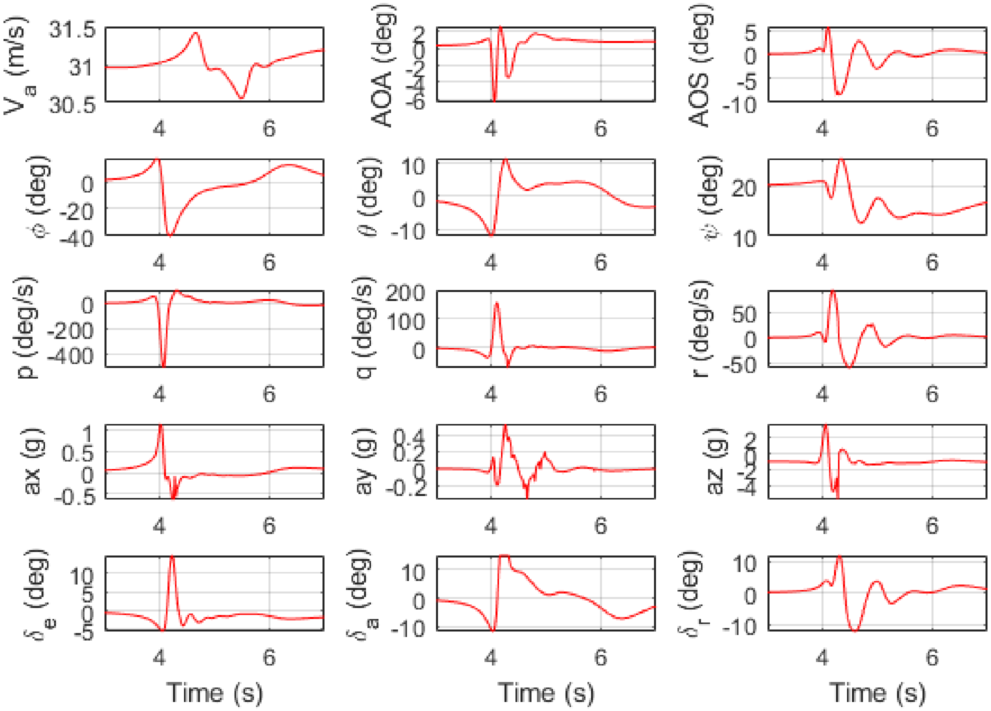

Figure 3-17. Phastball behind Cessna Citation 20-degree WVE.

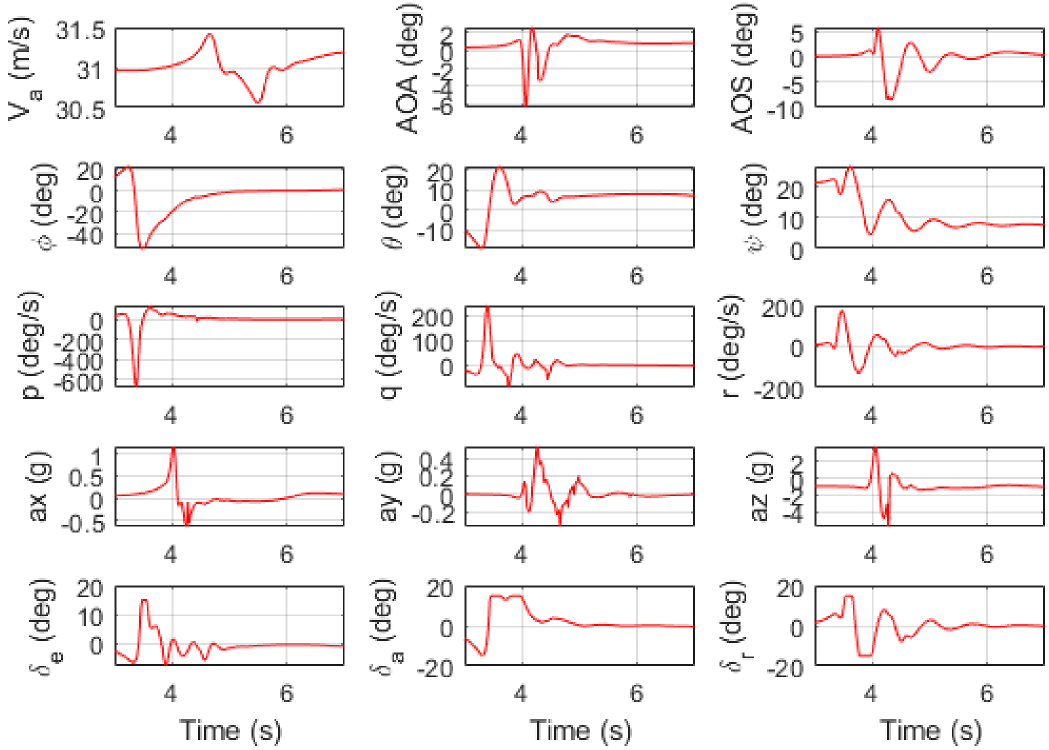

Figure 3-18. Phastball behind Boeing 737-800 20-degree WVE.

The 20-degree UAS WVE metrics are summarized in Table 3-5. In addition to the five longitudinal WVE metrics, six more lateral WVE metrics are focused: max AOS local, max p, max r, max a_y, max δ_a, and max δ_r. It can be observed that the maximum roll rate is a major indicator for 20 deg. UAS WVE in addition to the pitch rate. The body frame acceleration is another major indicator, however the impact on the vertical acceleration is less severe than for 90 deg. UAS WVE. The aileron and elevator control surface saturated during the WVE of both Cessna Citation and Boeing 737-800, which poses a hazard warning.

Table 3-5. Metrics for 20 deg. Wake encounter.

Leader aircraft	Max α_{local} (deg.)	Max β_{local} (deg.)	Max p (deg./s)	Max q (deg./s)	Max r (deg./s)	Max a_x (g)	Max a_y (g)	Max a_z (g)	Max δ_a (deg.)	Max δ_e (deg.)	Max δ_r (deg.)
Cessna 172	4.7	1	110	40	11	0.3	0.05	1.3	8	4	2.1
Cessna Citation	3	5	490	150	90	1.2	0.53	4.2	15	14	12
Boeing 737-800	5	8	680	240	160	2.2	0.93	6.1	15	15	15

3.1.1.5.3 Conclusions for Khawk55 and Phastball UAS wake encounter analysis

To summarize, both large jets show a significant hazard for sUAS in 90 and 20 deg. WVE cases. The strong vortices such as those generated by a Cessna Citation may cause control surface saturation which may lead to loss of control. This was seen in both 20 and 90 deg. WVE cases. UAS may stall during 90 deg. WVE behind a large jet. A large vertical acceleration may cause the structural failure which is another hazard observed from the WVE simulation. The Phastball UAS will have better control compared to the Khawk55 UAS because of its configuration and larger size.

3.1.1.6 UAS wake hazard metric and wake hazard zone prediction

Many researchers have looked into the wake separation rules for manned aircraft. The FAA is implementing wake separation rules at airports based on the categories of wake-generating and following aircraft, ranging from A Super (e.g., A380) to I Lower Small (e.g., C208). Roll Moment Coefficient (RMC) is utilized as the main metric for severity however, for the severity prediction of aircraft wake encounters, Roll Control Ratio (RCR) is often used as a severity metric since many manned aircraft experienced severe rolling during WVE [35, 36]. The RCR is defined as wake induced rolling moment divided by the aircraft maximum roll control power [32]. RCR is a dimensionless parameter which can be used for different configurations of aircraft. The advantage for using RCR as wake hazard criteria is that RCR is a dimensionless unit which can apply to any conventional type of aircraft. A 100% RCR means that the wake induced rolling moment exceed the maximum roll control power of the aircraft. An RCR of 20% configurationss is usually selected for manual flight, and 30% for automatic control of a manned aircraft. For the determination of RCR values, DLR further defined the safety operation criteria for manned aircraft including bank angle, airspeed deviation, descent speed, roll rate deviation, and load factor. The values of manned aircraft WVE criteria can be determined by pilot feedback, general flight control laws, and flight operation procedures [33, 34]. However, since manned aircraft is different than sUAS in moment of inertia, wing area, weight, flying speed, and so on, the criteria defined for sUAS may be quite different with manned aircraft.

3.1.1.6.1 Methodology

Based on the UAS WVE simulation studies in Section 3.1.1.5 as well as small UAS system identification and flight control experiences [21, 26–28, 35, 36], the following metrics are proposed for fixed-wing UAS wake hazard evaluation and predictions:

- Roll/pitch rate anomalies (p/q): Severe angular rate changes measured by inertial sensors are often the easiest wake encounter indicators for many UAS since flow anlge sensors may not be available due to their cost and maintainance challenges. And severe angular rates can cause control surface saturation since the onboard flight control laws will try to compensate for these disturbances
- Control ratio (δ_e , δ_a): The control surfaces for a UAS are constrained to a certain range (e.g., +-15 deg. For Khawk55 and Phastball UAS). A severe wake generated rolling or pitching may cause the controller to saturate and result in unexpected attitude or loss of control. Earlier studies showed that elevator may saturate during 90 deg. Wake encounters and aileron may saturate during 20 deg. wake encounters, which may generate significant safety issue for UAS.
- Angles of attack (α) and sideslip (β): Through the analysis, the researchers noticed that the UAS may stall while flying through the strong updraft portion of a wake field, due to

significant wake generated pitching moment. A potential stall (more than 20 deg. AOA) is noticed during 90 deg. wake encounters but not in 20 deg. wake encounters.

- Roll attitude anomalies (ϕ): Severe roll attitude values during wake encounters may also be dangerous since it may cause loss of vertical component of lift and go over the controller design limit. For example, Arduplane autopilot uses 45 deg. as the max desired roll angle.
- Structure load: Severe wake generated forces and moments may cause structure failures on an UAS (e.g., 10 g or above).

Based on the above metrics and proposed wake encounter modeling methods, a procedure for UAS wake hazard zone prediction at an airport is proposed as the following steps:

- Identify the wake generating aircraft information (flight path, wingspan, speed, weight, etc.) and the airport weather information (temperature, EDR, wind profile, etc.);
- Predict the wake vortex location using a wake transport and decay model;
- **Approach 1: Control ratio-based prediction (spatial analysis)**
  - Specify acceptable RCR and Pitch Control Ratio (PCR) for UAS WVE;
  - Run wake response model at different locations in the wake flow field to calculate wake induced moments and then generate predicted RCR and PCR values at different locations behind the wake (e.g., use HawkWakeSim VLM to calculate the wake induced roll moments when putting UAS at different lateral and vertical offsets from the wake vortex core for 10 deg. wake encounters);
- **Approach 2: UAS response and control-based prediction (spatiotemporal analysis)**
  - Specify acceptable UAS hazard metrics for potential wake encounter;
  - Use wake response model during the whole wake encounter time period to perform comprehensive wake encounter simulation studies to evaluate if any of the hazard metrics is exceeded (e.g., use HawkWakeSim VLM to simulate UAS WVE at 10 deg. encounter angle with the simulator time running from 0 to 10 sec.);
- Label red wake hazard zones based on obtained UAS responses.

3.1.1.6.2 Results and analysis for a typical UAS wake vortex encounter

A case study is demonstrated next using the above proposed UAS hazard metrics and wake hazard zone labeling methods. In this analysis, Phastball UAS WVE with wake vortices generated by a B737-800 during landing was simulated using HawkWakeSim v2.1-VLM. The simulated wake encounter response was analyzed using the previously-proposed wake hazard metrics and the two wake zone prediction methods. This research focuses on wake vortex encounters with small cutting angles such as 10 or 20 deg.

For approach 1 (control-ratio-based method), the wake hazard area is determined based on wake induced rolling moment coefficient and roll control ratio. Here, the RCR is defined as :

$$RCR = \frac{C_{l_{wake}}}{C_{l_{\delta_a}} \delta_{a_{max}}} \times 100\%$$

where $C_{l_{wake}}$ is the wake induced rolling moment coefficient, $C_{l_{\delta_a}}$ is the aileron to rolling moment control derivative for a UAS (e.g., 0.072 for Phastball UAS), and $\delta_{a_{max}}$ is the max aileron deflection angle for a UAS (e.g., 15 deg. For Phastball UAS).

The Phastball UAS was placed at different locations in the wake flow field. The wake induced rolling moment was then calculated using HawkWakeSim v2.1-VLM. Three example cases were run for the wake vortices generated by a Boeing 737-800 at 250, 175 and 100 m^2/s circulations, which correspond to the wake vortices at different ages of decaying. The hazard zones are labeled based on RCR values and shown in Figure 3-19 and Figure 3-20. The researchers chose an RCR of 0.3 as the threshold for this UAS hazard zone labeling based on this UAS system identification and flight test results. In other words, the blue (0.3-0.5), yellow (0.3-1), and red zones (> 1) are UAS wake hazard zones based on the researchers' suggestion. An RCR value of one or bigger means the wake generated rolling moment is equal to or bigger than what the max aileron control can compensate for, which is shown in red. Based on this analysis, a lateral separation of [-26, 26] m and a vertical separation of [-13, 13] m are predicted for 250 m^2/s wake circulation, where [0, 0] m means the center point of the two wake vortex cores. The predicted wake hazard zones for 175 and 100 m^2/s circulations are shown in Table 3-6. The overall trend of RCR for this UAS study matches with the trend for manned aircraft wake encounter analysis. It can be observed that UAS RCR plot has more white areas in between the two vortex cores compared with manned aircraft. This is probably caused by the dominant downdraft in this region and the smaller wingspan of Phastball UAS.

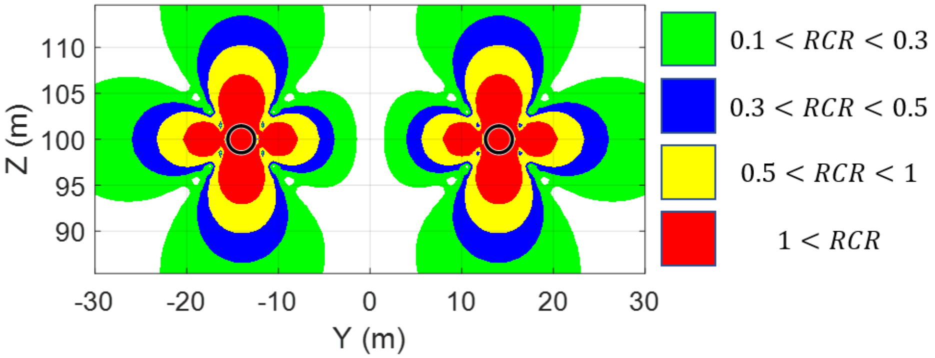

Figure 3-19. Wake induced roll control ratio for wake circulation of 250 m^2/s (Phastball UAS encountering of Boeing 737-800 wake).

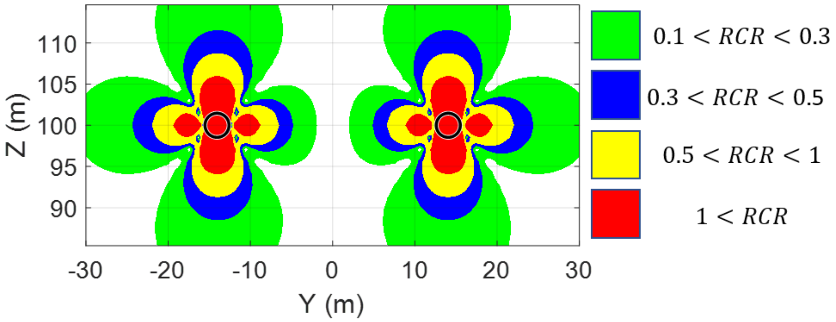

Figure 3-20. Wake induced roll control ratio for wake circulation of 175 m^2/s (Phastball UAS encountering of Boeing 737-800 wake).

Table 3-6. Example wake hazard zone prediction using approach 1 (Phastball UAS behind Boeing 737-800, 10 deg. encounter angle, 0.3 RCR).

Wake circulation	Lateral offset	Vertical offset
250 m^2/s	[-26, 26] m	[-13, 13] m
175 m^2/s	[-25, 25] m	[-12, 12] m
100 m^2/s	[-23, 23] m	[-8, 8] m

Using Approach 2, the wake hazard area can also be determined based on the area in which the aircraft maximum response falls outside of any one of the acceptable conditions defined in Table 3-6. Based on our earlier simulation studies in Section 3.1.1.5, the roll rate and roll control input are the two major indicators for UAS wake hazard determination at small encountering angles. In this analysis, the roll rate deviation was selected as 34.6 deg/s for Phastball UAS with attitude hold controllers based on aileron controller gains:

$$k * \delta_{a_{max}} = k_p * (\phi_d - \phi) + k_d * p$$

where k is the control ratio (0.3 for this case) and k_d is 0.13 for our PD roll hold controller, which can also be found in Section 3.1.1.4. The roll angle limit is set as 60 deg. based on manual flight data. Other wake hazard metrics for this case study are also provided in Table 3-7.

Table 3-7. Example wake Hazard Metrics for lateral WVE of Phastball UAS with attitude hold controller (WVE during straight line steady state flight).

Parameter	**Acceptable Conditions**
Roll Rate Deviation	$p \leq \pm 35°/s$
Roll Control Percentage	$\delta_a \leq \pm\ 30\%\ \delta_{a_{max}}$
Bank Angle Deviation	$\phi \leq \pm\ 60°$
Acceleration Deviation	$a_y \leq \pm\ 10g$

Using Approach 2 for HawkWakeSim simulations of a Phastball UAS WVE behind a B737 generated a safe operation distance of 15 m away laterally and 5 m away vertically from the C.G. of leading aircraft, when the wake circulation is 250 m^2/s. The estimated wake hazard zones are slightly different but comparable between approach 2 and approach 1. It is worth emphasizing here that it is more challenging to run the coupled aerodynamic and flight dynamic simulator during the whole wake encounter period (Approach 2) than only run the simulator at fixed locations in the wake flow field (Approach 1), since the estimated wake induced forces and moments may affect the later calculations. The initial results showed a comparable performance between these two approaches. More analysis needs to be done for different wake strength and for various wake encounter angles.

Figure 3-21 shows the labeled wake hazard area with strong cross wind from the west (20 knots at 10 m with 1/7 power law profile, medium EDR: 0.0121 $m^{2/3}\ s^{-1}$) and flight path angle discussed in the previous section. The port hazard region is marked green and starboard hazard region is marked red. As shown in the figure, the wake vortex starts to descend after forming. The aircraft trajectory was marked in black while t = 0 s indicated when the aircraft touched down at (0, 0, 0) m. Under the high cross wind condition, the wake vortex could be carried 950 m away from the runway and might cause wake hazards for sUAS operation this region.

More analysis and evaluation of the proposed UAS wake hazard metrics and wake zone categorization can be performed in the future, using different wake generating aircraft and UAS and varying weather conditions

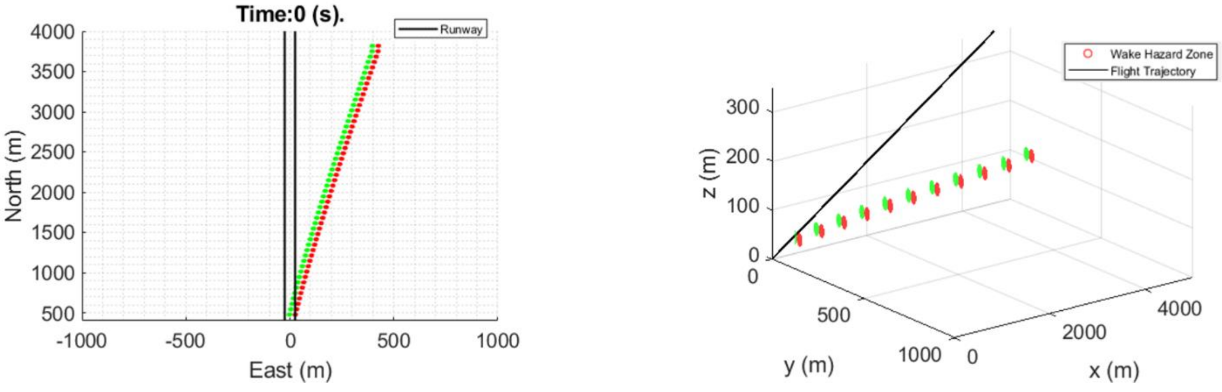

(a) X-Y Plot (Top View) (b) X-Y-Z Plot (Side View)

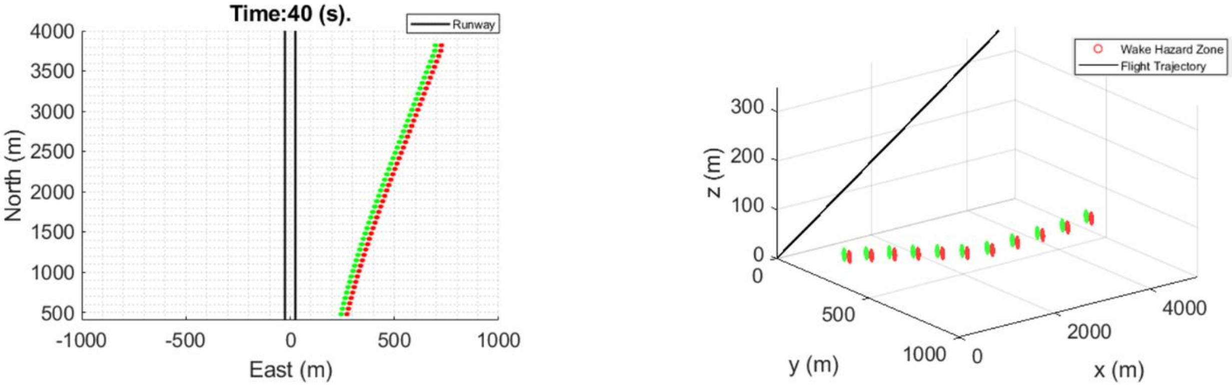

(c) X-Y Plot (Top View) (d) X-Y-Z Plot (Side View)

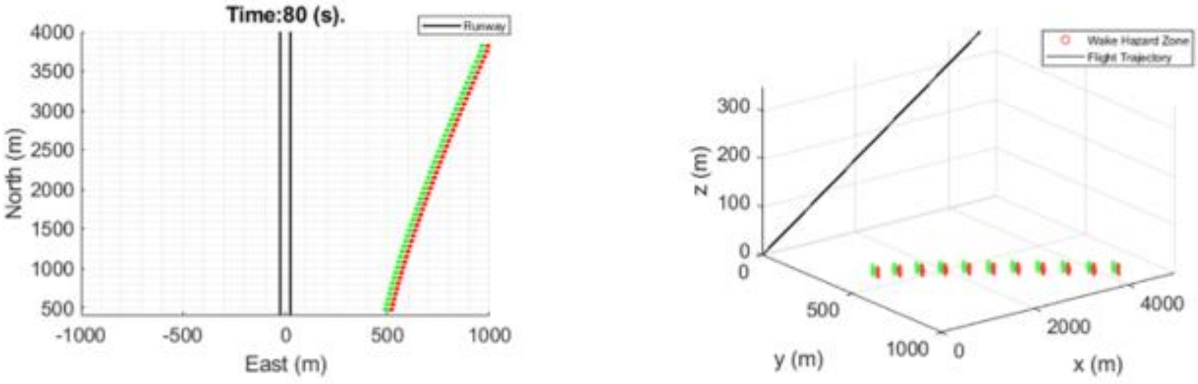

(e) X-Y Plot (Top View) (f) X-Y-Z Plot (Side View)

Figure 3-21. Wake hazard area prediction in strong cross-wind at airport (0, 40 and 80 s).

3.1.1.7 Improved attitude hold controller design and analysis for UAS wake encounter

For the WVE problem wherein disturbances are dramatic, the low-level attitude control law will have the most significant impact on the UAS response, as the response is likely independent of most high-level guidance logic. As such, inner loop roll, and pitch hold controllers with improved disturbance negation were the focus of this study.

A classical PID structure is used for both controllers, using attitude angle and rate feedback. PID controller is very common for small UAS and have shown to be effective for a wide range of UAS sizes and configurations, as evidenced by their wide use in open-source UAS autopilots, such as ArduPilot, PX4, and Paparazzi. Furthermore, the flexibility of PID controllers ensures the same control structure can be used for future simulations with different UAS, which is useful for later comprehensive analysis and comparisons. The roll/pitch hold PID control structure is shown in Figure 3-22.

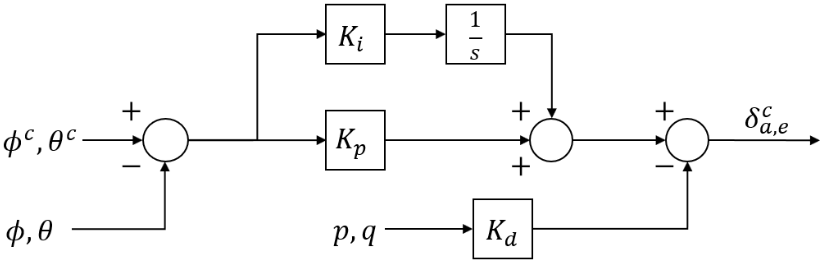

Figure 3-22. Roll and pitch hold controller structure.

The controller outputs a command that is sent to the servos, or actuators. The actuators used in this paper are modeled by second-order transfer function, which was identified from experimental data:

$$G_{act} = \frac{\omega_n^2}{s^2 + 2\zeta\,\omega_n\,s + \omega_n^2}$$

where ω_n = 30.7 rad/s is the natural frequency and ζ = 0.62 is the damping coefficient of the actuator.

3.1.1.7.1 Controller specifications

As no handling-quality requirements exist for small UAS, selecting controller specifications can be a delicate task. For this application, it is important to select a set of specifications that is independent of UAS-specific parameters, such as size, weight, or configuration. Instead, the researchers desire to select a set of specifications that can be used to design controllers for a variety of UAS. This provides a baseline for direct comparison of different UAS' response to the same wake vortex.

The specifications were selected based on manned aircraft handling quality and flight control system specifications [17, 18] and existing literature for small UAS multi-objective control design[19]. Two sets of specifications were used to design a nominal controller and a disturbance rejection controller (such as wake disturbances).

3.1.1.7.2 Nominal controller specifications

The first requirements deal with the stability of the single-input, single-output closed-loop systems, ϕ/ϕ_{cmd} and $\theta/\theta_{\text{cmd}}$. First, the system is required to be stable (all of the eigenvalues are in the left-hand plane). Second, the stability margins of the loop gain broken at the actuator must meet the requirements:

$$\begin{gathered}\text{Gain Margin (GM)} > 6\text{ dB}\\ \text{Phase Margin (PM)} > 45\text{ deg}\end{gathered} \tag{10}$$

The next requirements deal with the damping of the closed-loop system. These requirements differ for the longitudinal and the lateral-directional dynamic modes. The damping is required to be above the minimum values depending on frequency:

$$\zeta_{\mathrm{lon}} \geq \begin{cases} 0.04 & \omega_n < 1\mathrm{rad/s} \\ 0.4 & 1 \leq \omega_n < 20\mathrm{rad/s} \\ 0.25 & \omega_n \geq 20\mathrm{rad/s} \end{cases} \tag{11}$$

$$\zeta_{\mathrm{lat-dir}} \geq \begin{cases} 0.4 & \omega_n \leq 15\mathrm{rad/s} \\ 0.3 & \omega_n > 15\mathrm{rad/s} \end{cases} \tag{12}$$

The step response of the closed-loop system is required to have an overshoot less than 10%, and the gains are constrained based on the empirical methods discussed in [20].

$$\begin{aligned} K_i &\leq 0.4\, K_p \\ K_d &\leq 0.15\, K_p \end{aligned}$$

Lastly, minimum requirements for the Disturbance Rejection Bandwidth (DRB) and Disturbance Rejection Peak (DRP) are set. These criteria are defined based on the output sensitivity function of the roll or pitch angle, respectively. The DRB is computed as the frequency at which the sensitivity function crosses -3 dB, and the DRP is defined as the maximum magnitude of the sensitivity function. It has been shown that increasing DRB can lead to increased rejection of disturbances to the roll or pitch angles [21]. However, increasing DRB will also come at the cost of increasing DRP (commonly known as the "waterbed effect"). The disturbance rejection requirements are:

$$\begin{aligned} \mathrm{DRB} &\geq 0.9\mathrm{rad/s} \\ \mathrm{DRP} &\leq 5\mathrm{dB} \end{aligned}$$

The nominal controller was tuned by hand to achieve a desirable step response such that all specifications were met. A conservative design was selected to reduce the control surface activity. The roll and pitch controllers designed for the Khawk55 UAS are summarized in Table 3-8

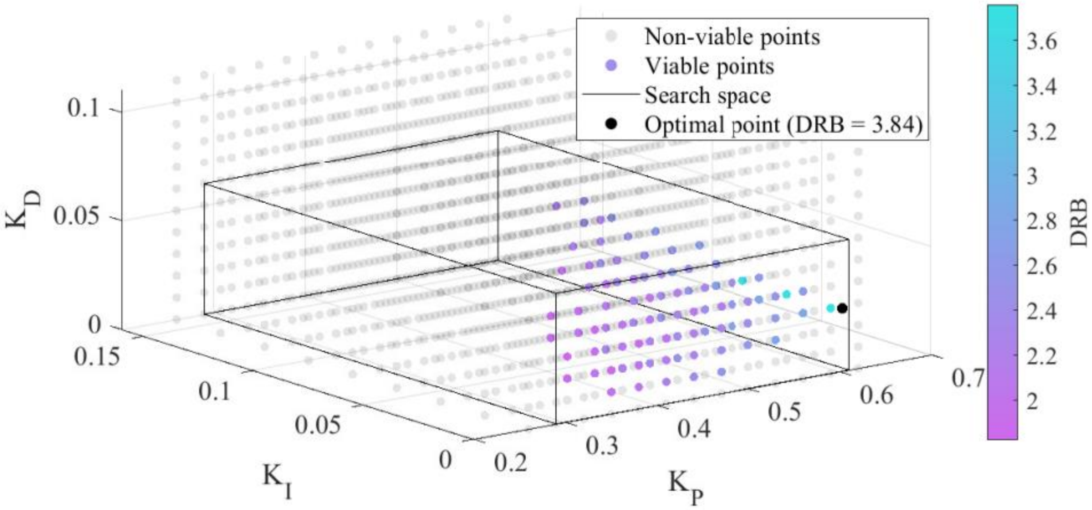

Figure 3-23. Design of disturbance rejection controllers through optimization.

3.1.1.7.3 Disturbance rejection controller

Several requirements were relaxed for the disturbance rejection controller, with the ultimate goal of increasing the DRB of the system. The stability margin and disturbance rejection specifications were relaxed by 20%. The minimum damping specification was reduced by 0.05 for all frequencies except the low-frequency longitudinal modes.

Additionally, the disturbance rejection controller was designed using an optimization strategy, rather than being tuned by hand. The DRB was maximized, subject to the constraints of the controller specifications. This was achieved by first performing a scatter analysis to identify a small search space. Then, pattern search optimization was performed to find the gain set that maximized the DRB. An example of this process is visualized in Figure 3-23.

Table 3-8. Khawk55 roll and pitch controller metrics.

	Roll controller		**Pitch controller**	
Metric	**Nominal**	**Dist. Rej.**	**Nominal**	**Dist. Rej.**
K_p	0.3	0.530	0.20	0.383
K_i	0.02	0	0	0
K_d	0.029	0.030	0.015	0.011
Overshoot (%)	5.1	10.0	0	0
GM (dB)	15.4	11.7	9.4	6.3
PM (deg)	76.2	44.3	101	87.0
DRB (rad/s)	1.8	2.8	2.3	4.9
DRP (dB)	3.0	5.5	2.5	6.0

3.1.1.7.4 Wake encounter simulation with the improved attitude hold controller

The methods discussed previously can be used for rapid small UAS WVE simulation and controller performance evaluation. In this section, initial simulation results will be shown and discussed. Four WVE scenarios are presented to demonstrate the effects of wake encounter angle, core radius size, and circulation strength on the encounter severity and controller performance. Response measurements such as roll and pitch angles, angular rates, body accelerations, and control activity are analyzed to evaluate severity and controller performance.

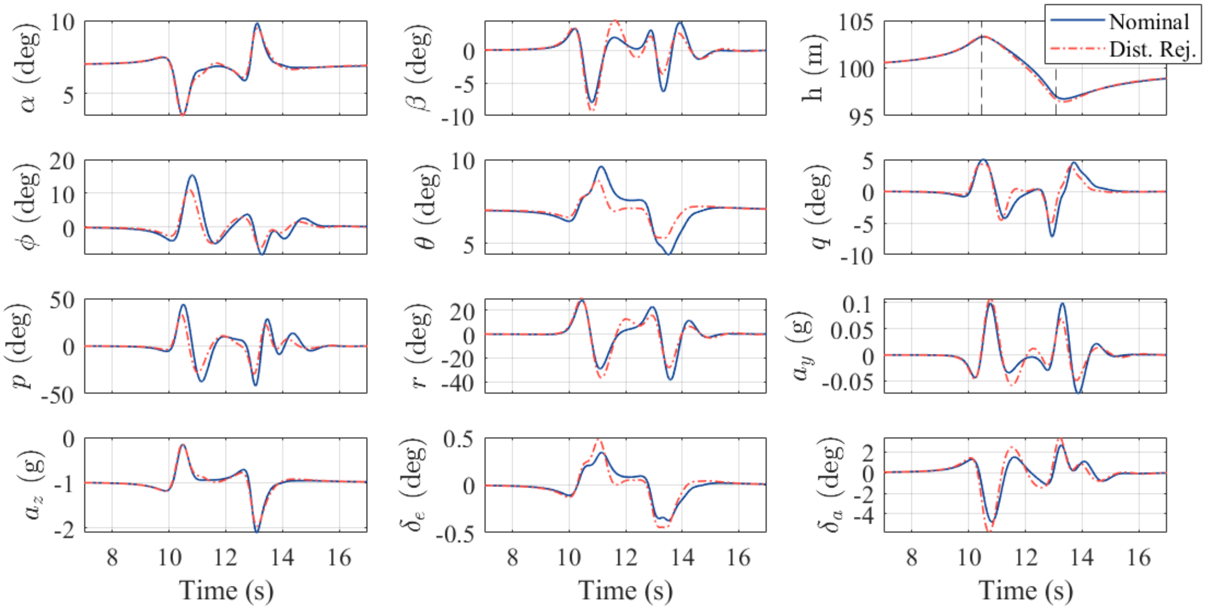

Figure 3-24. KHawk-55 30° wake vortex encounter (Γ=100 m^2/s, b=30 m).

The first case analyzed is shown in Figure 3-24. The UAS was simulated to encounter a wake vortex at a 30-degree angle. The wake was generated by an aircraft with a 30 m wingspan and has a circulation of 100 m^2/s and core radius of 1.2 m. This size of vortex is representative of a narrow-body airliner, such as a Boeing 737-800, that is about five miles away from the UAS.

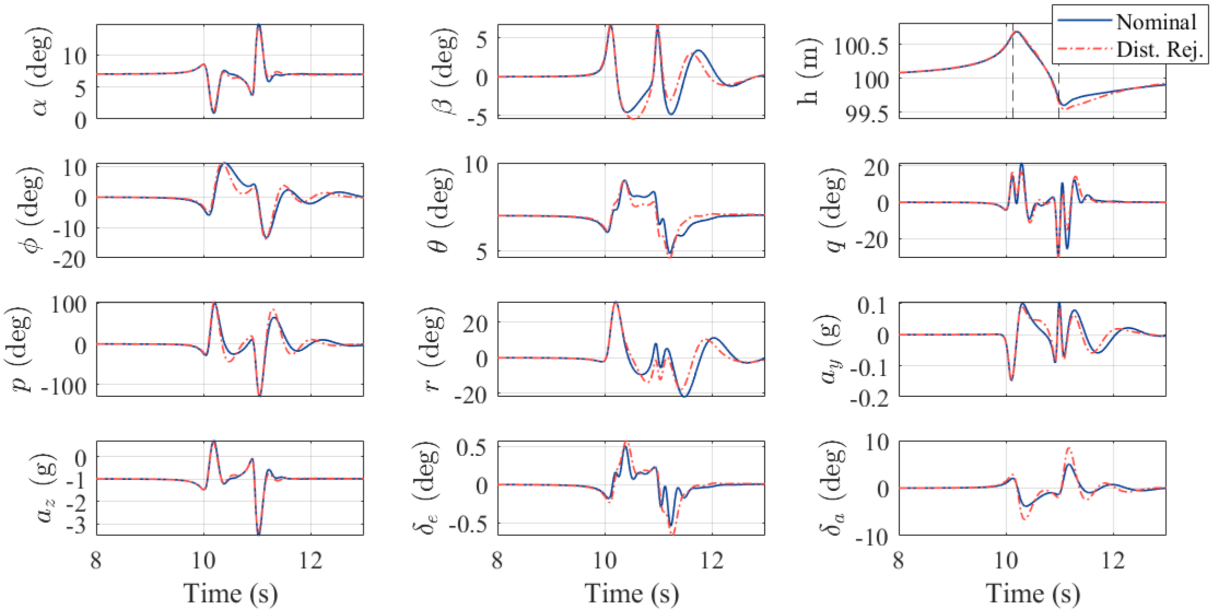

Figure 3-25. Khawk--55 30◦ wake vortex encounter (Γ = 20 m^2/s, b = 10 m).

The primary response of the UAS can be observed in the roll angle and roll rate plots, where the disturbance rejection controller reduces the peak of each response by about 25%. The pitch angle response is also reduced. The controller successfully attenuates disturbances at the cost of more aggressive control commands, which can be seen in the aileron and elevator plots. Finally, the altitude plot shows the trajectory of the UAS, with the position of the wake cores shown as black, dashed lines. The wake vortex pushes the UAS above the first core, then causes the UAS to rapidly loses altitude and cross the second vortex several meters below the core.

The disturbance rejection controller was very effective under the conditions of the previous case. However, for rapid WVEs, characterized by small vortex radii or near-perpendicular encounter angles, the different controllers resulted in very little difference in the UAS response. This can be seen in the encounter shown in Figure 3-25. The vortex was generated by an aircraft with a 10 m wingspan, has circulation strength of 20 m^2/s, and core radius of 0.4 m. This is representative of the wake of a single-engine general aviation aircraft. The controller cannot respond quickly enough and, as such, has less impact on the UAS response during the encounter. The UAS encounters both cores directly and responds with a large roll rate. However, because of the encounter brevity and low strength of the vortex, the roll angle excursions are still relatively small.

Similar trends can be seen for encounters where the UAS crosses perpendicularly behind the generating aircraft, even for wakes of larger sizes. This is demonstrated in Figure 3-26. Even with the wake generated from a 30-meter-wingspan aircraft, the response is too quick for the controller to alleviate. The UAS briefly experiences large vertical loads and pitch rates.

Lastly, the opposite phenomenon can be seen for slow, drawn out encounters. In Figure 3-25, the UAS was simulated to fly through the wake of the aforementioned small, general aviation aircraft. The wake is generated at a 10-degree climb angle, and the UAS crosses the wake at a 15-degree encounter angle. The encounter is slow and drawn out, and the UAS only crosses through one of the vortex cores. As such, even with the very small core radius, the disturbance rejection controller alleviates the roll response, though the difference is small. The roll angle is the largest of any of the four simulated scenarios, and the aileron saturates. This indicates the significant hazard presented by this type of vortex encounter, where the UAS is near the vortex core for a long period of time.

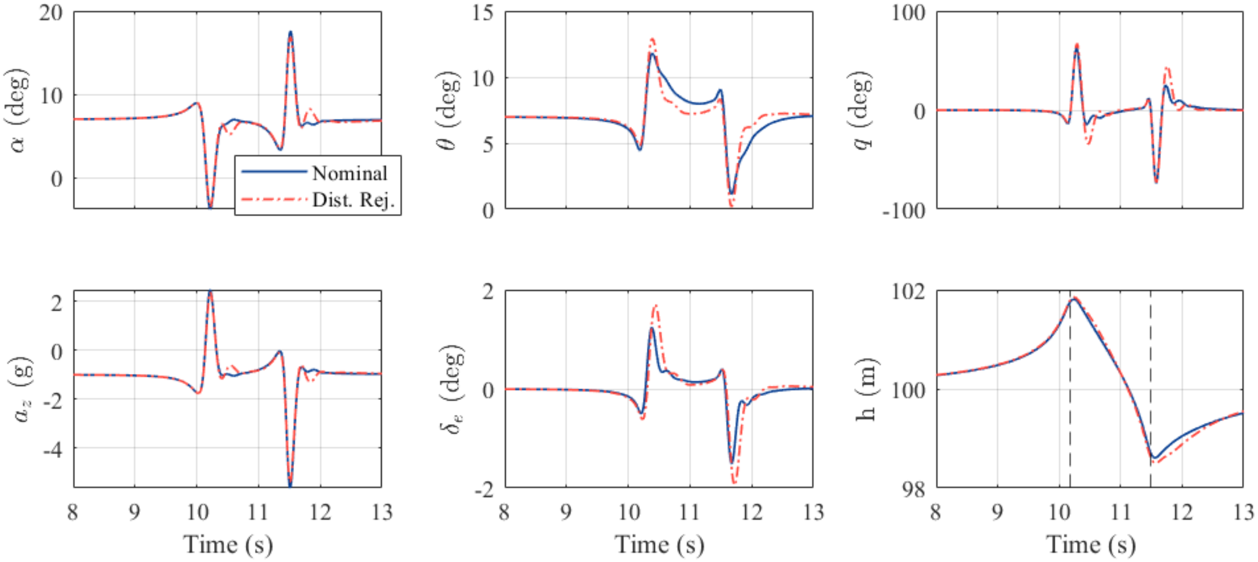

Figure 3-26. KHawk-55 30° wake vortex encounter (Γ=100 m^2/s, b=30 m).

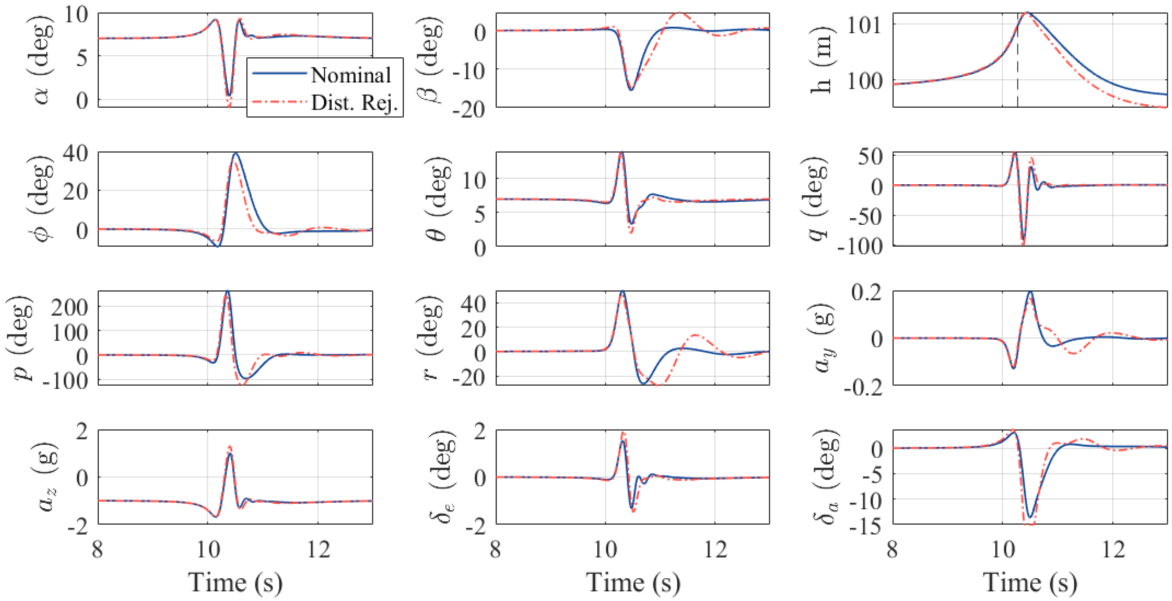

Figure 3-27. Khawk-55 30° wake vortex encounter (Γ=20 m^2/s, b=10 m).

3.1.1.7.5 Conclusions for simulation with an attitude hold controller

In summary, two inner loop attitude hold controllers were designed to evaluate the impact of the low-level flight control during the UAS WVE. These controllers were based on specifications for nominal conditions and for maximized disturbance rejection. Linear wind field approximation method is used for the prediction of UAS wake encounter responses. Simulation results showed that the disturbance rejection controller successfully attenuated the UAS WVE response for cases where the encounter was prolonged by either the vortex size or encounter angle. However, for rapid WVEs, such as during perpendicular flight across the wake, both controllers show similar performance.

3.1.2 Flight dynamics simulation using non-linear lift curve coefficients

The equations of motion for a fixed wing UAS are augmented to include one of the many non-linearities at play in wake vortex encounter simulation. This model is then used with a path-following controller to simulate two types of UAS wake vortex encounters.

3.1.2.1 Simulation scenarios

Computer simulations were conducted to study the effect of the wake vortex produced by a leader aircraft on a following aircraft's stability encountering the vortex. Here, the simulation results of four scenarios are presented.

Figure 3-28. shows top-view snapshots of each of these scenarios. Each scenario represents an event where the follower aircraft cruises near a runway while the leader aircraft is taking off. The two vortices generated from the two wing tips of the leader aircraft can affect the follower aircraft's stability. The results show how the vortex strength on the follower aircraft varies with its distance and orientation from the leader aircraft.

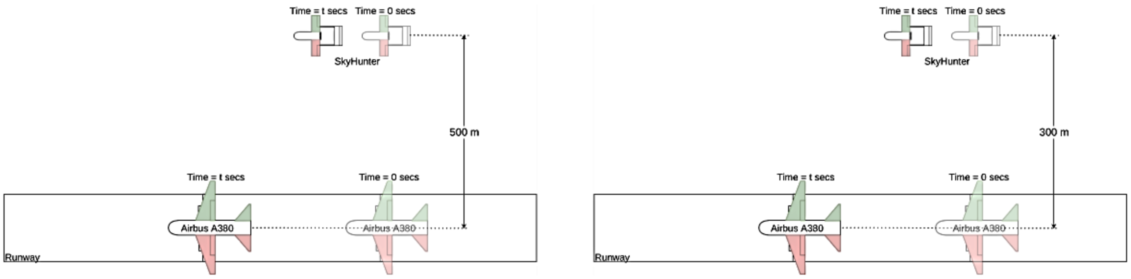

(a) Scenario 1 (ST1) (b) Scenario 2 (ST2)

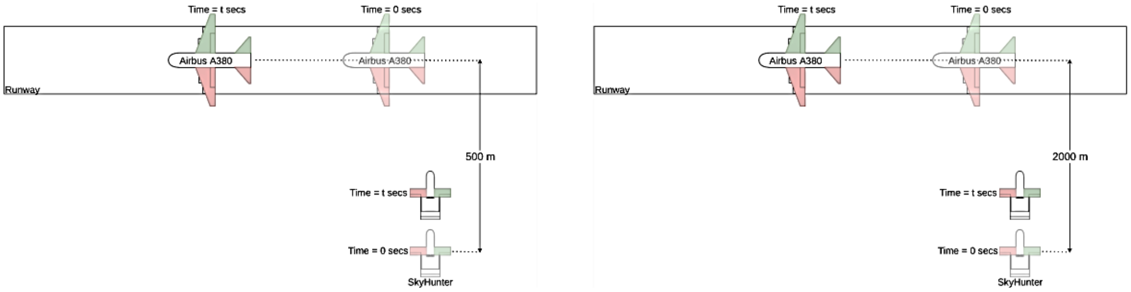

(c) Scenario 3 (ST3) (d) Scenario 4 (ST4)

Figure 3-28. Simulation scenarios.

In ST1 & ST2, the follower aircraft (a SkyHunter, described in Section 3.3.1) is flying at 350 ft AGL in parallel with the wake vortex-producing aircraft (an Airbus 380) with a 15 feet per second cross-wind. In ST3 & ST4, the follower aircraft (SkyHunter) is also flying at 350 ft AGL across the wake vortex produced by the leader aircraft (Airbus 380).

In the first two scenarios (ST1 & ST2) as shown in Figure 3-28, at a timestamp of 0 secs, the longitudinal distance of the leader aircraft from the follower aircraft is 0 m, and its longitudinal axis is in a parallel orientation with the longitudinal axis of the leader aircraft. The lateral distance of the leader aircraft from the follower aircraft in ST1 is 500 m and reduced to 300 m in ST2. In the last two scenarios (ST3 & ST4), depicted in Figure 3-28, the follower aircraft flight path is oriented at a right angle with the leader aircraft at a timestamp of 0 secs. The lateral distance of the leader aircraft from the follower aircraft is reduced from 2000 m (ST4) to 500 m (ST3).

Table 3-9. Leader aircraft specifications.

Aircraft model	Class	Mass	Wingspan	Take-off speed
		[kg]	[m]	[ms^{-1}]
Cessna 172	I	1,111	11	31
Boeing 737	II	41,410	34	77
Airbus A380	III	575,000	64	80

Table 3-10. Follower aircraft specifications.

Aircraft model	Mass	Wingspan	Cruise speed
	[kg]	[m]	[ms^{-1}]
SkyHunter	4	4	14

A leader aircraft model from 3 aircraft classes, class I, II, & III, is chosen in each scenario. The name and specifications of these leader aircraft are given in Table 3-9. A small UAV, a SkyHunter, is used as an example follower aircraft model; its specifications are shown in Table 3-10.

3.1.2.2 6 DOF Nonlinear equations of motion

Following [1], the aircraft's nonlinear dynamics are described using 6 DOF, 12-state Newton-Euler equations of motion. The aircraft is modeled as a rigid body of mass m, with inertia tensor J. The 12-state vector includes the aircraft's 3D position $p \equiv [p_x, p_y, p_z]^T$, attitude based on Euler angles (i.e., roll, pitch, and yaw) $\phi \equiv [\phi, \theta, \psi]^T$, translational velocity $v \equiv [u, v, w]^T$, and angular velocity $\omega = [P, Q, R]^T$. The aircraft is controlled using four control inputs, $u \equiv [\delta_t, \delta_e, \delta_a, \delta_r]^T$, which are throttle, elevator, aileron, rudder deflections, respectively. Equations of Motion for translational and angular momentum are

$$\dot{v} = -\omega \times v + \frac{1}{m} F_{G+A+T}$$

and

$$\dot{\omega} = J^{-1}(-\omega \times (J\omega) + M_{A+T})$$

respectively. Where, $F_{G+A+T} \equiv [F_x, F_y, F_z]^T$ represents the summation of forces generated in the body frame $\{b\}$ due to gravity, aerodynamics, and thrust. Similarly, $M_{A+T} \equiv [l, m, n]^T$ represents the summation of moments generated in $\{b\}$ due to aerodynamics and thrust.

Longitudinal and lateral directional force and moment coefficients are described by first-order Taylor series approximations. Lift force coefficients (C_L) and pitching moment coefficients (C_m) are expressed as a function of α, q, u, $\dot{\alpha}$, and δ_e . Lateral force coefficient (C_Y), rolling moment coefficient (C_l), and yawing moment coefficient (C_n) are expressed as a function of β, p, r, δ_a, and δ_r. The stability and control derivative coefficients for the aircraft are calculated using Advanced Aircraft Analysis (AAA) [22] software package.

The drag coefficient (C_D) is provided by the Prandtl nonlinear relationship:

$$C_D = \overline{C}_{D_0} + \frac{C_L^2}{\pi A R e}$$

Lift force coefficients (C_L) are modeled as a nonlinear function of α as follows [23]:

$$C_L = C_{L_{\alpha=0}} + C_{L_\alpha}\alpha - RCL(\frac{\alpha-A_0)}{ACL-A_0}) \tag{13}$$

$$RCL = C_{L_{\alpha=0}} + C_{L_\alpha}\alpha - C_{L_{max}}$$

$$N = 1 + \frac{C_{L_{max}}}{RCL}$$

The nonlinear C_L vs α (normalized) graph is shown in Figure 3-29.

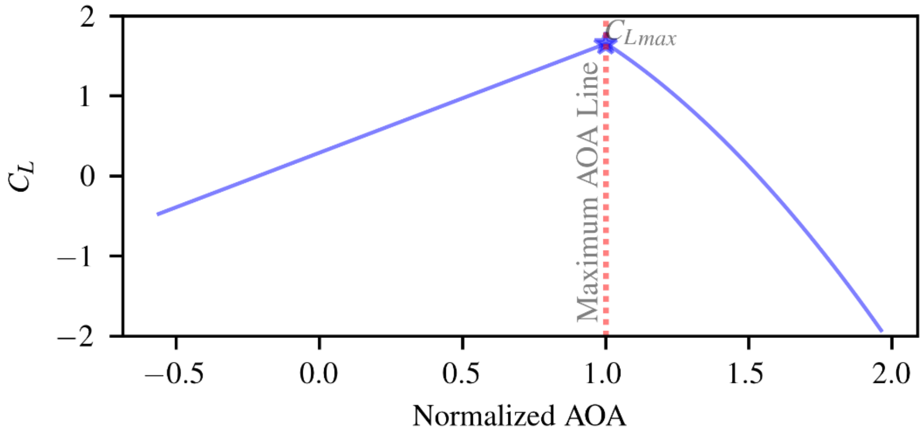

Figure 3-29. Nonlinear C_L versus α graph.

The aircraft relative airspeed vector, v_r^b, is defined (in the body frame) as the velocities of the UAV relative to the surrounding air mass velocity, v_w^b, also in the body frame. That is:

$$v_r^b = \begin{bmatrix} u_r \\ v_r \\ w_r \end{bmatrix} = v^b - v_w^b$$

From the airspeed vector, we can calculate the total airspeed V_a, the angle of attack α, and the sideslip angle β as

$$V_a = \sqrt{u_r^2 + v_r^2 + w_r^2}$$

$$\alpha = \tan^{-1}\left(\frac{w_r}{u_r}\right) \tag{14}$$

$$\beta = \sin^{-1}\left(\frac{v_r}{V_a}\right) \tag{15}$$

The follower aircraft encounters the wake vortex the leader aircraft produces if the distance between these two aircraft is within the impact range. The Burnham-Hallock vortex model gives the velocity distribution of the wake vortex, and its detailed implementation can be found in [6].

To accurately model the effect of wake vortex on the follower aircraft, the wing planform is divided into two sections: left and right. Each of the two wing sections experiences wake vortex velocity components as a function of the location of the section wing tip relative to the leader aircraft. This is expressed as external wind components in the body frame for the i^{th} wing section, ${v_w^b}^i$, positioned at the tip of the section. The wind relative airspeed vector corresponding to the i^{th} wing section is then converted into airflow angles (α_i and β_i) using Equations (14) and (15). The Lift coefficient corresponding to α_i, C_L^i, is calculated using Equation (13) and the rolling moment coefficient is calculated by

$$C_l = \frac{1}{b}\int_{-\frac{b}{2}}^{\frac{b}{2}} -\eta_i \frac{S_i}{S} C_L^i y^{bi} dy^{bi} \qquad (16)$$

where η_i is the dynamic pressure ratio, S_i is section planform area, b is the wingspan, and y^{bi} is the y-axis distance of the section tip from the center of gravity of the follower aircraft.

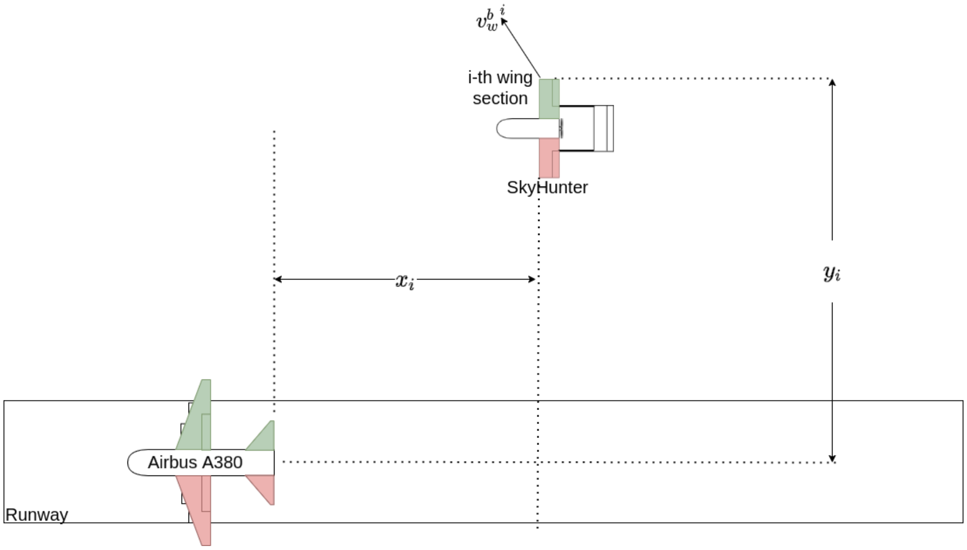

Figure 3-30. Wake vortex experienced by the i-th wing section tip located at (x_i, y_i) position relative to the leader aircraft.

The actuator dynamics is modeled by first order integrators with their respective time constants. The thrust is modeled as a cubic polynomial function of the throttle input, where the model coefficients are estimated through experimental measurements of the static thrust values at different throttle locations.

3.1.2.3 Simulation results with a path-following controller

Closed-loop simulation results of the four scenarios are presented in **Error! Reference source not found.** through**Error! Reference source not found.** Each figure shows follower aircraft closed-loop states such as AOA, roll attitude angle, and roll and pitch attitude rates. The AOA is normalized, where the maximum represents the follower aircraft's stall threshold. The details of a reinforcement-learning-based longitudinal state controller and model predictive control based lateral state controller are given in [24] and [25], respectively.

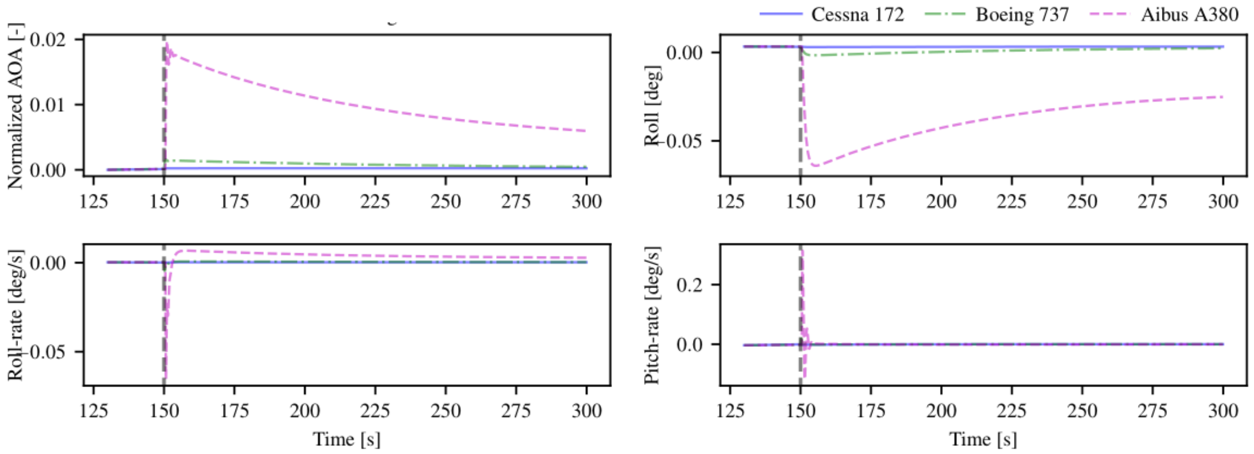

Figure 3-31. Follower aircraft states in ST1.

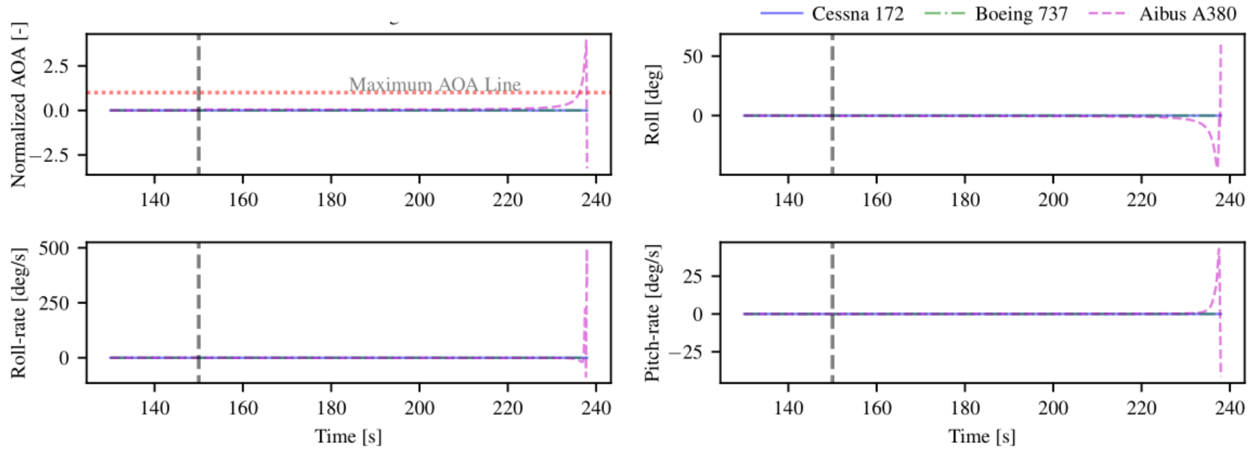

Figure 3-32. Follower aircraft states in ST2.

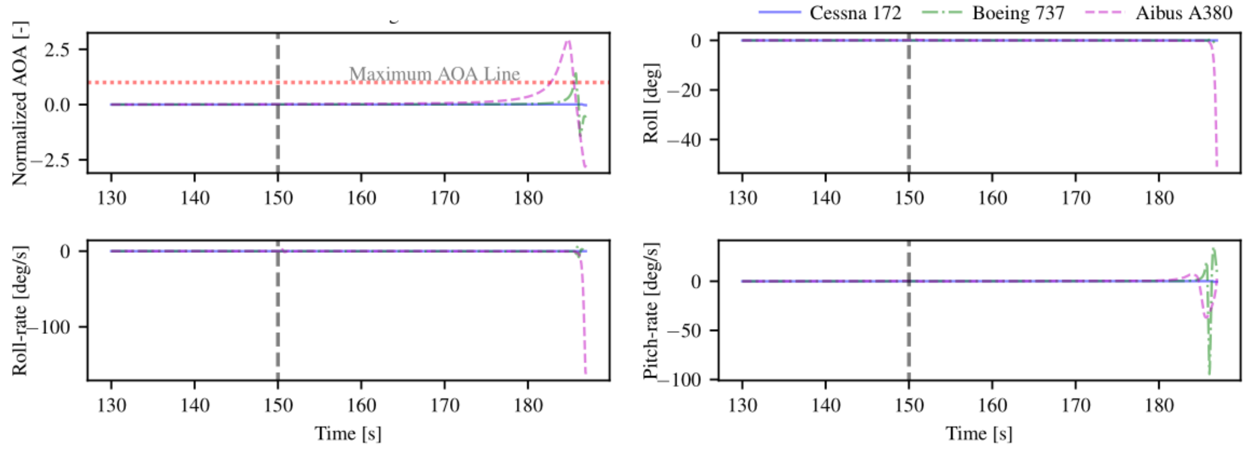

Figure 3-33. Follower aircraft states in ST3.

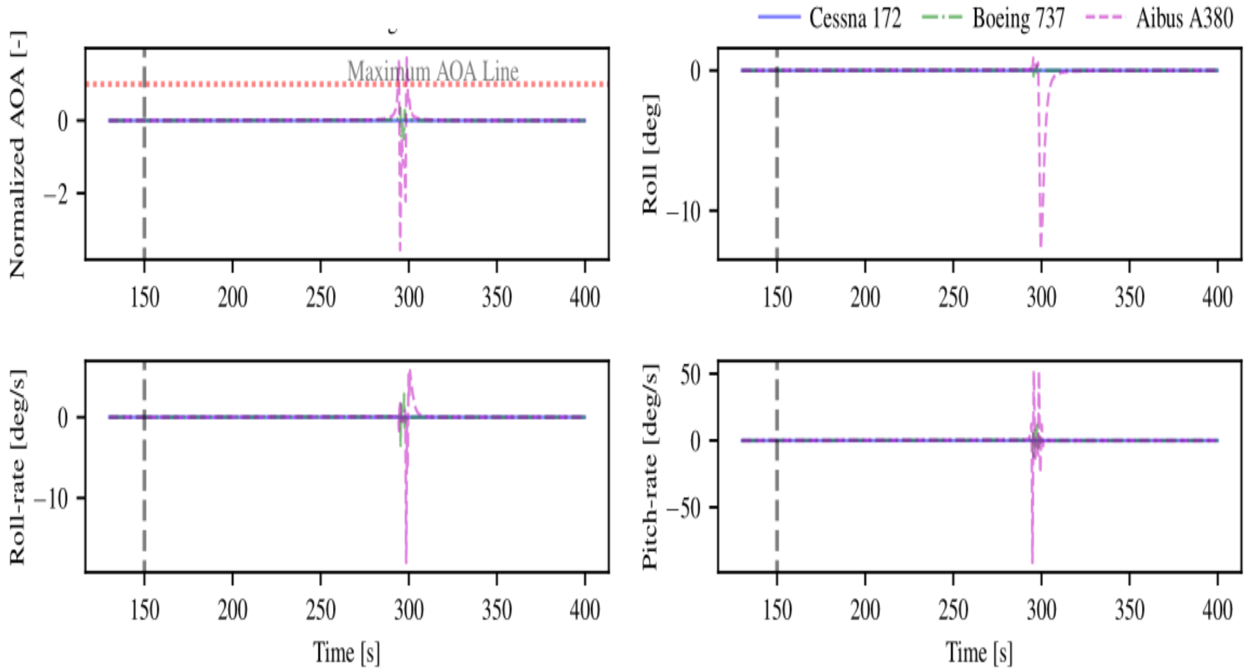

Figure 3-34. Follower aircraft states in ST4.

Comparing ST1 states with ST2 and ST3 states with ST4, it is shown that the impact of wing vortices on the follower aircraft decreases as the distance increases. Also, this impact is much more prominent in cross orientation (ST3 & ST4) than in parallel orientation (ST1 & ST2). In cross-orientation, different wing sections experience different AOA, which causes the follower aircraft to roll either left or right depending on its position and orientation (**Error! Reference source not found.** and**Error! Reference source not found.**). If one of the wing sections of the follower aircraft is too close to the wake vortex, the AOA for that wing section may exceed the max AOA (**Error! Reference source not found.** through**Error! Reference source not found.**). This causes abrupt rolling moments, sudden drops in altitude due to stall, and the aircraft enters a nonlinear and unsteady dynamic state. In ST2, the follower aircraft is at a 300 m distance at the beginning timestamp (150 secs) and reaches an unstable state condition at a timestamp of 230 secs, un-recoverable by the controller. In ST1, the distance at the beginning timestamp (150 secs) is increased to 500 m, and the aircraft stays stable due to a relatively small impact. On the other hand, in ST3, although the follower aircraft distance at the beginning timestamp (150 secs) is the same as ST1 (500 m), the aircraft reaches the un-recoverable state condition at about 190 secs timestamp. This un-recoverable state condition persists even when the distance is increased to 2000 m in ST4.

3.1.2.4 Estimation of a safe distance for a 90º wake encounter

Based on the same simulation process for the 4 cases reported above, a function has been created to determine acceptable distances behind a wake-generating aircraft for two twin-boom UAS with weights of 4, 6 and 27 kg (8.8, 13.2 and 59.4 lb)

A pictorial representation of an encounter is shown in Figure 3-35 and Figure 3-36, where the follower aircraft encounters the wing-tip wake vortices of the leader aircraft at a relative angle of 90 degrees. The distance d_0 is the lateral distance between the leader and follower at which an encounter is deemed “safe” when the UAS, flying at altitude h_{UAS}, arrives at the descending wake of the leader UAS, as shown in Figure 3-36. The definition of safe is when selected states of the UAS exceed pre-selected allowable, which are discussed later in this section. The times t_1, and t_f denote the time at the encounter of the first wake vortex and the time that the UAS exits the second wake vortex, respectively. These times are defined in terms of the speed of the leader aircraft (LAS). During the time, $\Delta t = t_1 - t_0$, the leader aircraft travels distance $D = LAS * \Delta t$, as shown in Figure 3-36. The simulated encounter occurs at the altitude at which the UAS encounters the wake. The Burnham-Hallock circulation model is used and the EDR is assumed to be 0.01 $m^{2/3}s^{-1}$. As with the simulation in the previous section, the AI path-following controller is used. The vertical separation of the generating aircraft and the UAS can be determined based on the sink rate of the vortices [59-60].

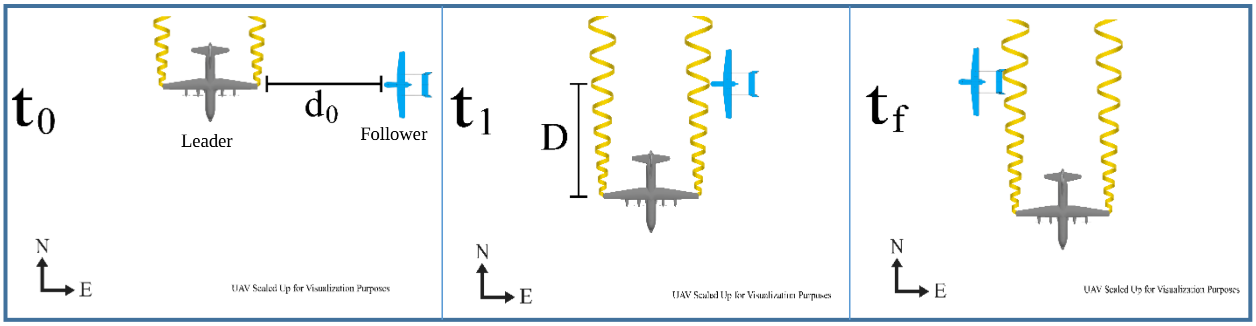

Figure 3-35. UAS encounters wake generated by leader aircraft at a 90^{o} relative angle (top view).

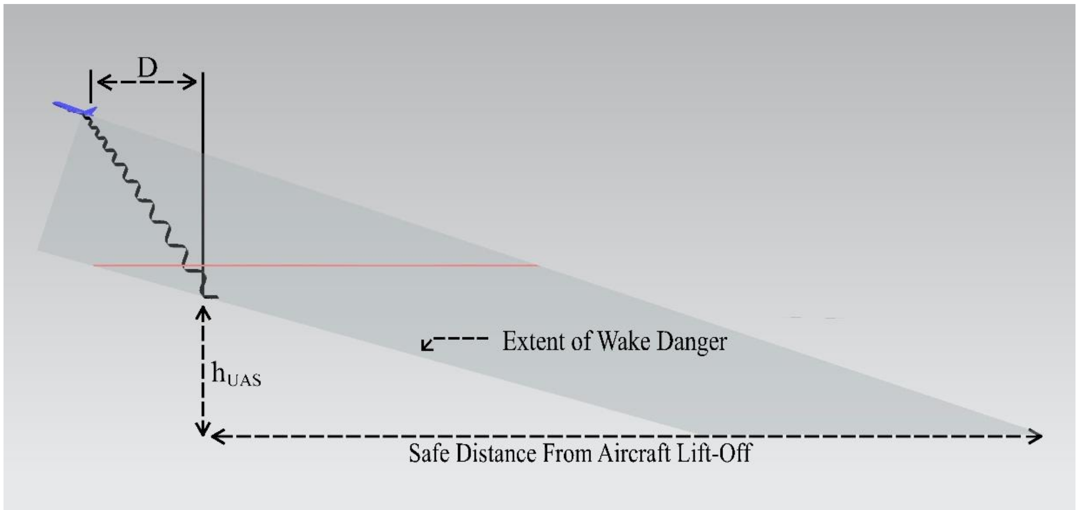

Figure 3-36. UAS encounters wake generated by leader aircraft at a 90^{o} relative angle (side view).

Three leader and three follower UAS of different sizes were considered; their specifications are given in Table 3-11 and Table 3-12.

Table 3-11. Leader aircraft specifications.

Leader Aircraft	Mass [kg]	Wingspan [m]	Take-off speed [m/s]
C 130	69,750	40	54
Boeing 737	41,410	34	77
Airbus A380	575,000	64	80

Table 3-12. Follower *UAS* specifications.

UAS	Mass [kg]	Wingspan [m]	Cruise speed [m/s]
SkyHunter	4	1.8	14
Boreas	6	2.4	17
Argus	27	2.9	31

Simulations were conducted for a range of d_0 (which, along with LAS, defines $\Delta t = t_1 - t_0$) to determine the minimum safe distance (d_0^{safe}) for a specific leader-follower pair and relative angle. Two different criteria used to determine d_0^{safe} are shown in Table 3. These criteria are constructed using limits or bounds on the follower aircraft's state variables, such as acceleration and angular rates. A failure or loss-of-control (LoC) event is ***assumed*** to occur if these bounds are violated.

Table 3-13. Criteria for abnormal states.State variable	Limits	
	Relaxed (Criteria-1)	Strict (Criteria-2)
Z-acceleration, a_z	> ±3 g	> ±3 g
Roll-rates, P	> ±60 deg/s	> ±40 deg/s
Pitch-rates, Q	> ±30 deg/s	> ±15 deg/s
Yaw-rates, R	> ±20 deg/s	> ±10 deg/s

Table 3-14. Minimum safe lateral distances, d_o, (in kilometers) for 90 degrees relative angle.

Leader Aircraft	Follower Aircraft

	SkyHunter	Boreas	Argus
C130	Criteria-1: 1.8	Criteria-1: 2.1	Criteria-1: 2.5
	Criteria-2: 2.1	Criteria-2: 2.5	Criteria-2: 3.5
Boeing 737	Criteria-1: 1.0	Criteria-1: 1.5	Criteria-1: 1.5
	Criteria-2: 1.5	Criteria-2: 2.0	Criteria-2: 2.5
Airbus A380	Criteria-1: 3.2	Criteria-1: 3.7	Criteria-1: 5.8
	Criteria-2: 3.7	Criteria-2: 4.2	Criteria-2: 7.4

Table 3-15. Minimum safe distances from leader aircraft takeoff (in kilometers) for UAS flight at 500 ft AGL.

Leader Aircraft	Follower Aircraft	
	SkyHunter	Argus
C130	Criteria-1: 9.6	Criteria-1: 6.0
	Criteria-2: 11.0	Criteria-2: 8.6
Boeing 737	Criteria-1: 7.0	Criteria-1: 4.7
	Criteria-2: 10.0	Criteria-2: 8.0
Airbus A380	Criteria-1: 23.2	Criteria-1: 19.1
	Criteria-2: 24.6	Criteria-2: 24.5

As in show in Table 3-15 the safe distance between leader aircraft and two different follower aircraft decreases as the size and cruise speed of UAS increases. Aircraft and UAS flight characteristics and safe distance criterion can be updated using KU's safe distance program.

3.1.3 Conclusions on modeling and simulation of UAS wake encounters and hazardous conditions

Simulations of UAS response to wake vortex encounters have shown excursions in states such as angle of attack, pitch rate, and roll rate which are beyond what the flight dynamics models are intended to cover. One way of using this information is to consider that if a UAS is likely to enter airspace in which it will encounter a wake vortex circulation which causes such departures from trim, it should be prohibited from entering that airspace. As such, classification of airspaces in terms of the maximum wake vortex circulation likely to be encountered may be appropriate. The process to establish such airspace is essentially the same as that presented in Section 2.3.

3.2 **Fully physics-based modeling using CFD for fixed wing UAS**

Theory, computation, and experiment are widely regarded as the triumvirate of the aircraft design process. However, for most practical applications such as aircraft stability analysis and flight controller design, a closed-form analytical theory is not possible. Because of this, researchers rely on extensive experimentation and computation to obtain accurate results. However, these two methods also pose their own shortcomings. Wind tunnel and flight tests, often seen as the apex of data reliability, require expensive testing facilities and highly sensitive equipment. This is especially true for full-scale flight tests which take months of planning and financial investment. On the other hand, computations pose a less cumbersome alternative to data acquisition. However, their shortcomings can include mathematical modeling inaccuracies, long simulation time, and extensive validation. As a result, researchers often rely on using a combination of these two methodologies to establish conclusions. For example, in [26] the dynamic stability derivatives were evaluated for three spin-stabilized projectiles using steady-state CFD methods and compared to experimental results. It was found that although the roll damping and Magnus moments in the supersonic regime were shown to be adequately predicted, the accuracy of the CFD for the Magnus moment inside the subsonic and transonic regime could not be clearly defined.

Another example is the investigation of the ability of Reynolds-Averaged Navier Stokes (RANS) simulations to predict the stability derivatives of the Standard Dynamics Model aircraft subjected to periodic pitch oscillations [27]. After comparing the computed stiffness and damping of the axial force, normal force, and pitching moment to experimental results, it was found that although the RANS solutions agreed satisfactorily in the low angle of attack range, the agreement strayed at higher angles of attack where non-linear aerodynamic phenomena became dominant. Similar computational-experimental comparisons of stability derivatives have been conducted by [28] and [29]. In [28], it was found that the static and longitudinal stability derivatives of the SACCON UAV obtained from computation agreed well with reference values. In [29], the same authors moved on to compute the dynamic stability derivatives of various missiles and aircraft using a variety of computational methods. After comparing empirical, semi-empirical, frequency-domain, and unsteady CFD results to experimental results, the authors concluded that time-dependent CFD methods provide the highest resolution but suffers heavily from computational requirements including simulation time.

Although these comparisons provide a solid foundation regarding comparisons between computational methodologies and experiments for stability derivatives and aerodynamic coefficients, there are major gaps in the literature which need to be addressed. One such gap is that the majority of published studies are using low-order computational methods. Most of these studies only provide comparisons to lab-based experiments where free-flight disturbances such as environmental turbulence and gusts are not accounted for. One such example of this is the work of [30] which used StarCCM+ to study the drag characteristics of a tricycle-style UAV landing gear. In their work, a second order in space and time scheme is used and the results are compared to wind-tunnel experiments. The reliability of these types of studies can be enhanced by either using a high-order Navier-Stokes (N.S) solver to minimize modeling inaccuracies or by performing a real flight test where environmental factors are accounted for. Two such studies which incorporate at least one of these improvements is the work by [31] and [32]. In [31], the structural and longitudinal flight-dynamics of a 14.7-pound, flexible flying wing drone with a wingspan of ten feet is analyzed using an open source VLM and compared against flight test results. In [32], the aerodynamic behavior of two full-scale drone rotor wakes are simulated using a 4th order Delayed Detached Eddy Simulation. The computed results are then compared against experiment which consisted of mounting a single, isolated rotor to a test stand.

The most reliable of studies, although scarce, is work which compares both high-fidelity, high-order computation and real flight test data. To the best of the researchers’ knowledge, the work shown in [33] is the only example of high-order computational solutions being compared against real flight-test data. Furthermore, it is rare to find literature which compares low-fidelity computational methods such as the VLM to high-fidelity, high-order Implicit Large Eddy Simulation (ILES) methods and flight-test data. The primary contribution of this work will address this shortcoming.

3.2.1 KHawk-55 UAS, problem description and computational meshes

3.2.1.1 KHawk-55 UAS configuration

Due to its simple geometry, a flying-wing UAS called KHawk-55 is studied in this paper. The KHawk-55 UAS was developed at the University of Kansas and is shown in Figure 3-37. It is a 2.57 kg flying-wing UAS with a 1.4m wingspan. The vehicle is controlled by two elevons and an electric brushless motor. The vehicle's mass properties and characteristics are summarized in Table 3-16.

The KHawk-55 UAS is constructed primarily from EPO foam. The underside of the UAS is reinforced with fiberglass laminate to support belly landings. A multi-hole probe is mounted on the nose of the aircraft for airspeed and air flow angle measurement. An onboard Microstrain GX3 Inertial Measurement Unit (IMU) measures the acceleration, angular rate, and attitude of the aircraft. A Ublox Leak-6H GPS receiver records position and velocity information. All peripheral hardware is connected to a Paparazzi TWOG autopilot which is used for command generation, automatic control, and data recording.

Figure 3-37. Isometric view of KHawk-55 UAS platform.

Table 3-16. KHawk-55 UAS specification.

Mass (kg)	Wingspan (m)	Cruise Speed (m/s)	Mean Aerodynamic Chord (m)	Wing Area (m^2)
2.57	1.4	18	0.36	0.497
Wingtip Chord (m)	Wingtip Max Thickness (m)	Wingtip Max Thickness Position From LE (m)	Mean Aerodynamic Chord Max Thickness (m)	Center Max Thickness Position From LE (m)

0.28	0.034	0.086	0.055	0.139

3.2.1.2 Problem description

Computation of two main types of aerodynamic parameters are addressed in this study: 1) Computation of total aerodynamic force and moment coefficients such as C_L, C_D, C_Y and C_l, C_m, C_n, which can be used to support research such as prediction of aircraft turbulence response; and 2) computation of stability and control derivatives $C_{L_0}/C_{L_\alpha}/C_{L_q}$, $C_{D_0}/C_{D_\alpha}/C_{D_q}$, $C_{m_0}/C_{m_\alpha}/C_{m_q}$, which can be used to support research such as aircraft design, aircraft flight simulator, and flight controller design.

To obtain as wide a variety of results as possible, low fidelity solutions are compared to a variety of low-and-high order, high fidelity computational solutions as well as flight test data. In addition, the high-fidelity computational results include both the full model as well as the half model with a symmetry plane assumption.

It is worth emphasizing that there are inherited pros and cons for parameters identified from each of the three types of methods. Aerodynamic parameters identified from flight test are derived values estimated using frequency or time domain method, and as in other methods there will be a range of uncertainty [34, 35]. The flight identified aerodynamic parameters are widely used in flight controller design and aircraft flight simulation. However, certain parameters such as C_{L_0} or C_{m_0} are very difficult to measure accurately in flights. Low-fidelity CFD methods such as the Vortex Lattice Method can provide a relatively quicker estimate of all the stability and control derivatives at a reasonable accuracy using small perturbation analysis. However, VLM cannot estimate viscous drag. High-order CFD, like those used in this study, have the advantage of including viscous effects and turbulence modeling. However, they suffer from long computational times, and larger memory requirements.

Results from this study will help determine when low-fidelity solutions are satisfactory for aircraft stability analyses or if a high-fidelity computation is required. This conclusion is essential due to the time-savings offered by low-fidelity computations.

3.2.1.3 Computational grids

For VLM, the wing geometry is divided into a set of lifting panels, and the total lift force is obtained by integrating lift on each panel individually. The KHawk55 geometry was divided into 3 parts: fuselage, main wing, and winglet, as shown in Figure 3-38. Since the main wing is the main contributor to lift generation, it was meshed with a higher resolution compared to the fuselage and winglet. The main wing, fuselage, and winglet were meshed with 192, 30 and 5 panels, respectively. A convergence study was performed to determine this resolution, as it provided results consistent with higher resolutions without having large computation times.

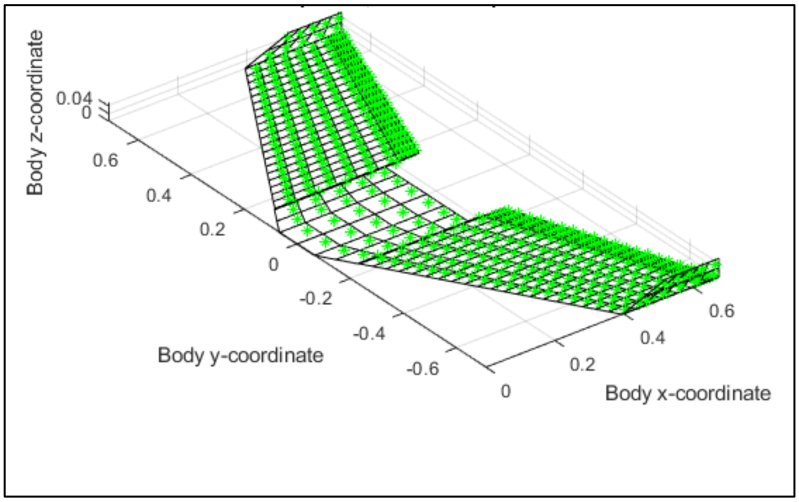

Figure 3-38. 3D panel distribution and collocation points for tornado mesh.

For the high-fidelity CFD domains, two sets of mixed meshes were generated in the proprietary meshing software, Pointwise: a half-model and full model. In both cases a spherical far-field with a radius of $100c$, where c is the center chord, was used to prevent any turbulence-based reflections from occurring at the far-field boundary conditions. Table 3-17 and (21.0) display the mesh metrics for the grids at each of the tested angles of attack. It should be noted that since viscous effects were included in the high-fidelity simulations, all meshes included a refinement region in the boundary layer as shown in Figure 3-39.

Table 3-17. High-fidelity CFD mesh metrics for zero degrees angle of attack.

Simulation ID	Mesh Order	Number of Elements	Number of DOFs per Equation	y_{equiv}^{+}
StarCCM (First Order Upwind) – Half Model	Linear	1,498,227	1,498,227	N/A
StarCCM (Second Order Upwind) – Half Model	Linear	1,498,227	1,498,227	N/A
StarCCM (Third Order MUSCL) – Half Model	Linear	1,498,227	1,498,227	N/A
HpMusic (p = 1) – Half Model	Quadratic	198,470	1,023,170	1.95
HpMusic (p = 2) – Half Model	Quadratic	198,470	2,904,191	1.35
HpMusic (p = 3) – Half Model	Quadratic	198,470	6,271,624	1.06
HpMusic (p = 2) – Full Model	Quadratic	1,029,840	16,164,019	0.94

Table 3-18. High-fidelity CFD mesh metrics for six degrees angle of attack.

Simulation ID	Mesh Order	Number of Elements	Number of DOFs per Equation	y^+_{equiv}
HpMusic (p = 1) – Half Model	Quadratic	198,470	1,023,170	1.99
HpMusic (p = 2) – Half Model	Quadratic	198,470	2,904,191	1.41

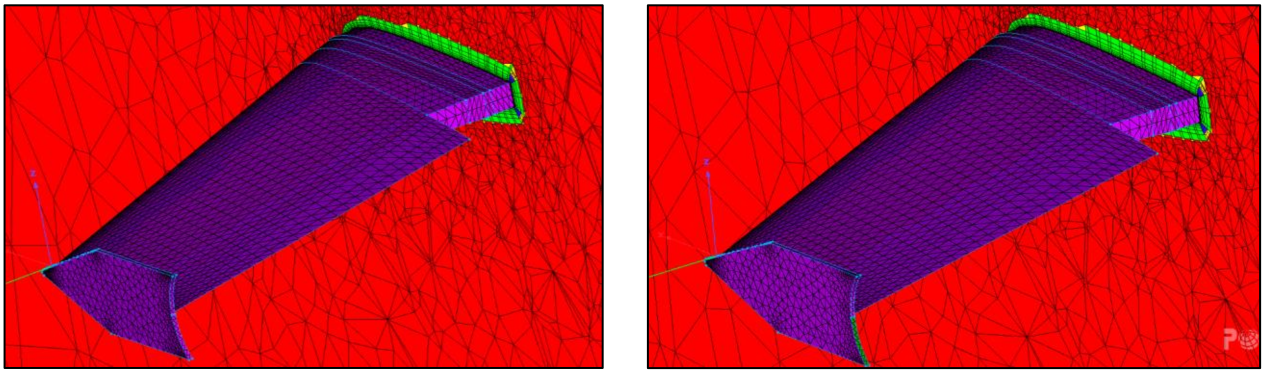

(a) Section view of HpMusic half-wing mesh

(b) Section view of StarCCM half-wing mesh

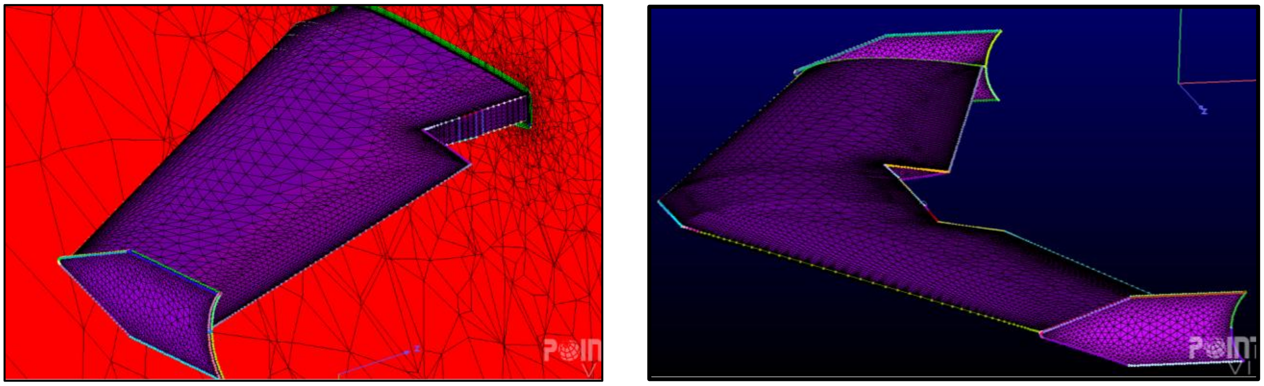

(c) Section view of HpMusic full-wing mesh

(d) Isometric view of HpMusic full-wing mesh

Figure 3-39. Computational renderings of KHawk55 mesh.

3.2.2 Flight test based system identification of UAS dynamics

3.2.2.1 Equations of motion

In the flight dynamics field, linearized models are commonly used to predict the forces and moments generated by an aircraft. Furthermore, the equations of motions themselves can be linearized to express the aircraft dynamics in state space form. These models provide an accurate representation of the aircraft dynamics around the trim condition. Typically, the aircraft dynamics are separated into 3DOF longitudinal and lateral-directional models, which are assumed to be decoupled.

Often, the focal point of the aircraft system identification process is to accurately estimate the stability and control derivatives. These constant terms are used to compute the lift and moment coefficients as a function of the aircraft state. The linear equations for the longitudinal forces and moments; lift, drag, and pitching moment, are given by

$$C_L = C_{L_0} + C_{L_\alpha}\alpha + C_{L_q}\hat{q} + C_{L_{\delta_e}}\delta_e \tag{17a}$$

$$C_D = C_{D_0} + C_{D_\alpha}\alpha + C_{D_q}\hat{q} + C_{D_{\delta_e}}\delta_e \tag{17b}$$

$$C_m = C_{m_0} + C_{m_\alpha}\alpha + C_{m_q}\hat{q} + C_{m_{\delta_e}}\delta_e \tag{17c}$$

where α is the angle-of-attack, $\hat{q}$ is nondimensionalized pitch rate, and δ_e is the elevator surface deflection. The lateral-directional force and moment coefficients can be defined similarly. At steady state flight, the aircraft pitch rate is zero, and the longitudinal equations simplify to

$$C_L = C_{L_0} + C_{L_\alpha}\alpha + C_{L_{\delta_e}}\delta_e \tag{18a}$$

$$C_D = C_{D_0} + C_{D_\alpha}\alpha + C_{D_{\delta_e}}\delta_e \tag{18b}$$

$$C_m = C_{m_0} + C_{m_\alpha}\alpha + C_{m_{\delta_e}}\delta_e \tag{18c}$$

3.2.2.2 System identification approach

In previous works, decoupled, linear state space models were identified from flight test data through system identification techniques. Piloted and automated frequency sweep maneuvers were performed to excite the UAS dynamics over a designed frequency range. Then, frequency response functions were generated from perturbation flight data and linear state space models were identified to fit to the measured frequency response. This capability was performed using CIFER, a commercial system identification software package. More information regarding the system identification results and procedure can be found in [36] and [37].

Identified models were validated with other flight data and then used to compute the nondimensional form of stability and control derivatives, such as those shown in (17). Monte Carlo style simulation was employed to compute the statistics of stability and control derivatives and to provide confidence intervals that will be used as a guideline for comparison with CFD results later in this study [37].

3.2.3 Low-fidelity numerical method

VLM is one way of estimating forces and moments on the aerodynamic surface. VLM is based on linear equations, which allows for rapid calculation of aerodynamic forces and moments [9].

Comparatively, high-fidelity CFD methods are based on the Navier-Stokes equations, typically resulting in higher accuracy but longer computation times when compared to VLM.

VLM was used to calculate aerodynamic forces and moments, and stability and control derivatives to provide comparison with high-fidelity CFD results. This was implemented via Tornado-VLM, an open source MATLAB toolbox [9]. VLM is developed based on lifting surface theory with Kutta-Jukovski theorem applied on each individual panel. The forces and moments are calculated by:

$$F = \sum_{i=1}^{N} \rho (V_{ind} \times \Gamma_{\mathrm{i}}) l_i \tag{19}$$

$$M = F\, r \tag{20}$$

where,

$$V_{ind} = V_{wind} + (COLLOC_{xyz} \times [p, q, r]) \tag{21}$$

and ρ is the air density, l_i is the vortex's transverse segment vector, V_{wind} is the freestream wind velocity, and $COLLOC_{xyz}$ is the collocation point, and $[p, q, r]$ are the Euler angular velocities (roll rate, pitch rate and yaw rate).

All the aircraft stability and control derivatives can be computed automatically in Tornado by applying a small perturbation to the aircraft states and approximating the derivatives from the finite difference.

3.2.4 High-fidelity numerical methods

3.2.4.1 Finite Volume Method

Some results in this work were generated using a commercial CFD package called STAR-CCM+. This package is based on the finite volume method and offers both low-and-high order computational schemes. For this work, the first and second order upwind schemes were used to produce the low spatial order results. Additionally, the third-order Monotonic Upstream-centered Scheme for Conservation Laws (MUSCL) was used to generate the high-order results by extending the stencil. The second-order BDF2OPT scheme was used for temporal integration. Lastly, because variable gradients are required at cell centers and at cell-face centers, the Hybrid Gauss-Least Squares was used for gradient reconstruction.

3.2.4.2 FR/CPR Method

A high-order Large Eddy Simulation (LES) tool called hpMusic [38] is used in the computational study. The tool is based on Flux Reconstruction (FR) or Correction Procedure via Reconstruction (CPR) method originally developed in [39] for hyperbolic partial differential equations. The method is capable of handling mixed unstructured meshes [40, 41] and also has some recent advancements in terms of highly-scalable GPU capability [42] and far-field aeroacoustic prediction methods[43]. Further developments were made to this tool and a review was presented in [44, 45]. This method belongs to discontinuous finite element methods, similar to the discontinuous Galerkin [46] and spectral difference [47] methods, but also has some unique advantages. Here is presented a brief introduction of the/CPR method starting from a hyperbolic conservation law governing inviscid flow.

$$\frac{\partial \mathbf{U}}{\partial \mathrm{t}} + \nabla \cdot \mathbf{F}(\mathbf{U}) = 0 \tag{22}$$

with initial and boundary conditions, where the vector **U** consists of conservative variables, and **F** is the flux. By discretizing the computational domain with non-overlapping elements, and introducing an arbitrary test function φ in each element, the weighted residual formulation of (22) on element V_i can be expressed as

$$\int_{V_i} \left[\frac{\partial \mathbf{U}}{\partial \mathrm{t}} + \nabla \cdot \mathbf{F}(\mathbf{U})\right] \varphi \mathrm{d}\Omega = 0. \tag{23}$$

The conservative variables inside one element are assumed to be polynomials and expressed by nodal values at certain points called solution points. After applying integration by parts to the divergence of flux, replacing the normal flux term with a common Riemann flux F_{com}^{n} and integrating back by parts, resulting in

$$\int_{V_i} \frac{\partial \mathbf{U}_{\boldsymbol{i}}}{\partial \mathrm{t}} \varphi \mathrm{d}\Omega + \int_{V_i} \varphi \nabla \cdot \mathbf{F}(\mathbf{U}_i)\, \mathrm{d}\Omega + \int_{\partial V_i} \varphi [F_{com}^{n} - F^{n}(\mathbf{U}_i)]\, \mathrm{dS} = 0 \tag{24}$$

Here, the common Riemann flux is computed with a Riemann solver

$$F_{com}^{n} = F_{com}^{n}(\mathbf{U}_i, \mathbf{U}_{i+}, \mathbf{n}) \tag{25}$$

where $\mathbf{U}_{i+}$ stands for the solution outside the current element, and **n** denotes the outward normal direction of the interface. The normal flux at the interface is:

$$F^{n}(\mathbf{U}_i) = \mathbf{F}(\mathbf{U}_i) \cdot \mathbf{n} \tag{26}$$

Note that if the face integral in (24) can be transformed into an element integral then the test function will be eliminated. In order to do so, a “correction field” δ_i is defined in each element as

$$\int_{V_i} \varphi \delta_i \, \mathrm{d}\Omega = \int_{\partial V_i} \varphi [F^{n}]\, \mathrm{dS} \tag{27}$$

where $[F^{n}] = [F_{com}^{n} - F^{n}(\mathbf{U}_i)]$ is the normal flux jump. Equations (24) and (27) result in

$$\int_{V_i} \left[\frac{\partial \mathbf{U}_{\boldsymbol{i}}}{\partial \mathrm{t}} + \nabla \cdot \mathbf{F}(\mathbf{U}_i) + \delta_i\right] \varphi \mathrm{d}\Omega = 0 \tag{28}$$

The final formulation for each solution point j is

$$\frac{\partial \mathbf{U}_{i,j}}{\partial \mathrm{t}} + \Pi_j[\nabla \cdot \mathbf{F}(\mathbf{U}_i)] + \delta_{i,j} = 0 \tag{29}$$

where Π_j denotes a projection to the polynomial space, and subscript j denotes the j-th solution point in a certain element.

For viscous flux involving the gradient of conservative variables, the researchers used the Bassi-Rebay 2 scheme [48]. No sub-scale stress models are used. Therefore, the present simulations are called ILES. For under-resolved flow features, the researchers employed an accuracy-preserving limiter to stabilize the simulation [49].

For problems with complex geometries, it is very challenging to generate a mesh without any bad elements, which may have nearly diminishing cell volumes. If a globally explicit time integration scheme is used, the global time step will be extremely small, making the simulation very expensive. With implicit schemes, the time step can be usually selected based more on the physical requirement. In the present study, the researchers employed an optimized backward difference formula, which is second-order accurate and A-stable (BDF2OPT)[50], and involves four time levels. The researchers employed an LU-SGS solver for the implicit system [51].

3.2.5 Results and discussions

In order to assess the performance between low-and-high fidelity computations against flight test, a variety of performance metrics were analyzed. These metrics include force and moment coefficients for two angles of attack and stability derivatives. Furthermore, to examine the reliance of the computational flow field on spatial order of accuracy, surface pressure coefficient profiles, and isosurfaces of Q-criteria are presented. It is important to note here that when applicable, the results are also compared against ‘uncertainty values’. These uncertainties are estimates of variances for the identified parameters; where variance is defined as the square of the standard deviation. In essence, confidence intervals represent the probability that the measured value lies within the upper and lower bounds. These confidence intervals are generated using extraneous factors such as numerical noise which may be included in the experiment.

The Reynolds number based on center chord, Re_c, was set to 444,000 to match the flight test condition and all CFD simulations for this work were conducted using the High Performance Computing Cluster at the University of Kansas. The cluster features a range of CPU and GPU hardware.

Lastly, a note regarding terminology. In this study, terms such as low-and-high fidelity and low-and-high order are used. Initially, these may seem interchangeable, but they are not. Low and high fidelity refers to the ability to which the underlying governing equations of the solver are able to describe the physical phenomena. For example, VLM, like the one implemented in Tornado, is based on potential flow theory. This theory does not include temporal transience, rotationality, along with a variety of other physical phenomena. This is why it is labeled a low-fidelity solver. On the other hand, high-fidelity solvers utilize the full-N.S equations which totally describe all aspects of fluid flow such as viscous effects, turbulence, etc. However, since solvers that attempt to approximate the full N.S equations can have varying orders of spatial accuracy, this is where the term low-and-high order solutions stems from. In essence, low-and-high order solutions are a subset of high-fidelity solutions.

3.2.5.1 Force and moment coefficients

The lift coefficients obtained by each case for zero- and six-degrees angle of attack are shown in Table 3-19 and 23.0. It is readily apparent that strong agreement between all of the computed solutions is obtained. This agreement is strongest for zero degrees angle of attack and less so for six degrees angle of attack. However, none of the computed solutions were able to match the flight test results within acceptable limits. For zero degrees angle of attack, the computational solution that matches closest to flight test data is the result obtained by Tornado. On the other hand, for six degrees angle of attack, the computed solution which lies closest to the flight test results is the full-model, third-order (p=2) HpMusic simulation. Lastly, there is a clear tendency of computed results to underpredict the lift coefficient. The solutions which lie closest to the flight test results for each angle of attack are isolated and plotted in Figure 3.11.

Table 3-19. Lift coefficient (C_L) results for zero degrees angle of attack.

Case ID	**Measured C_L**	**Percentage Difference to Flight Test**
Flight Test	0.3433	N/A
HpMusic (p=1) – Half Model	0.0706	-79.4
HpMusic (p=2) – Half Model	0.0735	-78.6
HpMusic (p=3) – Half Model	0.0677	-80.3
HpMusic (p=2) – Full Model	0.0650	-81.1
Tornado (VLM) – Full Model	0.1233	-64.1
StarCCM+ (First Order Upwind) – Half Model	0.0659	-80.8
StarCCM+ (Second Order Upwind) – Half Model	0.0655	-80.9
StarCCM+ (Third Order MUSCL) – Half Model	0.0706	-79.4

Table 3-20. Lift coefficient (C_L) results for six degrees angle of attack.

Case ID	**Measured C_L**	**Percentage Difference to Flight Test**
Flight Test	0.8221	N/A
HpMusic (p=1) – Half Model	0.4859	-40.9
HpMusic (p=2) – Half Model	0.4991	-39.3
HpMusic (p=2) – Full Model	0.5200	-36.8
Tornado (VLM) – Full Model	0.5014	-39.1

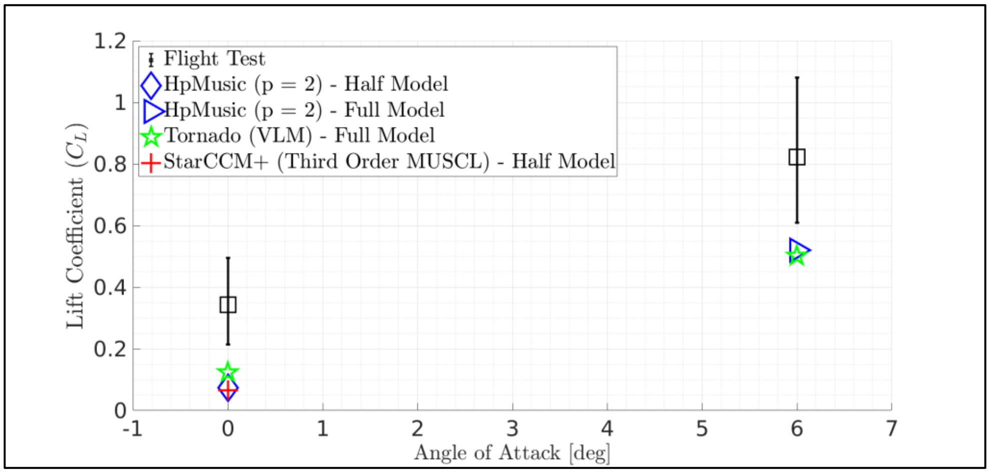

Figure 3-40. Total lift coefficient (C_L) at zero- and six-degrees angle of attack.

The drag coefficients at zero-degree and six-degree angles of attack are presented in Table 3-21 and 25.0 respectively. It is observed that the clustering between the computed solutions is less compact when compared to the clustering achieved for the lift coefficient. At zero degrees angle of attack, the outliers from the computational clustering are Tornado and the first order upwind STAR-CCM+ result. For six degrees angle of attack, the variation between the computational drag coefficients are much higher than the zero degrees angle of attack case and is mainly attributed to the results obtained by Tornado and the third-order (p=2) full-model HpMusic simulation. Although the agreement between computed solutions is not as compact as the results for the lift coefficient, the overall ability of the computed solutions to fall within the uncertainty limits of the flight test improved, as shown in Figure 3-41. At this point it is worth noting that the Tornado results have fallen within the flight test uncertainty band for only one of the four tested cases. Lastly, as was the case with the lift coefficient, it is worth noting that an under-predictive trend is again observable in the computational results.

Table 3-21. Drag coefficient (C_D) results for zero degrees angle of attack.

Case ID	**Measured C_D**	**Percentage Difference to Flight Test**
Flight Test	0.0204	N/A
HpMusic (p=1) – Half Model	0.0145	-28.9
HpMusic (p=2) – Half Model	0.0175	-14.2
HpMusic (p=3) – Half Model	0.0151	-26.0
HpMusic (p=2) – Full Model	0.0150	-26.5
Tornado (VLM) – Full Model	0.0012	-94.1
StarCCM+ (First Order Upwind) – Half Model	0.0318	55.9
StarCCM+ (Second Order Upwind) – Half Model	0.0198	-2.9
StarCCM+ (Third Order MUSCL) – Half Model	0.0188	-7.8

Table 3-22. Drag coefficient (C_D) results for six degrees angle of attack.

Case ID	**Measured C_D**	**Percentage Difference to Flight Test**
Flight Test	0.0849	N/A
HpMusic (p=1) – Half Model	0.0668	-21.3
HpMusic (p=2) – Half Model	0.0688	-19.0
HpMusic (p=2) – Full Model	0.0360	-57.6
Tornado (VLM) – Full Model	0.0157	-81.5

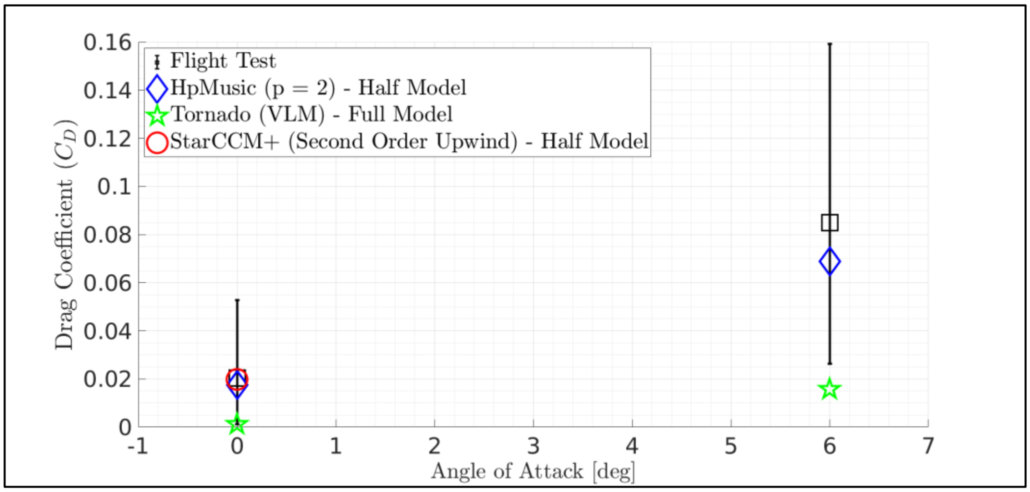

Figure 3-41. Total drag coefficient (C_D) comparison at zero- and six degrees angle of attack.

Table 3-23 and 27.0 shows the pitching moment at six-degree angle of attack respectively. Here, the computational clustering is stronger than that of the drag coefficient but weaker than the clustering obtained by lift coefficient. For zero degrees angle of attack it can be seen that the third-order (p=2), full-model, HpMusic simulation, as well as the low-fidelity Tornado result in the closest value to the flight test. At six degrees angle of attack the third-order (p=2) half model, HpMusic simulation was able to match the flight test result to within one percent of deviation. Furthermore, all computed solutions were able to stay within the flight test uncertainty band for both angles of attack, as shown in Figure 3-42.

Table 3-23. Pitching moment coefficient (C_m) results for zero degrees angle of attack.

Case ID	**Measured C_m**	**Percentage Difference to Flight Test**
Flight Test	-0.0278	N/A
HpMusic (p=1) – Half Model	-0.0340	-22.3
HpMusic (p=2) – Half Model	-0.0350	-25.9
HpMusic (p=3) – Half Model	-0.0320	-15.1
HpMusic (p=2) – Full Model	-0.0290	-4.3
Tornado (VLM) – Full Model	-0.0285	-2.5

Table 3-24. Pitching moment coefficient (C_m) results for six degrees angle of attack.

Case ID	Measured C_m	Percentage Difference to Flight Test
Flight Test	-0.0667	N/A
HpMusic (p=1) – Half Model	-0.0670	-0.4
HpMusic (p=2) – Half Model	-0.0720	-7.9
HpMusic (p=2) – Full Model	-0.0780	-16.9
Tornado (VLM) – Full Model	-0.0520	22.0

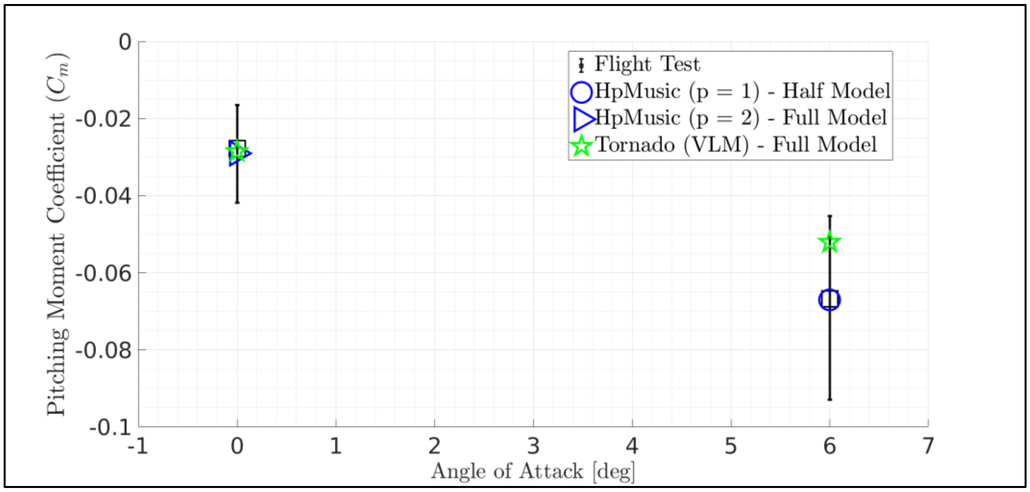

Figure 3-42. Pitching moment coefficient (C_m) comparison at zero and six degrees angle of attack.

After analyzing Figure 3-40, [44.0, and [45.0, it is apparent that Tornado is less accurate than N.S style methods at six degrees angle of attack. Of the three coefficients measured at six degrees angle of attack, Tornado was able to fall within the flight test uncertainty band for only one of them. However, at zero degrees angle of attack Tornado is able to provide similar results to the high-fidelity CFD results for lift and pitching moment and stay within the flight test uncertainty band for the drag coefficient. This indicates that low-fidelity VLM methods may still be used for this type of configuration at zero degrees angles of attack if used with enough panels to ensure resolution requirements are met. On the other hand, high-fidelity N.S solvers which utilize either a half-model or full model approach seem to produce the most reliability across all of the tested coefficients. However, one must take in to account the orders of magnitude more time it takes to generate a high-fidelity solution compared to a low-fidelity solution. Interestingly, high-order results for this application do not see much improvement over low-order results, indicating that low-order methods may be sufficient. Lastly, there is a clear tendency for the computed results to under-predict the tested coefficients when compared to flight test.

It should be noted that the bias terms in (18), C_{L_0}, C_{D_0}, and C_{m_0}, can be unreliable when estimated from flight data, especially when using frequency domain methods. These terms contain information about the trim condition, biases in the measurements, and modeling errors. As such, these terms often vary from flight-to-flight, especially for small, low-cost UAS which are prone to imperfections and asymmetries in their construction. As such, the flight test-identified stability derivatives, which are found in the sequel to this section, may serve as a more reliable reference point.

3.2.5.2 Stability derivatives

Because the force and moment coefficients were obtained for two separate angles of attack, a central difference can be carried out to obtain the stability derivatives. These stability derivatives are shown in Figure 3-43, [47.00, and [48.0. In Figure 3-43, it is observed that all of the HpMusic simulations, regardless of geometrical model or spatial order of accuracy, fall within the band of flight test uncertainty. Furthermore, the full model, third-order (p=2) HpMusic solution obtains the value closest to that obtained by the flight test. In terms of clustering, the two half-model HpMusic simulations agree to within 3% of each other, indicating that p-order convergence has been obtained. Lastly, it is shown that the results obtained by Tornado lie just outside the flight test uncertainty band.

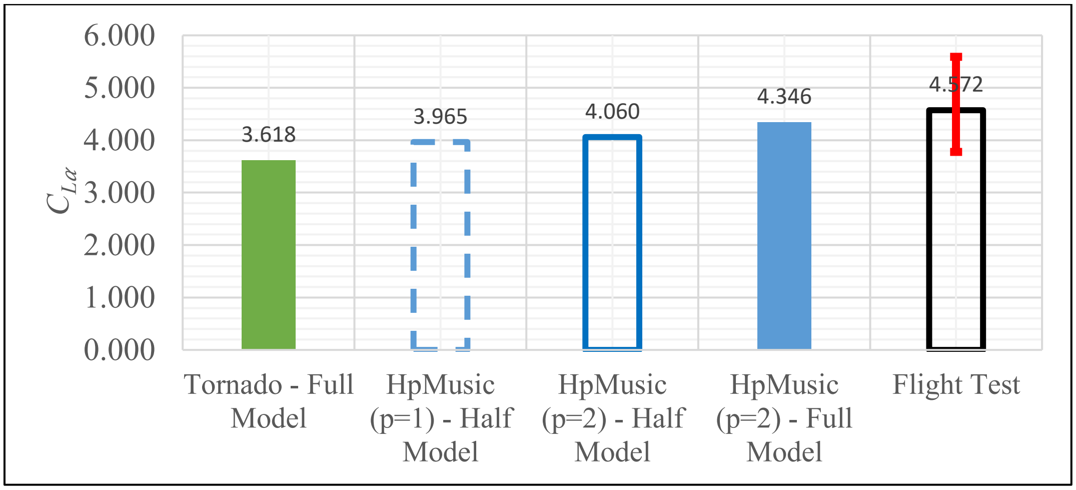

Figure 3-43. Comparison of C_{L_α} between flight test and computations.

In Figure 3.15, it is again seen that there is significant agreement between the low-and-high order half model HpMusic simulations. Both of these simulations fall within the flight test uncertainty band, indicating satisfactory agreement with flight test results. However, in contrast to the lift slope, the third-order (p=2) full model HpMusic simulation now sits just outside of the uncertainty band, similar to the Tornado results. This mismatch in C_{D_α} between the HpMusic full model and HpMusic half model is mainly attributed to the disagreement which occurs at six degrees angle of attack (See Table 3-22). Although unexpected, several probable factors have been identified as a cause for this mismatch. The most probable is the difference in mesh resolution. The full-model mesh is more than four times finer than the half body discretization and has a much thinner mesh to capture the boundary layer (See Figure 3-39). Another factor is the limiter setting used in the simulations. The limiter was much more active in the half-model simulations, limiting approximately 2% of all elements, than for the full body mesh which had the limiter activated for only ~0.006% of all elements. The last factor, which is analyzed more in depth in the following section, is the difference in boundary conditions. The half-model simulations include a symmetry plane boundary condition at the mid-span location. This boundary condition acts as a slip-wall which is not included in the full-model mesh. Although these factors have been identified as potential causes for the drag slope mismatch, the determination of the true cause is still under review.

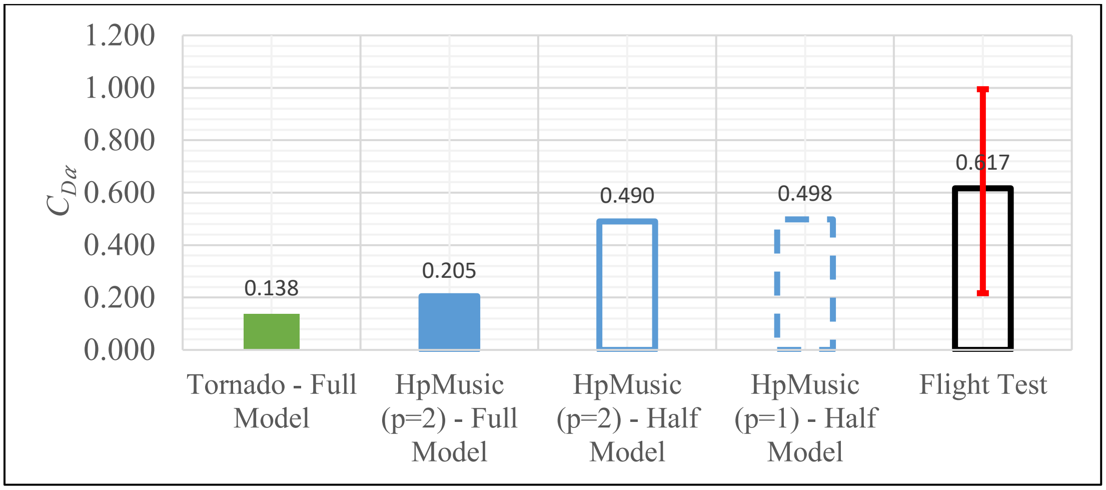

Figure 3-44. Comparison of C_{D_α} between flight test and comparison.

In Figure 3-45, it is observed that Tornado lies outside the uncertainty band. On the other hand, all of the HpMusic simulations agree within 95% uncertainty to flight test. It is interesting to note here that the clustering observed between $C_{L_\alpha}$and C_{D_α} for the HpMusic simulations using the half model is now significantly diluted. This suggests that high-order methods are required if C_{m_α} is desired.

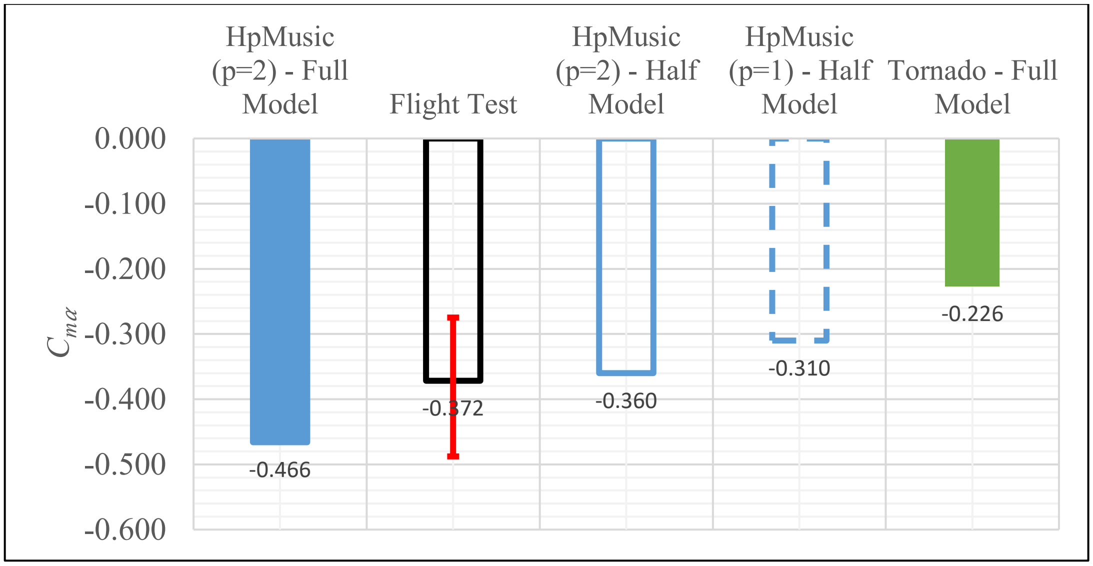

Figure 3-45. Comparison of C_{m_α} between flight test and computations.

To summarize the results shown for the stability derivatives, it was found that Tornado was not able to predict any of the stability derivatives to within 95% of flight test uncertainty. This again reinforces the notion that VLM methods are less accurate than N.S style methods. On the other hand, high-fidelity simulations, regardless of order or geometrical model used, tend to be much better suited in predicting the stability derivatives for this application. Lastly, the dilution in clustering between computed results when progressing from $C_{L_\alpha}$and C_{D_α} to C_{m_α} suggests that for $C_{L_\alpha}$and C_{D_α}, low order N.S-style simulations are sufficient whereas high-order methods are required if C_{m_α} is desired.

3.2.5.3 Flow topology via CFD

To assess the differences between computational order of accuracy and geometrical model used, additional comparisons of the flow topology via temporally averaged surface pressure coefficient and instantaneous Q-criteria were carried out.

In regard to the temporally averaged surface pressure coefficient shown in Figure 3-46a, it can be seen that all high-order solutions, regardless of model used, experience strong agreement up to 70% chord location. After 70% chord, the second and third order (p=1 and p=2) half model begin to deviate from the fourth order (p=3) half model and the third order (p=2) full model. This deviation in the results reaches its maximum point at approximately 90% chord. For the six degrees angle of attack case, shown in Figure 3-46b, it is observed that the deviation occurs mainly in vicinity of the Leading Edge (LE) instead of the Trailing Edge (TE). However, this deviation is primarily located on the suction side of the wing and is mainly attributed due to oscillations in the low-order solution. It is important to note here that even with the presence of the small oscillations for the low-order N.S solution shown in Figure 3-46b, the overall behavior of the surface pressure coefficient is the same.

These results indicate that the spatial order of accuracy for N.S solvers plays a much larger role than geometrical symmetry assumptions in determining proper flow representation. If accurate resolution of the surface flow topology is desired, a high order method must be used to avoid oscillations in the results.

(a.) Zero Degrees Angle of Attack

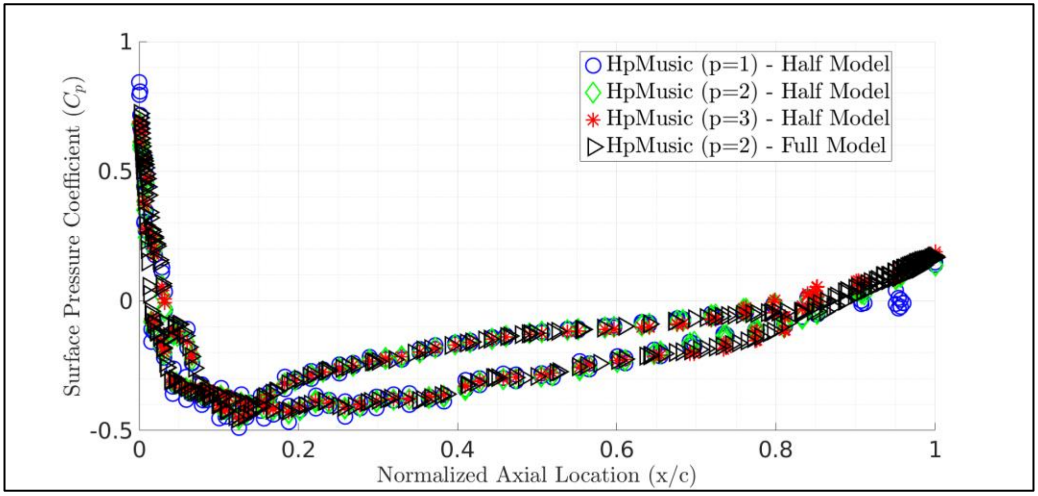

(b.) Six Degrees Angle of Attack

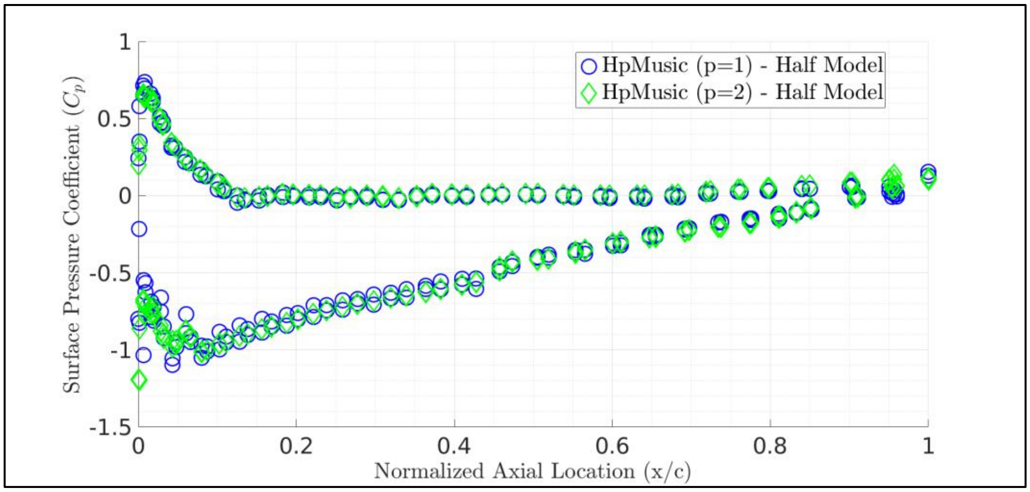

Figure 3-46. Time-averaged surface pressure coefficient measured at quarter span location.

Lastly, the isosurfaces of instantaneous Q-criterion colored by streamwise velocity are shown in Figure 3-47 and [51.00. All simulations seem to detect several distinct flow features. The first is a gradual laminar to turbulent transition along the aft portion of the suction side of the wing which quickly elevates to large-scale structures aft of the TE. The second is a delta-wing type vortex which begins at the LE of the wingtip, splits into two distinct vortices which travel along the streamwise direction of the wingtip and coalesces into one large turbulent region aft of the wingtip. One important discrepancy between the half and full model geometries is the flow at the mid span (symmetry) location. It can be seen that all half-models, regardless of angle of attack or spatial order of accuracy, display elevated levels of turbulence at this location when compared to the full model. This is attributed to the symmetry plane boundary condition which acts as a slip-wall. Furthermore, although the turbulence resolution increases in proportion to the spatial order of accuracy, the largest difference in turbulence resolution occurs between the low-order (p=1) and high order (p=2) solution. This is observed for both angles of attack and suggests that if an accurate depiction of the turbulent scales is desired, a spatial order of accuracy of p > 1 should be used.

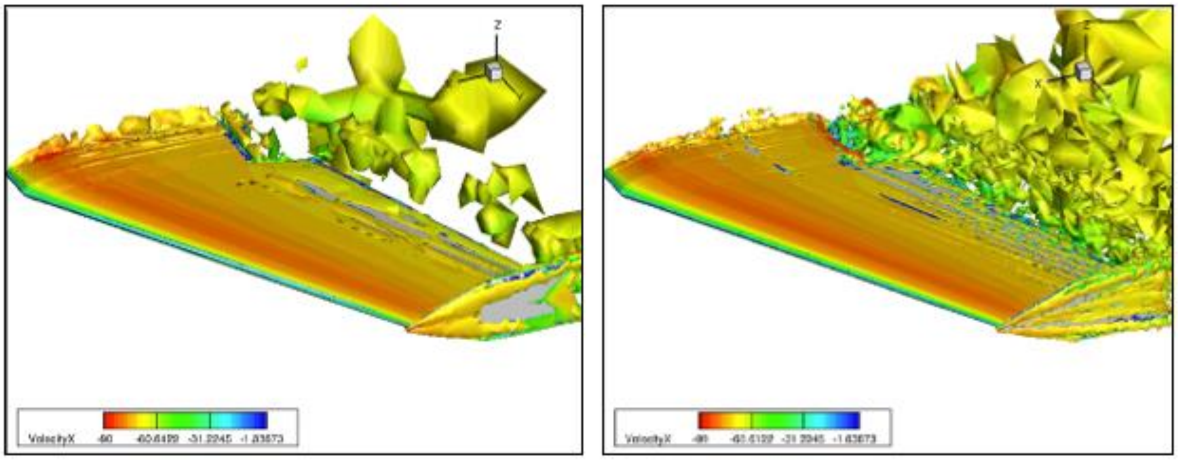

(a) HpMusic (p = 1) – Half Model

(b) HpMusic (p = 2) – Half Model

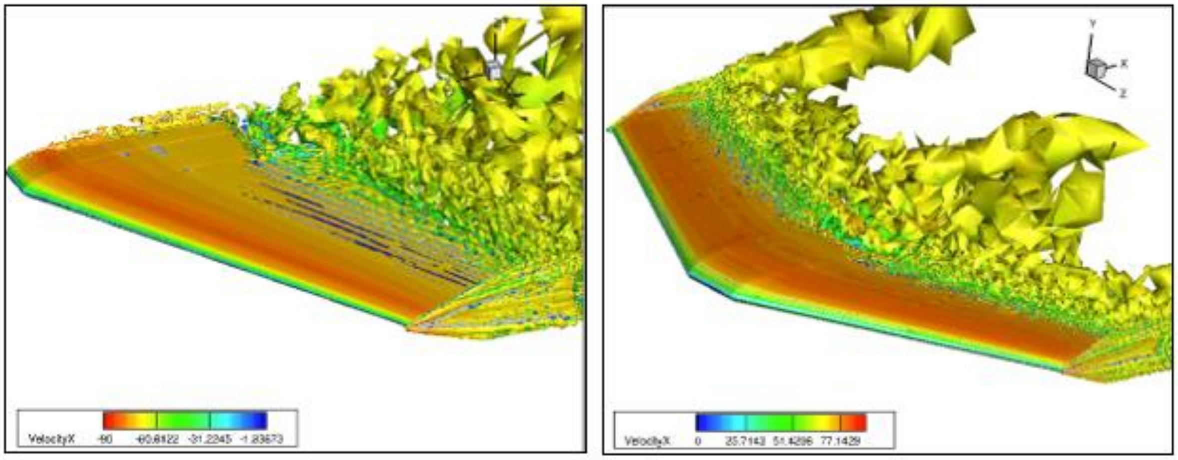

(c) HpMusic (p = 3) – Half Model

(d) HpMusic (p = 2) – Full Model

Figure 3-47. Isosurfaces of instantaneous Q criterion colored by streamwise velocity for zero angle of attack.

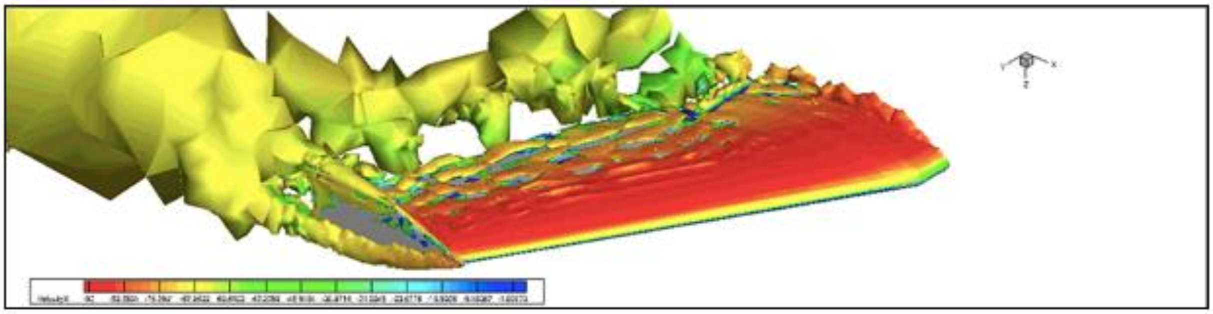

(a) HpMusic (p=1) – Half Model

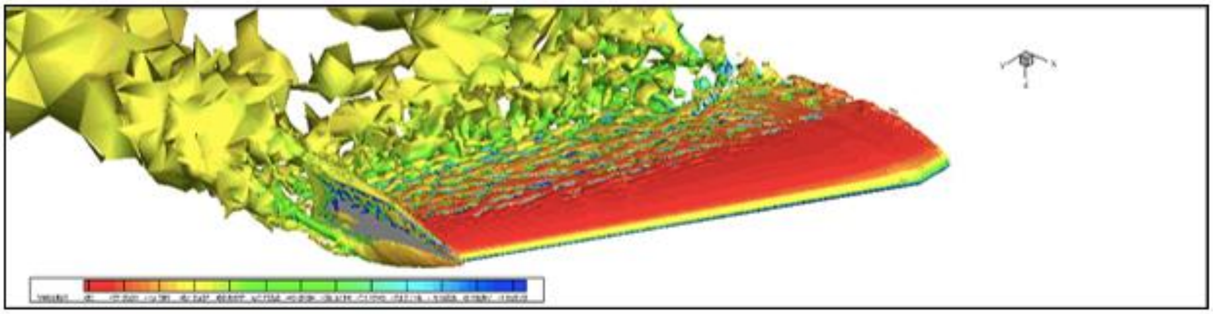

(b) HpMusic (p=2) – Half Model

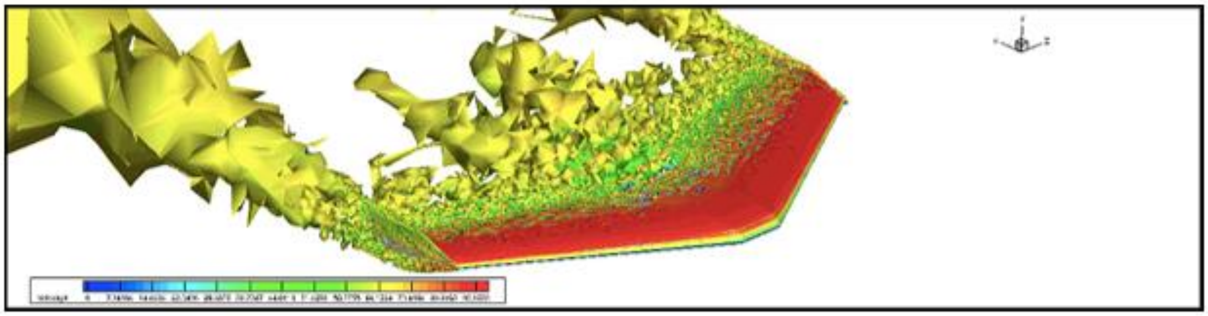

(c) HpMusic (p=2) – Full Model

Figure 3-48. Isosurfaces of instantaneous Q criterion colored by streamwise velocity for six degrees angle of attack.

3.2.6 Conclusions for CFD analyses

The aerodynamic coefficients and stability derivatives generated by a variety of low-and-high fidelity computational simulations were compared to flight test identified parameters for a small flying-wing UAS. It was found that at zero angle of attack, low-fidelity CFD methods such as the VLM offered comparable results to those obtained by low-and-high order N.S solvers. This suggests that VLM methods, such as the one offered by the open source code, Tornado, offers a suitable alternative to measure lift, drag, and pitching moment coefficients if the underlying low angle of attack assumption is not violated. However, at six degrees angle of attack, high order N.S solvers are recommended to obtain values similar to flight test identified parameters. In terms of stability derivatives, VLM methods provide less accurate results compared to N.S style methods.

Low-order N.S-style simulations appear to be sufficient to acquire C_{L_α} and C_{D_α} but not C_{m_α} where a high-order solution is required.

In addition, the time-averaged surface pressure coefficient at quarter-span location was compared for various low-and-high order solutions. It was found that low-and-high order results yielded similar behaviors in regions where the flow remains attached with the addition of minor oscillations shown by the low order solution. However, in regions experiencing flow separation, the spatial order of accuracy plays a larger role than using either a half model or full model in determining result agreement.

Lastly, the flow topology was analyzed via isosurfaces of Q-criteria colored by axial velocity. It was found that all HpMusic solutions utilizing the same geometrical model displayed the same flow features. However, the resolution of these features depended highly on the solution's spatial order of accuracy. Lastly, it was found that the largest increase in turbulence resolution occurred when transitioning from a low order method (p = 1) to a high order method (p = 2).

3.3 UAS flight testing

Flight tests of two types have been conducted: during "race track" or rectangular flight circuits at a local AMA field; and, during flights over wind machines producing the air velocity fields described earlier. The former flights were conducted with a number of UAS, including "kit" UAS as well as those designed and fabricated at KU.

3.3.1 UAS used for flight testing

The SkyHunter UAS, shown in Figure 3-49, is a commercially available UAS built mostly out of foam. The aircraft weighs 8.9 lb (4.04 kg) and has a 71-inch wingspan. The pusher motor has a maximum power of 80 W. Some other characteristics of the aircraft are presented in Table 3-25.

Figure 3-49. The SkyHunter UAS.

Table 3-25. Summary of SkyHunter characteristics.

Quantity		Value
Wing planform area, S	ft^2	4.44
Wing mean geometric chord, $\bar{c}$	in	9
Wing span, b	in	71
Aspect ratio, AR	~	7.83
Mass, m	lbm	8.9
Maximum flight time	min	~30
Maximum motor power	W	800
Aircraft Aerodynamic Center (AC) location aft of nose	in	19.67
Aircraft Center of Gravity (CG) location aft of nose	in	18.00
Static margin, SM	%	18.65

The Ranger UAS is a commercially available UAS. Its fuselage is made out of plastic while the wings are made out of foam. The aircraft weights 6 lb (2.72 kg) and it has a wingspan of 95.48 inches (2.4 m). A single pusher electric motor is mounted to the rear of the fuselage. Figure 3-50 shows a picture of the Ranger UAS. Some other characteristics of the aircraft are presented in Table 3-26.

Figure 3-50. Ranger UAS.

Table 3-26. Summary of Ranger characteristics.

Quantity		Value
Wing planform area, S	ft2	5.36
Wing mean geometric chord, $\bar{c}$	in	8.25
Wingspan, b	in	95.48
Wing aspect ratio, AR	~	11.81
Mass, m	lbm	6
Aircraft Aerodynamic Center (AC) location aft of nose	in	16.64
Aircraft Center of Gravity (CG) location aft of nose	in	15.4
Static margin, SM	%	15

The Aeroscout UAS is a commercially available UAS. Its fuselage and wings are both constructed out of foam. The aircraft weighs between 1.82 and 2.32 lb (0.83 - 1.05 kg), depending on if ballast was added prior to flight, and it has a wingspan of 43.2 inches. A single pusher electric motor is mounted to the rear of the fuselage. Figure 3-51 shows a picture of the Aeroscout UAS. Some other characteristics of the aircraft are presented in Table 3-27.

Figure 3-51. AeroScout UAS.

Table 3-27. Summary of AeroScout characteristics.

Quantity		Value
Wing planform area, S	ft2	2.24
Wing mean geometric chord, $\bar{c}$	in	7.48
Wingspan, b	in	43.2
Wing aspect ratio, AR	~	5.79
Mass, m	lbm	1.82-2.32
Aircraft Aerodynamic Center (AC) location aft of nose	in	12.53
Aircraft Center of Gravity (CG) location aft of nose	in	11.48
Static margin, SM	%	14.11

3.3.2 Flight tests conducted

3.3.2.1 Flights to induce loss of control

To establish the metrics to identify loss of control, there were two strategies employed: 1) reduction of the throttle while still commanding an altitude hold to cause the UAS to stall; 2) flights along a racetrack path in high wind conditions, such that the UAS would stall when turning away from the prevailing wind.

The first stage of generating datasets containing both stable and unstable flight segments involved ***reducing the cruise velocity*** of the SkyHunter UAS to its minimum cruise speed, commanding a small pitch up, and letting an unpredicted gust push the aircraft ***to stall***. While human intervention was sometimes required, the aircraft never entered "fatal" loss of control and was always recovered safely. The intensity of each stall was characterized by an onboard camera looking at flow tufts attached to the upper surface of the wing and horizontal tail; in stable, linear flight, the tufts will remain stationary as they are completely enveloped by the flow's boundary layer, as shown in Figure 3-52. When the aircraft is sent into loss of control by an unpredicted gust of no exorbitant magnitude, the boundary layer bursts and the tufts immediately detach from the wing, as shown in Figure 3-53, the intensity and speed by which the tufts detach can be related to loss of control intensity suffered by the aircraft.

Figure 3-52. Tufts during stable flight.

Figure 3-53. Tufts during unstable flight.

.

Figure 3-54 shows the flight path of this mostly autonomous, race-track flight. There were four stall occurrences. The altitude v. time plot shows the periodic moments of reduced speed, pitch up, and stall that occurred at 880, 1020, 1110 and 1190 seconds, of which three were recoverable. One stall required human intervention ($t = 880\text{s}$), while the others were recoverable by the autonomous flight system. When the pilot noted the stall, he took control, commanded maximum throttle, and recovered the aircraft, this path being the red track. In the lower portion of the figure, showing flight altitude, it can clearly be seen that the UAS lost a good part of its previous altitude.

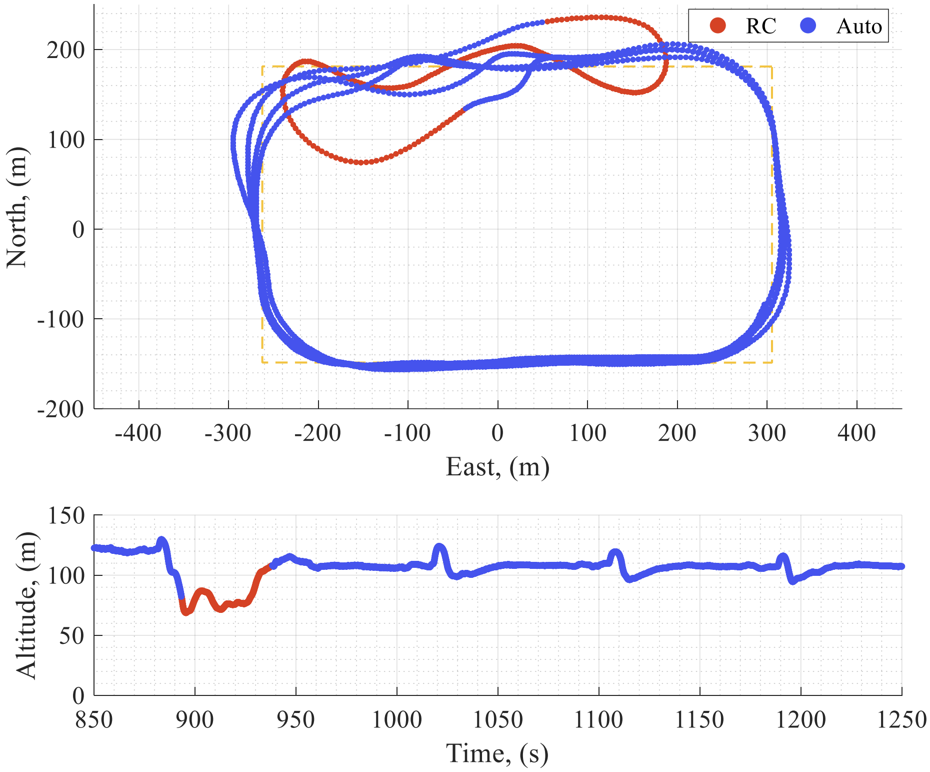

Figure 3-54. SkyHunter flight path in which loss of control was imposed with intentional stall events.

3.3.2.2 AeroScout piloted flights over wind machines

Preliminary flights over fans were conducted at the Lawrence Regional Airport under an FAA Airspace Authorization. Figure 3-55 shows the flight area setup. Of particular note, two cameras are always used during flights over fans, one with a lateral view and another with a longitudinal view of the encounter.

Figure 3-55. Flight test ground support around fans: ground station and two cameras with different views.

Figure 3-56. AeroScout upset by fans (fan on left with early air flow deflection "paddles").

Figure 3-56 is a photo of an AeroScout piloted by an experienced pilot alongside runway, to the south and east of the flight path, in a headwind encounter which caused a dramatic pitch and roll response. In this case, and several others, the UAS was recovered by the pilot. In two other flights, the UAS crashed and was severely damaged.

Figure 3-57 shows the flight path of the AeroScout during multiple flights over the fans by a pilot. The lower part of the figure shows the dramatic altitude changes down to within the fan airflow then recovering to a safer altitude as it passed over trees located alongside the airport.

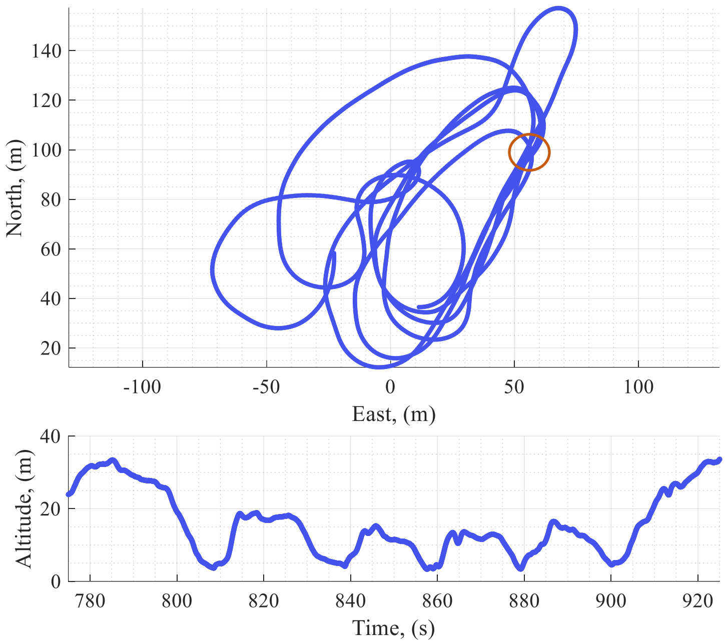

Figure 3-57. Flight path of the AeroScout under pilot command over fans (circled).

3.3.2.3 AeroScout autonomous flights over wind machines

Figure 3-58 shows the flight path of an AeroScout in autonomous mode over a fan. The altitude and lateral position control for this UAS was problematic: the low fidelity GPS unit did not allow the UAS controller to reliably fly over the fans.

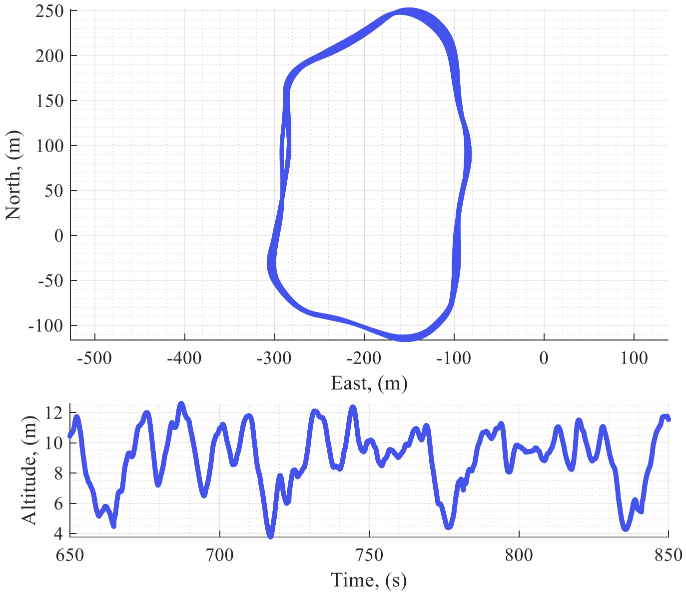

Figure 3-58. Flight path for an AeroScout autonomous flight over fans.

3.3.2.4 Autonomous SkyHunter flights over wind machines

Four autonomous flights were conducted in a single day over a set of wind machines set side-by-side. Figure 3-59 shows the intended flight path for a “headwind” encounter: through the center of the wind machine pair. The SkyHunter was fitted with a high fidelity GPS—overcoming guidance issues noted in earlier flights over fans. As such it was able to maintain altitude very well over the fans. However, the lateral control was less capable: of 22 total potential fan encounters, only 3 were close enough to note a significant influence of the fan on the UAS trajectory.

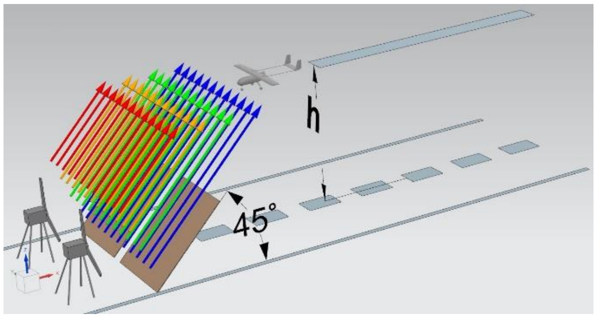

Figure 3-59. Schematic of a Head-on Encounter of a UAS with side-by-side wind machines.

Figure 3-60 through Figure 3-62 depict three encounters of the SkyHunter UAS with the fans. All flights were under autonomous flight control.

For the two good “headwind” encounters, that is, the flight path opposed the fan discharge: one flight was ½ wingspan off the center of the fans, and one was 1 wingspan off. In both cases, one fan was set to 100% and the other to 60%. In both cases there was a slight pitch-up followed by a pitch-down to return to the intended flight path. In the case which caused the greatest influence on the SkyHunter—a roll to 50 degrees shown in Figure 3-61—the UAS was clearly influenced by the lateral gradient of the fan velocity. In the other head-on case, the roll was insignificant.

In the third encounter, Figure 3-62, the fans were directing flow at 90 degrees to the UAS flight path. Although there definitely was a wing span-wise gradient in airflow, the pitch and roll response was barely identifiable.

Figure 3-60. UAS Headwind Encounter: South fan @ 60%, North @100%, 11 ft above fans, 5 ft laterally.

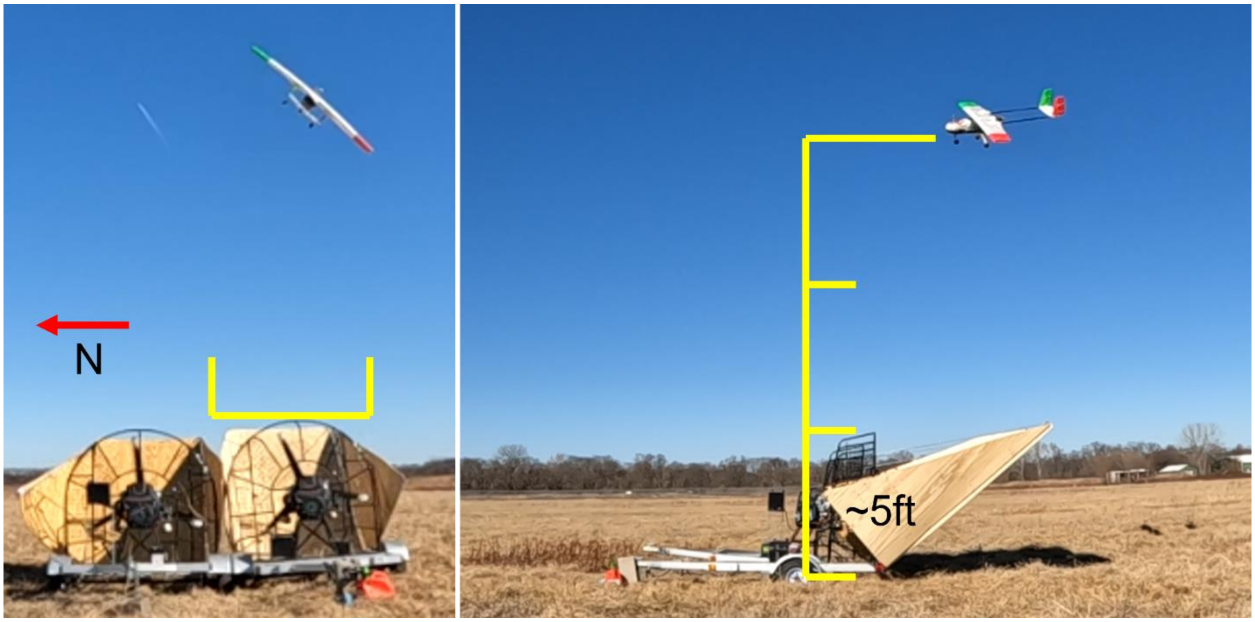

Figure 3-61. UAS Headwind Encounter: South fan @ 60%, North @100%, 11 ft above fans, 3 ft laterally.

Figure 3-62. UAS Side Encounter, Both Fans at 100%, 5 ft above fans, 5 ft laterally.

Focusing now on the UAS headwind encounter depicted in Figure 3-61, which produced a dramatic rolling response, the flight path and altitude history are presented in Figure 3-63. Note that the controller reduced altitude in the run-up to the fan encounters.

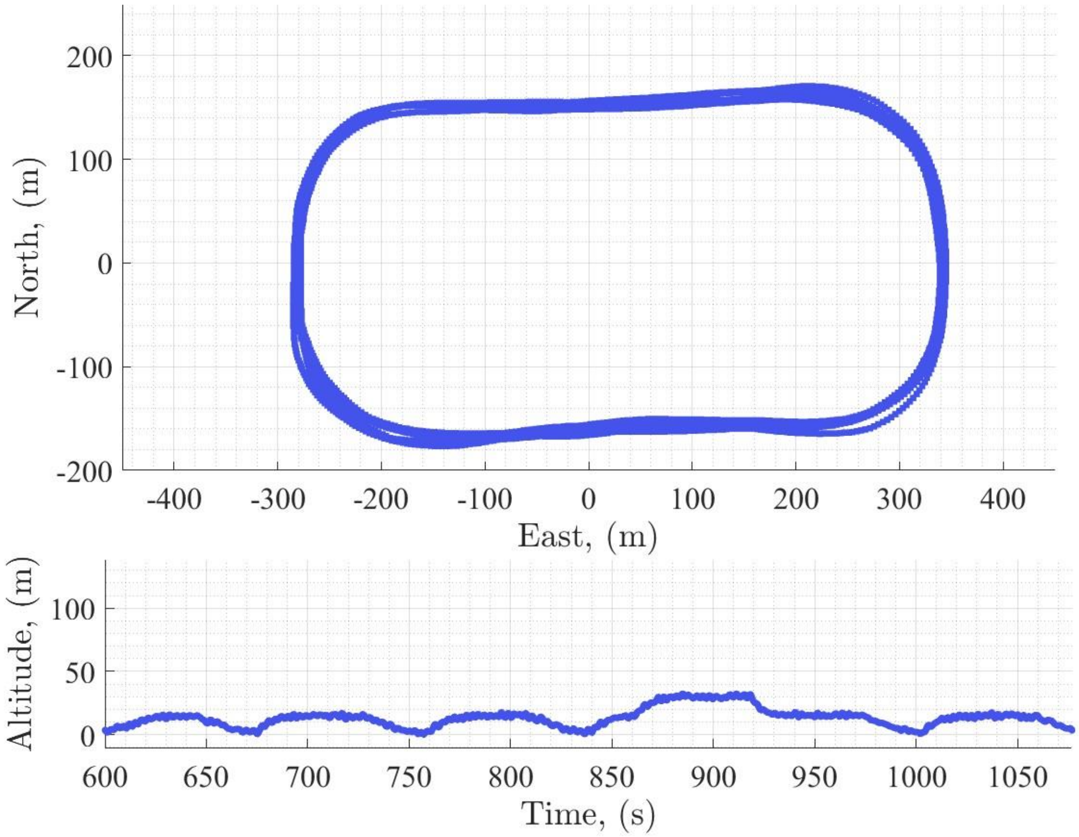

Figure 3-63. Flight path and altitude history for the SkyHunter.

3.3.3 *Comparison of flight tests with simulation*

The most identifiable headwind encounter of the SkyHunter over a set of wind machines is the subject of comparison between flight test and simulation.

3.3.3.1 Flight test results

The headwind encounter with the fans is characterized now in term of UAS states and the control inputs from the LQR controller. Figure 3-64 shows the angular rates recorded on-board the UAS. Note that the maximum predicted roll rate was nearly 300 degrees/second.

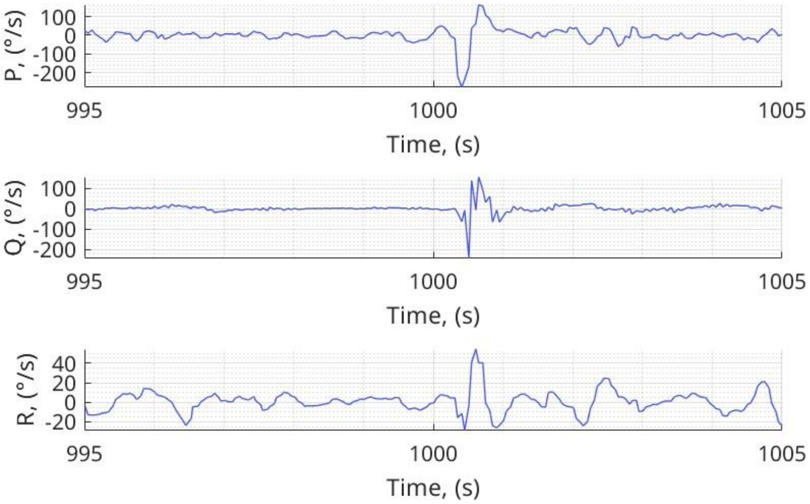

Figure 3-64. Roll, pitch and yaw rates recorded in the dramatic headwind encounter with the fans.

Figure 3-65 shows the control commands recorded on-board. Note that the elevator was commanded to 20 degrees and the aileron to 10 degrees—both very dramatic.

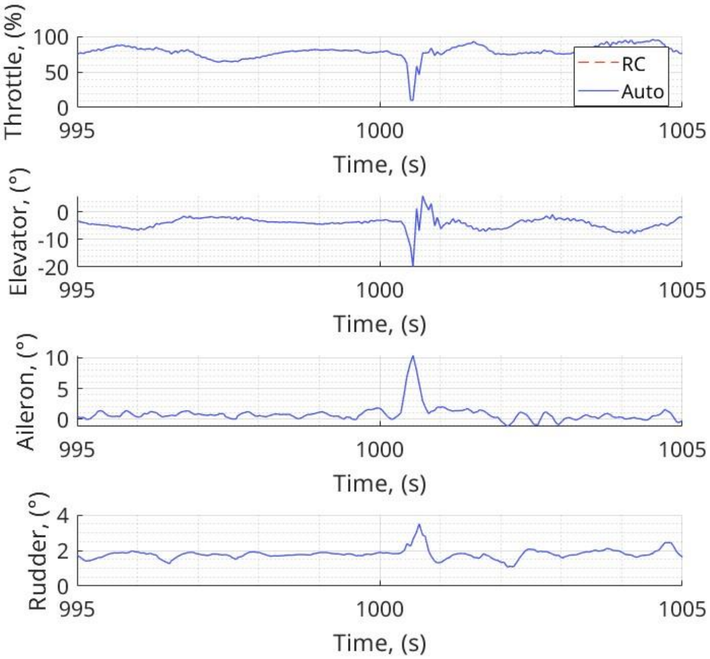

Figure 3-65. Control commands recorded in the dramatic headwind encounter with the fans.

Finally, Figure 3-66 shows the roll (top) and pitch (bottom) angles, both the commanded values from the guidance logic and the measured values. Note that the maximum measured roll angle was -40 degrees.

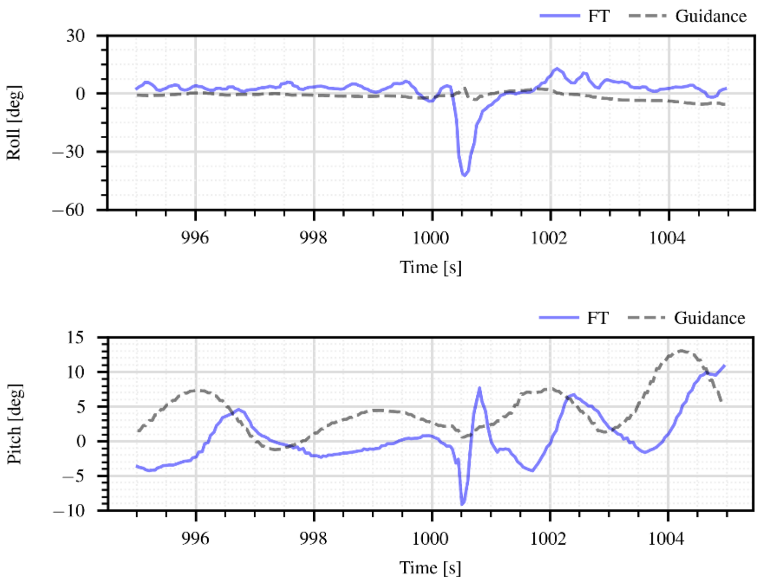

Figure 3-66. Roll and pitch angles, both commanded by the guidance algorithm and measured.

3.3.3.2 Comparison of simulation of SkyHunter wake encounter with flight test data

The response of the SkyHunter was simulated using the dynamic model and an LQR controller described in Section 3.1.2.3 The wind field used to emulate the wake through which the UAS flew in simulation was estimated using the measured air velocities during the characterization of the wind machine air velocity output. Note although the estimated wind field was not a perfect emulation of wake, it could help the verification process and quantify the accuracy of simulations capturing the passage of a UAS through a wind field.

Figures 3-65 and Figure 3-68 compare the UAS states from simulation and flight test. The linear aerodynamic model of the UAS is sufficient when the aircraft is in the benign portion of flight; however, it has deficiencies in accurately representing the longitudinal states of UAS during the wake encounter. The lateral-directional states are relatively better simulated though there are both magnitude and phase errors.

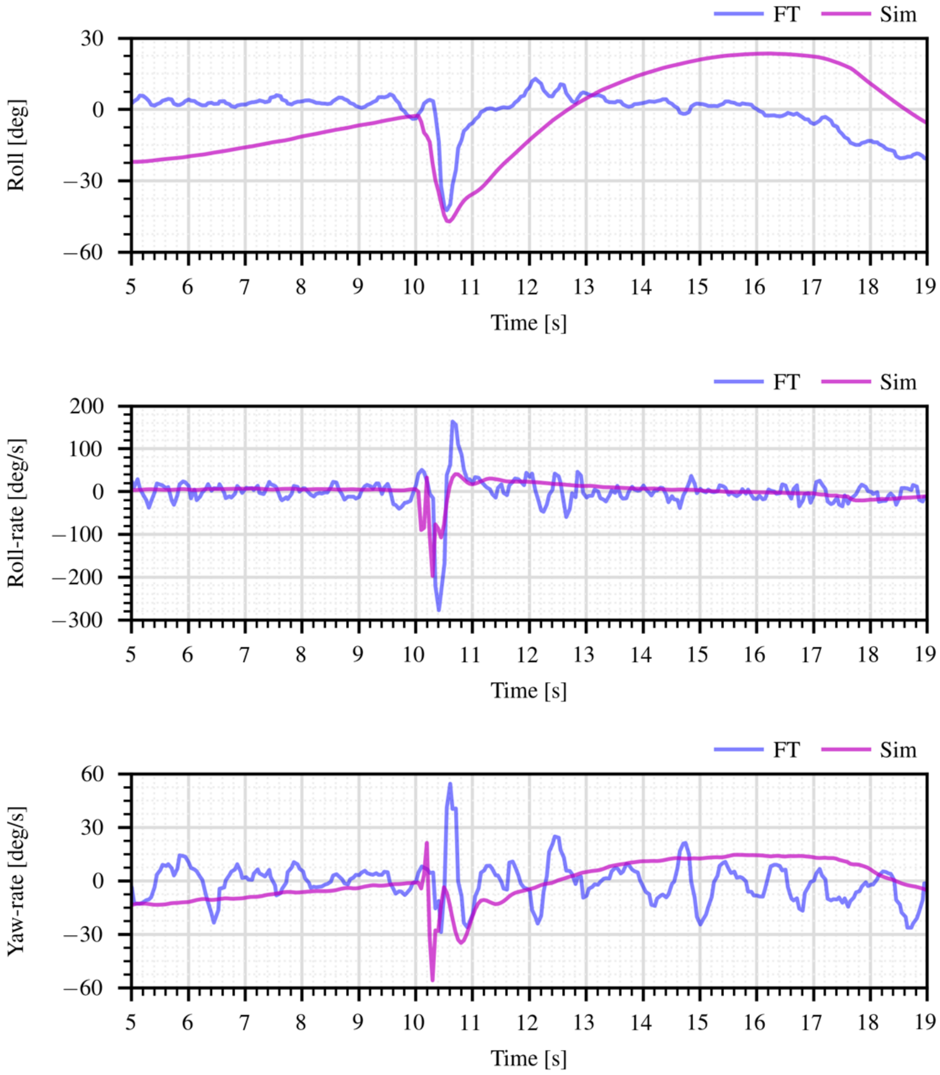

Figure 3-67. Comparison of UAS longitudinal states between simulation and flight test.

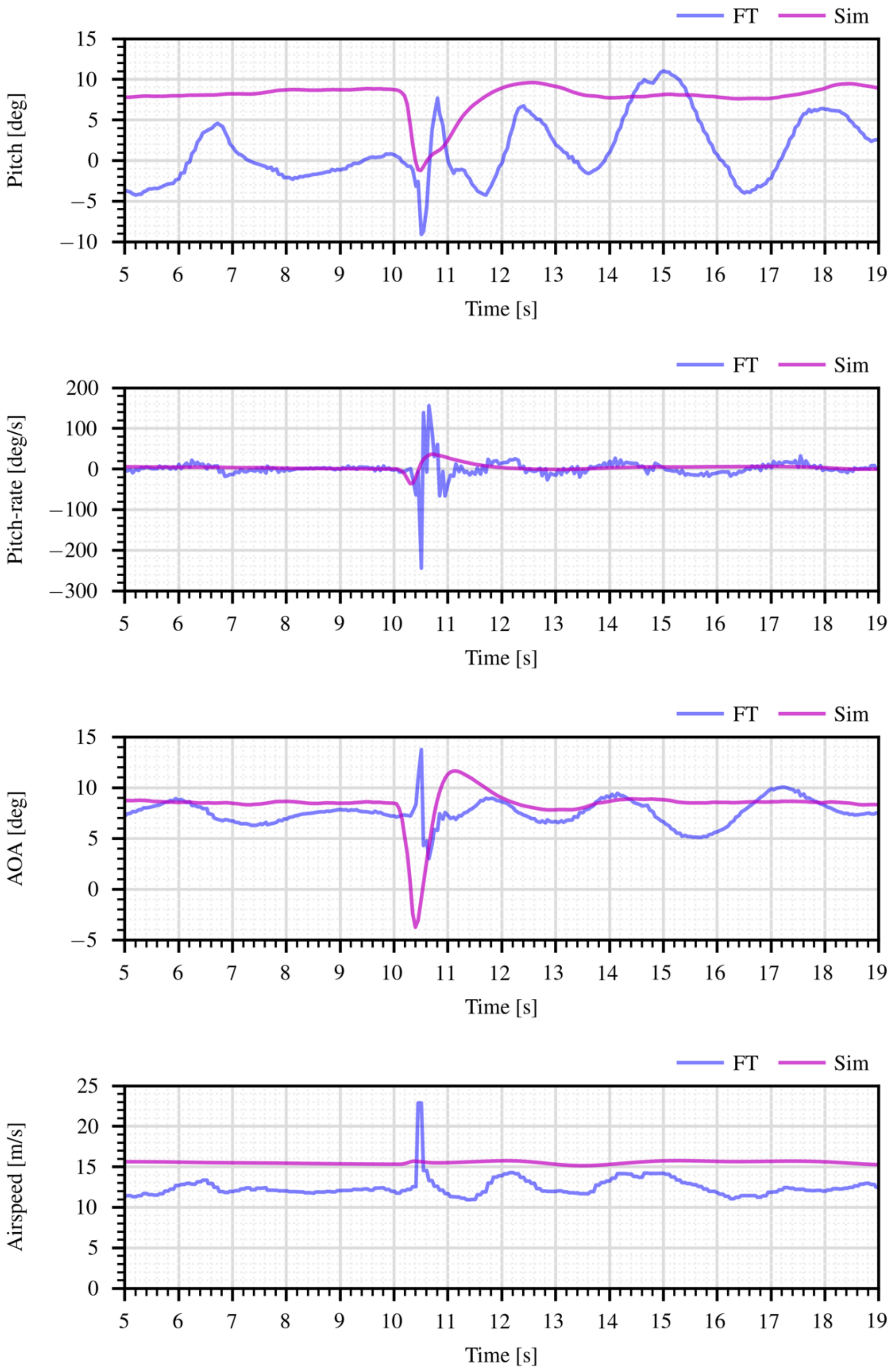

Figure 3-68. Comparison of UAS lateral-directional states between simulation and flight test.

3.3.3.3 Commentary on comparison of simulation and flight test

The observed inaccuracies in the simulation results could be categorized into the magnitude and phase, which is directly impacted by unsteady aerodynamics due to the rapid changes in the strength of wind during the encounter. Flight data analysis revealed that the key factors in generating unsteady aerodynamics to be the body-axis angular accelerations. These aerodynamic angular accelerations are shown to result in a phase shift between control input and the variables to be controlled, sometimes the control leading the motion, and sometimes lagging.

3.3.4 Uncertainty analysis: A case for flight-test validated simulation models

It is standard practice to develop six degrees of freedom simulations for fixed-wing aircraft based on appropriate equations of motion. A common approach is to model aerodynamic forces and moments as differentiable functions and expand them in a Taylor series. The stability and aircraft control derivatives are presented as first order, linear Taylor expansions as well. Although effective in the benign portions of the flight envelope, the mathematical structure induces uncertainties in the predictions of aerodynamic forces and moments when the aircraft encounters a wake vortex or when the aircraft enters loss of control. In this work, new methods are developed to assess the magnitude of uncertainties and to determine if these models can provide reliable predictions of response when the UAS encounters external disturbances, such as a wake vortex. The basis for determining reliability is through comparison between simulation and flight test.

Comparison was performed on several flight portions which contain different flight dynamics. To enable efficient selection of flight data from different phases of flight, classification algorithms were developed and utilized. The classification algorithms can classify the flight into straight-line cruise flight, level turn flight, ascending flight, and descending flight. In this report, analysis is made for a straight-line cruise flight portion, a level turn flight portion, an ascending flight portion, a descending flight portion, a flight portion where the aircraft went into dangerous conditions and was entering loss of control, and a flight portion in which an attempt was made to stall the aircraft. To conduct a more general analysis, Monte Carlo (MC) simulations are performed instead of only performing a single simulation. In the Monte Carlo analysis, several simulations are performed in which the simulation parameters (e.g. the stability and control derivatives) are randomly varied within predefined ranges. This allows for a more general analysis which takes simulation parameter uncertainty into account.

Attention is directed to two aspects when comparing the simulation to flight data. (1) How close is the Base Model (BM) to the flight data (where the base model is a simulation which uses the nominal simulation parameters without any added variation)? (2) How do the Monte Carlo simulations compare to flight data?

Analysis shows that the BM could capture the flight data rotation rates (P, Q and R) to some extent. The BM simulation could capture the roll rate and pitch rate better than the yaw rate. The roll rate BM simulations captured the trends in the flight data in all six analyzed flight portions. However, the magnitudes of the captured trends did not match the flight data. They were smaller in many cases. The pitch rate BM simulations had small modeling errors in three of the flight portions. Large pitch rate modeling errors are seen in the other three flight portions. The yaw rate simulation using the BM did not capture flight data appropriately.

As for the MC simulations, the aircraft rotation rates recorded in the flight data were mostly captured inside the regions covered by the MC simulations. However, despite taking the defined parameter uncertainty into account, there are flight sections that are not captured by the MC simulations. Also, the overall trends seen in MC simulations were smoother than the flight data trends in more than one flight portion.

The results indicate that the methods used for simulation are able to capture the flight data to some extent. However, there are limitations to the validity of the methods. Higher fidelity and more complex modeling methods may be necessary to obtain adequate simulations. Performing actual flight tests is needed to evaluate the accuracy of simulations and to investigate phenomena which are not well modeled in simulations.

Details of the Monte Carlo simulation setup are presented in Section 3.3.4.1. A presentation of the methods used for classifying the flight data into different phases is presented in Section 3.3.4.2. Monte Carlo simulations results are presented and discussed in Section 3.3.4.3. Finally, conclusions are made in Section 3.3.4.4.

3.3.4.1 Monte Carlo (MC) simulation setup

Following standard practice, a six degree of freedom simulation for the SkyHunter UAS is developed. The simulation is based on fixed-wing aircraft non-linear equations of motion, and it considers coupling effects between longitudinal and lateral-directional motion of the aircraft, to some extent. Aerodynamic forces and moments are modeled using linearized first order equations that depend on the use of stability and control derivatives. Details about this method of modeling fixed-wing aircraft can be found in flight dynamics textbooks such as [1, 52, 53].

Stability and Control Derivatives (SCDs) can be obtained using software tools such as AAA [22] or Athena Vortex Lattice [54]. In this work AAA is used to obtain the SCDs. AAA software uses physics-based and semi-empirical methods to estimate the stability and control derivatives. These methods provide a relatively quick approach for obtaining SCDs, when compared to wind tunnel modeling or modeling based on flight test data (a.k.a. System Identification). However, there is uncertainty in the obtained estimates.

In order to address the presence of uncertainty in the stability and control derivatives, Monte Carlo simulations are performed in this analysis. That is, instead of using a single set of SCDs (i.e. a single set of simulation parameters), several simulations are performed, each having a different set of SCDs. Using Monte Carlo simulations aims to take parameter uncertainty into account while comparing simulation with flight data.

In addition to uncertainty in SCDs, there can often be an error in the trim angles of the aircraft control surfaces. For example, for straight line level wings flight condition, aileron trim angle is expected to be zero. However, in actual flight, uneven weight distribution around the aircraft may require a non-zero aileron deflection to maintain level wings. The Monte Carlo simulations aim to address this uncertainty in control surface trims by adding a constant bias to the recorded control surface deflections when performing simulations. The bias is picked from a normal distribution with a standard deviation of $\sigma = 0.5$ degrees.

The Monte Carlo simulations are performed by:

1. First, defining a mean value (μ) for each SCD and a standard deviation (σ) according to which the SCD is allowed to vary. The mean value (μ) is defined as the AAA estimate. The standard deviation (σ) is defined according to the Table 3-28.

Table 3-28. Defined mean values and standard deviations for each SCD.

Lateral-Directional SCDs			Longitudinal SCDs		
SCD	μ (AAA est.)	σ (% of μ)	SCD	μ (AAA est.)	σ (% of μ)
$C_{Y\beta}$	-0.502	± 20	$C_{L\alpha}$	4.985	± 5
C_{Yp}	0.044	± 50	C_{Lu}	0.002	± 20
C_{Yr}	0.345	± 30	$C_{m\alpha}$	-0.898	± 10
$C_{l\beta}$	-0.451	± 20	C_{mq}	-20.870	± 20
C_{lp}	-0.469	± 15	$C_{m\dot{\alpha}}$	-7.407	± 40
C_{lr}	0.259	± 40	C_{mu}	0.00028	± 20
$C_{n\beta}$	0.155	± 15	C_{Lde}	0.597	± 25
C_{np}	-0.120	± 90	C_{mde}	-2.175	± 25
C_{nr}	-0.186	± 25			
C_{Ydr}	0.188	± 25			
C_{lda}	0.312	± 25			
C_{ldr}	0.006	± 25			
C_{nda}	-0.040	± 25			
C_{ndr}	-0.097	± 25			

2. Next, a defined number of simulations (N) are performed. Each simulation uses a set of SCDs obtained by sampling the derivatives from normal distributions having mean (μ) and standard deviation (σ) as defined above. The SCDs used in each simulation are held constant but each simulation uses a different set of SCDs. The number of simulations performed in this analysis was $N = 2000$ simulations. This number of simulations allows having around 8 simulations using SCD outside of the 2σ bound. (This is because a normal distribution has the characteristic that 95.4% of values are inside the 2σ bound as shown in Figure 3-69.)

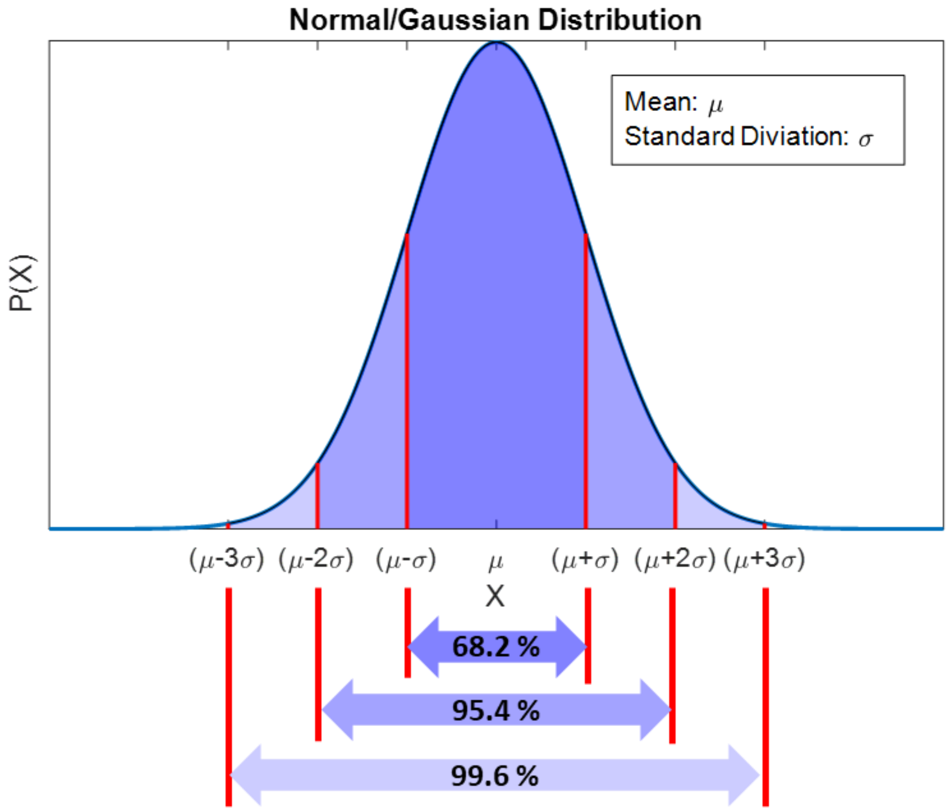

Figure 3-69. Percentage of values within 1σ, 2σ and 3σ bounds for a normal distribution.

3. To account for uncertainty in control surface trim angles, a bias is added to the control surface deflections recorded in the flight data before performing simulations. The bias for each simulation is obtained from a normal distribution that has zero mean and a $\sigma = 0.5°$ standard deviation. The bias value used in each simulation is held constant, but each simulation uses a different bias.
4. For each simulation, the initial conditions of the states and controls are obtained from the flight data.
5. During simulation, the aircraft controls at each time step are obtained from the recorded flight data.
6. Simulation is performed for a defined time portion (say 10 seconds of flight) and the state propagation over time is recorded.
7. The simulation states are compared to the flight data measurements visually (through plots) and statistically (through calculation of Root-Mean-Squared-Error (RMSE) between simulation and flight data).

3.3.4.2 Classification of flight test data

In order to test the reliability of the six degree of freedom dynamic model at different flight phases, algorithms are utilized to effectively and efficiently classify flight data at each time period into different flight phases. Flight data is categorized into four types of flight:

1. straight, level flight (cruise)
2. level turn

3. ascent
4. descent

To perform this task, the unsupervised machine learning technique of "clustering" is used, because of its capacity to quickly classify large amounts of data into a given number of categories.

Classification of flight data into cruise, level-turn, ascent, and descent is done in two steps. First, data is clustered into ascent, descent, and level flight. Then, level flight portions are further classified into level-turning or cruise (straight-level) flight. The measurements chosen for use in the first clustering process are vertical flight path angle (γ) and ascent rate ($-V_D$). Since both of these values are more positive when the aircraft is ascending, more negative when the aircraft is descending, and close to zero when aircraft is flying level (i.e. γ and $-V_D$ have three distinct mean values), they are ideal for use in a clustering algorithm. For clustering the data into ascent, descent, and level flight, MATLAB's built-in k-means clustering function is used to cluster the data using (γ and $-V_D$) as the inputs. The number of clusters is defined as k = 3 (three means around which to cluster the data). This clustering method was tested on 15 flight test data files utilizing three different fixed wing UASs. Results were visually verified by plotting the 3D path of the aircraft with each of the classified flight types indicated (e.g. see Figure 3-70.). The k-means algorithm is able to consistently classify the flight tests into portions of ascent, descent, and level flight.

After the flight test data is classified into ascent, descent, and level flight, the level flight portion is further classified into cruise and level-turn flight. The measurements chosen for use in this clustering step are roll angle (ϕ), yaw rate (R), and time rate of change of heading angle ($\dot{\psi}$), as they are all strongly related to whether or not the aircraft is turning. However, this is a slightly more challenging task as trim conditions, wind, and gusts make the measured attitude and rotational rates less consistently indicative of whether the aircraft is turning or not. The k-means method, as described for classifying ascent, descent, and level flight, was attempted for classifying turning vs straight flight. However, k-means clustering proved unable to consistently distinguish turning from straight flight. After some research and testing, another method of unsupervised machine learning clustering was selected: fuzzy c-means clustering.

Fuzzy-c means clustering is similar to k-means clustering in that it uses an algorithm to cluster input data around a given number of means. However, it differs in that it utilizes fuzzy logic (non-binary logic) in its grouping. Instead of assigning each data point to exactly one cluster (group), it assigns a membership value to each group from 0 to 1 for each data point. For example, if one data point very strongly correlates to a group, it may be assigned a membership value of 0.9 to that group. Having this membership value allows the user to select how strongly a measurement must correlate to a group before it is classified as being in that group. This flexibility, along with the more complex methods used by MATLAB's fcm (fuzzy c-means) function, proved capable of consistently classifying level flight data into cruise and turning categories when ($|\phi|$, $|R|$, and $|\dot{\psi}|$) are used as inputs and the number of clusters is specified as c = 2 (two clusters). The absolute value of each measurement is used because left turn is not distinguished from right. Through testing on several sets of flight test data, it was determined that a membership value to the turning cluster of 0.35 generally yields the best results for classification, however, in the function, this is left as an optional input if the user desires to tune it to the aircraft or a specific circumstance. A higher minimum turn membership value would classify less of the flight as turns and vice versa.

An example of the performance of the developed classification algorithms on an entire flight is presented in Figure 3-70. The algorithms correctly identify the level turn flight portions at the corners of the flight pattern. Straight line flight portions are also properly identified. Ascent and descent flight portions are identified during take-off and landing and during the duration of the flight.

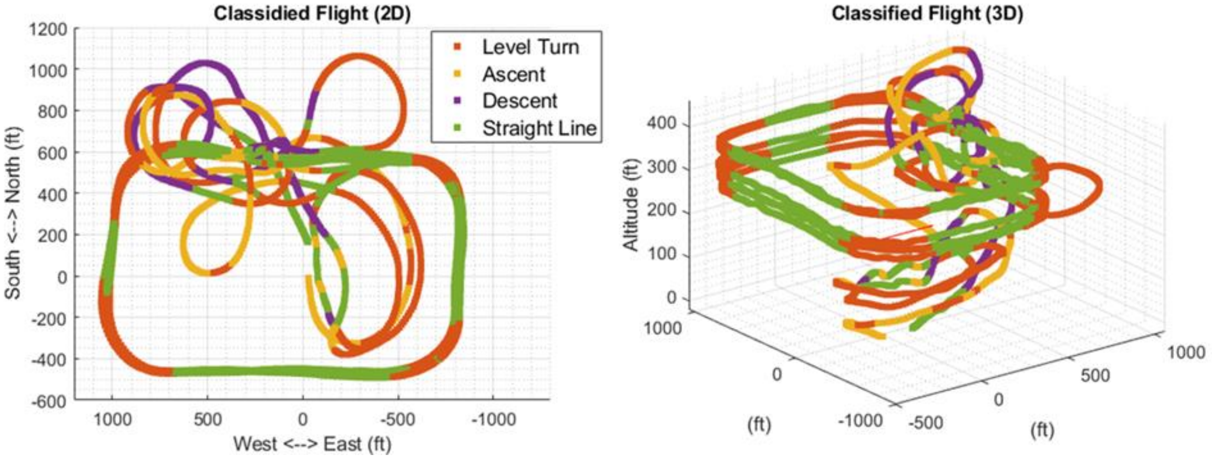

Figure 3-70. Classification of flight into different phases.

3.3.4.3 Modelling uncertainty and comparison to flight test data

Comparison results are presented and discussed for the following flight portions:

1. A straight-line cruise flight portion
2. A level turn flight portion
3. An ascending flight portion
4. A descending flight portion
5. A flight portion in which the aircraft was entering loss of control
6. A flight portion in which an attempt was made to stall the aircraft

3.3.4.3.1 Categorizing simulations according to Root-Mean-Square-Error (RMSE)

In the MC simulation plots presented below, simulation results are color coded into three categories. The categories indicate how close the simulation is to the flight data in terms RMSE. The RMSE of each simulation ($RMSE$) is calculated, with the flight data considered as the true value. Then, the standard deviation of all the RMSE errors (σ_{RMSE}) is calculated. The minimum RMSE out of all the simulations ($RMSE_{MIN}$) is also identified. The simulations are then categorized as follows:

- Blue Simulation: $RMSE < (RMSE)_{MIN} + \sigma_{RMSE}$
- Yellow Simulation: $(RMSE)_{MIN} + \sigma_{RMSE} \leq RMSE < (RMSE)_{MIN} + 2\sigma_{RMSE}$
- Red Simulation: $(RMSE)_{MIN} + 2\sigma_{RMSE} \leq RMSE$

That is:

Blue simulations: are closest to the flight data (have lowest RMSE). These are the simulations that have RMSE ranging from the minimum RMSE up to the minimum RMSE + σ_{RMSE}.

Yellow simulations: are the second closest to the flight data (according to RMSE). These are the simulations that have RMSE ranging from (the minimum RMSE + σ_{RMSE}) up to (the minimum RMSE + 2*σ_{RMSE}).

Red simulations: are farthest from the flight data (have largest RMSE). These are the simulations that have RMSE larger than (the minimum RMSE + 2*σ_{RMSE}).

3.3.4.3.2 Results from straight-line cruise segment

A benign straight-line flight portion is analyzed in this section. The longitudinal and lateral-directional states and controls, as recorded in the flight data, are presented in Figure 3-71. MC simulation results are presented in Figure 3-72. to Figure 3-74. for the angular rates, that is, roll rate (P), pitch rate (Q), and yaw rate (R).

As seen in Figure 3-71., the aircraft was cruising at around 46 ft/s in this flight portion. The aircraft roll angle (ϕ) was small, indicating wings level flight condition. Aircraft altitude was held at 370 ft AGL ± about 5 feet, indicating straight-line flight. An Artificial Neural Network (ANN) flight controller was in command of the aircraft. This flight is considered as a benign straight-line level wing flight portion.

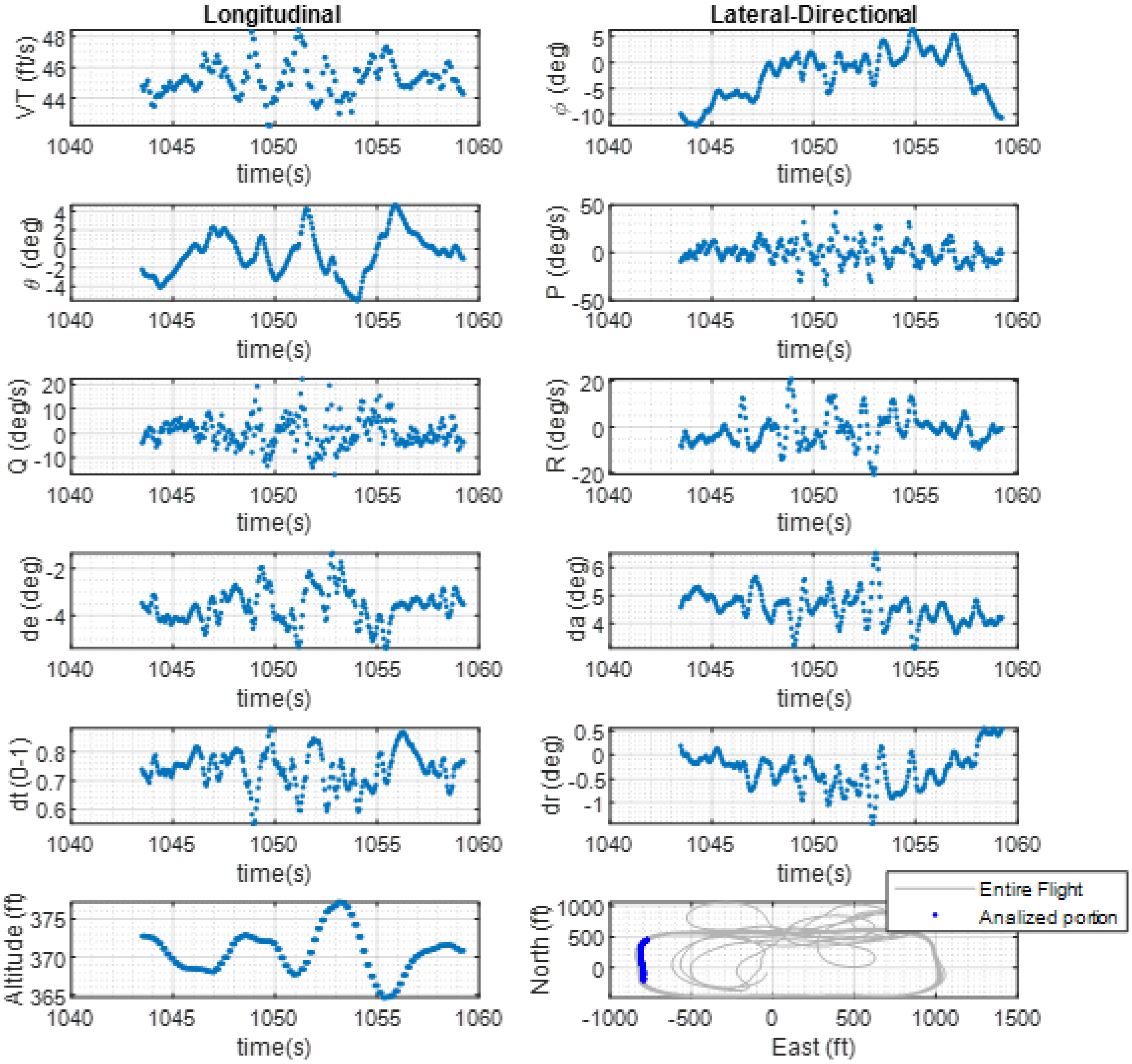

Figure 3-71. Flight data of straight-line cruise flight portion.

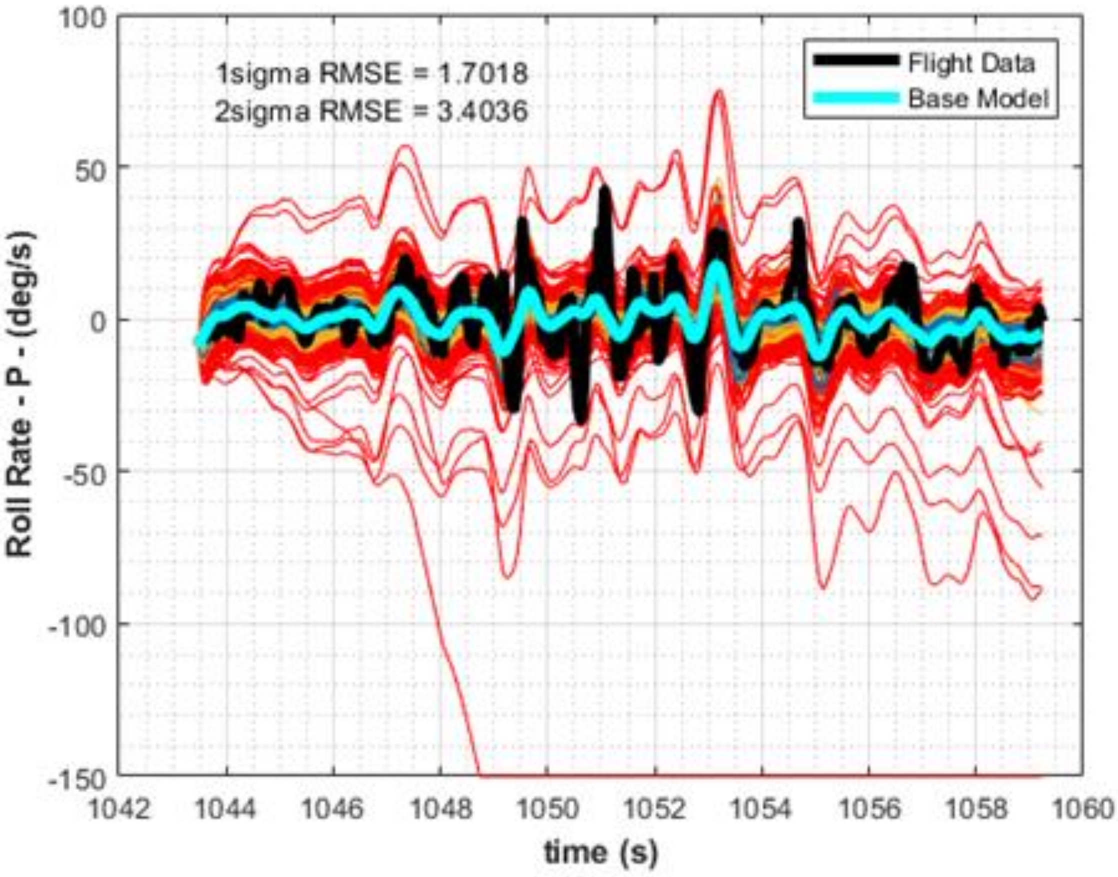

Figure 3-72. Comparing MC simulations to flight data for straight-line flight portion: roll rate.

Analysis of the roll rate (P) MC simulations indicates that:

- The base model, shown in cyan, (which is the simulation that uses the mean values of all the SCDs as obtained from AAA without any modifications) is able to capture the trends in the flight data to some extent. However, there are errors in the magnitudes of change in the base model compared to the flight data. In some instances, these errors can be quite large (± ~30 degrees per seconds) as seen in the time range between 1050 and 1052 seconds.
- Throughout the flight portion, the flight data is mostly contained in the range spanned by the MC simulations. However, there are small sections where the flight data was located in regions where only a few red simulations are located, indicating that these sections did not conform to the majority of the simulations.

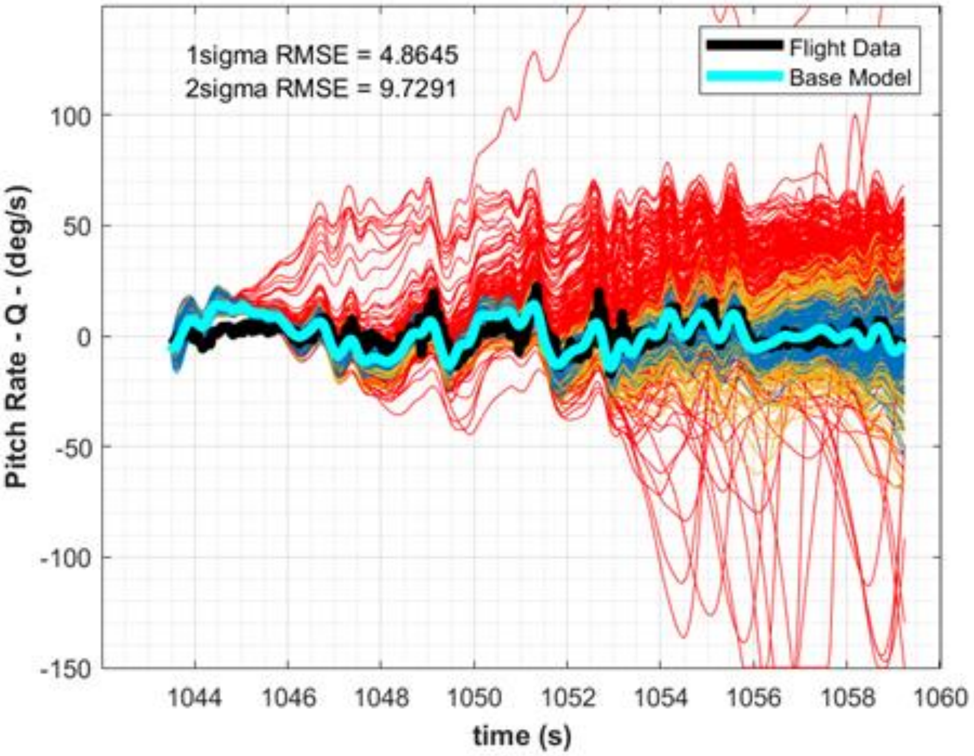

Figure 3-73. Comparing MC simulations to flight data for straight-line flight portion: pitch rate.

Analysis of the pitch rate (Q) MC simulations indicates that:

- The base model is able to capture the trends in the flight data for the majority of the flight portion. The errors between the base model simulation and the flight data are small for the majority of flight.
- It can be seen that the pitch rate (simulated using the base model) has smaller errors compared to the roll rate. The simulation seems to have better performance in modeling the pitch rate than modeling the roll rate.
- There is a portion at the beginning (1044 to 1046 seconds) where the pitch rate (modeled by all the MC simulations) did not match the flight data.
- Other than the above-mentioned section of flight, the flight data was completely contained in the region spanned by the MC simulations. However, the region spanned by the MC simulation was pretty wide (ex: going from -50 to 50 deg/s towards the end of the flight portion).

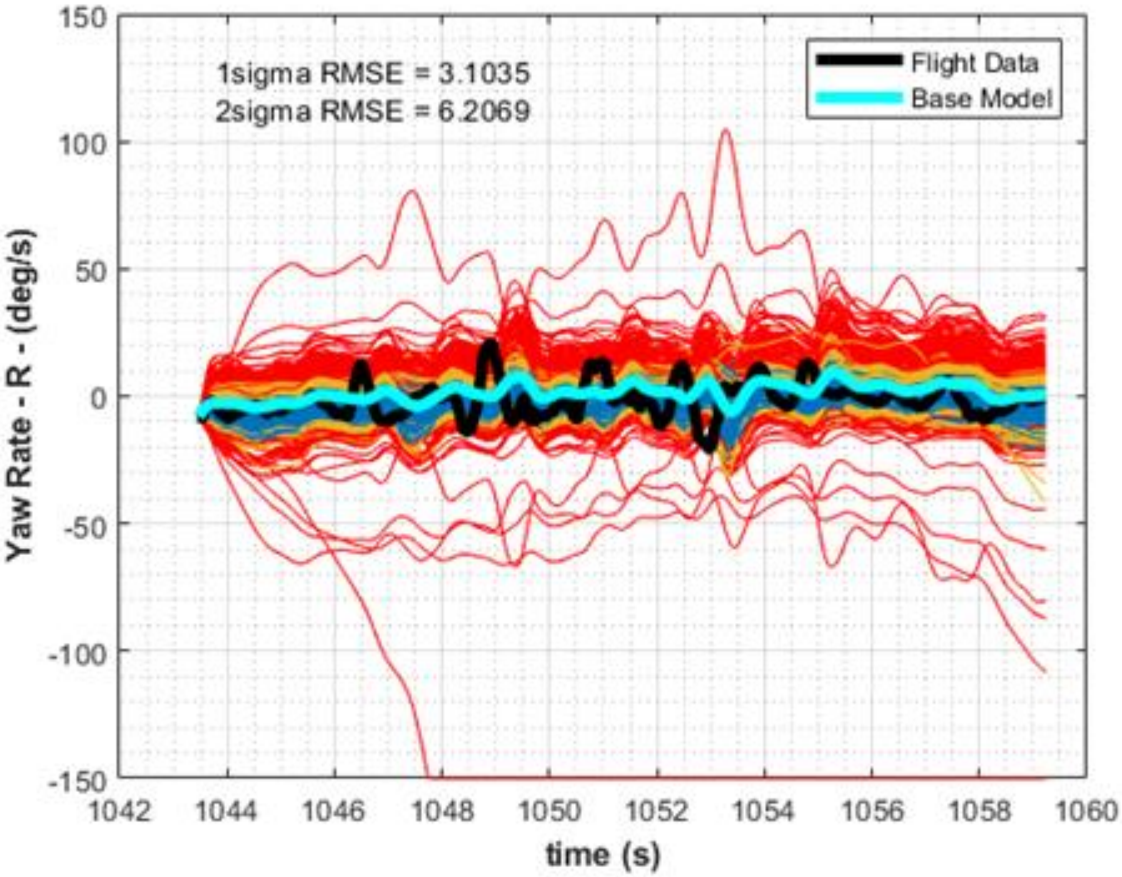

Figure 3-74. Comparing MC simulations to flight data for straight-line flight portion: yaw rate.

Analysis of the yaw rate (R) MC simulations indicates that:

- The base model was not properly capturing the trends in the flight data. The flight data showed changes in yaw rate that were not seen in the base model simulation in some sections. Additionally, in some sections (ex: 1052-1054, and 1048-1050), the base model showed an opposite trend compared to the flight data. That being said, despite not capturing the trends, the base model was not too far off in value from the flight data in many sections.
- The flight data was completely inside the region covered by the MC simulations. However, between 1052 and 1054 seconds, the flight data was located in a region where only a few simulations exist.

Overall:

- In this flight portion, the base model was mostly capturing the pitch rate flight data well. The roll rate and yaw rate were not captured as well as the pitch rate.
- The flight data rates were mostly inside the regions covered by the MC simulations.

3.3.4.3.3 Results from level turn segment

In this section, a flight portion in which the aircraft was performing a 90-degree change in heading level turn is analyzed. Recorded flight data is presented in Figure 3-75. MC simulation results for the rotation rates are presented in Figure 3-76. to Figure 3-78.

As seen in the flight data, the aircraft is performing a 90-degree change in heading at the South-West corner of the flight track. The airspeed remains around 45 ft/s and the altitude remains around 370 feet. The aircraft rolls to the left as it performs the turn and reaches a roll angle of around -22 degrees. The pitch angle of the aircraft remains around zero. An ANN controller is in command of the aircraft during this flight portion.

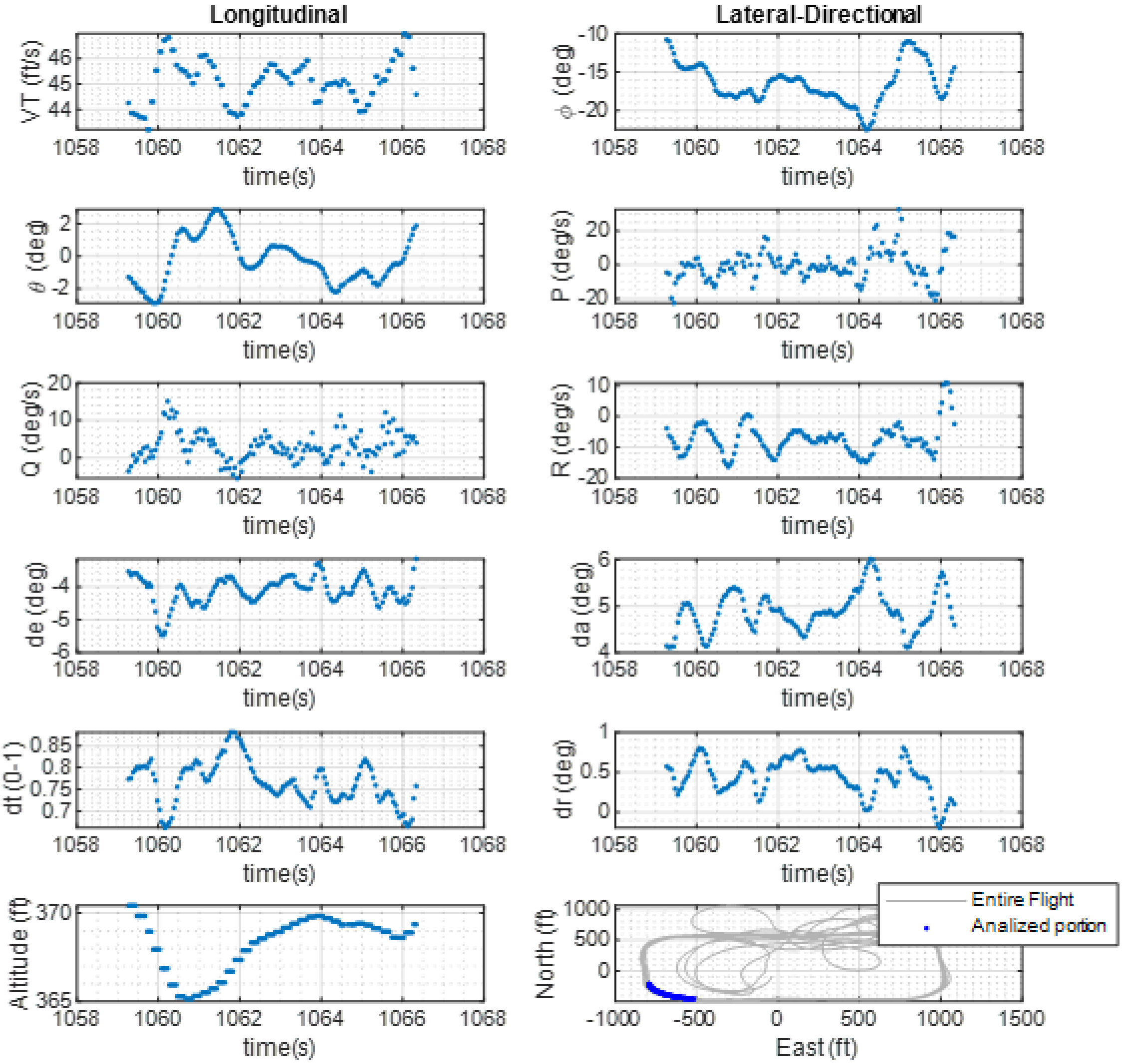

Figure 3-75. Flight data of level turn flight portion.

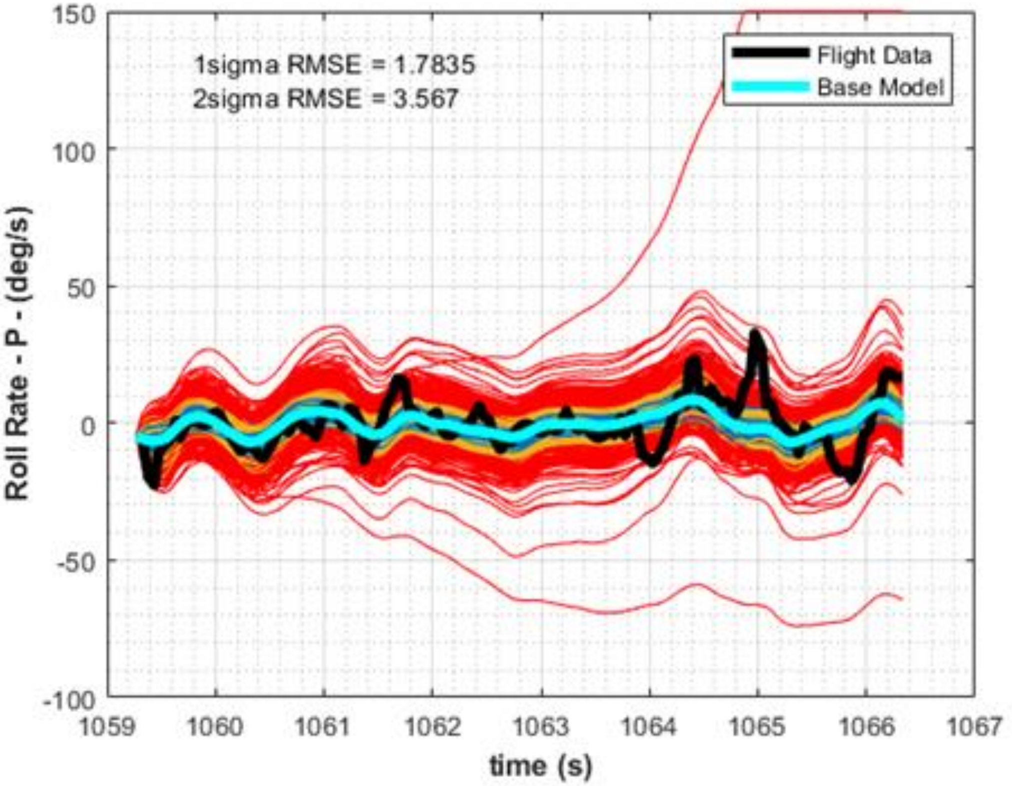

Figure 3-76. Comparing MC simulations to flight data for a level turn flight portion: roll rate.

Analysis of the roll rate (P) MC simulations indicates that:

- The base model is able to capture the trends in the flight data to some extent. However, there are errors in the magnitudes of change in the base model compared to the flight data. In some instances, these errors can be quite large (± ~30 degrees per second) as seen around the 1065 second mark.
- Throughout the flight portion, the flight data is mostly contained in the range spanned by the simulations.

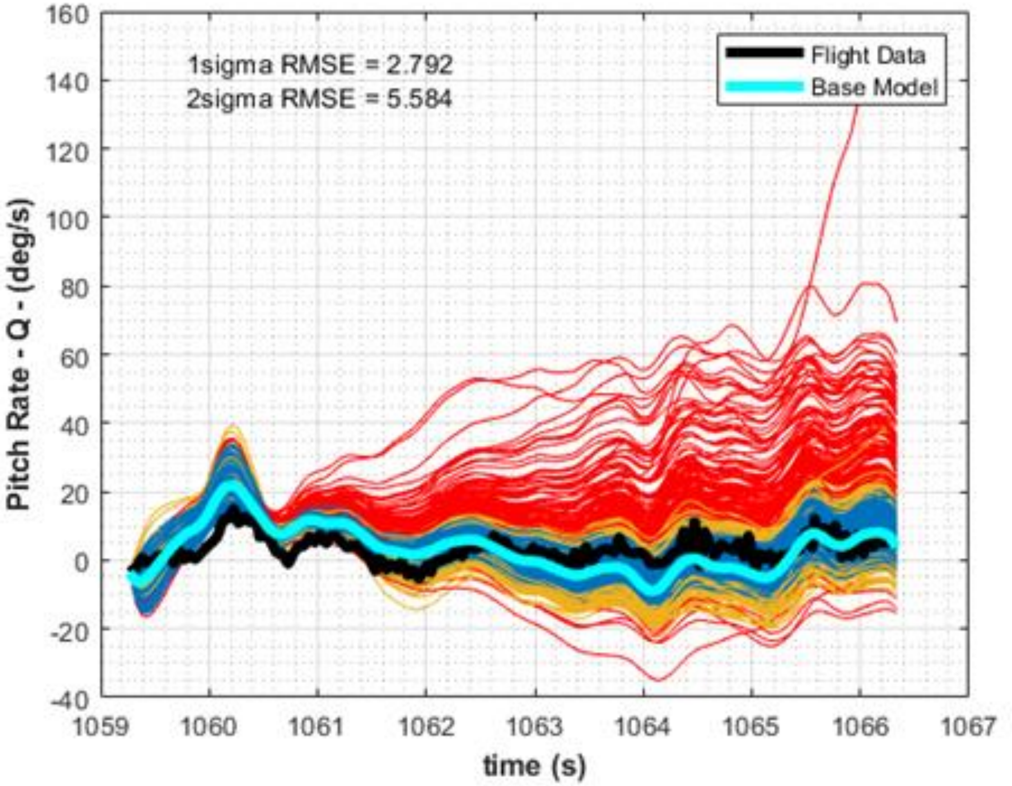

Figure 3-77. Comparing MC simulations to flight data for a level turn flight portion: pitch rate.

Analysis of the pitch rate (Q) MC simulations indicates that:

- The base model is able to capture the trends in the flight data for the majority of the flight portion. The errors between the base model simulation and the flight data are not too large during the flight portion.
- There is a portion at the beginning (around t = 1060 seconds) where the pitch rate modeled by all the MC simulations did not match the flight data.
- Other than the above-mentioned section of flight, the flight data was completely contained in the region spanned by the MC simulations. However, the region spanned by the MC simulation was pretty wide (ex: going from -20 to 60 deg/s towards the end of the flight portion).

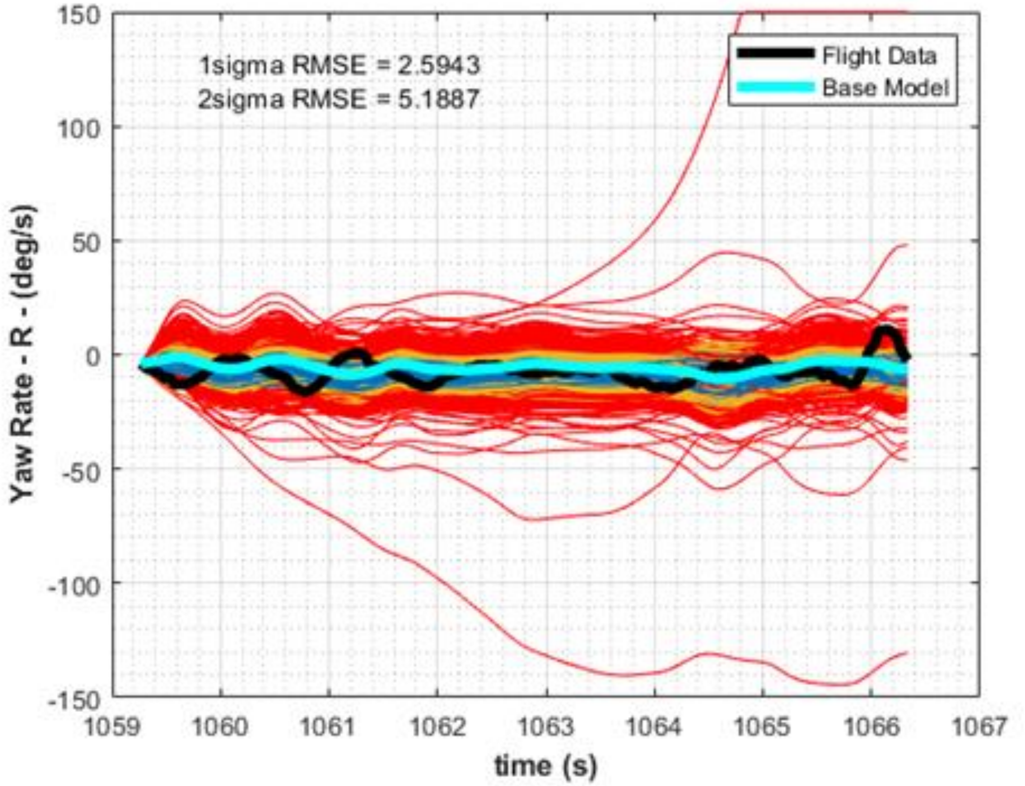

Figure 3-78. Comparing MC simulations to flight data for a level turn flight portion: yaw rate.

Analysis of the yaw rate (R) MC simulations indicates that:

- The base model was not too far from the flight data during this flight portion. However, this was not difficult since the flight data does not have large yaw rates in this portion. Any simulation that keeps the yaw rate changes small would not contain large errors in this flight portion.
- The flight data was completely inside the region covered by the MC simulations.

Overall:

- The base model was not too far from the flight data for the pitch rate and yaw rate in this flight portion. The base model was capturing the overall trends in roll rate, to some extent. However, there are errors between the magnitudes of the base model and the flight data which can be quite large in some sections.
- The flight data was mostly inside the regions covered by the MC simulations.

3.3.4.3.4 Analysis of an ascending flight segment

In this section a portion of flight in which the aircraft is ascending is analyzed. The flight data is presented in Figure 3-79. The MC simulations of the rotation rates are presented in Figure 3-80. to Figure 3-82.

This ascending flight portion is obtained from manual take-off. The aircraft took off from the ground and reached around 200 ft AGL. Airspeed was ranging between around 30 and 55 ft/s.

The pilot was performing a clockwise turn during this portion and the roll angle, ϕ, went to large values (~40 degrees). The aircraft pitch angle, θ, was also varying during the flight and ranged between 0 and 20 degrees. Moderate/ large rotation rates are present in this flight portion. This flight portion contains larger variation in the states when compared to a straight-line level flight portion.

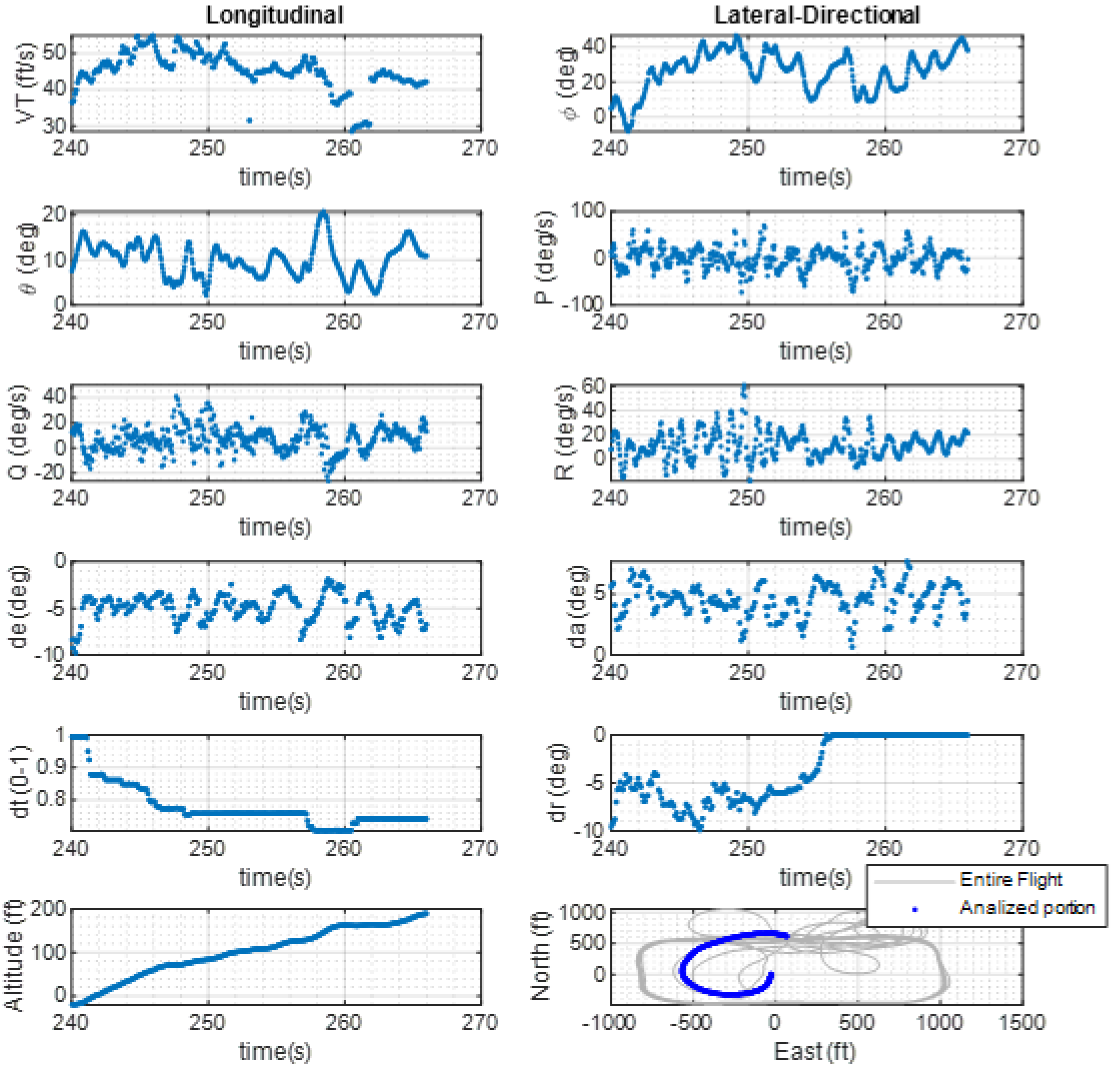

Figure 3-79. Flight data of ascending flight portion.

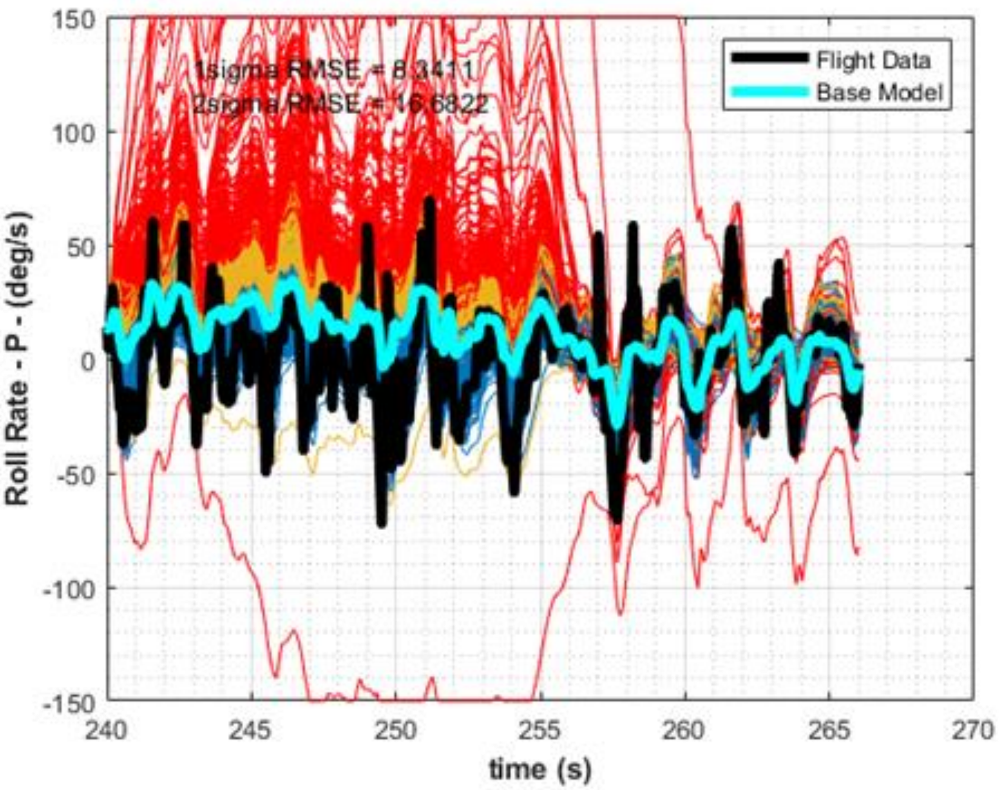

Figure 3-80. Comparing MC simulations to flight data for ascending flight: roll rate.

Analysis of the roll rate (P) MC simulations indicates that:

- The base model is mostly failing to capture the changes present in the flight data with the appropriate magnitudes. The base model appears to be "a moving average" of some sort of the flight data response. It can capture trends in the flight data but it cannot capture the response with the appropriate magnitudes.
- Despite taking parameter uncertainty into account and the very wide range of the MC simulation states, there are flight portions that are not captured by the majority of the MC simulations. E.g., around 250 sec. and 254 sec.
- The first 15 seconds of data had much larger ranges in the MC simulations than the last 10 seconds. This may be explained by the rudder deflection going to zero (and staying there) at around the 256 seconds mark.

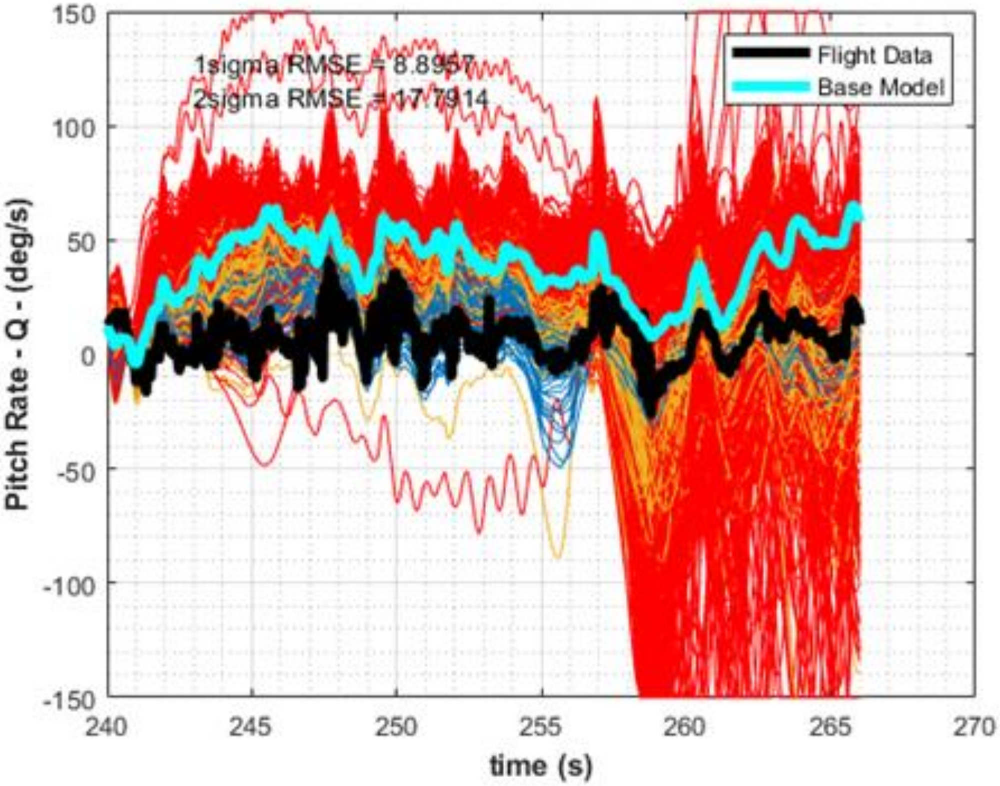

Figure 3-81. Comparing MC simulations to flight data for ascending flight: pitch rate.

Analysis of the pitch rate (Q) MC simulations indicates that:

- The base model is performing poorly in terms of simulating correct values. However, it is able to capture proper trends in the data. A large offset (i.e., modeling error) is present but proper trends are captured in the simulation. E.g., see following time ranges: 242-250, 253-262.
- Despite taking parameter uncertainty into account and the very wide range of the MC simulation states, the flight portion is not entirely captured inside the region covered by the majority of the MC simulations. E.g., see around 244 sec.
- The range covered by the MC simulations noticeably increased after the 257 second mark and it became extremely large.

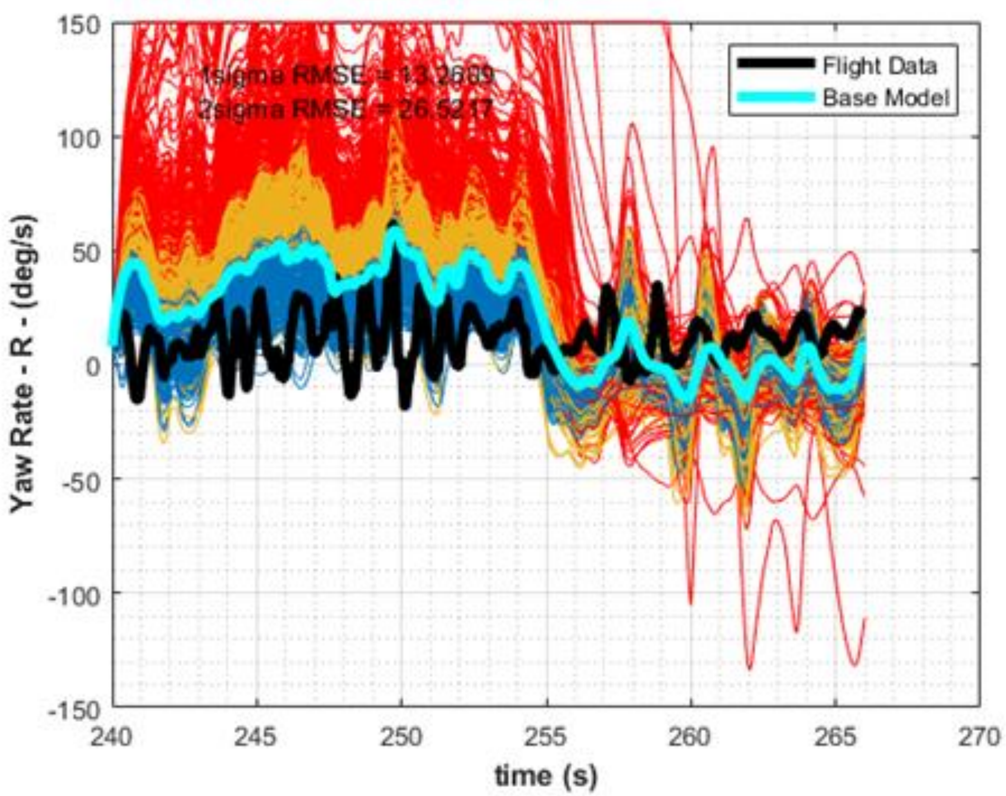

Figure 3-82. Comparing MC simulations to flight data for ascending flight: yaw rate.

Analysis of the yaw rate (R) MC simulations indicates that:

- The base model is not capturing the trends in flight data appropriately. For example, the base simulation is shifted above the flight data in the first 15 seconds. In the last 10 seconds, the simulation seems to be delayed compared to the flight data.
- The flight data is outside the region covered by the MC simulations in several locations.
- Similar to the roll rate, the first 15 seconds of data had much larger ranges in the MC simulations than the last 10 seconds. Again, this may be due to the rudder deflection going to zero in the last 10 seconds.

Overall:

- The base model did not capture the flight data appropriately. The roll rate showed correct trends, but the trends were not captured with correct magnitudes. The pitch rate also showed correct trends, but the simulation had a bias. (Results were shifted above the flight data in the first 15 seconds of simulation.) The yaw rate also has the bias error in the first 15 seconds. In the last 10 seconds, the simulated yaw rate seems to be delayed, when compared to the flight data.
- The roll rate had better results compared to the pitch and yaw rate in this portion.
- There are several portions where the flight data is not captured in the regions covered by the MC simulations.
- The MC simulations were spread over large values in this flight portion.

3.3.4.3.5 Analysis of a descending flight segment

In this section, a portion of flight in which the aircraft is descending is analyzed. The flight data is presented in Figure 3-83. The MC simulations of the rotation rates are presented in Figure 3-84. to Figure 3-86.

This descending flight portion is obtained from a manual landing. The pilot took the aircraft from an AGL altitude of around 200 ft down to zero ft. The airspeed varied in the range between about 25 and 50 ft/s. There is a large variation in aircraft pitch and roll angles (θ and ϕ) in this flight portion. The throttle setting (dt) ranged between 50 % and 0%, making this the only flight portion in this report section that goes to 0 % throttle.

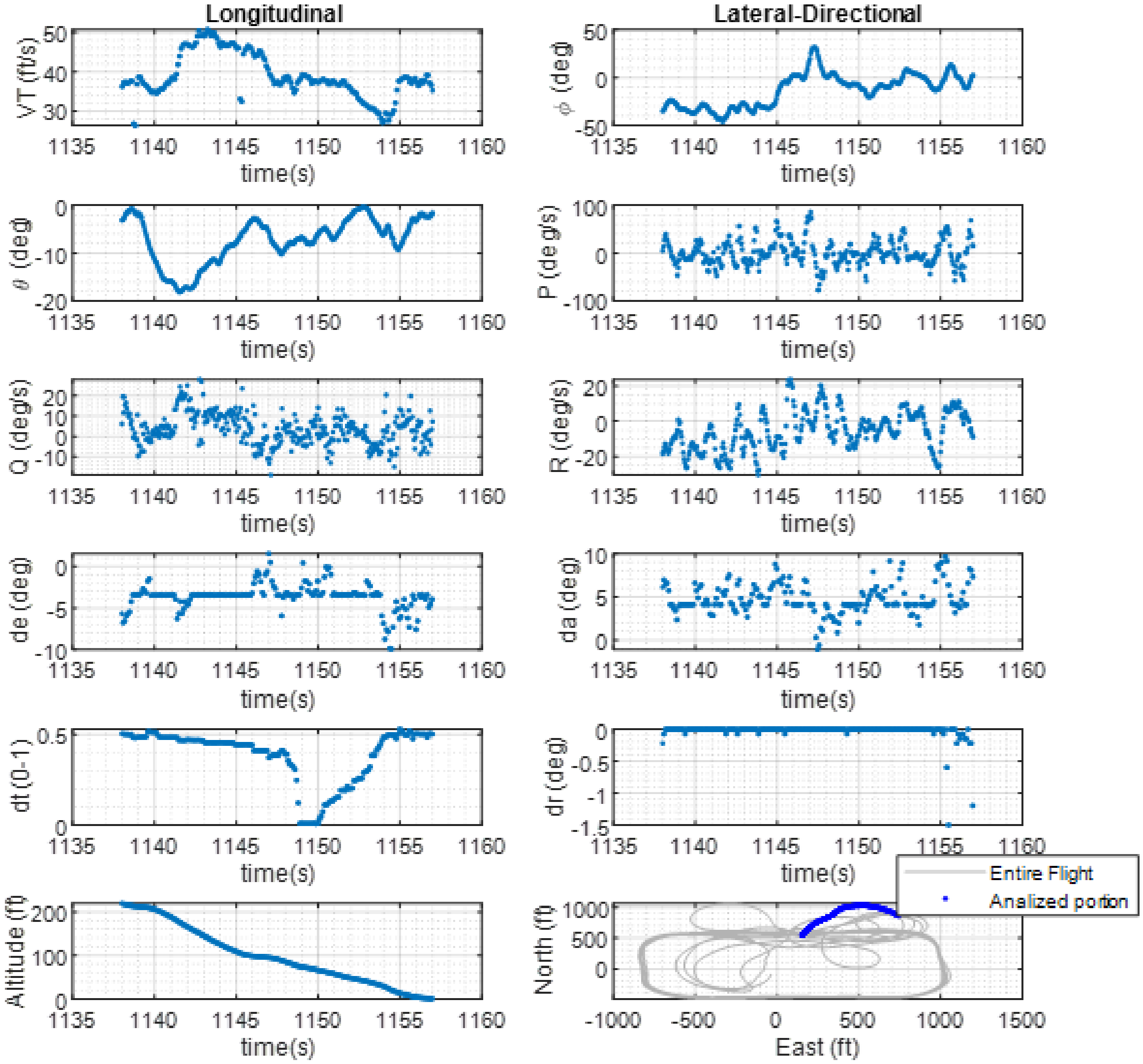

Figure 3-83. Flight data of descending flight portion.

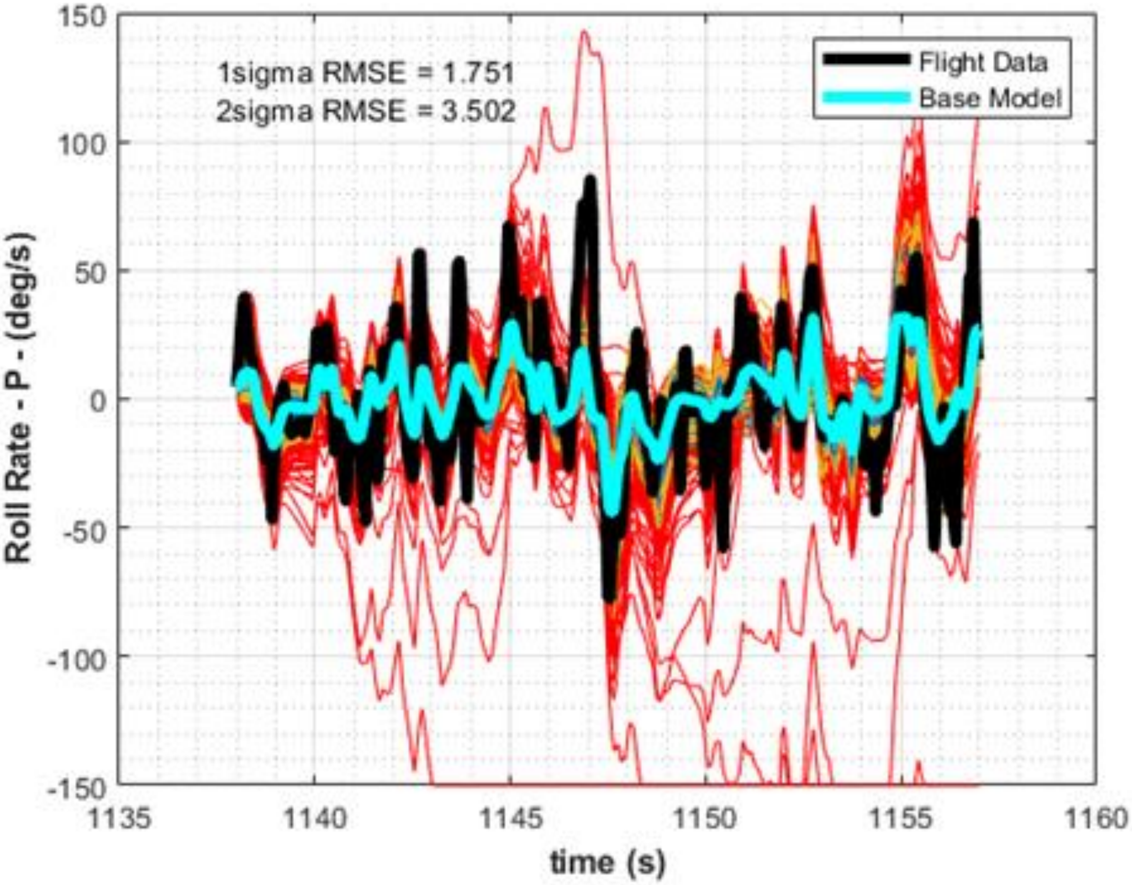

Figure 3-84. Comparing MC simulations to flight data for descending flight: roll rate.

Analysis of the roll rate (P) MC simulations indicates that:

- The base model is capturing trends present in the flight data correctly. However, the base model shows smaller magnitudes of changes compared to the flight data.
- The MC simulations are mostly capturing, or close to capturing, the flight data. However, in many cases, the flight data is at the edge, or even outside, the region covered by the MC simulations.

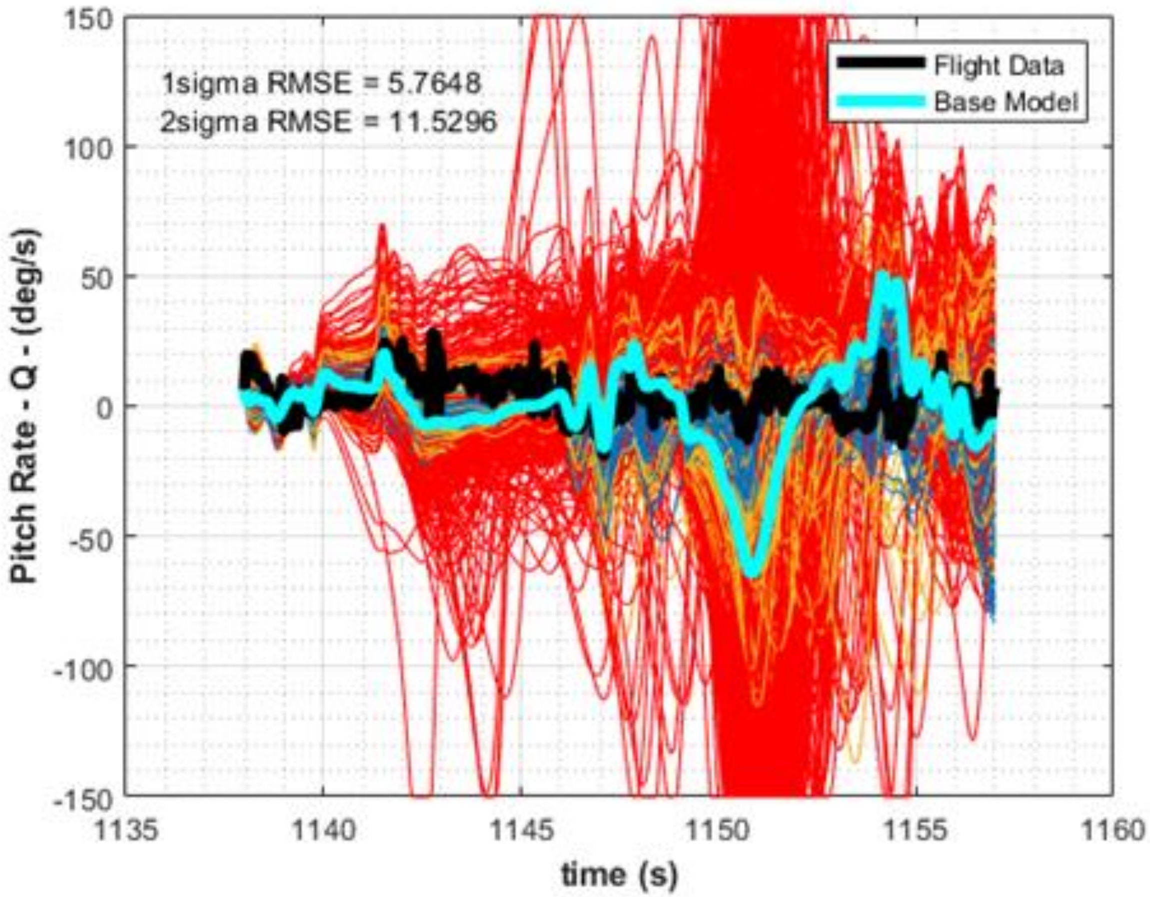

Figure 3-85. Comparing MC simulations to flight data for descending flight: pitch rate.

Analysis of the pitch rate (Q) MC simulations indicates that:

- The base model is performing poorly in this flight portion. It is failing to capture the correct trends and values in the flight data in several instances. For example, around the 1151 time mark, the model had large errors in capturing the flight data. Looking at the flight data, the poor modeling around the 1151 time stamp may be related to the low throttle setting around that time.
- The flight data is mostly captured in the regions covered by the MC simulations.
- The MC simulation predictions are extremely wide in the 1150 and 1153 time range. Again, this may be related to the low throttle setting in this time range.

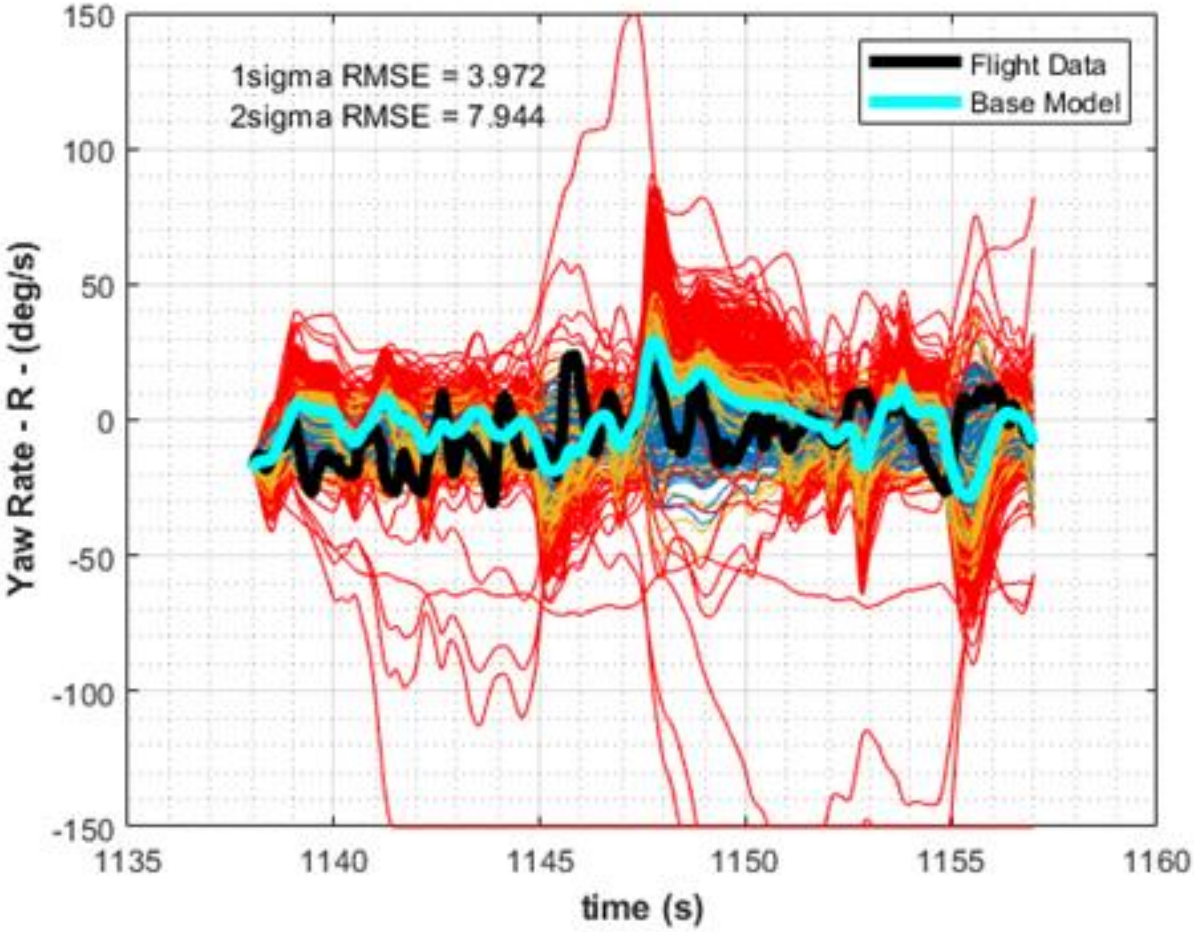

Figure 3-86. Comparing MC simulations to flight data for descending flight: yaw rate.

Analysis of the yaw rate (R) MC simulations indicates that:

- The base model is not capturing the variations in the flight data appropriately. In some cases, the base simulation seems to be delayed compared to the flight data. In other cases, the base simulation is showing dynamics that are different from the flight data.
- The flight data is mostly inside the region covered by the MC simulations. However, there are sections where the flight data is at the outskirts of the regions covered by the majority of the MC simulations. E.g., around the 1139, 1144, and 1146 time-marks.

Overall:

- In this flight portion, the base model was capturing the trends in the flight data for the roll rate. The pitch and yaw rate modeling did not capture the trends in the flight data properly.
- Most flight portions were captured in the regions covered by the MC simulations.

3.3.4.3.6 Results for an entry into loss of control segment

A flight portion in which the aircraft went into dangerous conditions and was entering Loss of Control (LoC) on a windy day is analyzed in this section. Flight data is presented in Figure 3-87. MC simulation results are presented for the angular rates in Figure 3-88. to Figure 3-90.

The aircraft was performing a turn at the South-West corner of the flight path. ANN was in command of the aircraft. The aircraft was flying at around 50 ft/s. The altitude of the aircraft varied between around 370 and 320 ft. At around 677 seconds, the aircraft started going into an undesirable behavior where the nose of the aircraft started pitching down as seen in the pitch angle (θ). As a result, the airspeed started increasing. At the same time, the aircraft was at a large negative roll angle (ϕ). The aircraft pitched down more than 50 degrees and rolled to the left more than 40 degrees. The pitch rate value became very high (larger than -60 deg/s). Flight conditions became dangerous, and the human pilot took control of the aircraft to bring it back to safety.

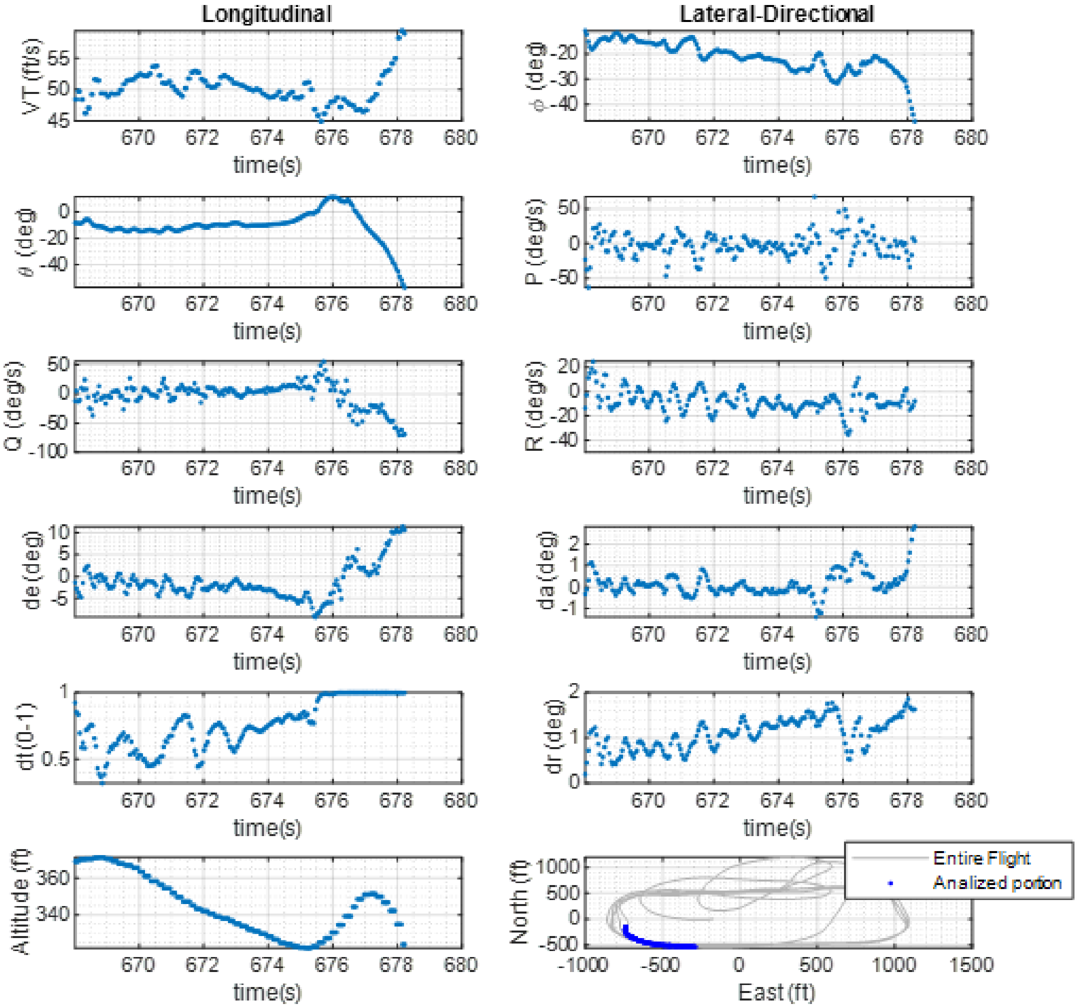

Figure 3-87. Flight data of flight portion entering Loss of Control (LoC).

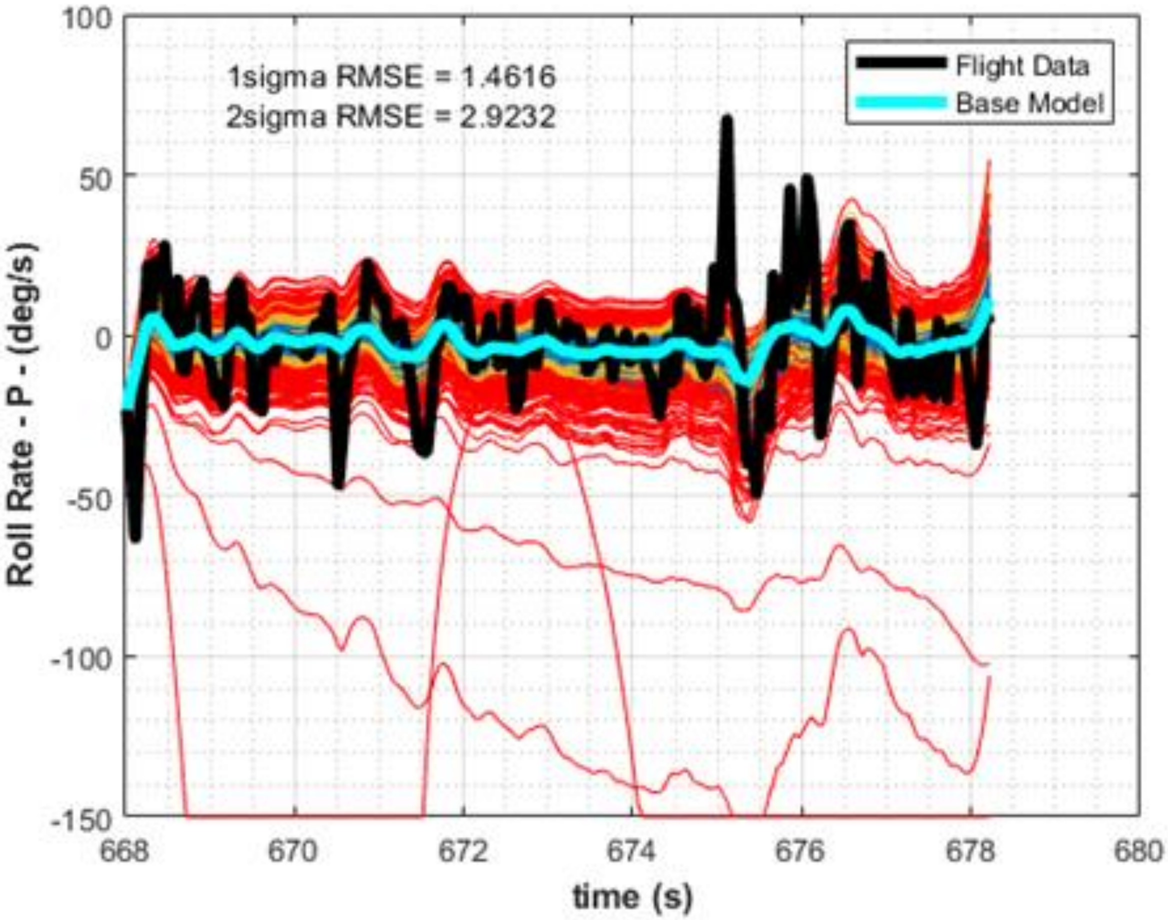

Figure 3-88. Comparing MC simulations to flight data for flight entering LoC: roll rate.

Analysis of the roll rate (P) MC simulations indicates that:

- The base model is failing to capture the changes present in the flight data with the appropriate magnitudes. The base model appears to be "a moving average" of some sort of the flight data response. It can capture a little bit of the trend in the flight data but it cannot capture the response with the appropriate magnitudes.
- Similar comments can be made about each of the MC simulations. These simulations are much smoother than the flight data.
- There are multiple flight sections that are not captured in the range of the MC simulation curves (ex: around 668 sec., 670.5 sec, 675 sec, and 676 sec).

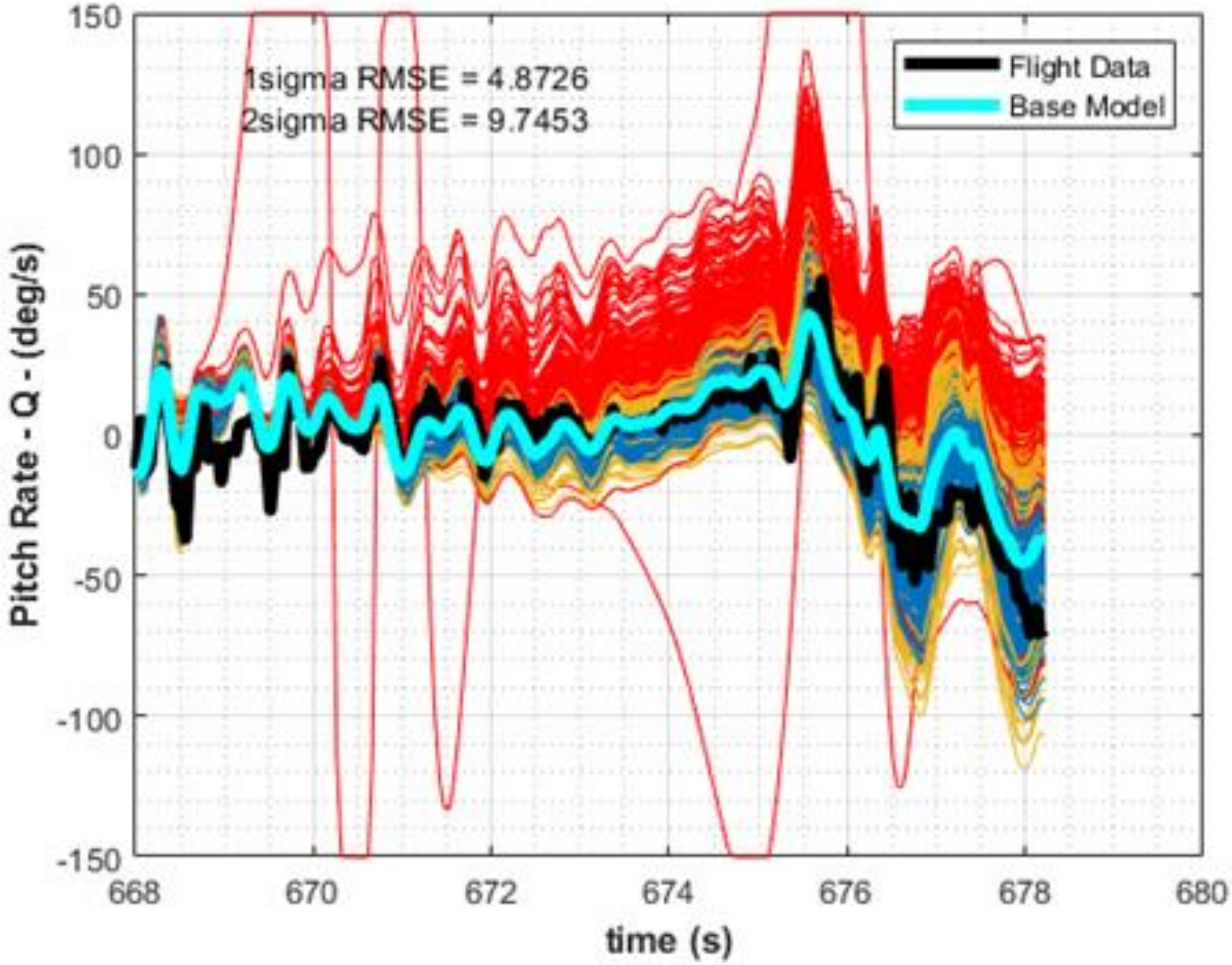

Figure 3-89. Comparing MC simulations to flight data for flight entering LoC: pitch rate.

Analysis of the pitch rate (Q) MC simulations indicates that:

- The base model is able to capture the trends in the flight data for the majority of the flight portion. The errors between the base model simulation and the flight data are not too large. However, towards the end when the aircraft was getting into undesirable behavior, a noticeable error between the base model and the flight data is observed.
- There is a portion at the beginning (around t = 669 to 670 seconds) where the pitch rate modeled by all the MC simulations did not match the flight data.
- Other than the above-mentioned section, the flight data was mostly contained in the region spanned by the MC simulations. However, the region spanned by the MC simulation was large (ex: going from -100 to 25 deg/s towards the end of the flight portion). It is trivial for flight data to be captured by such a wide range.

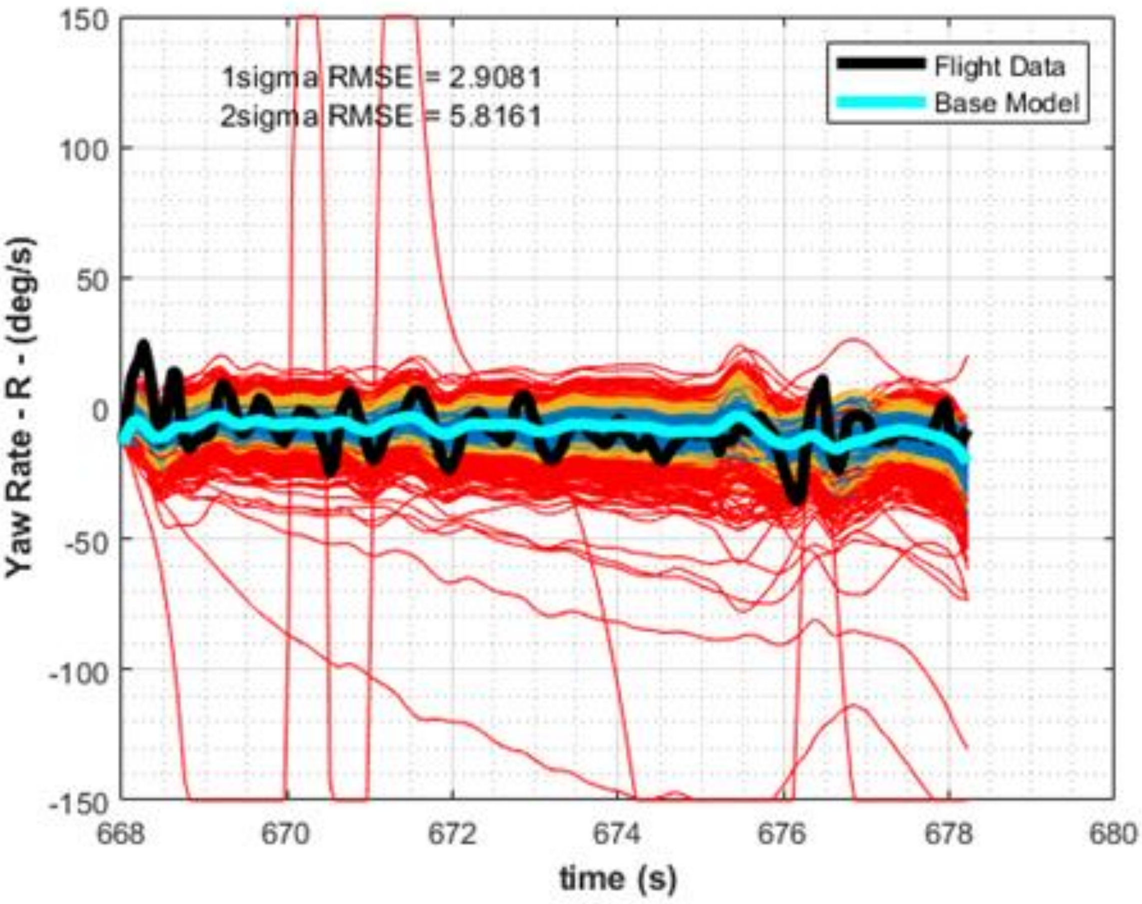

Figure 3-90. Comparing MC simulations to flight data for flight entering LoC: yaw rate.

Analysis of the yaw rate (R) MC simulations indicates that:

- The base model is not capturing the dynamics in the flight data with the appropriate magnitudes. Flight data has many peaks and troughs, but these features are not modeled by the base model. Again, like the roll rate simulation, the base model appears to be acting as some sort of "moving average" of the information in the flight data.
- The flight data is mostly inside the region of the MC simulations. However, during the initial second of simulation, the flight data was outside the MC simulation range. Also, around t = 676.5 seconds, the flight data was at the outskirt of the MC simulations region.

Overall:

- The base model simulation was close to the flight data only for the pitch rate. However, even pitch rate simulation was not close to the flight data towards the end of the flight portion (when the aircraft was getting into undesirable behavior). If simulation continued for a longer duration and the aircraft went into further undesirable behavior, the observed errors may have increased further.

- The base model did not capture the roll and yaw rates well. The base model simulation was much smoother compared to the flight data. The peaks and troughs in the flight data were not captured with the appropriate magnitudes. The roll and yaw rate simulations appeared to behave as a "moving average" of some sort of the information in the flight data.
- For all three rotation rates (P, Q and R), although most sections of the flight data are inside the MC simulations regions, there are sections of flight when the flight data was not captured. The MC simulations did not capture these sections of flight despite taking the defined parameters uncertainty into account.
- For the roll rate and yaw rate, again, despite taking the defined parameter uncertainty into account, the MC simulations did not capture the behavior in the flight data appropriately. The MC simulations appeared smoother (showed less variation) when compared to the flight data.

3.3.4.3.7 Results for a stall segment

In this section a portion of flight in which an attempt was made to stall the aircraft is analyzed. The flight data is presented in Figure 3-91. The MC simulations of the rotation rates are presented in Figure 3-92. to Figure 3-94.

An attempt to stall the aircraft is performed in this flight section. The flight portion starts with the aircraft flying at around 40 ft/s. Then, the autopilot is given a step command to reduce the airspeed to 20 ft/s. The command is given at around the 1108 seconds time stamp. The aircraft reduces its speed and its altitude is seen to decrease over time. Sudden changes in throttle command (dt), elevator deflection (de), and pitch rate (Q) are observed at this transition. For the first couple of seconds after the reduced airspeed command is sent (1108 to 1110), the aircraft pitch angle is seen to increase as the airspeed decreases. At around the 1125 second mark, the human pilot takes control of the aircraft and increases the throttle command abruptly. Airspeed increases to about 50 ft/s then goes to 40 ft/s.

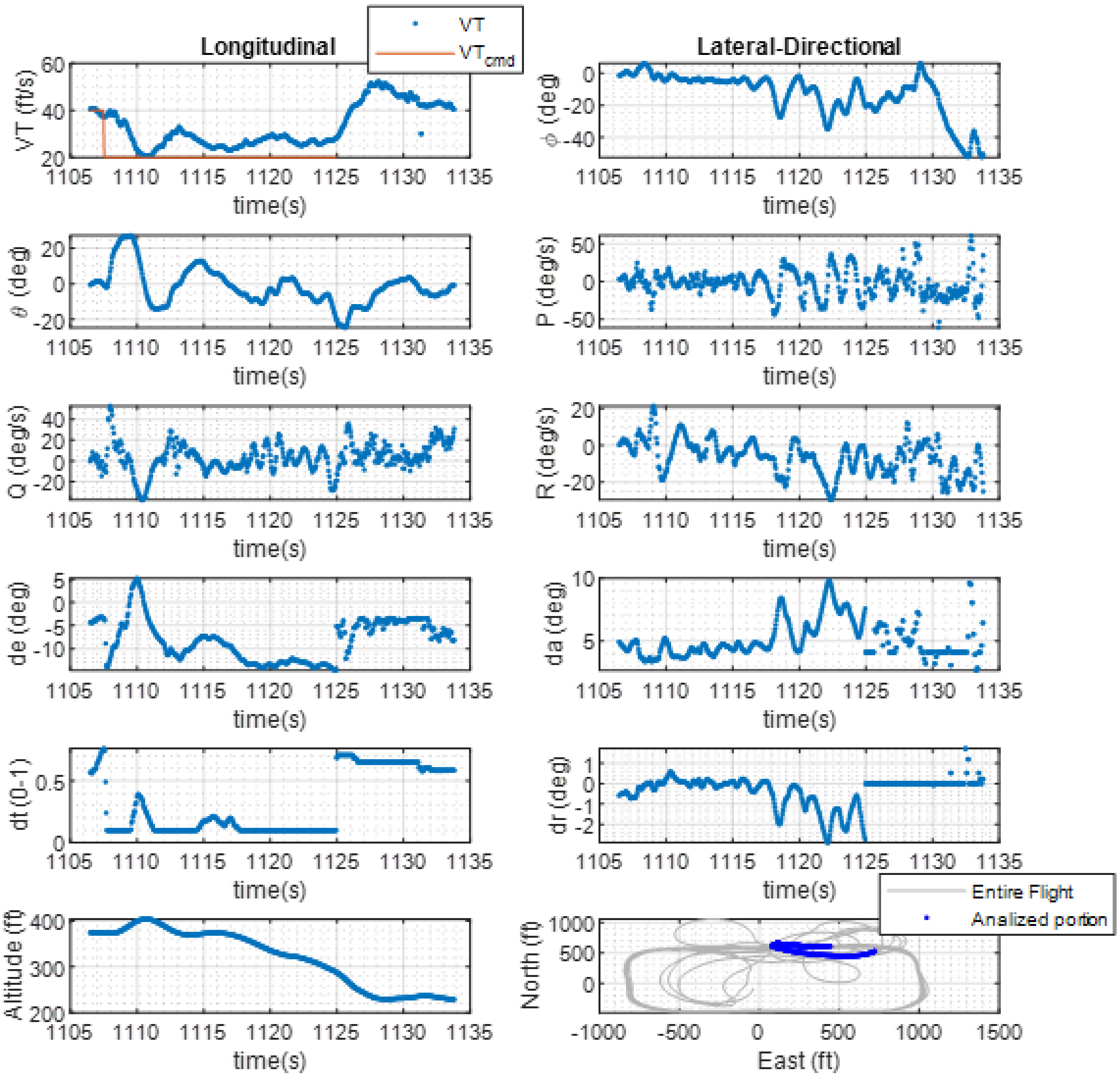

Figure 3-91. Flight data of attempted stall flight portion.

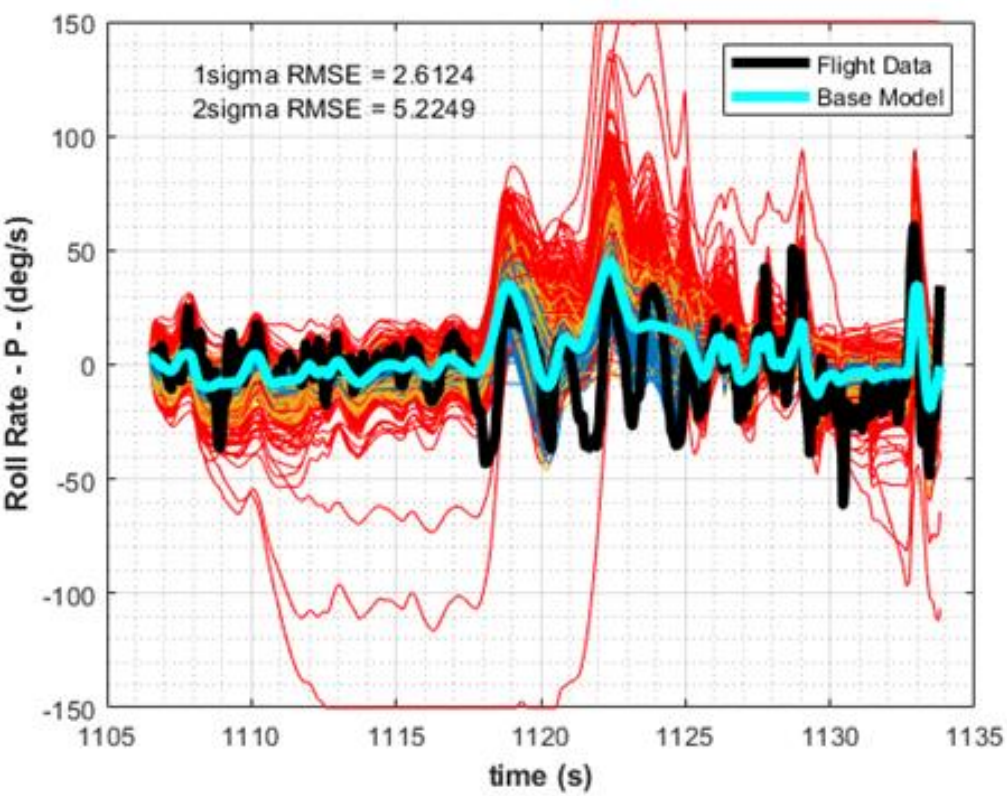

Figure 3-92. Comparing MC simulations to flight data for attempted stall: roll rate.

Analysis of the roll rate (P) MC simulations indicates that:

- The base model is capturing trends present in the flight data. However, the base model shows smaller magnitudes of changes than the flight data.
- The MC simulations are capturing the flight data. However, between 1117 and 1125, there are portions that are not captured by the MC simulations or are barely inside the MC simulations region.

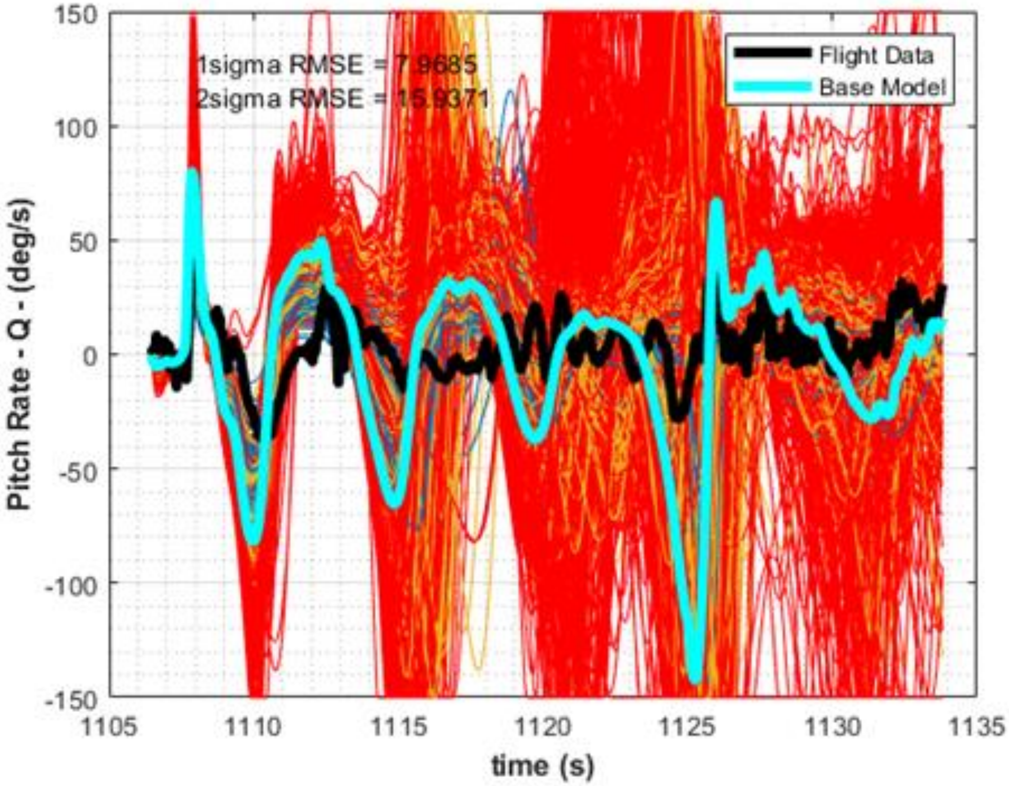

Figure 3-93. Comparing MC simulations to flight data for attempted stall: pitch rate.

Analysis of the pitch rate (Q) MC simulations indicates that:

- The base model is not capturing the flight data properly. In some sections, the model is showing similar trends to the flight data, but the magnitudes are exaggerated (ex: 1106 – 1113). In other sections, the modeled trends are not similar to the flight data (ex: around the 1120 and 1129 time-marks.)
- The region covered by the MC simulations is extremely wide in several flight sections. That makes it trivial for the flight data to be captured in these sections. Accounting for the defined parameter uncertainty in this flight portion results in widely different simulation results.
- Similar to other analyzed flight portions, there are sections in which the flight data is not captured by the MC simulations. (E.g. around 1109 and 1112 seconds).

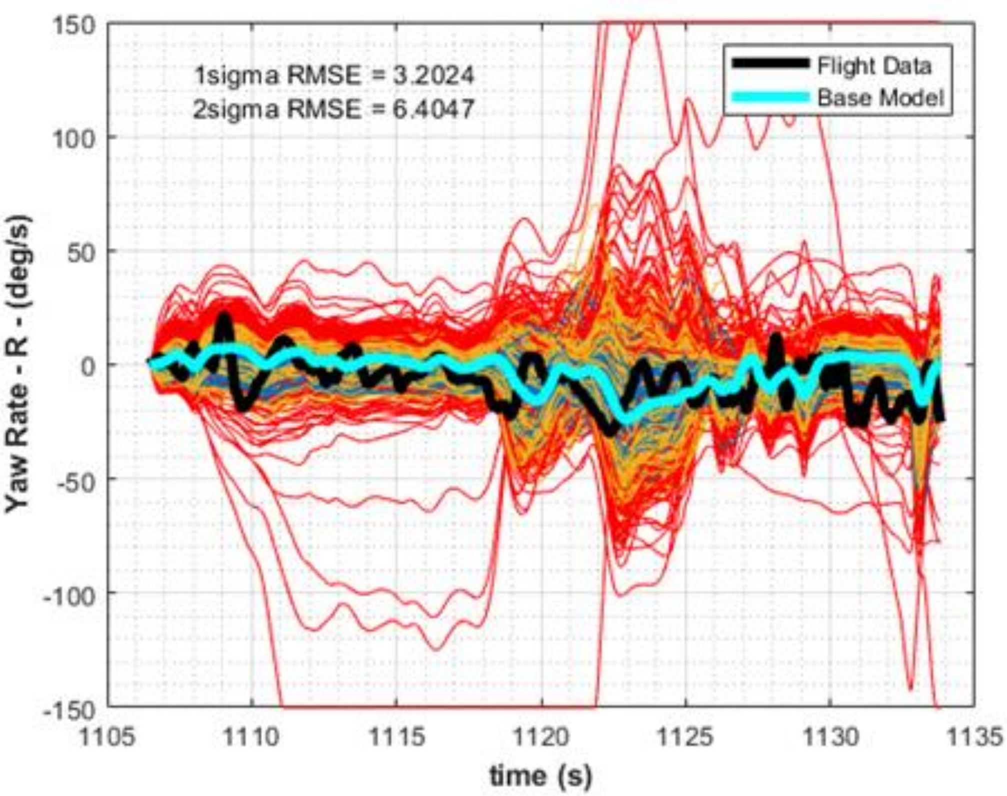

Figure 3-94. Comparing MC simulations to flight data for attempted stall: yaw rate.

Analysis of the yaw rate (R) MC simulations indicates that:

- The base model is not capturing the variations in flight data appropriately. The base model does not deviate too far from flight data. However, it is showing smoother trends when compared to the flight data and in some cases appears to show incorrect trends or delayed trends when compared to the flight data.
- The flight data is mostly inside the region covered by the MC simulations.

Overall:

- The base model is not capturing the flight data properly. In some cases, the correct trends are captured but they are over- or under- estimated. In other cases, the trends are not captured properly.
- The flight data is mostly captured in the regions covered by the MC simulations. However, despite taking the defined parameter uncertainty into account, there are sections of flight that are not captured by the MC simulations.

3.3.4.4 Conclusions for model uncertainty analysis

For ease of comparison between the identified flight portions, key takeaways are tabulated in Table 3-29. to Table 3-34:

Table 3-29. Straight-line cruise.

	Flight Data vs. Base Model Simulation	Flight data vs. MC simulation	Extreme deviations	Relevant Figure #
P	Model captures trends to some extent, does not capture peaks.	Simulation contained most flight.	1050-1052 s	75.00
Q	Model mostly captures trends.	Flight beginning not contained by simulation.	1044-1046 s	76.0
R	Model not properly capturing trends, sometimes reverses trends.	Simulation contains most flight, barely contains some peaks.	1052-1054 s	77.0

Table 3-30. Level turn.

	Flight Data vs. Base Model Simulation	Flight data vs. MC simulation	Extreme deviations	Relevant Figure #
P	Model captures some trends, does not capture peaks.	Simulation contains all flight. Peaks sometimes reach ends of range.	1065 s	79.0
Q	Model mostly captures trends. Small errors between magnitudes.	Simulation does not contain beginning, range is wider than roll rate.	1060 s	80.0
R	Model captures most of flight. Flight data has no major changes in yaw rate.	Flight data completely contained in simulation.	N/A	81.0

Table 3-31. Ascending flight.

	Flight Data vs. Base Model Simulation	Flight data vs. MC simulation	Extreme deviations	Relevant Figure #
P	Model mostly fails to capture changes, captures some trends.	Simulation contains most of flight, range is much narrower near the end.	240-255 s	83.0
Q	Model mostly fails to capture changes, captures trends.	Simulation contains most flight data although range is largely offset.	242-250 s, 253-262 s	84.0

R	Model does not accurately capture flight.	Simulation misses some flight portions, has wide range near start.	240-255 s	85.00

Table 3-32. Descending flight.

	Flight Data vs. Base Model Simulation	Flight data vs. MC simulation	Extreme deviations	Relevant Figure #
P	Model captures trends, does not capture peaks.	Simulation contains most flight. Peaks sometimes reach ends of range.	1143-1144 s, 1146 s	87.0
Q	Model fails to capture trends and values in several sections.	Flight contained within simulation range, range is large due to throttle.	1151 s	88.0
R	Model does not capture trends or peaks.	Flight mostly contained within simulation range.	1139 s, 1144 s, 1146 s	89.0

Table 3-33. Entry into Loss of Control.

	Flight Data vs. Base Model Simulation	Flight data vs. MC simulation	Extreme deviations	Relevant Figure #
P	Model fails to capture changes and most of trends.	Simulations does not contain peaks of data, range is smoother than flight.	668 s, 670.5 s, 675 s, 676 s	91.0
Q	Model captures most trends and peaks. Error increases dramatically during LoC.	Beginning of flight not contained within range. Size of range makes containment trivial.	669-670 s	92.0
R	Model does not capture trends or peaks.	Simulation did not contain beginning, but contained most of flight.	669 s, 676.5 s	93.0

Table 3-34. Stall.

	Flight Data vs. Base Model Simulation	Flight data vs. MC simulation	Extreme deviations	Relevant Figure #
P	Model mostly captures trends but not peaks.	Simulation contains most flight data.	1117-1125 s	95.00

Q	Model does not capture magnitudes, captures some trends.	Beginning of flight not contained within range. Size of range makes containment trivial.	1106-1113 s, 1120 s, 1129 s	96.0
R	Model does not capture trends, error is small.	Simulation contains most of flight data.	N/A	97.0

Based on the previous analysis, the following conclusions are made regarding the base model:

Analysis of the presented flight portions shows that the base simulation model could capture the flight data rotation rates to some extent. However, there are errors in the simulation that are large in some sections. The base simulation was better at modeling the roll and pitch rates than modeling the yaw rate. The roll rate modeling was capturing the trends in the flight data for all the analyzed flight portions. However, these trends were not captured with the proper magnitude. The simulated roll rates had smaller magnitudes than the flight data. The simulated pitch rate was close to the flight data in three of the flight portions (straight line cruise flight, level turn, and the portion entering into LoC). Large modeling errors were present in the other three flight portions. The simulated yaw rate did not capture the trends in the flight data well.

Based on the previous analysis, the following conclusions are made regarding the MC simulations:

The majority of the analyzed flight data was captured inside the regions covered by the Monte Carlo simulations. However, there are sections in each of the analyzed flight portions where the flight data was outside or at the outskirts of the MC simulation ranges. Despite taking the defined parameter uncertainty into account, these sections of flight were not captured by the simulations. Additionally, the trends seen in the MC simulations were smoother than actual flight data trends in some cases. This indicates that, despite taking parameter uncertainty into account, simulations did not model the variations in flight data with the appropriate magnitudes.

3.3.4.5 Bottom line for uncertainty analysis

There are limitations in the simulations used to model flight. More complex and higher fidelity modeling approaches are necessary to overcome these limitations. However, the most important take-away is that performing actual flight tests are necessary to update simulation models. If the various aerodynamic coefficients, including stability derivatives, are not identified through flight test, the expectation is that the simulation will likely deviate significantly from actual flight. Further, uncertainty analysis is helpful to investigate which phenomena are not adequately modeled, for example, nonlinearities and the effects of external disturbances such as ambient turbulence.

3.4 Correlation-based LoC metrics

Identifying the conditions leading to UAS loss of control is a key goal of this project. Although heuristic metrics, e.g., control authority limitations and exceedance of stall angle of attack make sense, Sliding Window Correlation of aircraft states may prove to be a better indication of approach to loss of control.

SWC analysis was first proposed in [55] as a means of capturing hidden relationships, lost through traditional correlation methods; for many nonlinear dynamical systems (in this case, aircraft), these hidden relationships can only be seen once certain specific conditions are met (e.g., during unsteady flight). Where traditional correlation analysis methods provide a single measure of relation between complete datasets, SWC finds the localized correlation coefficients within a window around each timestep. SWCs are excellent at discovering and tracking connections that can change over time; most used in neuroimaging, SWCs evaluate dynamic functional connectivity: the phenomenon by which brain activity can change over time while performing the same action [56-58]. Parallels can be drawn to aircraft behavior and performances, which can differ wildly during an unstable flight envelope compared to stable linear flight. Using SWC will help determine how the same control surface inputs can result in completely different and sometimes unexpected outputs within this unstable flight envelope. While neuroimaging uses SWC to find changes in input to make the same output, the reverse can be done for aircraft to track how the same inputs can produce different outputs in unstable flight.

3.4.1 Methodology

The correlation between two datasets is defined as the statistical relationship between them, with no preference to causality, i.e., the strength in their relation has no influence on their statistical interdependence. However, impartiality to causality does not necessarily dictate absence of causality. Differentiating correlation strengths is a common method of comparing the same systems in different environments to determine the effects of the environment on the system, in this case, the effects of unstable flight on dynamic state relationships. SWC can be thought of as an increase in precision of correlation coefficient from global set comparisons of differing environments to local set comparisons of the same dynamic environment.

The global relationship strength between two sets of N measurements is defined as r, where $r: \mathbb{R}^{2N} \rightarrow \mathbb{R} \in [-1,1]$; $|r|$ defines the relationship strength, while the sign of r defines the type of relationship. Conventionally, $|r| \approx 0.5$ is a fuzzy limit that determines whether the relationship is strong ($|r| > 0.5$) or weak ($|r| < 0.5$). SWC defines a local correlation coefficient, r_n, within a time-variant set of correlation coefficients, R, where $R = \{r_1, \dots, r_n, \dots, r_N\}: \mathbb{R}^{2N} \rightarrow \mathbb{R}^N \in [-1,1]$, following the same definitions as the global r coefficient declared above, as shown in Figure 3-95.. The local range for each r_n is defined by a window of size Z for all N timesteps, as shown in Figure 3-96. While there persist many methods to evaluate the correlation between datasets, Pearson’s r coefficient is the chosen method for this work.

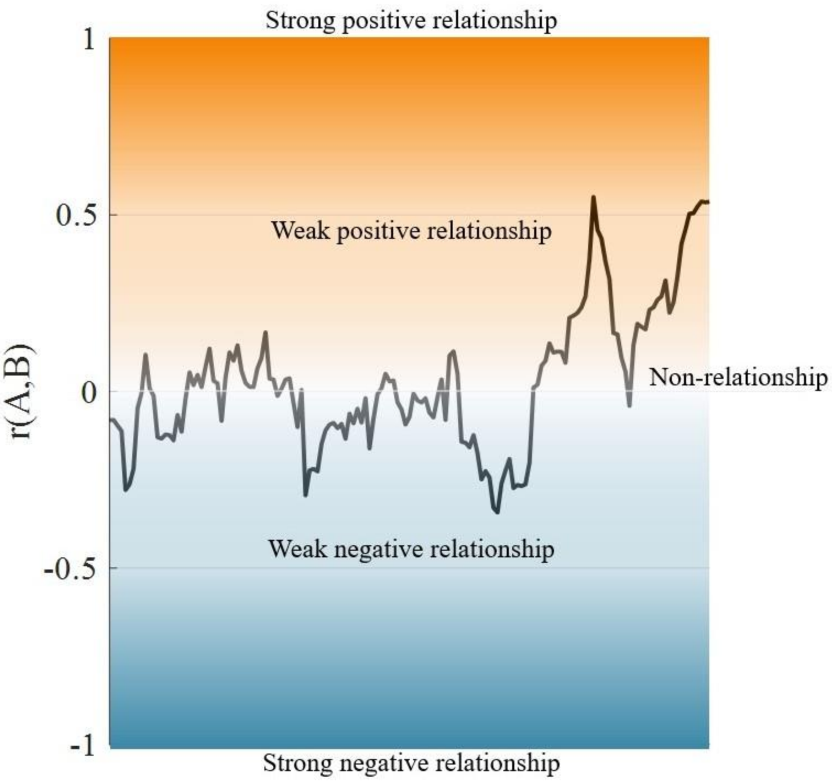

Figure 3-95. Interpretation of relationships strength via correlation coefficient.

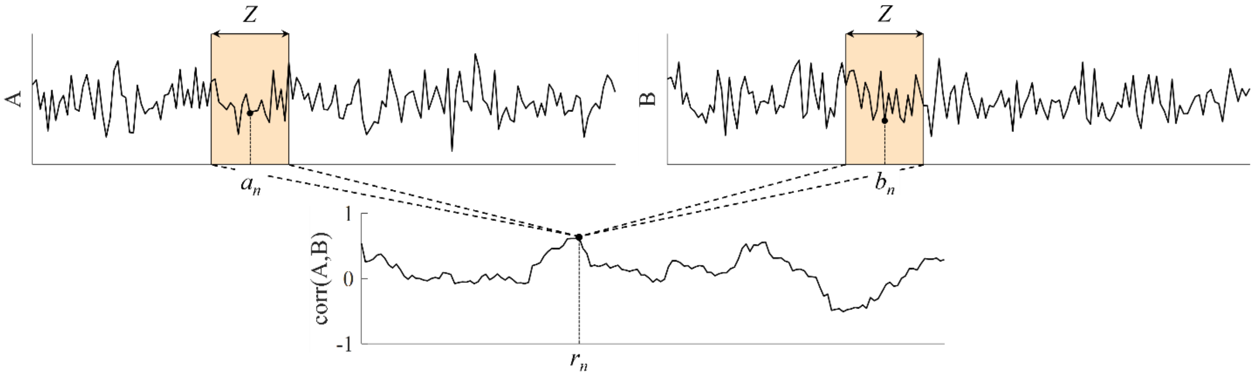

Figure 3-96. Visualization of a local correlation coefficient.

The dynamics of aircraft are historically known to be nonlinear, especially so in unstable flight. However, the Hartman-Grobman theorem dictates that linear analysis methods hold within a local neighborhood; therefore, Pearson's linear correlation coefficient can be applied locally. Pearson's r, correlation between two sets, A and B, is defined as the ratio between the covariance of the two sets, σ_{AB}, and the product of the standard deviation of each set, $\sigma_A\sigma_B$. For a discrete sample space of N data points, $A = \{a_1, \dots, a_n\}$ and $B = \{b_1, \dots, b_n\}$, Pearson's r can be calculated as follows:

$$(A, B) = \frac{\sum_{i=1}^{N}(a_i - \bar{a})\left(b_i - \bar{b}\right)}{\sqrt{\sum_{i=1}^{N}(a_i - \bar{a})}\sqrt{\sum_{i=1}^{N}\left(b_i - \bar{b}\right)}}$$

Where $\bar{a}$ and $\bar{b}$ is the unweighted sample mean of each set:

$$\bar{a} = \frac{1}{N}\sum_{i=1}^{N} a_i$$

Reducing the scale of Pearson's r into a local range of Z datapoints centered around the n^{th} measurement results in the following:

$$r_n(A,B) = \frac{\sum_{n-\frac{z}{2}}^{n+\frac{z}{2}}(a_i - \bar{a}_n)\left(b_i - \bar{b}_n\right)}{\sqrt{\sum_{n-\frac{z}{2}}^{n+\frac{z}{2}}(a_i - \bar{a}_n)}\sqrt{\sum_{n-\frac{z}{2}}^{n+\frac{z}{2}}\left(b_i - \bar{b}_n\right)}}$$

$$\bar{a}_n = \frac{1}{Z}\sum_{n-\frac{z}{2}}^{n+\frac{z}{2}} a_i$$

3.4.2 Correlation behaviors

Breakdown of the linearized, mathematical flight model leads to localized, temporary, hidden relationships that can serve as the prerequisite indicators of unstable flight and loss of control. Two types of correlation behaviors are seen when an aircraft transitions from linear-stable flight to unstable-nonlinear flight:

1. Breakdown of strong relationships:

$$|r_{stable}| > 0.5 \rightarrow |r_{unstable}| < 0.5$$

2. Strengthening of non-relationships:

$$|r_{stable}| < 0.5 \rightarrow |r_{unstable}| > 0.5$$

Strong relationships are typically formed between dynamic states within the same reference frames, with the strongest being the relationship between an aircraft's control surface and subsequent states known to be linked and justified in a linear mathematical dynamic model. Pearson's correlation coefficients are henceforth denoted by "r" followed by the correlated states paired in parenthesis

- Aileron v. Roll Rate, $r(\delta_a, P)$
- Elevator v. Pitch Rate, $r(\delta_e, Q)$
- Rudder v. Yaw Rate, $r(\delta_r, R)$
- Aileron v. Sideslip Angle, $r(\delta_a, \beta)$
- Elevator v. Angle of Attack, $r(\delta_e, \alpha)$
- Rudder v. Sideslip Angle, $r(\delta_r, \beta)$
- Etc.

Alternatively, weak relationships are formed by states that cross the longitudinal and lateral-directional reference frames or have minimal reference in the linear mathematical model, such as:

- Aileron v. Yaw Rate, $r(\delta_a, R)$
- Rudder v. Roll Rate, $r(\delta_r, P)$
- Aileron v. Angle of Attack, $r(\delta_a, \alpha)$
- Elevator v. Sideslip Angle, $r(\delta_e, \beta)$
- Etc.

In both cases, SWC is looking for the point when a linearized, mathematical model fails as an indication of when an aircraft has entered an unstable flight regime.

Specific to strong relationship breakdown is transition into an adverse control region, a major prerequisite to loss of control, which is defined as the portion of flight where the type of relationship changes into the other type, or in other words:

$$\operatorname{sgn}(r_{stable}) = \left({}^{+}/_{-}\right) \rightarrow \operatorname{sgn}(r_{unstable}) = \left({}^{-}/_{+}\right)$$

This adverse region is named such as traditional understanding of aircraft dynamic coupling is not only weakened, but instead a reversed behavior is observed between previously understood relationships, such as pitching downwards from upwards elevator deflection, rolling left from right aileron up deflection, etc. At this moment it should be restated that correlation analysis is blind to causality between data sets, therefore, the adverse region is not a portion of flight where control surfaces operate inversely to convention, but instead, the region of flight where external disturbances are great enough that said disturbances have greater influence over the aircraft than the control surfaces do, namely during wake vortex encounters and highly turbulent flight. A graphical representation of both correlation behaviors is presented in Figure 3-97. and Figure 3-98.

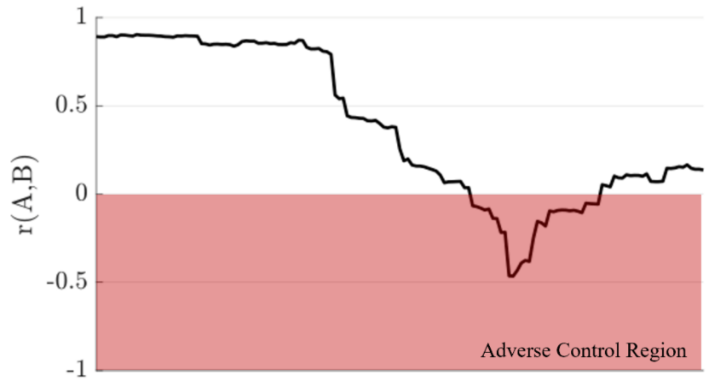

Figure 3-97. Breakdown of a strong relationship into the temporary adverse control region.

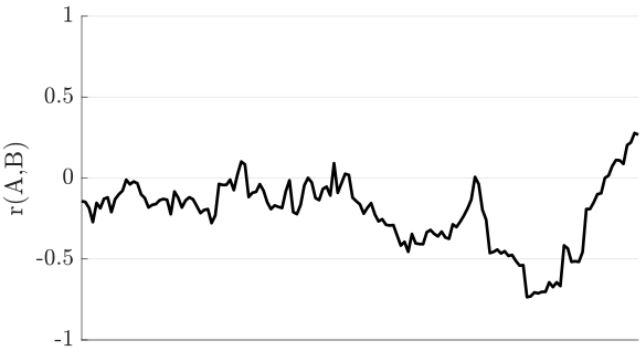

Figure 3-98. Strengthening of a weak relationship.

3.4.3 Correlation-based loss of control prediction from flight test data

To demonstrate the use of Sliding Window Correlation to identify loss of control, the results compiled early in the project are discussed first. That is, flights of the SkyHunter with intentional stall events and flights of the AeroScout over simulated wake vortex encounters with an early fan configuration will be discussed first. The early fan configuration had the fans placed in-line and with one fitted with a ramp and another with paddles, in both cases to deflect the fan outputs upward. Then, more recent results with the SkyHunter flights in autonomous mode over simulated wake vortex encounters are discussed. For these flights, the fans were both fitted with ramps and set in a side-by-side configuration to maximize the possibility of the UAS flying over the fan discharge.

3.4.3.1 Flight tests with intentional stall events and preliminary flights over wind machines

Due to the sheer volume of datasets acquired from this work, it is infeasible to present them all, therefore, this report will focus on comparing three types of trends seen:

1. Stable flight
2. Unstable flight
3. Loss of Control

The stable flight will serve as a baseline for the types of correlations one can expect from these systems, while the unstable flight will focus on how these correlations change when external disturbances affect the system: for the SkyHunter it will be autonomously recovered stalls, and for the Aeroscout, the recoverable engagements. Finally, loss of control datasets will focus on the effect of the correlation trend entering the adverse control region and having multiple relationships change significantly: for the SkyHunter it will be human-intervention recovery, and for the Aeroscout, the fully unrecoverable disturbances. Flight trajectories for these portions are shown in Figure 3-99 through Figure Figure 3-101.

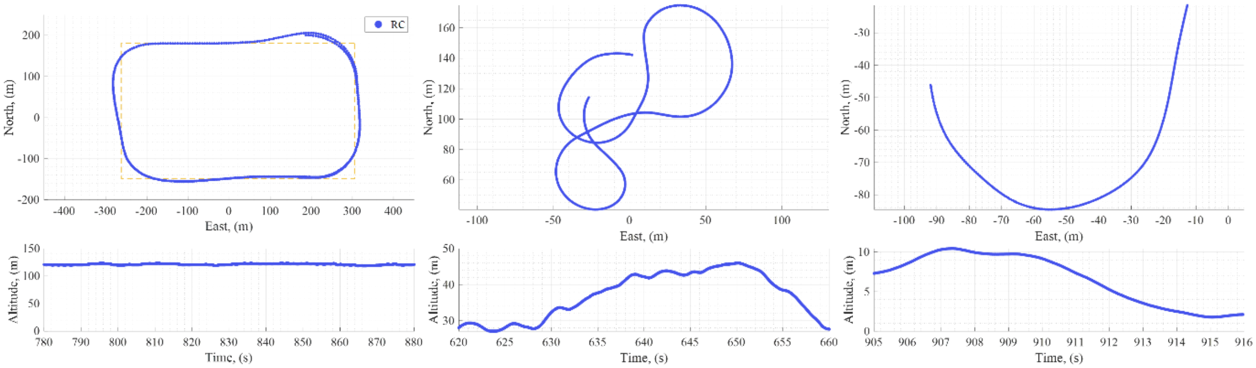

Figure 3-99. Stable flight trajectory of SkyHunter (left), manual Aeroscout (middle), autonomous Aeroscout (right).

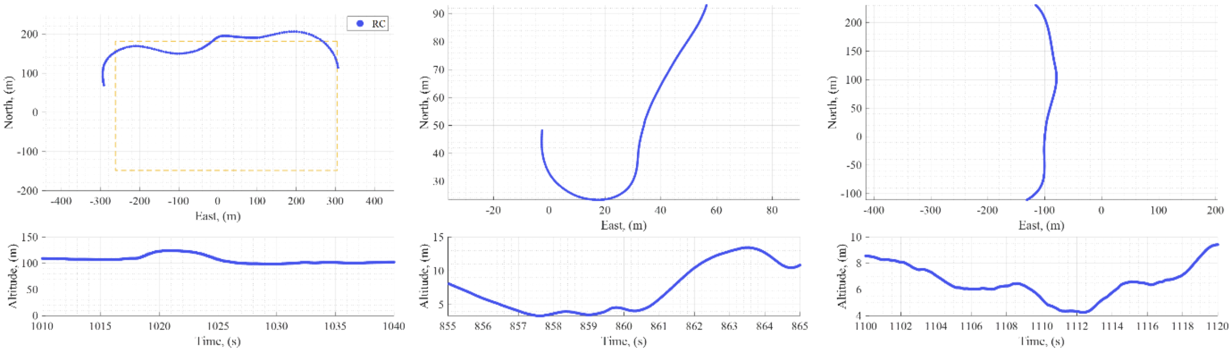

Figure 3-100. Unstable flight trajectory of SkyHunter (left), manual Aeroscout (middle), autonomous Aeroscout (right).

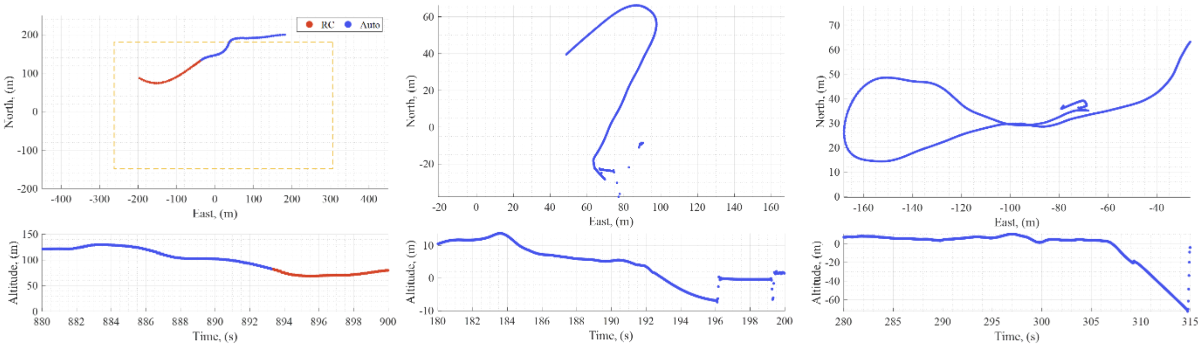

Figure 3-101. LoC flight trajectory of SkyHunter (left), manual Aeroscout (middle), autonomous Aeroscout (right).

3.4.3.1.1 Stable flight

The stable flight offers a baseline for the type of behaviors one can expect during linear, stable flight. To remove variability in the SWC trend, a lateral maneuver is included in the datasets. The strong relationships in Figure 3-102. through Figure Figure 3-105 show strong correlations in linear flight, as expected. In some portions the relationship weakens, but never more than one at a time. In order of strongest to weakest, the identified relationships are as follows:

- Q v Elevator – strong negative
- P v. Aileron – strong positive
- Elevator v. α – strong negative
- R v. Rudder - strong negative
- Aileron v. β – strong positive
- Rudder v. β – strong positive

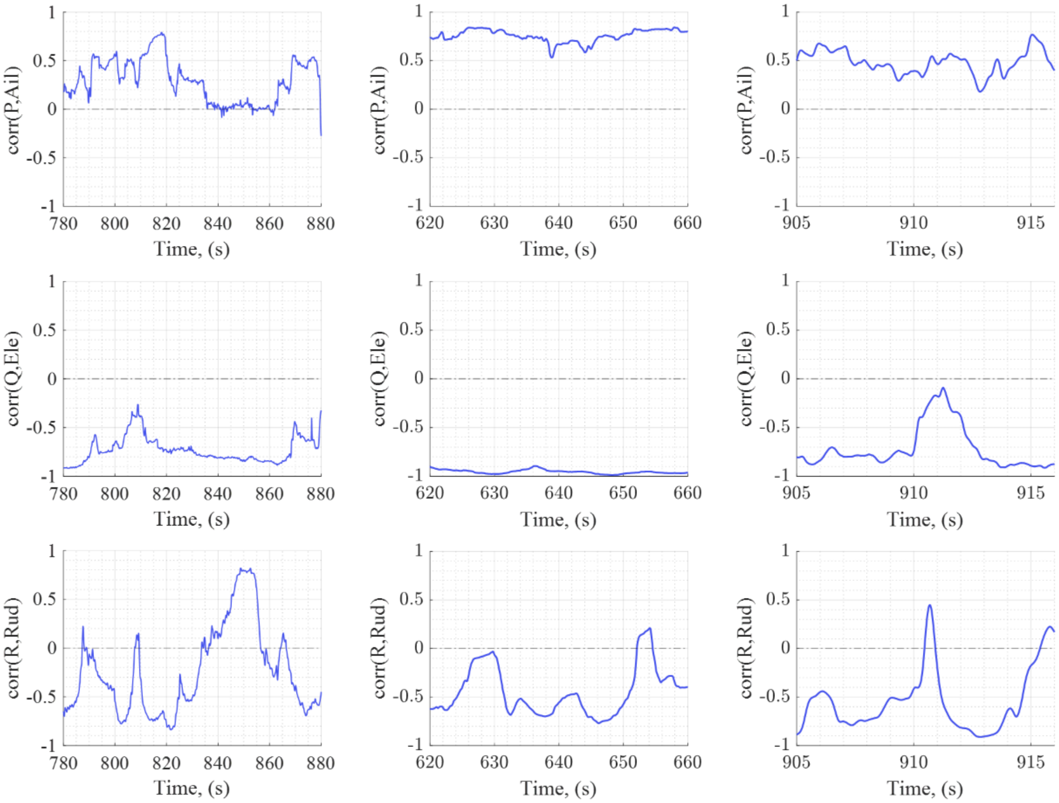

Figure 3-102. Stable flight strong angular relationships {SkyHunter (left), manual Aeroscout (middle), autonomous Aeroscout (right)}.

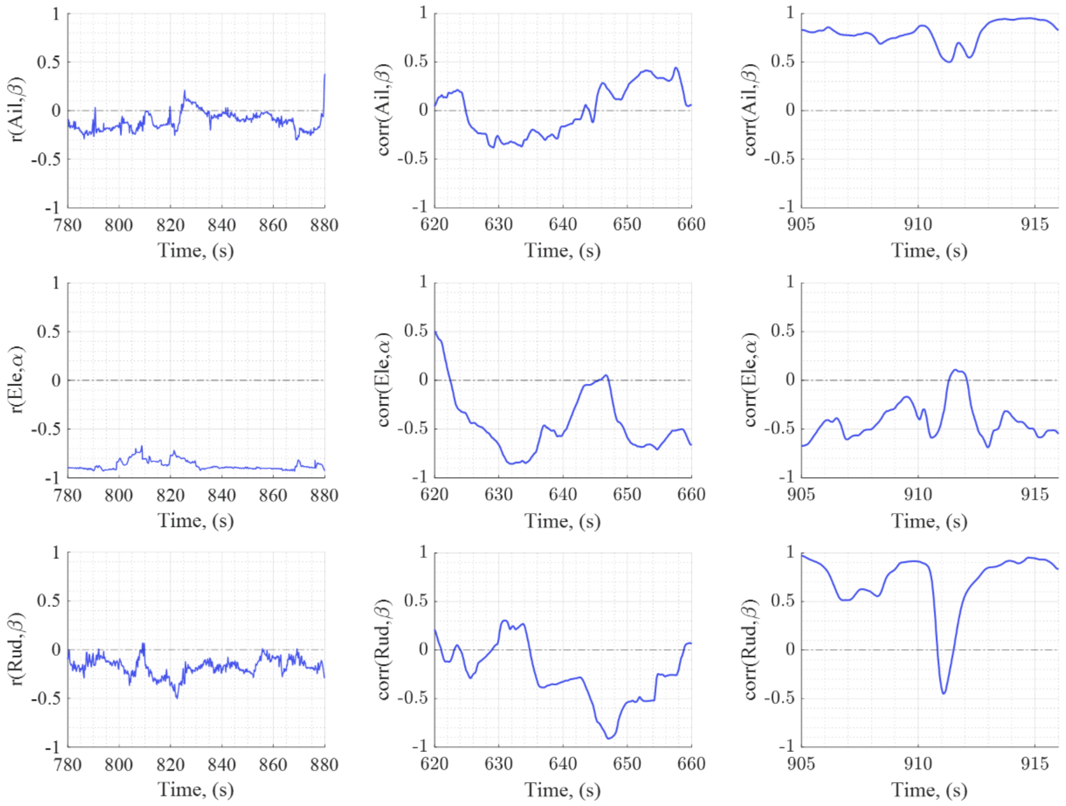

Figure 3-103. Stable flight strong airflow relationships {SkyHunter (left), manual Aeroscout (middle), autonomous Aeroscout (right)}.

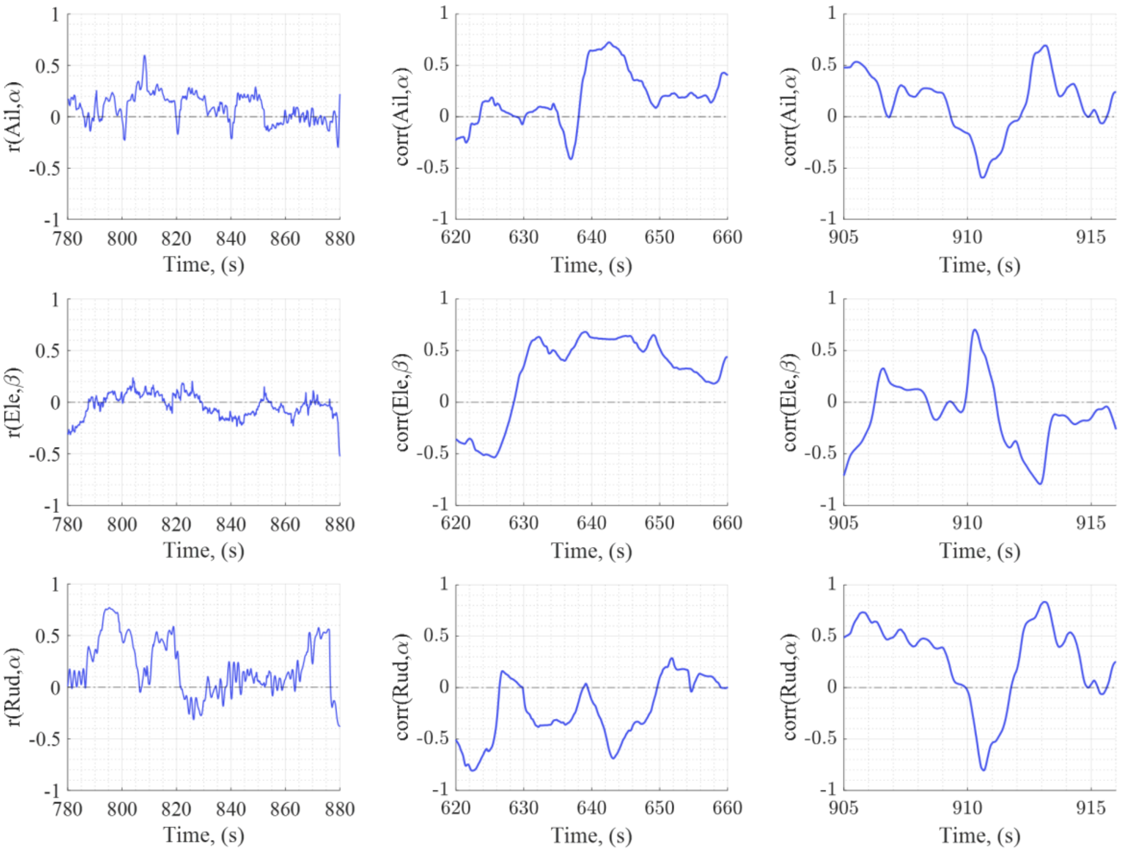

Figure 3-104. Stable flight weak airflow relationships {SkyHunter (left), manual Aeroscout (middle), autonomous Aeroscout (right)}.

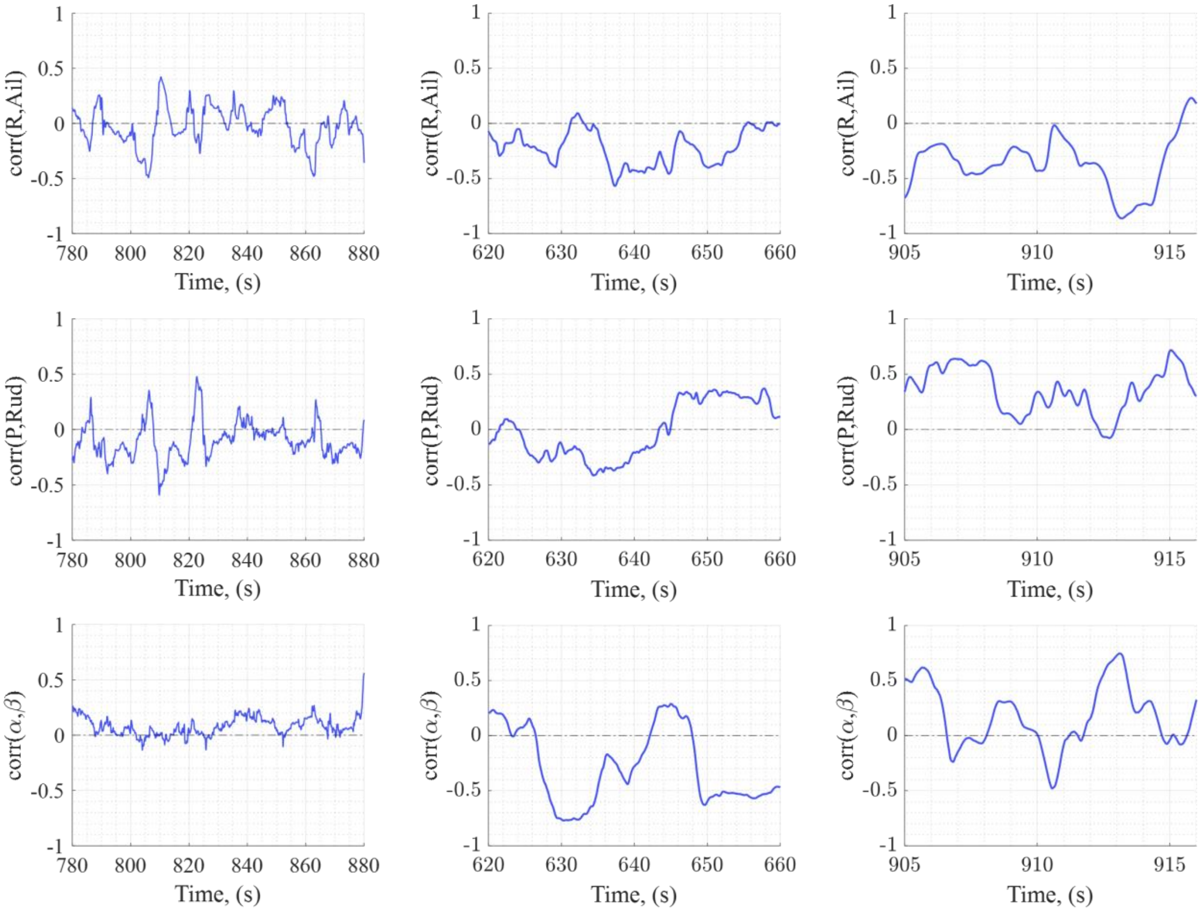

Figure 3-105. Stable flight weak angular relationships {SkyHunter (left), manual Aeroscout (middle), autonomous Aeroscout (right)}.

3.4.3.1.2 Unstable flight

As the aircraft undergoes external disturbances, temporary changes in correlation are seen in the period of unstable flight, (i.e., $t = 1020s,\ t = 858s,\ t = 1112s$ for the SkyHunter, Manual, and Auto flights). Figure 3-106. through Figure Figure 3-109 show periods of a weakened relationship, but also portions where an adverse relationship is formed from conventionally strong relationships, while Figure 3-108. and Figure Figure 3-109. show the weak relationships increase in strength during the disturbance with no preference to sign.

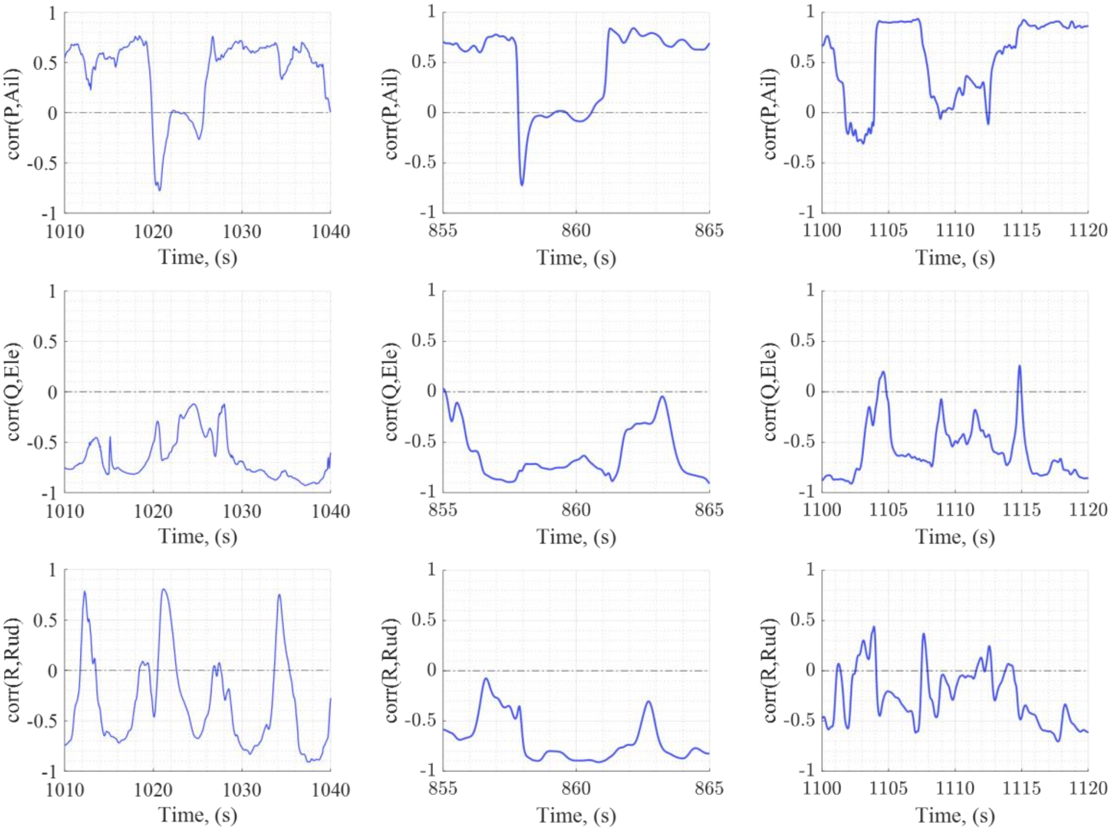

Figure 3-106. Unstable flight strong angular relationships {SkyHunter (left), manual Aeroscout (middle), autonomous Aeroscout (right)}.

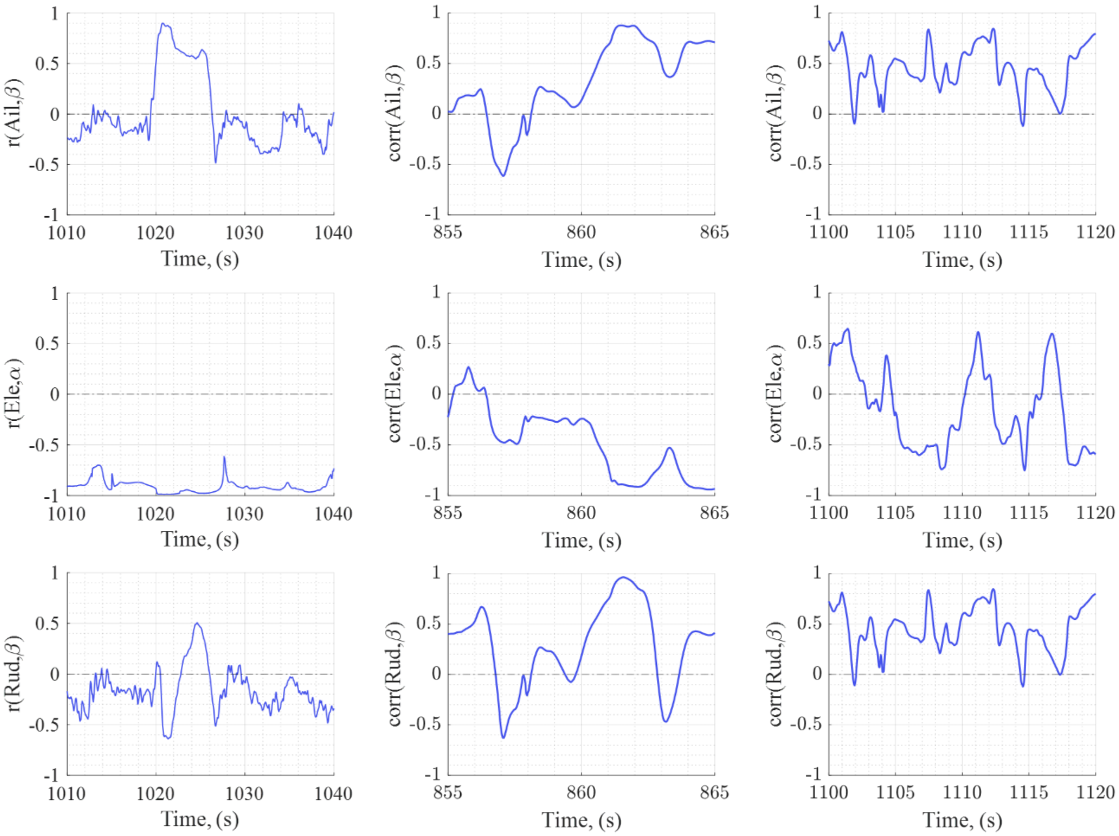

Figure 3-107. Unstable flight strong airflow relationships {SkyHunter (left), manual Aeroscout (middle), autonomous Aeroscout (right)}.

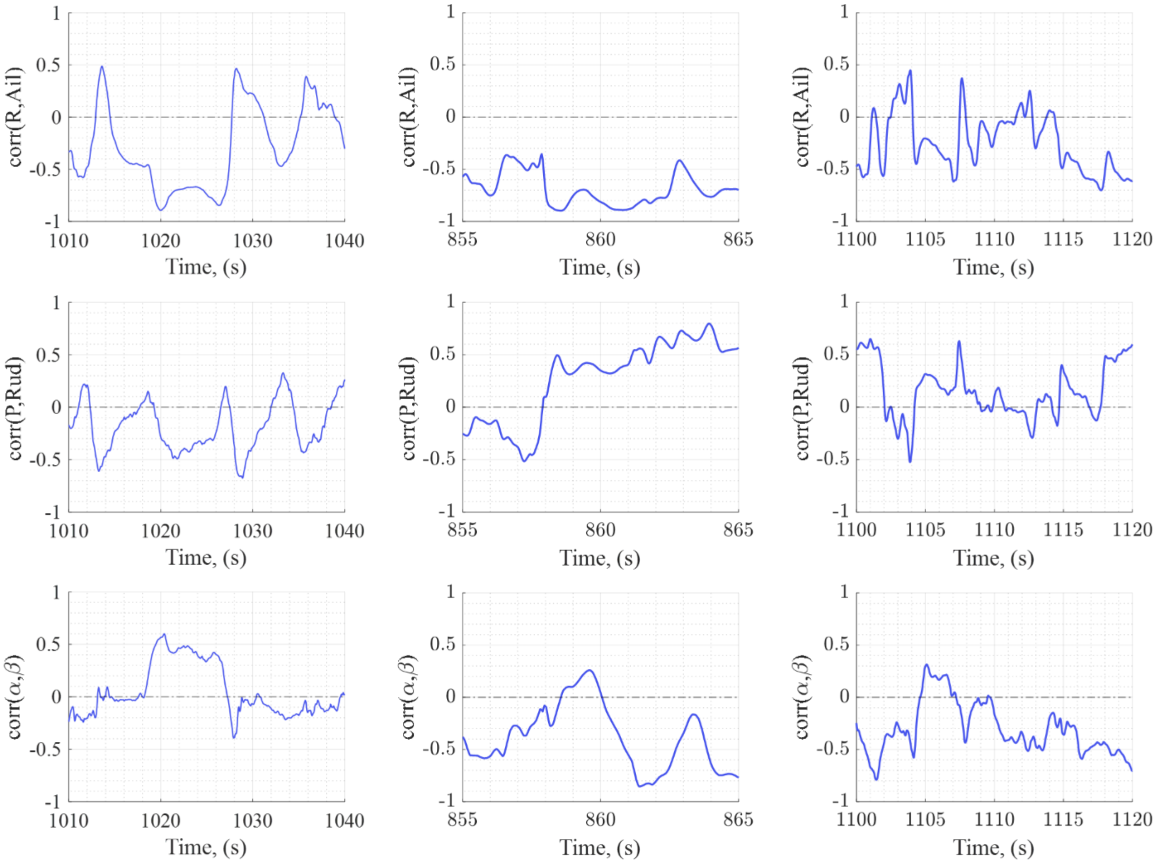

Figure 3-108. Unstable flight weak angular relationships {SkyHunter (left), manual Aeroscout (middle), autonomous Aeroscout (right)}.

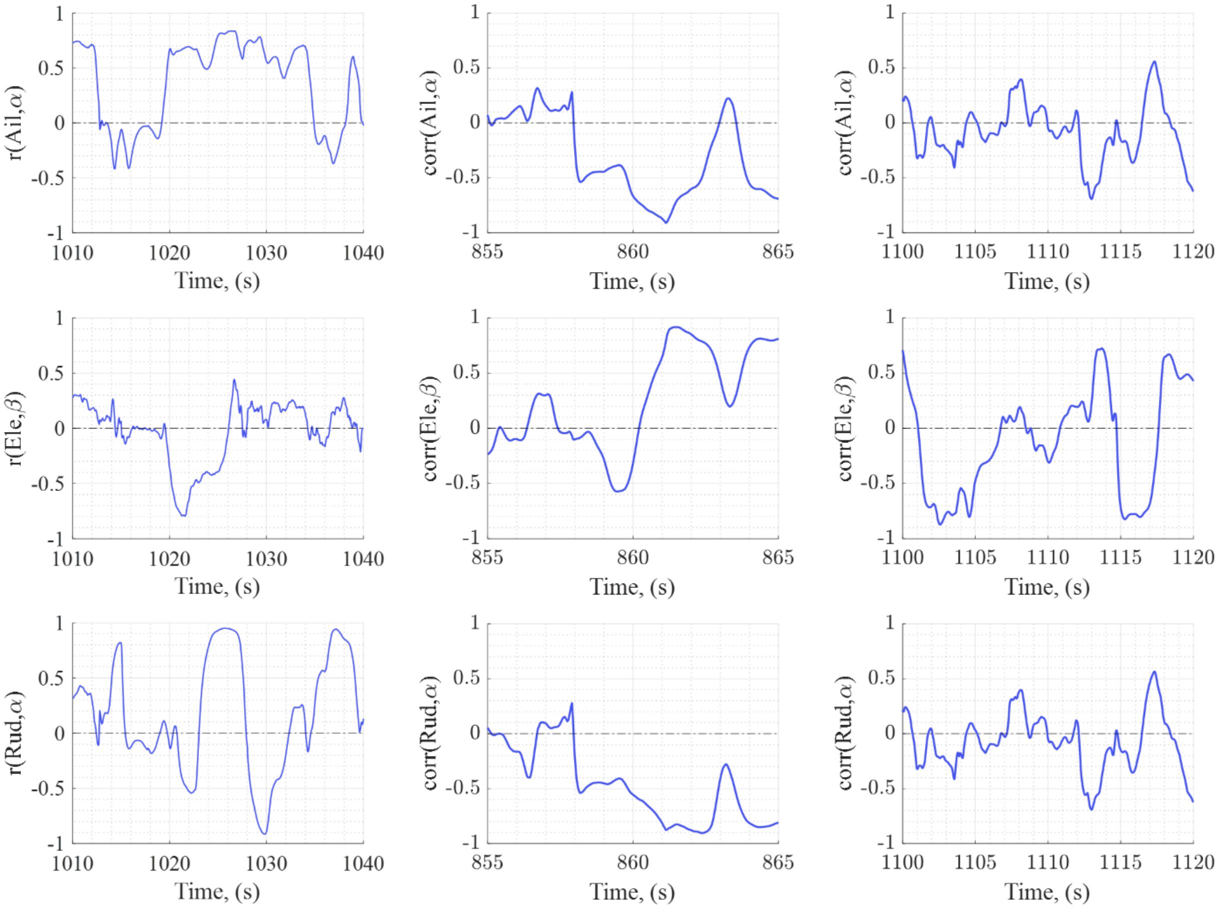

Figure 3-109. Unstable flight weak airflow relationships {SkyHunter (left), manual Aeroscout (middle), autonomous Aeroscout (right)}.

3.4.3.1.3 Loss of control observations

The LoC correlation trends are shown in Figure 3-110. to Figure Figure 3-113. Much like the unstable flight correlations, the same behavior of weakening strong relationships and strengthening weak relationships are seen when the aircraft undergoes the external disturbance. However, unlike the previous datasets, these trends see significantly more correlations deviating from conventional patterns. Combining the correlation trends together allows for a method of predicting the LoC probability of the aircraft using hidden relationships revealed from Sliding Window Correlations.

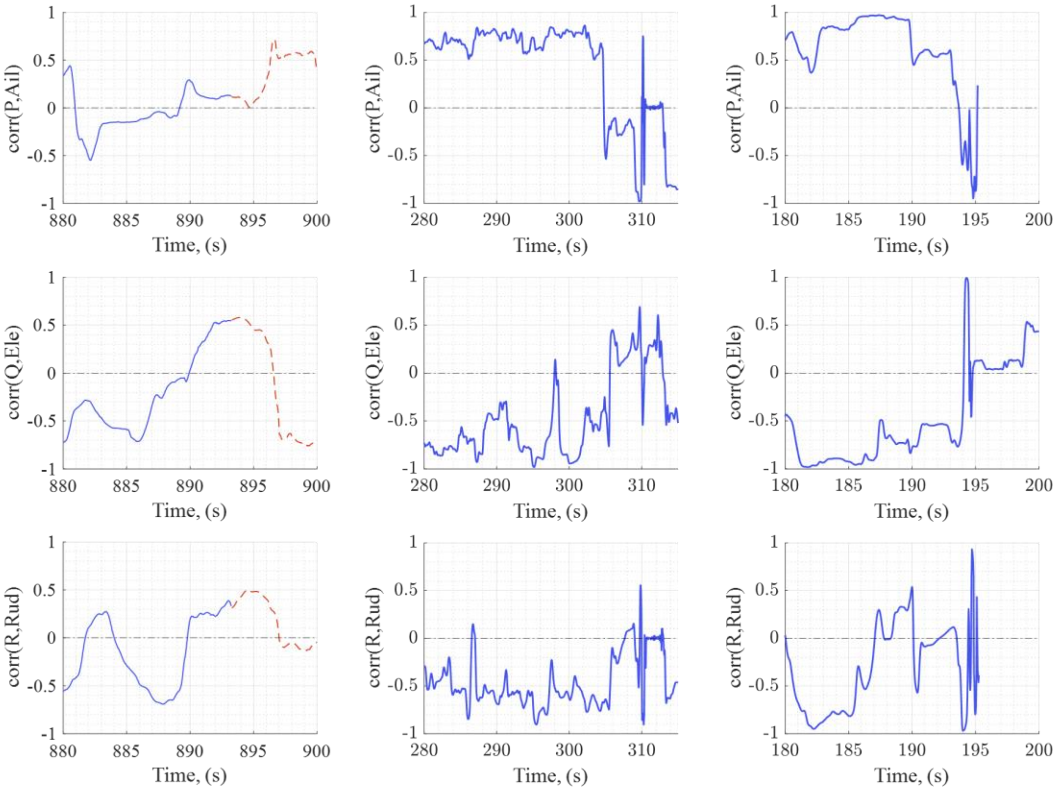

Figure 3-110. LoC strong angular relationships {SkyHunter (left), manual Aeroscout (middle), autonomous Aeroscout (right)}.

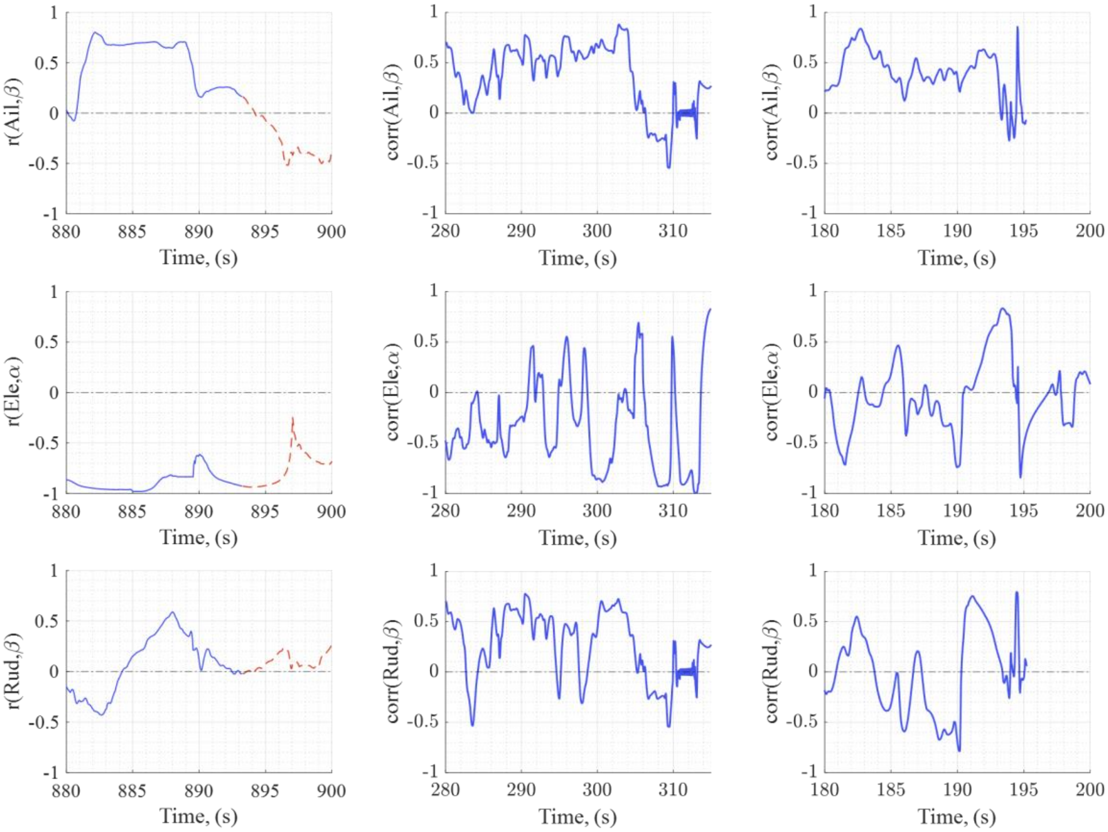

Figure 3-111. LoC strong airflow relationships {SkyHunter (left), manual Aeroscout (middle), autonomous Aeroscout (right)}.

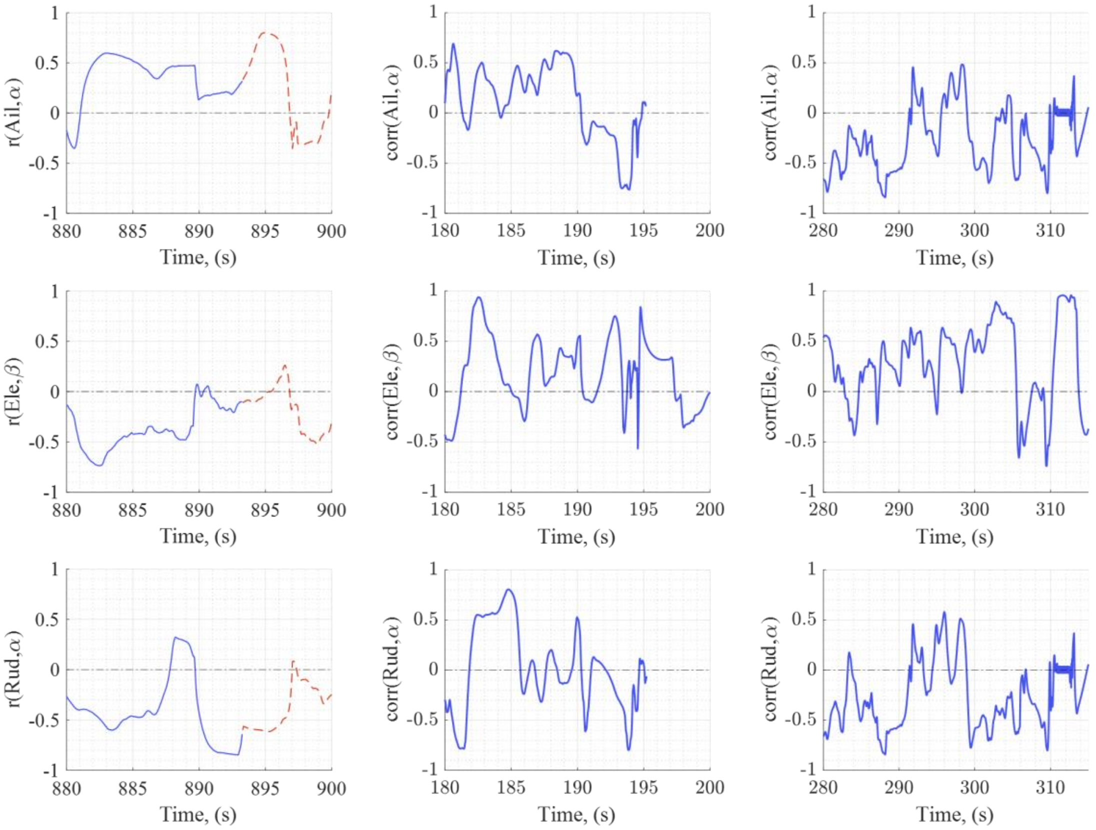

Figure 3-112. LoC weak airflow relationships {SkyHunter (left), manual Aeroscout (middle), autonomous Aeroscout (right)}.

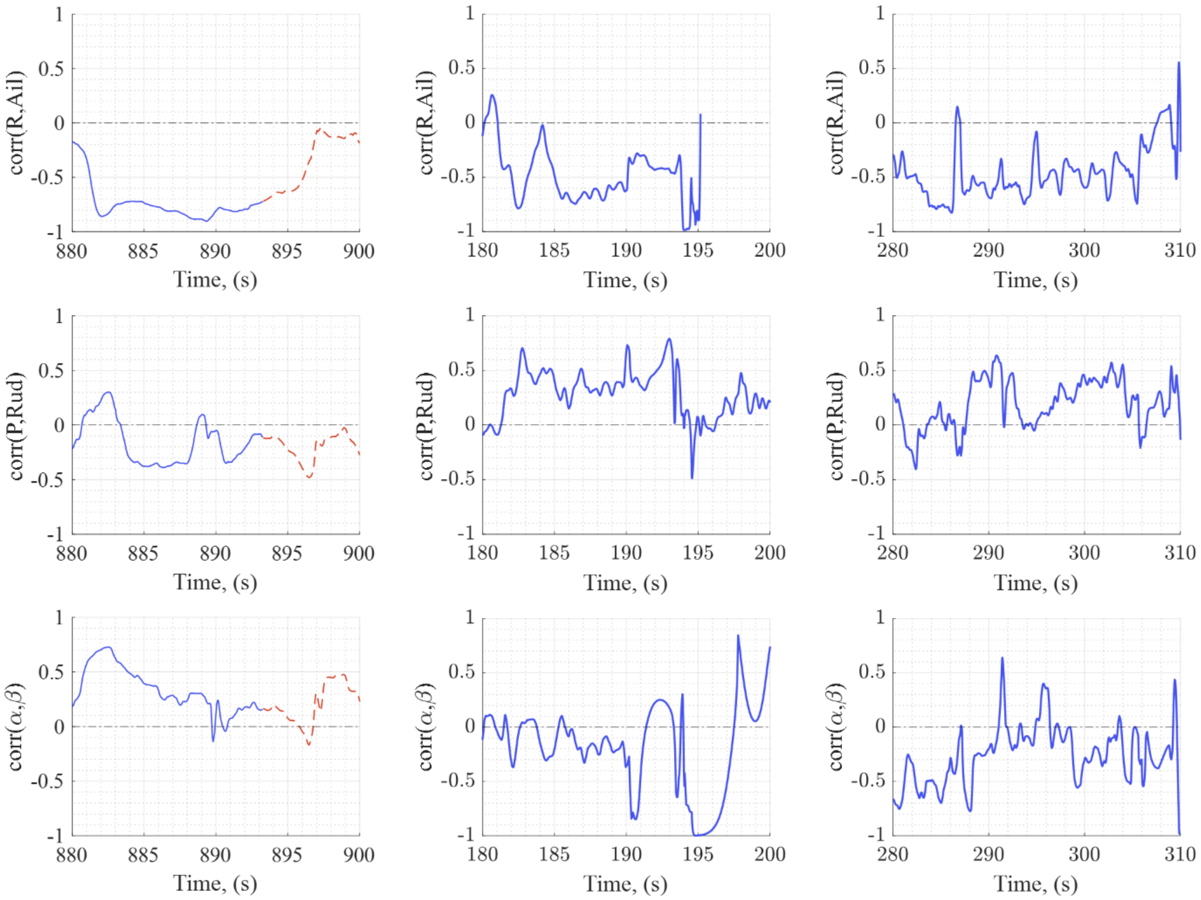

Figure 3-113. LoC weak angular relationships {SkyHunter (left), manual Aeroscout (middle), autonomous Aeroscout (right)}.

3.4.3.2 Final autonomous flights over wind machines

For the autonomous SkyHunter flights over fans, as noted earlier, only one encounter produced a response potentially leading to loss of control. Figure 3-114 shows the many correlations of states during the encounter with the fans. Essentially all of the correlations were dramatic, indicative of a potential entry into loss of control.

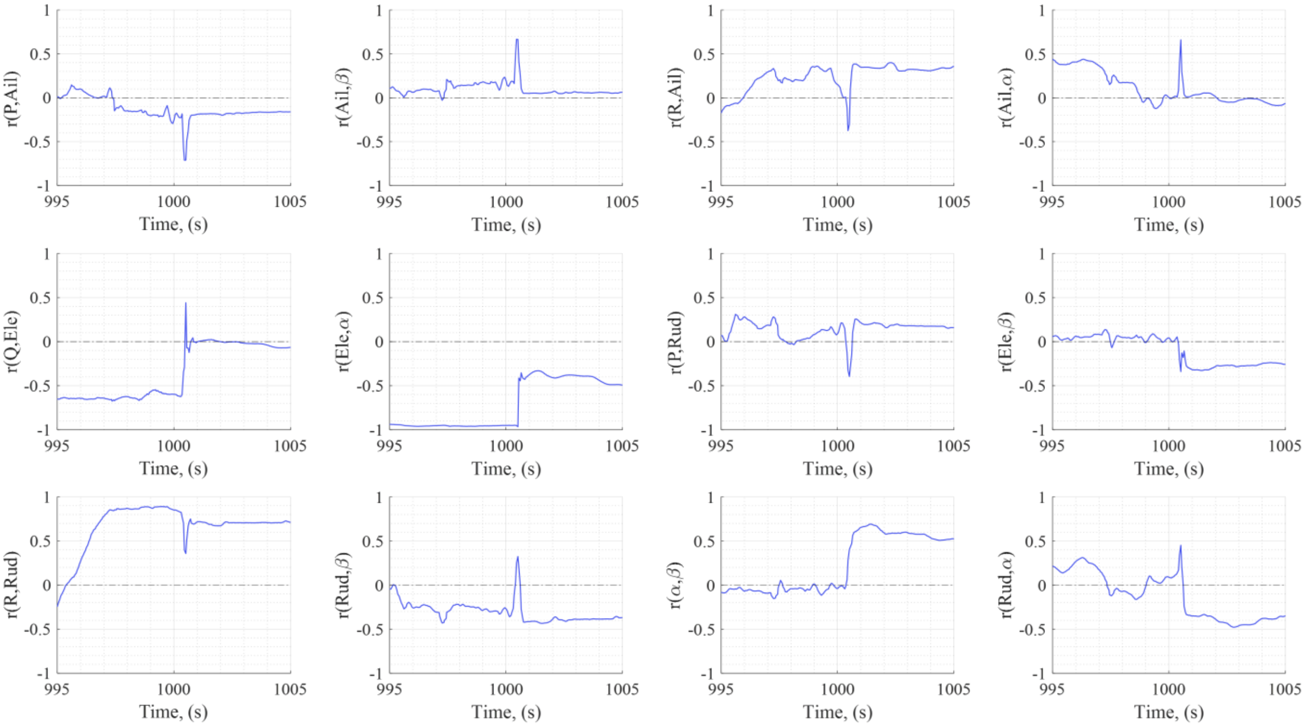

Figure 3-114. SkyHunter state correlations during the dramatic rolling response in a headwind encounter.

3.4.3.3 Loss of control prediction

Since the conditions for unstable flight vary amongst the relationships, the correlation trends are adjusted such that $r \in [-1,1] \rightarrow P_{LoC} \in [0,1]$, where P_{LoC} is the probability of loss of control obtained from the collective of all correlation trends. For a direct comparison between correlation trends to be made, each trend is remapped from $[-1,1] \rightarrow [0,1]$ as follows:

- $P_{LoC}(R, Rud) = 1 - \frac{r(R,Rud)+1}{2}$
- $P_{LoC}(Q, Ele) = \frac{1+r(Q,Ele)}{2}$
- $P_{LoC}(R, Rud) = \frac{1+r(R,Rud)}{2}$
- $P_{LoC}(\beta,\ Ail) = 1 - \frac{r(\beta,\ Ail)+1}{2}$
- $P_{LoC}(\alpha,\ Ele) = \frac{1+r(\alpha,\ Ele)}{2}$
- $P_{LoC}(\beta,\ Rud) = \frac{1+r(\beta,\ Rud)}{2}$
- $P_{LoC}(\alpha,\ Ail) = \mathrm{abs}\big(r(\alpha,\ Ail)\big)$
- $P_{LoC}(\beta,\ Ele) = \mathrm{abs}\big(r(\beta,\ Ele)\big)$
- $P_{LoC}(\alpha,\ Rud) = \mathrm{abs}\big(r(\alpha,\ Rud)\big)$
- $P_{LoC}(R, Ail) = \frac{1+r(R,Ail)}{2}$
- $P_{LoC}(P, Rud) = 1 - \frac{r(P,Rud)+1}{2}$

- $P_{LoC}(\alpha,\beta) = \text{abs}\big(r(\alpha,\beta)\big)$

These trends can be combined through a weighted average where the strongest trends are weighted higher depending on the changes in trends seen during unstable flight.

For this work, the strong angular relationships are seen to have the most extreme changes during encounters, followed by the strong airflow relationships. The strengthening of weak relationships tends to occur after strong relationships are weakened, however, they are also much more variable than strong relationships, therefore these trends are weighted at a lower value. Figure 3-115 through Figure 3-117 show both the weighted average and flat average of the collective correlation trends overlaying a backdrop of the correlations that comprise the final probability.

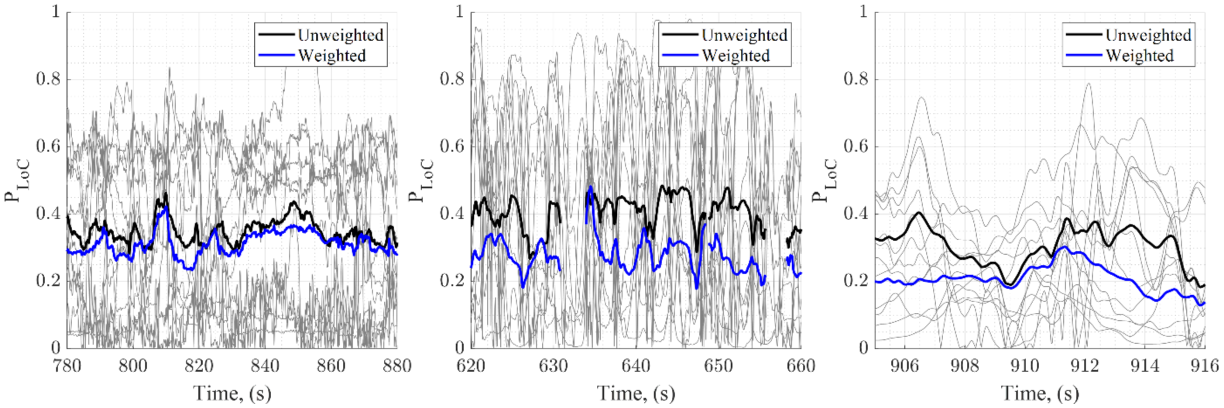

Figure 3-115. Loss of control probability for stable flight envelope {SkyHunter (left), manual Aeroscout (middle), autonomous Aeroscout (right)}.

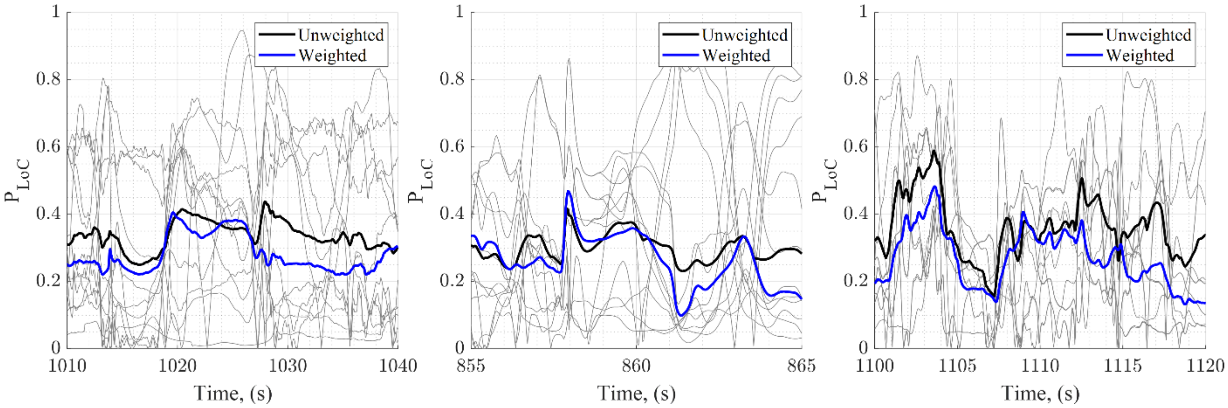

Figure 3-116. LoC probability for unstable flight envelope {SkyHunter (left), manual Aeroscout (middle), autonomous Aeroscout (right)}.

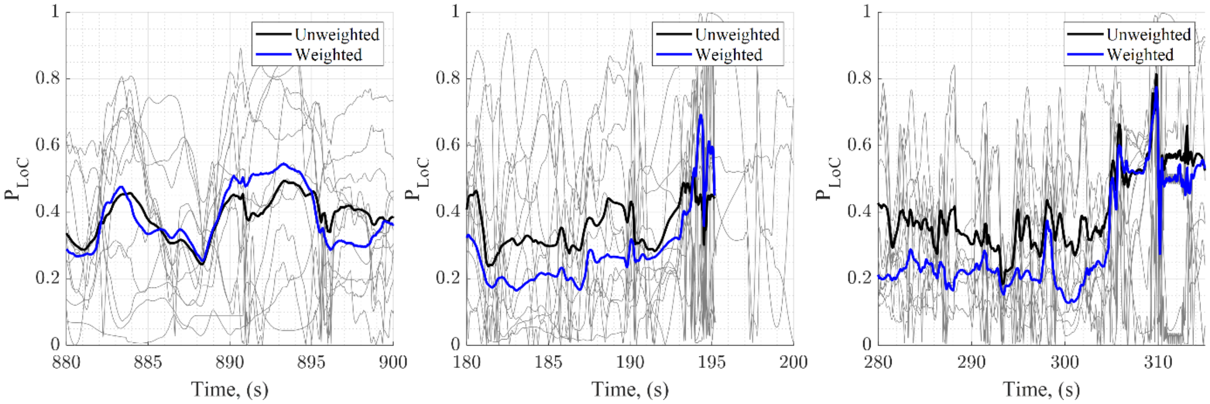

Figure 3-117. LoC probability for LoC envelope {SkyHunter (left), manual Aeroscout (middle), autonomous Aeroscout (right)}.

For the autonomous SkyHunter headwind encounter which caused a dramatic rolling response, the probability of loss of control was not dramatic but, as seen in Figure 3-118, definitely indicated an increased probability of loss of control relative to the probability at any other time in the flight. For comparison, Figure 3-119 shows the probability of loss of control gives no indication of a loss of control.

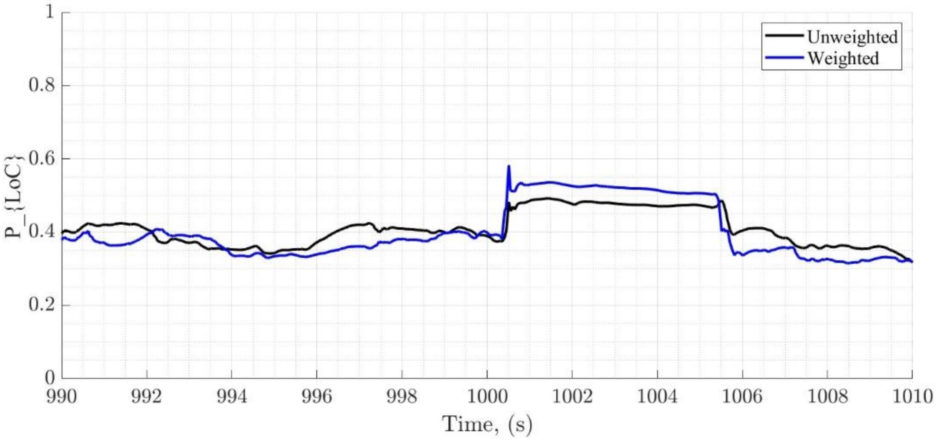

Figure 3-118. LoC probability for SkyHunter during dramatic rolling response in a headwind encounter.

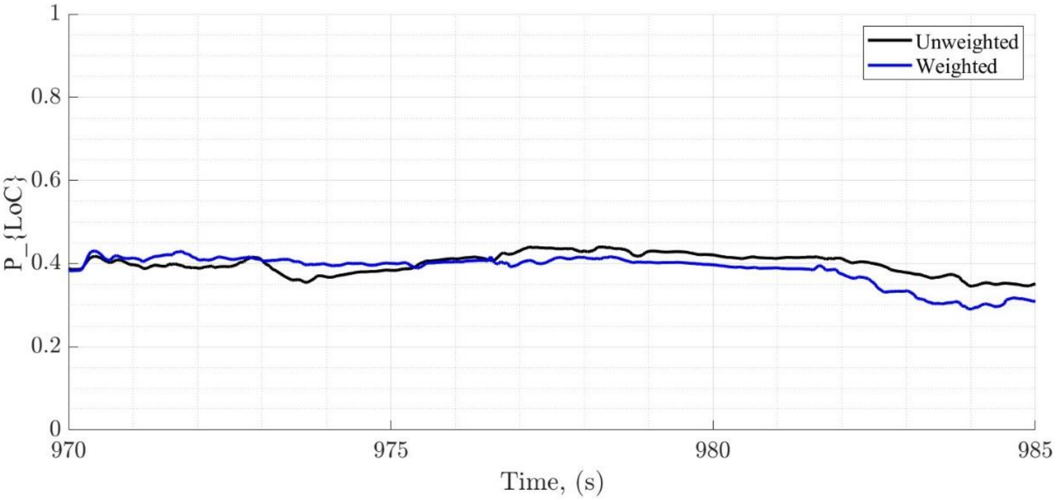

Figure 3-119. LoC probability for SkyHunter during a barely identifiable response in a headwind encounter.

3.4.3.4 Conclusions for correlation-based loss of control metrics

In conclusion, SWC is a not only a viable method of mapping hidden relationships between changing outputs of neural activity, but it can also be successfully used to find hidden relationships between changing inputs that related to aircraft stability. Local linear analysis allows for the use of the linear Pearson's *r* correlation method to find correlation trends between nonlinear relationships.

The flight results show that not only can SWC be used to determine times of unstable flight, but a weighted average of the trends also allows multiple relationships to collectively influence the final probability of LoC without providing false-positives that only cause certain relationships to go unstable. Note that SWC is infinitely scalable between any measured aircraft state and using any desired cumulation method as long as the correlation trends are remapped to a uniform probability scale. Further, SWC has the potential to be calculated in essentially real time, thereby allowing LoC identification in real time, which would then be available to the flight controller.

3.5 Safety analysis for UAS

Research has indicated that there are two good methods to mitigate the severity of adverse wake vortex encounters. The first and most obvious is physical/temporal separation. Based on knowledge of the behavior of wake vortices, volumes of airspace below the flight path of large aircraft can be categorized by the maximum (safe) circulation for a given UAS. In Section 2.3, the maximum circulation was assumed, very conservatively, to be the ambient circulation in the atmosphere, thereby avoiding needing to know the vorticity which causes LOC. Alternatively, such categorizations could be fluid, that is, based on ambient meteorological conditions which establish the EDR.

A less obvious mitigation strategy is to afford the UAS with a robust controller, capable of identifying the onset of loss of control and use the control strategy to decrease the potential for loss of control. An adjunct to this capability is a propulsion system with excess power such that the UAS can “power through” the onset of loss of control. The availability of excess power at the fingertips of a highly trained pilot has been shown to prevent loss of control in many instances during flight testing over wind machines, simulating passage through a wake vortex. Therefore, having such a capability in a robust controller may also be useful.

3.5.1 Physical/temporal separation

If an allowable wake vortex circulation in a WVE can be determined through simulation and/or test, wake hazard (“no-fly”) zones can be established—using the process described in Section 2.3. These zones could be established at both the approach and departure ends of runways as well and, to account for operations on either side of the runway, also consider the presence of cross-winds.

Figure 3-120 depicts the side view of the volume of airspace considered hazardous for UASs in the vicinity of an aircraft departing an airport. In this figure, an aircraft on takeoff generates twin vortices, which descend (and will drift laterally, which is not seen in this view). Since the vortices are dissipating, for any given EDR, there will be a distance below the departing aircraft at which the vortices will not pose a danger for a given UAS. This is a line in the figure labelled the “Extent of Wake Danger”. Further, for a UAS flying at any given altitude, there will be a distance from the generating aircraft lift-off point beyond which there will be no danger because the wake will have dissipated. This distance is noted as “Safe Distance From Aircraft Lift-Off” in the figure. Further, note that at any given altitude, there will be no danger if the UAS is flying above the flight path of the generating aircraft.

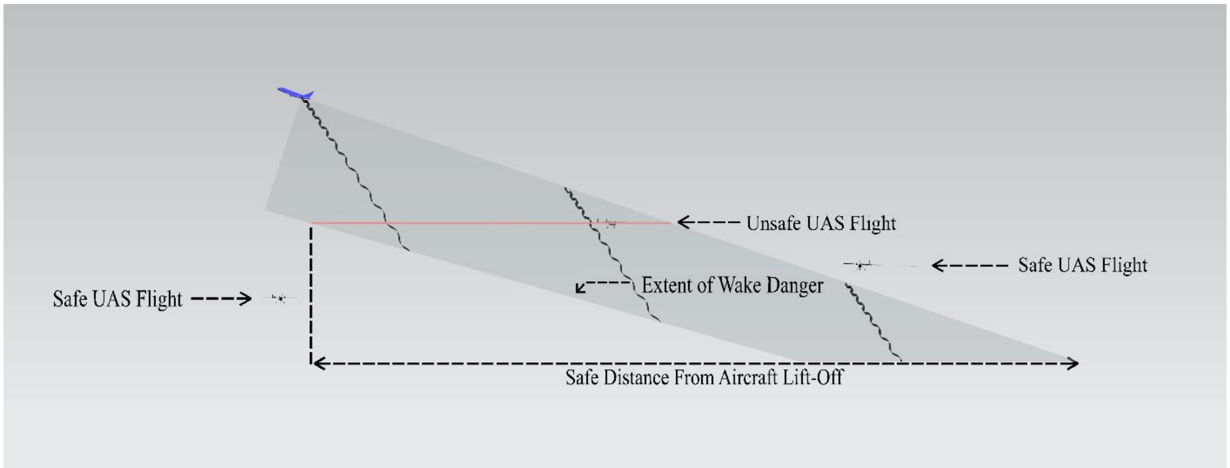

Figure 3-120. Wake Hazard Zone in vicinity of a departing wake-generating aircraft.

Figure 3-121 is an isometric view of the airspace depicted in Figure 3-120. Note here that the volume of airspace dangerous for UAS is expanded laterally to recognize the effect of cross-winds. A similar volume of airspace can also be developed—and would look essentially the same—for the arrival side of an airport. Since aircraft can arrive from either direction, of course, one or the other wake hazard airspace volumes would dominate. An obvious complication is that may airports have intersecting runways, which would result in more complicated wake hazard zones.

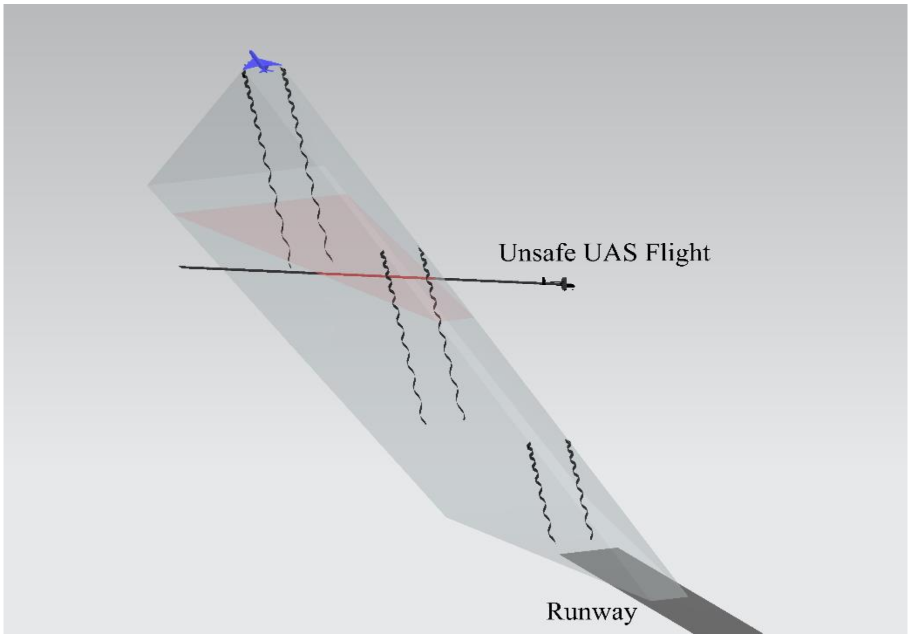

Figure 3-121. Isometric view of the Wake Hazard Zone in the vicinity of a departing aircraft.

In Section 3.1.2.4, the safe distances for 3 different UAS in a 90^o WVE with 3 different wake-generating aircraft are given. These distances establish the “Extent of Wake Danger” line in Figure 3-120 (and the lower surface of the wake hazard zone in Figure 3-121).

Finally, it would be possible to create wake hazard zones for:

- Different classes of generating aircraft, for instance, A-380 class, Boeing 737 class, and commuter class (like in the current RECAT separation standards for transport aircraft)
- Different classes of UAS based on their susceptibility to loss of control, for instance, based on UAS weight
- Different values of cross-wind velocity
- Different EDR values, since wake vortices dissipate at a dramatically higher rate as the EDR increases

3.5.2 Loss of control mitigation with robust controllers

One of the key motivations of this work was to investigate the impact of controller robustness in mitigation of the severity of wake vortex encounters. To achieve this goal, three distinctly different flight controllers were tested onboard the SkyHunter UAS on a day with winds up to 15 feet per second, and gusts reaching 22 feet per second. For reference, the SkyHunter UAS typically flies at a cruise velocity of 45 feet per second and stalls at 30 feet per second, so these wind conditions could easily lead to a stall, thus emulating the impact of a wake encounter. The base LQR autopilot was switched mid-air with Model Predictive Controllers (MPC), and ANN-based flight controllers. All of these switches were performed during flight to minimize the impact of operating conditions in the assessment of each controller. Flight test results, specifically for the tracking of commanded velocity and roll angle, are shown in Figure 3-122 and Figure 3-123.

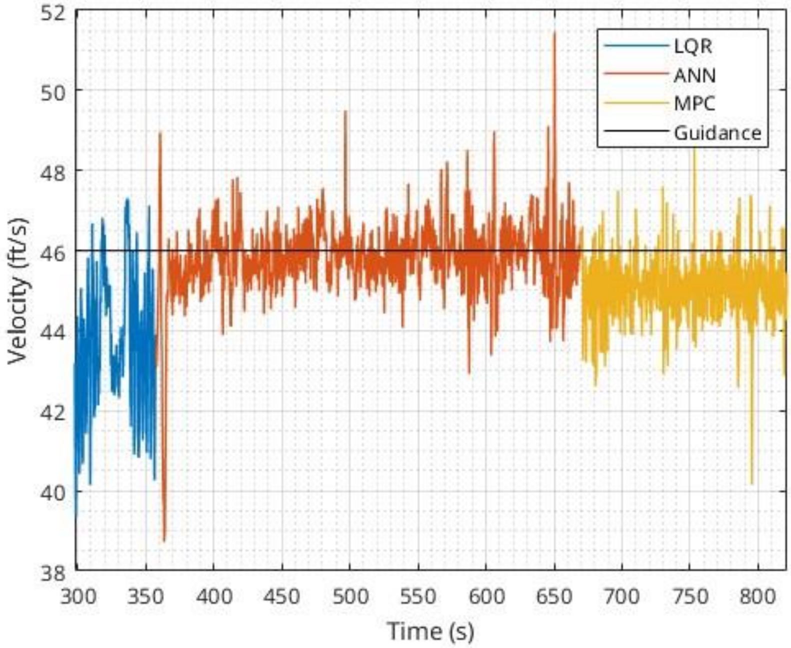

Figure 3-122. Velocity tracking during high wind SkyHunter flight test for three different controllers.

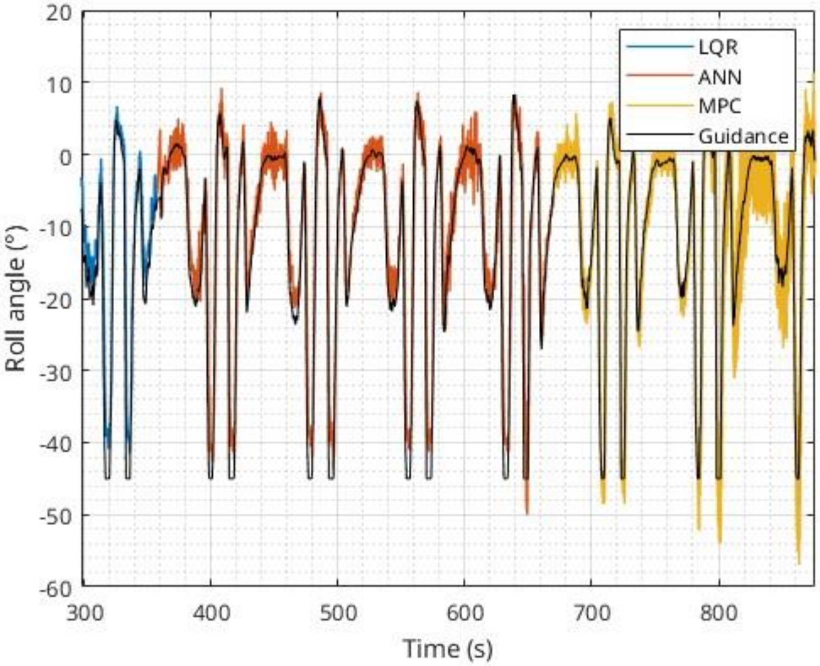

Figure 3-123. Roll angle tracking during high wind SkyHunter flight test for three different controllers.

Each controller performed well in maintaining high levels of tracking in both roll angle and velocity commands during these high wind conditions. However, there is a quantifiable difference between the overall tracking difference of each controller as shown by the RMSE in Table 3-35. The ANN controller had the best performance in both velocity and roll tracking, while the MPC tracked second best and the LQR controller ranked last. These results emphasize the importance of controller performance during adverse conditions such as those expected during wake turbulence encounters.

Table 3-35. Root mean squared error for roll angle and velocity tracking during high wind flight test.

Controller	Roll angle RMSE (°)	Velocity RMSE ($\frac{ft}{s}$)
Linear Quadratic Regulator (LQR)	18.08	2.833
Artificial Neural Network (ANN)	16.53	0.941
Model Predictive Control (MPC)	17.25	1.209

3.6 References

[1] J. Roskam, *Airplane Flight Dynamics and Automatic Flight Controls*. DARcorporation, 1998.

[2] B. Etkin, "Turbulent wind and its effect on flight," *Journal of Aircraft*, vol. 18, no. 5, pp. 327–345-327–345, 1981.

[3] N. N. Ahmad and F. Proctor, "Review of idealized aircraft wake vortex models," in *52nd Aerospace Sciences Meeting*, 2014, pp. 0927-0927.

[4] A. Dogan, S. Venkataramanan, and W. Blake, "Modeling of aerodynamic coupling between aircraft in close proximity," *Journal of Aircraft*, vol. 42, no. 4, pp. 941–955-941–955, 2005.

[5] Y. Gu, S. Gururajan, B. Seanor, H. Chao, and M. R. Napolitano, "Building better tools: Experimental UAV research at west virginia university," in *2013 American Control Conference*, 2013, pp. 1454–1459-1454–1459.

[6] P. Tian, A. He, H. Chao, Z. C. Zheng, and Y. Gu, "Wake encounter simulation and flight validation with UAV close formation flight," in *AIAA Guidance, Navigation, and Control Conference*, 2017, pp. 1910-1910.

[7] A. He, Z. C. Zheng, H. Chao, P. Tian, and Y. Gu, "A study on wake turbulence encounter during UAV formation flight using coupled aerodynamics/flight dynamics simulation," in *8th AIAA Atmospheric and Space Environments Conference*, 2016, pp. 3439-3439.

[8] R. W. Beard and T. W. McLain, *Small unmanned aircraft: Theory and practice*. Princeton university press, 2012.

[9] T. Melin, "A vortex lattice MATLAB implementation for linear aerodynamic wing applications," *Master's Thesis, Department of Aeronautics, Royal Institute of Technology (KTH), Stockholm, Sweden*, 2000.

[10] B. Etkin, *Dynamics of atmospheric flight*. Courier Corporation, 2012.

[11] S. K. Rahmani, Z. J. Wang, J. Matt, H. Chao, and C. Zheng, "Comparison of low-and high-order CFD based estimates of forces, moments and aerodynamic coefficients with UAS flight test data," in *AIAA AVIATION 2022 Forum*, 2022, pp. 4065-4065.

[12] C. Rice *et al.*, "Autonomous close formation flight control with fixed wing and quadrotor test beds," *International Journal of Aerospace Engineering,* vol. 2016, 2016.

[13] M. B. Rhudy, Y. Gu, J. N. Gross, and H. Chao, "Onboard wind velocity estimation comparison for unmanned aircraft systems," *IEEE Transactions on Aerospace and Electronic Systems,* vol. 53, no. 1, pp. 55–66-55–66, 2017.

[14] A. K. McGrail, *Onboard parameter identification for a small UAV*. West Virginia University, 2012.

[15] Z. Lin, J. Matt, H. Chao, C. Zheng, and M. Ewing, "Wake Vortex Encounter Modeling and Simulation for Small Fixed-Wing UAS with Inner Loop Attitude Controller," in *AIAA AVIATION 2022 Forum*, 2022, pp. 4066-4066.

[16] D. Fischenberg, "A method to validate wake vortex encounter models from flight test data," in *27th International Congress of the Aeronautical Sciences*, 2010, pp. 2010–6-2010–6.

[17] M. Specification, "" Flight Control System-Design, Installation and Test of Piloted Aircraft, General Specification for," 1975.

[18] C. L. Blanken, R. H. Hoh, D. G. Mitchell, and D. L. Key, "Test guide for ADS-33E-PRF," 2008.

[19] H. P. Flanagan, S. G. Hagerott, and H. Chao, "Model Based Roll Controller Tuning and Analysis for Small UAS in Turbulent Environments," in *2018 International Conference on Unmanned Aircraft Systems (ICUAS),* 2018, pp. 1398–1407-1398–1407.

[20] J. J. Matt, H. Flanagan, and H. Chao, "Evaluation and Analysis of ArduPilot Automatic Tuning Algorithm for the Roll Tracking Controller of a Small UAS," in *AIAA Scitech 2021 Forum*, 2021, pp. 0016-0016.

[21] T. Berger, C. M. Ivler, M. G. Berrios, M. B. Tischler, and D. Miller, "Disturbance rejection handling qualities criteria for rotorcraft," in *72nd Annual Forum of the American Helicopter Society, West Palm Beach, USA*, 2016.

[22] "Advanced Aircraft Analysis," in *Advanced Aircraft Analysis*, ed: DARcorporation, 2022.

[23] M. Vedantam, S. Keshmiri, G. Garcia, and W. Huang, "Fixed Wing Aircraft Perching," in *AIAA Guidance, Navigation, and Control Conference*, 2017, pp. 1915-1915.

[24] M. Chowdhury and S. Keshmiri, "Design and flight test validation of an AI-based longitudinal flight controller for fixed-wing UASs," in *2022 IEEE Aerospace Conference (AERO),* 2022, pp. 1–12-1–12.

[25] M. Chowdhury, S. Keshmiri, and J. Xu, "Design and Flight Test Validation of a UAS Lateral-directional Model Predictive Controller," in *2021 International Conference on Unmanned Aircraft Systems (ICUAS),* 2021, pp. 639–646-639–646.

[26] J. DeSpirito, S. I. Silton, and P. Weinacht, "Navier-Stokes predictions of dynamic stability derivatives: evaluation of steady-state methods," *Journal of Spacecraft and Rockets,* vol. 46, no. 6, pp. 1142–1154-1142–1154, 2009.

[27] S. Schmidt and D. M. Newman, "Estimation of dynamic stability derivatives of a generic aircraft," in *Proceedings of the 17th Australasian Fluid Mechanics Conference*, 2010.

[28] B.-g. Mi, H. Zhan, and B.-b. Chen, "New systematic CFD methods to calculate static and single dynamic stability derivatives of aircraft," *Mathematical Problems in Engineering,* vol. 2017, 2017.

[29] B. Mi and H. Zhan, "Review of numerical simulations on aircraft dynamic stability derivatives," *Archives of Computational Methods in Engineering,* vol. 27, no. 5, pp. 1515–1544-1515–1544, 2020.

[30] F. Götten, M. Havermann, C. Braun, M. Marino, and C. Bil, "Wind-tunnel and CFD investigations of UAV landing gears and turrets–Improvements in empirical drag estimation," *Aerospace Science and Technology,* vol. 107, pp. 106306-106306, 2020.

[31] D. K. Schmidt, W. Zhao, and R. K. Kapania, "Flight-dynamics and flutter modeling and analyses of a flexible flying-wing drone-invited," in *AIAA Atmospheric Flight Mechanics Conference*, 2016, pp. 1748-1748.

[32] S. Yoon, P. V. Diaz, D. D. Boyd Jr, W. M. Chan, and C. R. Theodore, "Computational aerodynamic modeling of small quadcopter vehicles," in *American Helicopter Society (AHS) 73rd Annual Forum Fort Worth, Texas*, 2017.

[33] U. Kowarsch, C. Öhrle, M. Keßler, and E. Krämer, "Aeroacoustic simulation of a complete H145 helicopter in descent flight," *Journal of the American Helicopter Society*, vol. 61, no. 4, pp. 1–13-1–13, 2016.

[34] M. B. Tischler and R. K. Remple, *Aircraft and rotorcraft system identification*. American Institute of Aeronautics and Astronautics Reston, VA, 2012.

[35] E. A. Morelli and V. Klein, *Aircraft system identification: theory and practice*. Sunflyte Enterprises Williamsburg, VA, 2016.

[36] H. P. Flanagan, H. Chao, and S. G. Hagerott, "Model based roll controller tuning and frequency domain analysis for a flying-wing UAS," in *2019 International Conference on Unmanned Aircraft Systems (ICUAS),* 2019, pp. 721–728-721–728.

[37] J. J. Matt, S. G. Hagerott, B. C. Svoboda, H. Chao, and H. P. Flanagan, "Frequency Domain System Identification of a Small Flying-Wing UAS," in *AIAA SCITECH 2022 Forum*, 2022, pp. 2407-2407.

[38] Z. J. Wang *et al.*, "Towards industrial large eddy simulation using the FR/CPR method," *Computers & Fluids,* vol. 156, pp. 579–589-579–589, 2017.

[39] H. T. Huynh, "A flux reconstruction approach to high-order schemes including discontinuous Galerkin methods," in *18th AIAA computational fluid dynamics conference*, 2007, pp. 4079-4079.

[40] T. Haga, H. Gao, and Z. J. Wang, "A high-order unifying discontinuous formulation for the Navier-Stokes equations on 3D mixed grids," *Mathematical Modelling of Natural Phenomena,* vol. 6, no. 3, pp. 28–56-28–56, 2011.

[41] Z. J. Wang and H. Gao, "A unifying lifting collocation penalty formulation including the discontinuous Galerkin, spectral volume/difference methods for conservation laws on mixed grids," *Journal of Computational Physics,* vol. 228, no. 21, pp. 8161–8186-8161–8186, 2009.

[42] E. Jourdan de Araujo Jorge Filho and Z. J. Wang, "Efficient implementation of the FR/CPR method on GPU clusters for industrial large eddy simulation," in *AIAA Aviation 2020 Forum,* 2020, pp. 3031-3031.

[43] M. A. Alhawwary and Z. J. Wang, "Implementation of a FWH approach in a high-order LES tool for aeroacoustic noise predictions," in *AIAA Scitech 2020 Forum*, 2020, pp. 1724-1724.

[44] H. T. Huynh, Z. J. Wang, and P. E. Vincent, "High-order methods for computational fluid dynamics: A brief review of compact differential formulations on unstructured grids," *Computers & fluids,* vol. 98, pp. 209–220-209–220, 2014.

[45] Z. J. Wang, "High-order computational fluid dynamics tools for aircraft design," *Philosophical Transactions of the Royal Society A: Mathematical, Physical and Engineering Sciences*, vol. 372, no. 2022, pp. 20130318-20130318, 2014.

[46] B. Cockburn, G. E. Karniadakis, and C.-W. Shu, *Discontinuous Galerkin methods: theory, computation and applications*. Springer Science & Business Media, 2012.

[47] Y. Liu, M. Vinokur, and Z. J. Wang, "Discontinuous spectral difference method for conservation laws on unstructured grids," in *Computational fluid dynamics 2004*: Springer, 2006, pp. 449–454-449–454.

[48] F. Bassi and S. Rebay, "A high order discontinuous Galerkin method for compressible turbulent flows," in *Discontinuous Galerkin Methods*: Springer, 2000, pp. 77–88-77–88.

[49] Y. Li and Z. J. Wang, "A convergent and accuracy preserving limiter for the FR/CPR method," in *55th AIAA Aerospace Sciences Meeting*, 2017, pp. 0756-0756.

[50] V. Vatsa, M. Carpenter, and D. Lockard, "Re-evaluation of an optimized second order backward difference (BDF2OPT) scheme for unsteady flow applications," in *48th AIAA aerospace sciences meeting including the new horizons forum and aerospace exposition*, 2010, pp. 122-122.

[51] S. Yoon and A. Jameson, "Lower-upper symmetric-Gauss-Seidel method for the Euler and Navier-Stokes equations," *AIAA journal*, vol. 26, no. 9, pp. 1025–1026-1025–1026, 1988.

[52] R. F. Stengel, *Flight dynamics*. Princeton university press, 2022.

[53] M. R. Napolitano, *Aircraft Dynamics*. Wiley, 2012.

[54] M. Drela and H. Youngren, "Athena Vortex Lattice," ed: MIT, 2019.

[55] D. Schulz and J. P. Huston, "The sliding window correlation procedure for detecting hidden correlations: existence of behavioral subgroups illustrated with aged rats," *Journal of neuroscience methods*, vol. 121, no. 2, pp. 129–137-129–137, 2002.

[56] S. Shakil, C.-H. Lee, and S. D. Keilholz, "Evaluation of sliding window correlation performance for characterizing dynamic functional connectivity and brain states," *Neuroimage*, vol. 133, pp. 111–128-111–128, 2016.

[57] M. G. Preti, T. A. W. Bolton, and D. Van De Ville, "The dynamic functional connectome: State-of-the-art and perspectives," *Neuroimage*, vol. 160, pp. 41–54-41–54, 2017.

[58] F. Mokhtari, M. I. Akhlaghi, S. L. Simpson, G. Wu, and P. J. Laurienti, "Sliding window correlation analysis: Modulating window shape for dynamic brain connectivity in resting state," *Neuroimage*, vol. 189, pp. 655–666-655–666, 2019.Tian, P., He, A., Chao, H., Zheng, Z. C., & Gu, Y. (2017). Wake encounter simulation and flight validation with UAV close formation flight. In *AIAA Guidance, Navigation, and Control Conference* (p. 1910).

[59] He, A., & Zheng, Z. C. (2015). Aerodynamic Simulation of Wake Encounter for Aircraft Close Formation Operations. In 7th AIAA Atmospheric and Space Environments Conference (p. 3319).

[60] Xu, J., Le Pichon, T., & Keshmiri, S. (2019, July). Multi-eye guidance method for uavs path following. In 2019 IEEE National Aerospace and Electronics Conference (NAECON) (pp. 620-626). IEEE.

[61] Xu, J., & Keshmiri, S. (2022, March). Multi-Scale and Multi-Reference Longitudinal Guidance Logic for UAS. In *2022 IEEE Aerospace Conference (AERO)* (pp. 1-8). IEEE.

4 RESPONSE MODELLING FOR MULTIROTOR UAS

One of the early opportunities for integration of multirotor vehicles into the National Airspace System can be found in the inspection and security of controlled airport environments. Within these environments, the sUAS can be strategically deconflicted with manned traffic relatively easily. However, another threat exists in these environments are the high-intensity wakes generated from landing and departing aircraft, which are invisible to the pilot and the sUAS. While these have posed a significant danger to manned aviation, their impact on sUAS remains unknown. Understanding the operating limits of the vehicles can provide guidance on when and where they can be safely used in the airport environment. Prediction of these safe operational areas requires highly accurate aerodynamic models for the vehicle to understand how they interact with spatially and temporally varying wake structures along with accurate knowledge of the external wind field, both of which represent significant challenges. However, as noted in previous publications on multi-rotor performance provide limited information from flight tests that are useful for validating both high-fidelity CFD and dynamic models used in developing advanced control schemes [1-3]. This work presents a framework for providing free-flight measurements of simulated wake encounters to allow for model identification and control margin assessment.

Several works have investigated fixed-wing sUAS wake encounters, namely those of Wang et al. [4] and Barbeau and Jacob [5]. In these works, detailed frameworks and flight-testing procedures were developed for assessing sUAS-sUAS wake encounters. Of note, both works demonstrated the potential for upset even with the lower tip vorticity associated with the lightweight vehicles (<55 lbs). Further, the wake encounters generated in these works were relatively small in size (several meters), requiring high precision positioning to ensure the trailing vehicle was exposed to the leader’s wake. Little has been published on wake encounters between multirotor sUAS and full-sized crewed aircraft. Therefore, the scope of this work will be limited to these encounter scenarios with correspondingly larger wake structures.

Previous studies by the OSU team [6, 7] traced the primary vehicle design uncertainties to thermal drift, aliasing due to vibrations and blade passage, insufficient resolution of the thrust and strain data, and uncertainty in the attitude and velocity provided by the flight controller. Additionally, refined flight-testing techniques have led to better control over external uncertainties such as wind and temperature effects. Reynolds-dependent thrust and performance models have been developed and refined using PIV measurements of the wake evolution in the presence of the body [8], which has informed reduced order models of the thrust characteristics amenable to system identification [9, 10]. However, these models do not incorporate the fast dynamics anticipated in the gust encounters and will need to be expanded to allow for rapid variations in blade loading.

This research discusses the wake models used to generate the gust profiles using the crosswind fans, which were necessary to simulate full-scale vehicle wake encounters. Following the gust encounter development, an overview of the instrumented sUAS is presented with a specific focus on the thrust load measurement capabilities. Finally, encounters between the wind gradients and the multirotor vehicle are discussed to demonstrate the measurement techniques and their capabilities to make direct performance measurements in the simulated wake encounters. Specific emphasis is placed on estimating vehicle response and individual rotor loads during these encounters to inform future model development. Data demonstrating the variation in individual rotor performance is presented and will be used as a baseline for model identification using techniques outlined by Sun et al. [11].

4.1 Gust encounters considered

The specific gust encounter scenarios considered in this work correspond to sUAS flights conducted in relatively close proximity to the runway environment, typical of proposed airport inspection operations. The simulated wake structure was modeled for a heavily loaded B747-400 using a Burnham-Hallock model [12] and Cessna 172 to generate the tangential velocity components, as shown in Figure 4-1, where the ΔV corresponds to the velocity differential between the left and right wing/rotor tips of the vehicle relative to its location within the wake structure. B747-400 model certainly represents a worst-case encounter scenario but also provides the widest possible range of testing conditions for the sUAS. Of particular interest is not only the sUAS response to quasi steady-state winds, but also the response due to the gradients encountered near the vortex core boundary. For fixed-wing aircraft, these gradients represent the common mechanism associated with loss of control, however the small size of most sUAS platforms means they generally do not experience the same extreme changes in local velocity across their rotor disks. Further, two encounter scenarios were proposed for investigation, namely a sUAS flight parallel to the runway, and another perpendicular with offset distances defined by well-clear boundaries between taxi and runway locations. Each scenario results in different wake gradient experienced by the sUAS, as shown in **Error! Reference source not found.** and Figure 4-3.

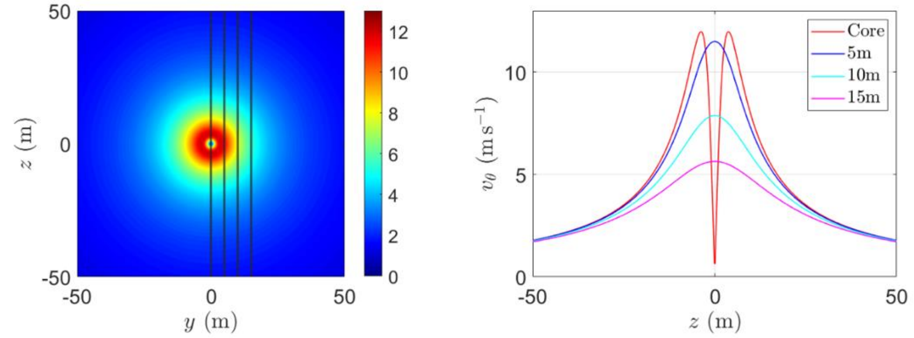

(a) BH Vortex for B747-400

(b) Tangential velocity for B747-400

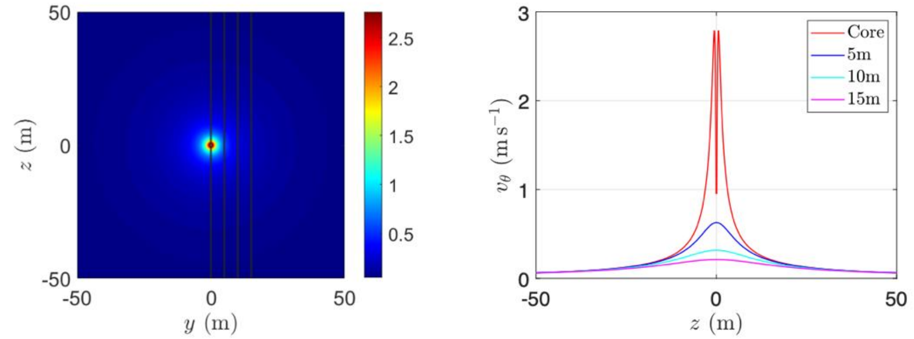

(c) BH Vortex for Cessna 172

(d) Tangential velocity for Cessna 172

Figure 4-1. Wake vortex generated for B747-400 and Cessna 172 using Burnham Hallock Model.

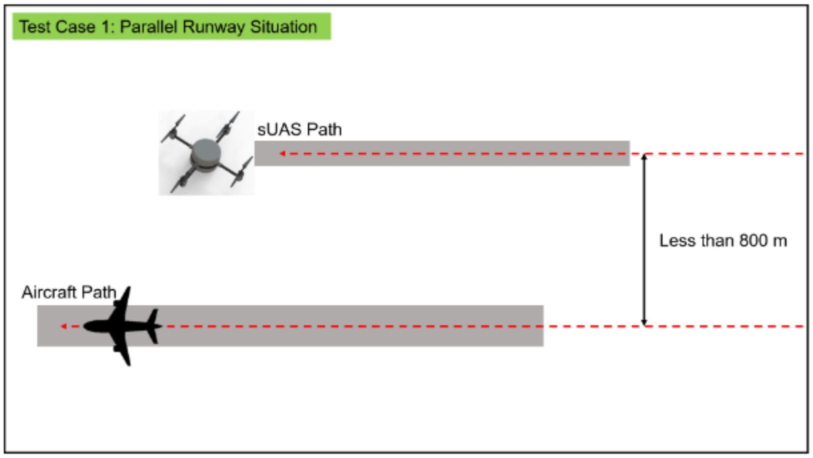

Figure 4-2. Example of one encounter scenario, sUAS flying parallel to the runway.

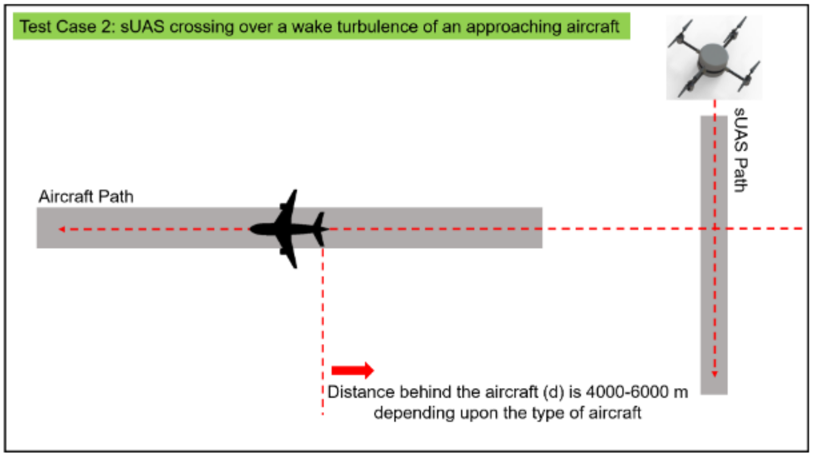

Figure 4-3. Example of second scenario, sUAS flying perpendicular to the runway.

4.2 Multirotor vehicle design

A highly instrumented Gen-2 quadrotor vehicle was designed and fabricated in-house at the Ohio State University, as shown Figure 4-4.

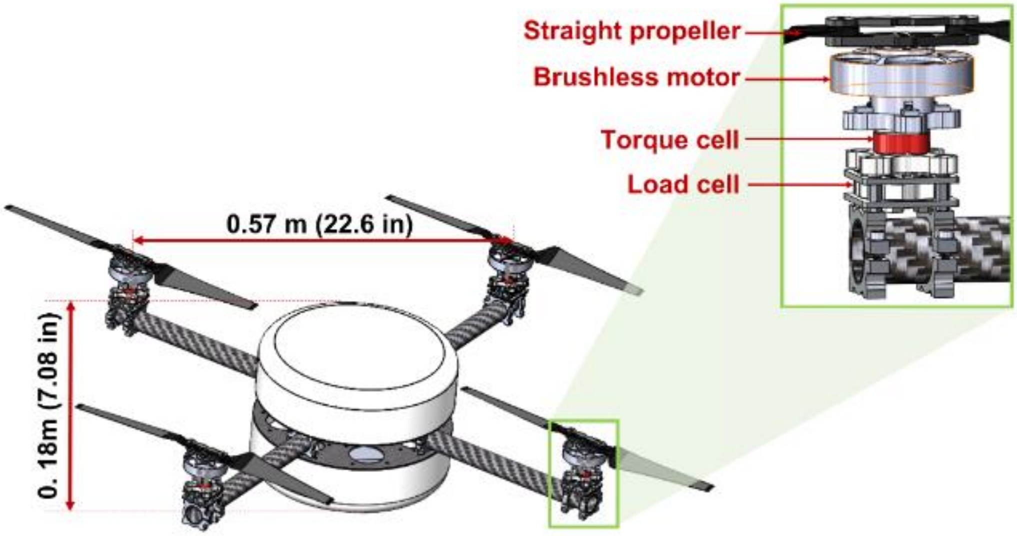

Figure 4-4. Instrumented flight vehicle designed at the Ohio State University with a motor mount shown close up.

An intricate motor mounting system was designed and constructed with load and torque cell integration capabilities in order to resolve the aerodynamic forces and moments acting on the rotors during flight. Each arm of the vehicle is equipped with a LTH300 Donut 22.67 kg (50 lb) Futek load cell to assess the thrust produced by each rotor in flight, which allows for a decoupled analysis of the trim state of the vehicle by separating out the forces produced by the rotors and the resulting moment acting on the body. This includes the effects of airframe, rotor-body, rotor-rotor, and moments generated in the forward flight by the inclination and asymmetric lift of the rotor disk.

The vehicle is 0.57 m long, 0.57 m wide and 0.18 m high and weighs approximately 3.72 kg. The vehicle is constructed primarily of carbon fiber and aluminum components with a fiberglass aerodynamic fairing for the central body and is stable up to flight speeds of approximately 20 ms^{-1}. The propulsion system is comprised of four T-Motor Antigravity MN5006 KV450 brushless motors arranged symmetrically about a central fuselage and are rated at 650 W and weigh 0.170 kg. The motors are matched with F35A 3-6s ESCs to provide throttle control and sufficient current to allow for higher flight speeds. T-motor MS1503 straight propellers are used, which are composed of carbon fiber and have a characteristic length and pitch of 38.1 cm and 14.22 cm, respectively.

Current and voltage consumption measurements for each of the four arms are resolved from an onboard power distribution board. A Pixhawk 4 flight controller paired with a Raspberry Pi 3B+ companion computer is employed to control the quadrotor during flight. Data acquisition is the main function of the companion computer and captures data at a constant sampling frequency of 200~Hz. Data communicated by the Pixhawk includes a description of the vehicle orientation and rotation within 3-dimensional space expressed as a quaternion, angular rates, accelerations, and velocities. Furthermore, a Real-Time Kinematic (RTK) GPS system is paired with received Pixhawk data to reduce uncertainty within attitude estimates. Additional details about the compositions and instrumentation of the Gen-2 flight vehicle have been discussed in McCrink *et al* [7].

4.3 Flight testing in the gust scenario

The upset criteria for multirotor UAS are fundamentally different than fixed wing vehicles but also depend greatly on the directionality and intensity of the gust encounter. Due to this sensitivity, the team invested heavily in developing wind measurement capabilities to characterize the flow field leading to upset.

Multiple flights were conducted through the gust profile using the instrumented multirotor at 2.44 m (8 ft) and 10 ms^{-1} ($32.8fts^{-1}$). Twelve passes were flown with azimuth angles varying between 0° and 90°. The flights were in an autonomous mode with a commanded, fixed course at a constant ground speed. Of note, the ambient winds were on the order of 5-10 kts in a quartering crosswind. These flights, all flown under similar ambient conditions, resulted in very different vehicle responses. This is likely due to a combination of asymmetries in the gust, and complex interactions between the rotor wake and environment.

The multirotor vehicle is geometrically symmetric, however opposing rotors rotate in opposite directions for yaw control. Therefore, when the vehicle is yawed at 90°, the leading rotors have the opposite rotational sense (rotating outward, away from the body) compared with the 0° yaw case. In addition to the thrust, other vehicle state variables were recorded including the vehicle attitudes, velocities, and position.

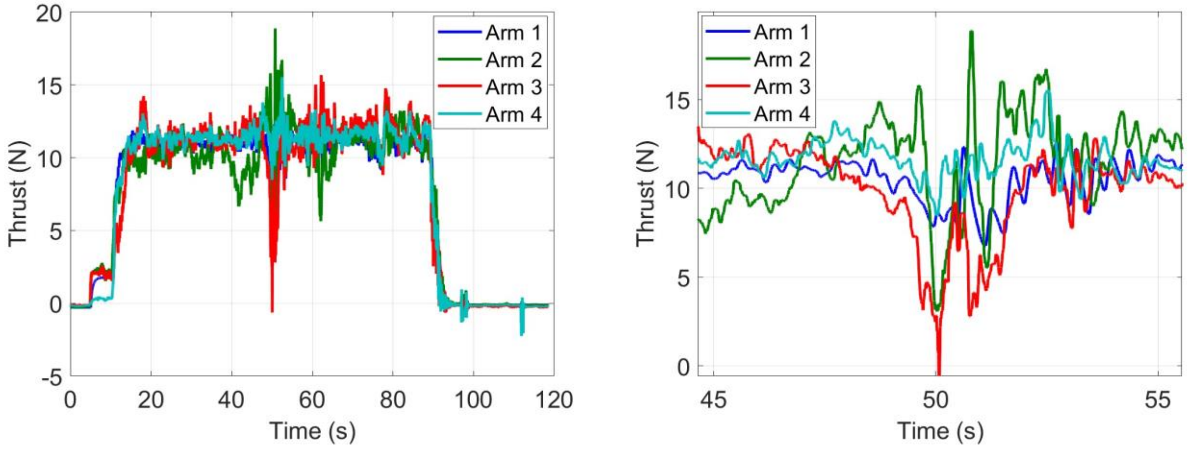

Figure 4-5. Raw thrust for each arm during gust encounter.

Figure 4-5 shows the raw thrust measured for each arm during one of the gust encounters. In this figure, the gust upset is clearly visible near the 50 second mark. Note the severe reduction in thrust occurring in arms 2 and 3, which corresponds to the arms closest to the fans. The zoomed-in view of the encounter (on the right) demonstrates large variations in rotor thrust occurring as the vehicle encounters the increasing lateral winds generated by the first three fans. In this case, the gradient induces oscillations in both the pitch and roll axes of the vehicle on the order of ±30◦ and with angular rates exceeding 120 degs−1, shown in Figure 4-6).

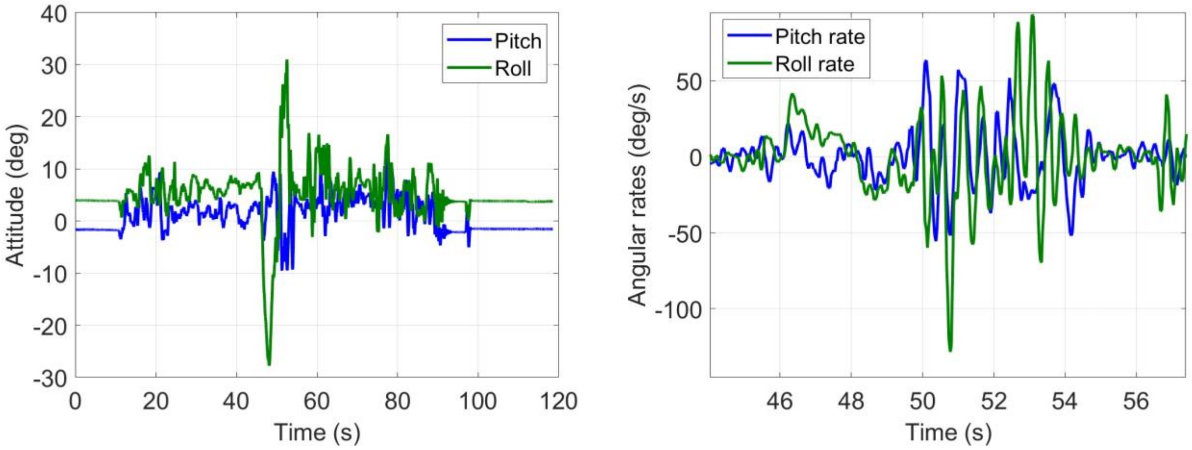

(a) Vehicle attitude (b) Vehicle rates

Figure 4-6. Attitude (left) and rates (right) for the vehicle during the flight test in gust scenario.

The increasing crosswind component leads to increased oscillations in the attitude of the vehicle which the onboard flight control system does not immediately damp. As the crosswind component diminishes moving from fans 4 to 6, the oscillations are quickly damped and the vehicle stabilizes. This behavior was noted for all encounters, and was not measurably sensitive to the vehicle yaw orientation.

The thrust data presented is directly measured at the base of the motors, and therefore captures the non-linear effects of changing inflow conditions. Kinematic corrections were applied to remove the inertial effects of vehicle motion to isolate the rotor loads. A common approach to modeling multirotor sUAS is through thrust maps, or a simplistic mapping between commanded rotor RPM and thrust. Figure 4-7 demonstrates what the thrust might look like from a simple linear model relating measured RPM to thrust using the motor constants provided by the manufacturer. This figure clearly shows that this simple approximation works relatively well when the vehicle is operated in a quasi-steady environment, before the gust encounter. The expanded image, as shown in Figure 4-7b, however, indicates that such models do not capture the sizeable variation in thrust during the gust encounter. It is clear from this data that more complex thrust models are necessary to accurately model the response of multirotor flight control systems to such upsets.

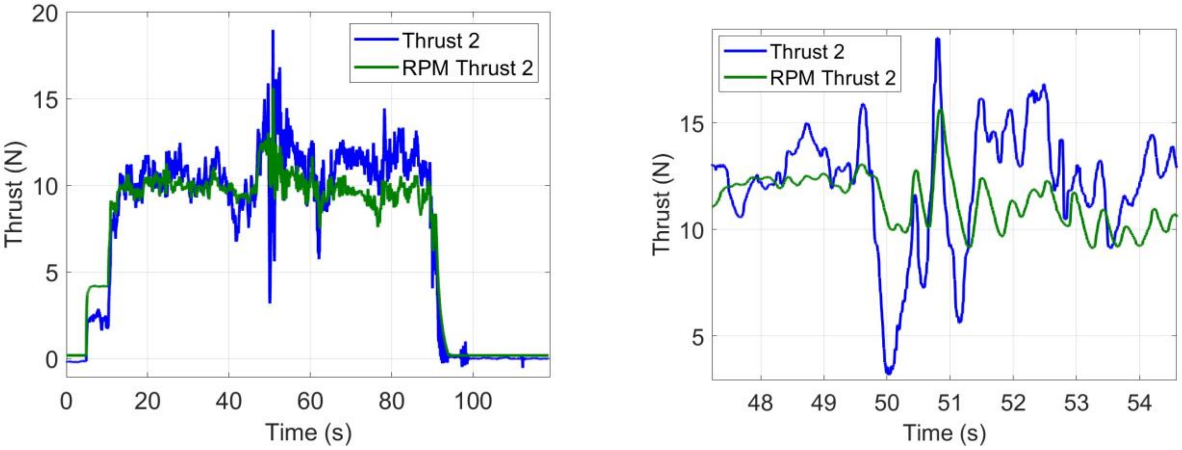

(a) all data (b) zoomed-in view

Figure 4-7. Comparison of raw thrust (blue) to the linear RPM based model (green) for arm 2

4.4 Loss of control metrics for multirotors

This work presented the modeling and experimental framework for assessing multirotor upset conditions due to gust and wake encounters. Wake encounters were developed based on canonical vortex models sized to represent large transport aircraft such as the Boeing 747 and smaller general aviation aircraft such as the Cessna 172. These represent opposite ends of the wake generation spectrum, but considering both situations allows for safe operating distances to be established for sUAS operating in various airport environments. The encounter scenario corresponding to a sUAS flight perpendicular to the runway was chosen for parameterization and experimental evaluation. A baseline gust encounter was extracted from the vortex models and a large array of outdoor fans configured to closely match the computed wind gradients. Characterization of the fan-generated gust encounter was performed using a reconfigurable sonic anemometer, sized specifically for future integration into the sUAS test vehicle. Details on the calibration of the anemometer using a large wind tunnel were presented, which indicates the anemometers have sufficient lateral accuracy for accurately capturing the complex flow field produced by the fan array. Results for operating the fans in an open-loop fashion indicates that the intended gust profile can be reproduced. After demonstrating the gust generation and measurement, a highly-instrumented multirotor was flown through the gust. These flights produced highly unstable oscillations in the vehicle, which were quickly damped by the flight controller after the encounter. Based on the data presented, it is clear that the thrust produced by each rotor undergoes significant oscillations from the steady-state trim condition preceding the encounter, and in some cases actually drops below zero. Comparative results were presented for a simplistic thrust model, which assumes the thrust is proportional to the individual rotor RPM. This simple model does not capture the large upset loads imposed by the gust encounter, and therefore indicates that the higher-order rotor models are required to assess the capabilities of onboard flight controllers in dealing with such encounters near the stability limits of the vehicle. Of note, the vehicle has also been operated in steady-state winds on the order of those induced by the fans, with no noticeable instabilities. Further work is underway to understand the impact of the gust gradient on the rotor loads, and to quantify the ability of the flight control system to react to such encounters.

The testing did not lead the team to make any quantitative assertions on wake upset criteria. Of the upsets that the team did encounter, the majority were at ambient wind speeds approaching the vehicle's flight speed. In this state, the fore/aft rotors have substantially different trim loads, and the mechanism associated with loss of control seemed to be related to either blade stall or rotor wake ingestion. In either case, a substantial departure occurred from measured thrust and the predictions from RPM-based thrust models. *This is akin to a control reversal in fixed-wing parlance, and the onboard controller had no ability to null the roll/pitch rates encountered.* The encounter lasted for approximately 1 second, and while this was enough to upset the vehicles attitude, it quickly recovered once the external disturbance was removed. The team observed that the rotor-rotor, rotor-body, and rotor-wake interactions were all of first-order importance to predicting the response characteristics of the vehicle. The team has previously used ROTCFD in our group to perform multirotor performance analyses, but have noted that even this advanced rotorcraft software had difficulties in accurately capturing rapidly time varying upset conditions. Hence, no additional computational investigations were performed as part of this work. One note, the idea of control reversal does apply to understanding multirotor upset, however without a full dynamic model of the vehicle, it has the same general features as a motor/esc/propulsion system failure. Most multirotor UAS do not have full feedback from each propulsor (current /voltage /RPM /IMU) to understand where the departure in commanded versus produced forces originate from. Full feedback from the propulsion system would allow for positive identification of loss of control using fairly straightforward linear rotor performance models and should be prioritized for future investigations.

4.5 References

[1] P. Ventura Diaz and S. Yoon, "High-fidelity computational aerodynamics of multi-rotor unmanned aerial vehicles," in *2018 AIAA Aerospace Sciences Meeting*, 2018, pp. 1266-1266.

[2] A. Thai, R. Jain, and S. Grace, "CFD Validation of Small Quadrotor Performance using CREATETM-AV Helios," in *VFS 75th Annual Forum & Technology Display*, 2019.

[3] Z. Wang *et al.*, "A comprehensive approach to study aerodynamic and aeroacoustic performances of small multicopter unmanned aerial systems," in *2018 AIAA Aerospace Sciences Meeting*, 2018, pp. 0268-0268.

[4] C. H. J. Wang, J. C. Nathanael, E. M. Ng, B. F. Ng, and K. H. Low, "Framework for the Estimation of Safe Wake Separation Distance between Same-Track Multi-Rotor UAS," ed.

[5] Z. Barbeau and J. D. Jacob, "Experimental Flight Test of Small UAS Wake Vortex Encounters," ed.

[6] A. Singhal, R. Thorpe, M. McCrink, and J. W. Gregory, "Flight Test Vehicle for Determination of Multi-Rotor UAV Trim Conditions," 2019.
[7] M. McCrink, D. Seth, and S. Herz, "Flight Test Measurement of Quadrotor Performance at Varying Sideslip Angles," 2022.
[8] D. Shukla and N. Komerath, "Low Reynolds number multirotor aerodynamic wake interactions," *Experiments in Fluids,* vol. 60, no. 4, pp. 1–14-1–14, 2019.
[9] S. Yoon, P. V. Diaz, D. D. Boyd Jr, W. M. Chan, and C. R. Theodore, "Computational aerodynamic modeling of small quadcopter vehicles," in *American Helicopter Society (AHS) 73rd Annual Forum Fort Worth, Texas*, 2017.
[10] M. L. Sutkowy, A. Pandey, M. McCrink, and J. W. Gregory, "Rotor Wake Structure Development in Low Reynolds Number Conditions," in *2018 AIAA Aerospace Sciences Meeting*, 2018, pp. 1830-1830.
[11] S. Sun, C. C. de Visser, and Q. Chu, "Quadrotor gray-box model identification from high-speed flight data," *Journal of Aircraft*, vol. 56, no. 2, pp. 645–661-645–661, 2019.
[12] N. N. Ahmad and F. Proctor, "Review of idealized aircraft wake vortex models," in *52nd Aerospace Sciences Meeting*, 2014, pp. 0927-0927.

5 UAS FLUTTER FLIGHT TESTING

5.1 Introduction to flutter analysis

The unexpected onset of aeroelastic flutter may be the most catastrophic and deadly setback that could occur during the certification process of a new aircraft design. Aeroelastic flutter occurs when an aircraft's aerodynamic and structural modes become unstable, resulting in unbounded structural oscillations. If an aircraft experiences flutter and corrective action is not immediately taken, the unstable structural response may cause severe damage to the vehicle, loss of aircraft, or loss of life.

For new or modified aircraft to pass certification requirements, flight testing must be accomplished that demonstrates freedom from flutter, proper damping margins, and non-rapid reduction of damping over the proposed flight envelope [1]. Historically, compliance with these requirements have been verified by operating the aircraft at progressively higher dynamic pressures until flutter onset is perceived to be imminent [2]. Unfortunately, this classical method is vulnerable to atmospheric turbulence and unintended deviations from the targeted flight condition since energy may be inadvertently added to the aircraft's structure, which could excite an unstable aeroelastic response. Furthermore, this test methodology cannot positively identify the flight conditions associated with flutter onset in a safe manner. Specifically, it is inadvisable to target a dynamic pressure corresponding to an aircraft's flutter boundary since any perturbation may result in unbounded and destructive structural oscillations. As a result, classical test procedures cannot be safely applied at the flutter onset condition and are restricted to a predictive nature[3]. With the growing desire to certify UAS for commercial operations, safe and accurate flight-test methodologies must be employed to demonstrate conformity with regulatory requirements.

The Parametric Flutter Margin (PFM) method developed by Roizner *et al.* [4] addresses the inadequacies of classical flutter flight testing techniques by allowing data to be collected in a safe manner at flight conditions exceeding the nominal aircraft's flutter boundary. The driving principle of the PFM method is that an aeroelastic system can be modified in a prescribed manner such that the flutter onset speed is artificially increased by the addition of a stabilizing element. The effects of such a stabilizing element are later accounted for by closing a hypothetical single-input single-output feedback system. A known excitation force is applied coincidently to the stabilizing element's position and the resulting structural dynamics are measured in order to compute Frequency Response Functions (FRF) [5]. The phase cross-over frequency is identified and the corresponding gain margin is noted for the given flight condition. This process is repeated for increasing dynamic pressures to obtain a gain margin versus velocity curve. Of particular interest is the velocity corresponding to a gain margin of 0 dB, which indicates the unmodified system's flutter boundary. Due to the addition of the stabilizing element, PFM flutter testing can be conducted at airspeeds exceeding the nominal flutter speed. Consequently, the PFM method may be utilized to positively identify the nominal aircraft's flutter boundary in a safe manner.

5.2 Design of flutter flight test vehicle

The Flutter Flight Test Vehicle shown in Figure 5-1 was developed for investigating the applicability of the experimental PFM method for small-scale UAS operating in a free-flight environment. The vehicle is a traditional tractor-style, tail-dragger monoplane design featuring a high-mounted wing and conventional empennage. Geometric and performance specification of the Flutter Flight Test Vehicle are listed in Table 5-1.

Figure 5-1. Flutter Flight Test Vehicle CAD rendering (left), and flying (right).

Table 5-1. Geometric and performance specification of the Flutter Flight Test Vehicle.

Characteristic	Metric	English
Length	1.7 m	65 in
Wingspan	3.4 m	134 in
Wing Area	1.15 m^2	1790 in^2
Horizontal Tail Area	0.17 m^2	260 in^2
Vertical Tail Area	0.06 m^2	100 in^2
Flying Weight	15.0 kg	33 lb
Stall Speed	9 m/sec	29 ft/sec
Cruise Speed	20 m/sec	66 ft/sec
Maximum Speed	35 m/sec	115 ft/sec

The Flutter Flight Test Vehicle has a straight, un-tapered rectangular wing featuring an SD-7043 airfoil and an aspect ratio of 10. The wing was constructed by joining 3D printed airfoil sections together along the front and rear spars. The airfoil sections were constructed from Nylon 12 material and manufactured using a Selective Laser Sintering machine. The front and rear spars were machined from aluminum 6061-T6 extrusions. Both the front and rear spars span the entire length of the wing and have a 1 in x 1 in hollow square cross-section and 0.75 in diameter hollow circular geometry, respectively. The flexible wing is equipped with 16 ADX333 3-axis accelerometers. Each wing half contains 8 accelerometers, which are equally distributed along the front and rear aluminum spars. Figure 5-2 shows the accelerometer distribution along the vehicle's right-wing half.

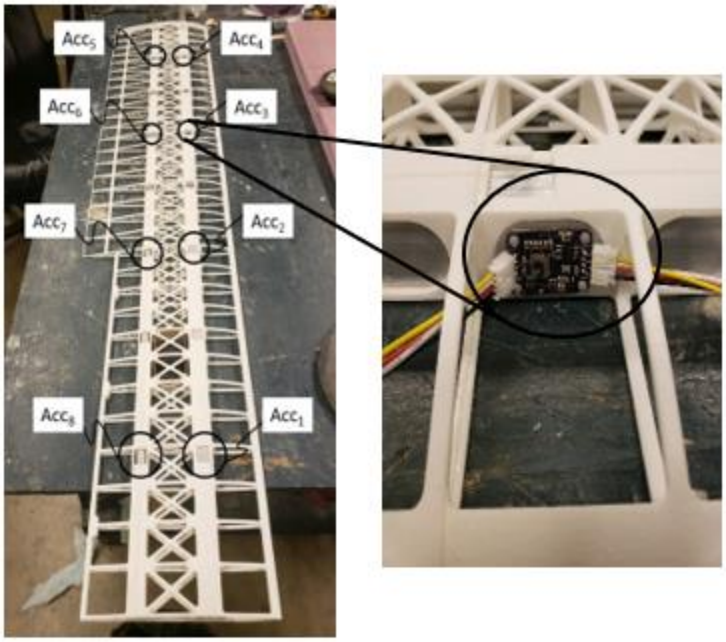

Figure 5-2. Accelerometer distribution of right wing.

The excitation force required for the PFM method is generated by the custom made electro-mechanical excitation pod depicted in Figure 5-3. The excitation pod system consists of a shaker assembly and command and control circuit board contained within a 0.61 m x 0.07 m cylindrical fiberglass structure mounted to each wingtip of the Flutter Flight Test Vehicle. The moving mass is driven by a linear voice coil motor and transverses a 60 mm long guide shaft such that the perturbation function acts perpendicular to the local chord line. Additionally, an MPU-9250 IMU is mounted to the moving mass such that the force applied to the wing's structure can be computed via Newton's laws of motion. A closed-loop position controller implemented through the command and control circuit board incorporates feedback from a Hall effect sensor and is utilized to track desired sinusoidal motion up to 20 Hz. The command and control circuit board is equipped with an additional MPU-9250 such that the flexible wing's plunge and torsional dynamics may be measured. Experimental data associated with both the excitation pod and flexible wing's distributed accelerometers are stored to a local micro-SD card at 200 Hz for post-test data reduction.

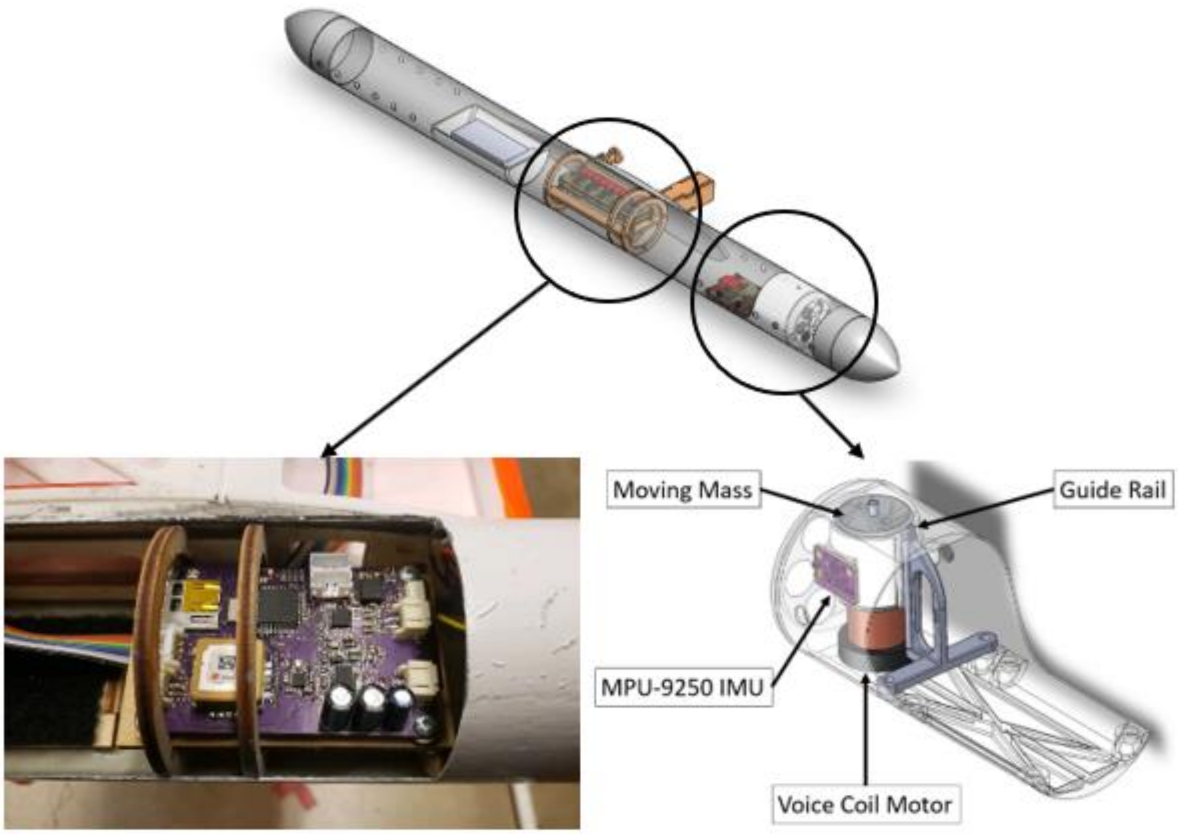

Figure 5-3. Excitation period (top center), command and control board (bottom left), and shaker assembly (bottom right).

In order to characterize the flexible wing's structural dynamic modes, the PFM method was used to analyze acceleration data collected throughout the Ground Vibration Testing (GVT) and flight-testing campaigns. Leveraging past research conducted by Karpel *et al.*, the transfer function of interest, defined in (30), was identified by utilizing MATLAB's *tfestimate* function.

$$T(i\omega) = \frac{-a_{st}(i\omega)}{a_{mv}(i\omega)} \tag{30}$$

An FRF of the Flutter Flight Test Vehicle's right main wing associated with a GVT performed in accordance with the experimental PFM method is presented in Figure 5-4. The experimental data used to identify the Bode plot presented below was collected by performing a 2 Hz-20 Hz frequency sweep with the excitation pod system described above. This Bode plot represents the transfer function between the right wing's base and moving mass acceleration signals and was evaluated through MATLAB's *tfestimate* function. By referencing the gain sub-plot, distinct peaks can be observed at an input frequency of approximately 3.8 Hz and 16.9 Hz. When compared to the dynamics perceived during the GVT trial, it can be concluded that these gain peaks correspond to the natural frequency of the flexible wing's first bending mode, and first torsional mode, respectively.

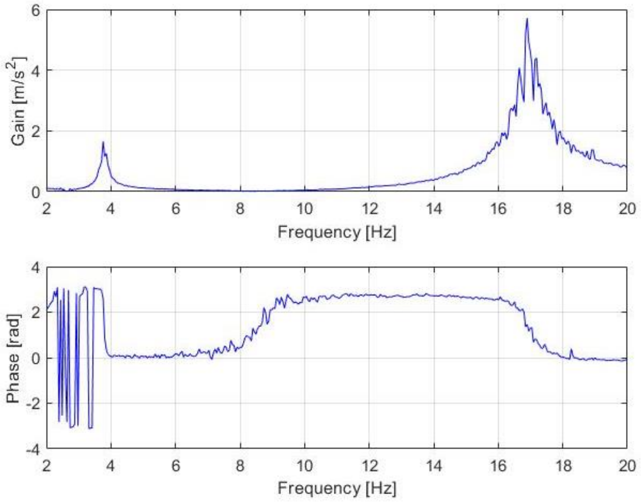

Figure 5-4. Right Wing's GVT FRF gathered in accordance with the experimental PFM Method.

A FRF of the Flutter Flight Test Vehicle's flexible main wing corresponding to a flight test performed at a True Airspeed (TAS) of 31.3 m/s is presented in Figure. 5.5. The data associated with Figure 5-5 was collected by performing a 2 Hz – 20 Hz frequency sweep over a 30 second period of straight-and-level, unaccelerated flight. In Figure 5-5, the right wing's identified transfer function is plotted in addition to the symmetric and anti-symmetric modes' experimentally derived FRFs. By noting the gain sub-plot, peaks in the symmetric mode's trendline can be observed at an input frequency of approximately 4.5 Hz and 17.4 Hz, which correspond to the first symmetric bending and first symmetric torsional modes, respectively. Additionally, the anti-symmetric trend line indicates the presence of the first anti-symmetric torsional mode at 16.2 Hz.

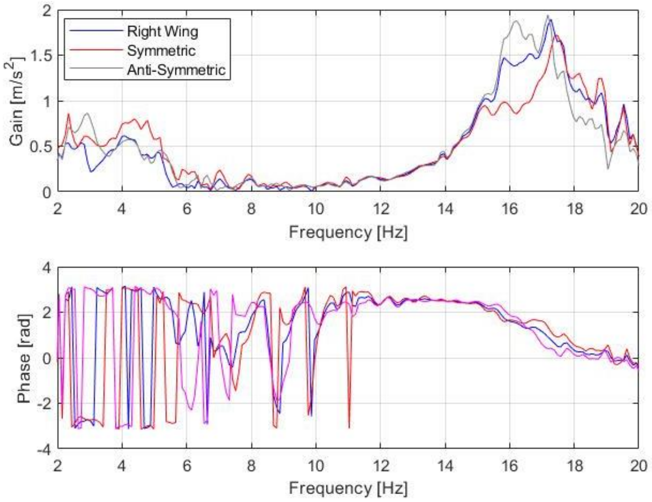

Figure 5-5. Right Wing's Flight Test FRF (TAS = 31.3 m/s).

5.3 References

[1] F. A. Regulations, "Part 23 Airworthiness Standards: Normal, Utility, Acrobatic and Commuter Category Airplanes," *Washington, DC: Federal Aviation Administration, Department of Transportation*, 1991.

[2] M. W. Kehoe, "A historical overview of flight flutter testing," in *AGARD Structures and Materials Panel Meeting,* 1995.

[3] F. Roizner, D. E. Raveh, and M. Karpel, "Safe flutter tests using parametric flutter margins," *Journal of Aircraft,* vol. 56, pp. 228–238, 2019.

[4] F. Roizner and M. Karpel, "Parametric flutter margin method for aeroservoelastic stability analysis," *AIAA Journal,* vol. 56, pp. 1011–1022, 2018.

[5] J. Sodja, F. Roizner, R. De Breuker, and M. Karpel, "Experimental characterisation of flutter and divergence of 2D wing section with stabilised response," *Aerospace Science and Technology,* vol. 78, pp. 542–552, 2018.

6 CONCLUSIONS

The over-arching goal of the wake vortex encounter research reported here is to identify the severity of such encounters *and* to recommend mitigations to reduce the severity of an encounter. In this context, “severity” means the degree to which the UAS response experiences loss of control. So, there are two basic questions: how is the response reliably predicted and how is loss of control identified?

The process to evaluate the severity of a WVE has been based on simulation using mathematical models of the aircraft dynamics and its navigation and control system. However, the validity of the simulations has been called into question because the predicted response states in a simulated WVE, such as angle of attack, pitch rate, etc., which are “abnormal”—that is, very different than the states associated with normal maneuvers—and which also possibly violate the assumptions on which the mathematical models are based.

The identification of the states which lead to loss of control is a difficult task. Based on flight testing in which loss of control has been observed, it has been established that the UAS states are not only highly abnormal but also that the basic assumptions on which the mathematical model are based have been violated. Therefore, one strategy is to ***not*** actually identify the conditions leading to or establishing LOC, but to, instead, for a given vortex strength, determine the combination of states for which the mathematical model begins to fail. This combination of states (for a given vortex strength) would establish the “Limit of Reliable Simulation” (LoRS) and, to be conservative, establish vortex circulation conditions into which the UAS should not fly. LoRS criteria, such as maximum allowable vertical acceleration, among others, have been suggested in Sections 3.1.1.6 and 3.1.2.4. Taking this path, then, establishes the vortex strength the UAS should not be allowed to encounter, that is, a predictable volume of airspace into which the UAS should not enter to be assured the mathematical model predicts UAS response which does not violate the assumptions of the mathematical model and, importantly, does not involve LOC. In other words, this strategy might admit that LOC ***might*** happen if the UAS enters this airspace: no one knows for sure, but being cautious makes sense.

Another strategy to avoid loss of control is to avoid the consideration of LOC at all and to, instead, prohibit a UAS from flying into any airspace in which the magnitude of the vortex strength is greater than the ambient circulation in the atmosphere—perhaps, a circulation of 75 m^2/s. This strategy is the easiest to apply since the airspace below and beside a wake-generating aircraft for which the circulation is greater than ambient is simple to define, and has been presented in this report, in Section 2.3. This “no-fly zone” or “wake hazard zone” could be established for combinations of wake-generating aircraft and UAS class as well as measures of the meteorological conditions to include ambient eddy decay rate and cross-wind velocity. Or, to be even more conservative, it could be established as the volume of airspace for the worst case combination of all environmental conditions.

Considering mitigation strategies based on wake hazard zones in general, over time, simulation models may get better, thereby expanding knowledge of what wake vortex circulations are safe for a given UAS. Also, flight testing UAS flying through actual wake vortices may provide information on what are safe vortex circulation intensities. As such, the expanse of the wake hazard zones could be reduced by petition by a UAS operator who conducts the flight-test-validated simulations and/or flight tests needed to establish the vortex strength which would lead to LOC for their UAS(s). To do so, they would need to perform analysis and flight testing of the same type reported in this study.

Another LOC mitigation strategy is to have a flight controller which increases robustness towards external disturbances. For example, flight test experiments in the presence of hazardous winds demonstrated the value of robust flight controllers capable of handling modeling errors and the nonlinear and unsteady aerodynamics encountered in flight. In particular, an artificial neural network flight controller was shown to be slightly better than MPC and LQR controllers. Controller robustness may also be improved by increasing situational awareness in the autopilot. The result would be a controller capable of sensing and identifying the risk of entering a loss of control condition. One such concept is using the sliding window correlation process reported here; that is, real-time calculation of state and control surface correlation to “inform” the controller when the observed correlations are abnormal, indicating approach to LOC.

Yet another LOC mitigation strategy is to take advantage of what has been demonstrated by highly skilled sUAS pilots, that is, by using reserve thrust to “power through” the onset of loss of control. Including such a mitigation strategy in an adaptive controller may also increase the resilience of a UAS in a wake vortex encounter.

Regarding the current state-of-the-art in sUAS flight simulation, a case can be made that fundamental research, possibly funded by NASA, might improve flight dynamics models to include nonlinear aerodynamic forces and moments. CFD may also provide some methods to improve physics-based models in wake encounter simulations.

Finally, one path to determining the severity of a wake vortex encounter is to conduct sUAS flight tests through actual aircraft wakes. The identification of the location of the wake vortex pair trailing a wake-generating aircraft is notoriously difficult. However, novel approaches to find the wakes and measure the velocity field therein would enable the value of such flights.